MICROSCALE DYNAMICS IN SUSPENSIONS OF NON-SPHERICAL PARTICLES

BY

AMIT KUMAR

DISSERTATION

Submitted in partial fulfillment of the requirements
for the degree of Doctor of Philosophy in Chemical Engineering
in the Graduate College of the
University of Illinois at Urbana-Champaign, 2010

Urbana, Illinois

Doctoral Committee:

Professor Jonathan J. L. Higdon, Chair
Professor Kenneth S. Schweizer
Assistant Professor Charles M. Schroeder
Assistant Professor Brendan A. Harley

Abstract

Numerical simulations were performed to investigate the microscale dynamics in suspensions of spherical and non-spherical particles. Two new algorithms were developed to enable studies with accurate hydrodynamics. The first algorithm was a high accuracy Stokesian Dynamics technique (SD) extended to a generic non-spherical particle shape. The many body interactions were computed using a novel scheme employing one body singularity solutions. Near field lubrication interactions employed standard asymptotic solutions for nearly touching convex particles. The second algorithm was a reduced precision near-field lubrication based method called Fast Lubrication Dynamics (FLD). In addition to the near field interactions, we introduced a novel isotropic resistance in FLD to match the mean particle mobility from the more detailed SD. The resulting FLD algorithm was shown to give results comparable to that from the detailed SD, while requiring only a fraction of the latter's computational expense.

In a first series of studies using the SD technique, we computed the transport properties in equilibrium suspensions of spheres and dicolloids. The latter particle shape was modeled as two intersecting spheres of varying radii and center to center separations. It was found that the infinite frequency viscosity as well as the short-time translational self-diffusivity are non-monotonic function of aspect ratio at any given non-dilute volume fraction with the minima in viscosity and the maxima in self-diffusivity around an aspect of 1.5. In contrast, the short-time rotational self-diffusivity was found to be a monotonically decreasing function of the aspect ratio at any given volume fraction.

In a second series of studies using the SD technique we investigated the microstructure, orientation, and rheology in suspensions of spheres and dicolloids over a wide range of volume fractions $0 \leq \phi \leq 0.55$. The particles had a very short range repulsive interparticle

interaction. The microstructure in suspensions of all particle shapes was found to be disordered for volume fractions $\phi \leq 0.5$, while a string like ordering was observed in suspensions of spheres and other particles with small degree of anisotropy at $\phi = 0.55$. Both the first and the second normal stress differences were negative for volume fractions up to $\phi = 0.5$, but some were positive at the highest volume fraction studied here ($\phi = 0.55$). The orientation behavior was found to be a function of both the fore-aft symmetry and the degree of anisotropy. For particles with fore-aft symmetry, in comparison to infinite dilution, a shift to higher orbit constants (increased alignment in the flow-gradient plane) was observed at low volume fractions. On the other hand, the particle lacking fore-aft symmetry showed virtually no change in its orientation distribution at low volume fractions. At higher volume fractions ($\phi \geq 0.2$), in comparison to the dilute suspensions, a shift towards lower orbit constants (increased alignment with the vorticity axis) was observed for all particle shapes. The degree of this alignment was found to increase with volume fraction for particles with small degree of anisotropy, while it was found to plateau at relatively low volume fractions in suspensions of particles with the largest degree of anisotropy. The observed orientation behavior was explained using a novel analysis technique based on the coupling of particle's angular velocity and hydrodynamic stresslet through the mobility tensor.

Next, we investigated microstructure and orientation in Brownian suspensions of spheres and dicolloids using the FLD algorithm. Results are reported for two different volume fractions, $\phi = 42\%$ and $\phi = 55\%$. The 42% sample had a long range repulsive electrostatic interaction, while the 55% sample had hard-sphere type interaction. Particles with small degree of anisotropy showed microstructural transitions similar to that of spheres. In contrast, particles with relatively larger degree of anisotropy showed a significantly different microstructural behavior. At low shear rates, irrespective of the degree of anisotropy, an orientationally disordered state was observed. Upon further increase in the rate of shear, an increase in flow alignment is obtained, with the maximum flow alignment typically observed between $Pe = 1$ and $Pe = 20$ depending on the particle shape. With a further increase in the rate of shear, an increase in vorticity alignment is seen for all particle shapes. The degree of anisotropy and volume fraction was found to have a significant impact on the extent of increase in the flow or the vorticity alignment.

Using FLD simulations we next investigated the phase behavior and rheology in charged colloidal suspensions at a volume fraction of $\phi = 0.33$. It was shown that for a given screening length of the repulsive interaction, there existed a range of surface potentials for which both the ordered and disordered metastable states exist. This range was found to have a strong dependence on shear rate and was found to have a maximum width around $Pe = 0.5$, where $Pe = \dot{\gamma}a^2/D_0$. The presence of both the ordered and disordered metastable states allowed us to simultaneously characterize both the branches of viscosity as a function of shear rate. It was observed that the disordered branch can have a lower viscosity than the ordered branch at low shear rates ($Pe < 0.05$ in this study). This was attributed to the much smaller long-time self-diffusivity in the ordered state, which leads to a greater distortion of the microstructure and hence stress at the same shear rate. At higher shear rates, on the other hand, ordered states with close packed planes aligned in the flow-vorticity direction were able to minimize the distortive effects of shear, and hence have lower viscosities than the corresponding disordered states. The microstructural dynamics revealed in these studies explains the anomalous behavior and hysteresis loops in stress data reported in the literature.

In a last series of studies using the FLD algorithm, we investigated the shear thickening phenomena in suspensions of spheres. Using a short range repulsive force to control the gap-size in a shearing suspension, it was shown that the suspension viscosity has a much weaker logarithmic dependence on the minimum gap size present in the suspension. This dependence of the viscosity on the minimum gap size was shown to persist even at volume fractions as high as $\phi = 0.62$. This study poses intriguing questions about the origins of discontinuous shear thickening in these systems which is commonly observed in experiments.

To my parents

Acknowledgments

First of all, I would like to thank my adviser Prof. Jonathan J. L. Higdon. I've learned a lot working with him, both inside and outside of research, and I sincerely value this education.

I would also like to thank my current and former group members, including Kenneth Higa and Michael Bybee. I particularly enjoyed going to lunch with Kenny and the numerous discussions we had on wide ranging topics. I would also like to thank my friends in Urbana, particularly my former roommates Nitish Korula and Nitish Nair.

Above all, I would like to thank my parents and my sister for their unconditional love and support without which this work would not have been possible.

This work was supported by the National Science Foundation and by the National Institute for Nano-Engineering program at Sandia National Labs.

Table of Contents

Chapter 1

Introduction

Suspensions of nanoparticles have found widespread applications in a variety of settings including coatings, paints, food products, and personal care products among others (Larson, 1998). In more recent times, there has been an explosion of interest in nanoparticles as a tool for realizing the goals of nanotechnology (Hamley, 2003). Some modern applications of these nanoparticles include targeted drug delivery (Goldberg *et al.*, 2007), self assembly into advanced materials like photonic band gap materials (Xia *et al.*, 2000), treating cancer using magnetic hyperthermia (Pankhurst *et al.*, 2003), enhancement of thermal conductivity using nanofluids (Eastman *et al.*, 2001), as a probe of rheological properties in microrheology (Mason & Weitz, 1995; Squires & Brady, 2005), and enhanced mixing in microfluidics (Lopez & Graham, 2008).

Given the wide ranging applications envisioned for particle suspensions, it is therefore of great interest to gain and advance the fundamental understanding of such systems–a goal which motivated this work. A particular focus of this work is to elucidate the microstructural and orientational dynamics in suspensions of non-spherical particle. In this work we study such systems using numerical simulations. The most challenging aspect in these simulations is the computation of the hydrodynamic interaction between the particles, i.e. the interaction between the particles transmitted though the stresses generated in the suspending fluid. We present two new algorithms in this work for computing the hydrodynamic interactions with varying level of precision and computational expense. First is the Stokesian Dynamics technique which has been extended here to model hydrodynamic interactions between particles of arbitrary non-spherical shape. This method, presented in chapter (2), accurately captures both the far-field many body interactions as well as the near field lubrication interactions. Second is the Fast Lubrication Dynamics technique in which we have replaced

the computationally expensive many body interactions in Stokesian Dynamics by a properly calibrated isotropic resistance. The near field is retained with some modifications. This method is presented in chapter (6).

A series of studies employing the aforementioned algorithms are also presented. All of our studies on non-spherical particles were restricted to the recently synthesized dicolloidal particles (Johnson *et al.*, 2005; Mock *et al.*, 2006; Kim *et al.*, 2006). A dicolloidal particle was modeled in this work as two intersecting spheres of varying radii and center to center separation. In chapter (2) we present hydrodynamic transport properties like viscosity and self-diffusivity in equilibrium suspensions of dicolloids. These studies were performed using the Stokesian Dynamics technique. In chapter (3) we present orientational, microstructural, and rheological behavior in sheared suspensions of dicolloidal particles also studied using the Stokesian Dynamics technique. All the studies detailed next were performed using the Fast Lubrication Dynamics technique. In chapter (4), we present the microstructural and orientational behavior in sheared suspensions of Brownian dicolloids. Next, in chapter (5), we present the phase behavior and its rheological consequences in sheared suspensions of charged Brownian spheres. In chapter (7) we present some preliminary results from our studies on the shear thickening phenomena. We conclude by summarizing the important aspects of this study in chapter (8).

References

Eastman, J. A., Choi, S. U. S., Li, S., Yu, W., & Thompson, L. J. 2001. Anomalously increased effective thermal conductivities of ethylene glycol-based nanofluids containing copper nanoparticles. *Applied Physics Letters*, **78**, 718–720.

Goldberg, M., Langer, R., & Jia, X. 2007. Nanostructured materials for applications in drug delivery and tissue engineering. *Journal of Biomaterials Science, Polymer Edition*, **18**, 241–268.

Hamley, I. W. 2003. Nanotechnology with Soft Materials. *Angewandte Chemie International Edition*, **42**, 1692–1712.

Johnson, P.M., van Kats, C.M., & van Blaaderen, A. 2005. Synthesis of Colloidal Silica Dumbbells. *Langmuir*, **21**(24), 11510–11517.

Kim, J.W., Larsen, R.J., & Weitz, D.A. 2006. Synthesis of nonspherical colloidal particles with anisotropic properties. *Journal of American Chemical Society*, **128**(44), 14374–14377.

Larson, R. G. 1998. *The Structure and Rheology of Complex Fluids*. Oxford University Press.

Lopez, M., & Graham, M. D. 2008. Enhancement of mixing and adsorption in microfluidic devices by shear-induced diffusion and topography-induced secondary flow. *Physics of Fluids*, **20**, 053304.

Mason, T. G., & Weitz, D. A. 1995. Optical Measurements of Frequency-Dependent Linear Viscoelastic Moduli of Complex Fluids. *Physical Review Letters*, **74**, 1250–1253.

Mock, E.B., Bruyn, H. De, Hawkett, B.S., Gilbert, R.G., & Zukoski, C.F. 2006. Synthesis of

Anisotropic Nanoparticles by Seeded Emulsion Polymerization. *Langmuir*, **22**(9), 4037–4043.

Pankhurst, Q. A., Connolly, J., Jones, S. K., & Dobson, J. 2003. Applications of magnetic nanoparticles in biomedicine. *Journal of Physics D: Applied Physics*, **36**, R167–R181.

Squires, T. M., & Brady, J. F. 2005. A simple paradigm for active and nonlinear microrheology. *Physics of Fluids*, **17**, 073101.

Xia, Y. N., Gates, B., Yin, Y. D., & Lu, Y. 2000. Monodispersed colloidal spheres: Old materials with new applications. *Advanced Materials*, **12**, 693–713.

Chapter 2

PME Stokesian Dynamics for Non-Spherical Particles

Synopsis

A PME Stokesian Dynamics algorithm has been developed to model hydrodynamic interactions in suspensions of non-spherical dicolloidal particles. Dicolloids, which have recently been synthesized by a number of independent research groups (Johnson *et al.*, 2005; Mock *et al.*, 2006; Kim *et al.*, 2006), consist of two intersecting spheres of varying radii and center to center separation. One body resistance tensors and disturbance velocity fields are computed for general linear flows using a superposition of Stokes singularities along the symmetry axis of the dicolloid particles. The coefficients and the locations of the singularities are optimized to minimize the norm of the velocity error on the particle surface. The one-body solution provides all coefficients required for the far field many-body interactions in the Stokesian dynamics algorithm. These generalize the analytical results for spheres employed in the classic algorithm. Modified lubrication interaction tensors are developed for dicolloids for the singular near field lubrication interactions. Accuracy of the one-body solutions and two-body generalized Stokesian dynamics solutions are validated by comparison with high precision numerical solutions computed with the spectral boundary element method of Muldowney & Higdon (1995). The newly developed PME Stokesian dynamics algorithm was used to study transport properties in dicolloidal suspensions over a range of volume fractions ($\phi \leq 0.5$). The effects of the degree of anisotropy on the properties of the suspension are discussed. For these mildly anisotropic particles, the transport properties remain close to those of spheres, however certain interesting trends emerge, with non-monotonic viscosity dependence as a function of increasing aspect ratio. The minimum viscosity in concentrated suspensions is lower than that for spheres with equal volume fraction over a range of volume fractions.

2.1 Introduction

In recent times, the synthesis of a variety of non-spherical colloidal particles has generated considerable interest in a wide variety of fields. Applications envisioned for such particles range from assembly into advanced materials (Glotzer & Solomon, 2007) and to drug delivery (Mitragotri & lahann, 2008) among others. A number of research groups (Johnson *et al.* (2005),Mock *et al.* (2006), Kim *et al.* (2006)) have focused on synthesis of dicolloids (dimers composed of two colloidal spheres) or oligomers involving higher numbers of constituent spheres. Sizes for these particles range from 100 nanometers up to several microns. In contrast to anisotropic particles such as long rods or discs, these particles are of modest aspect ratio typically in the range of 1 to 2. The attraction of the new particles is that they may be assembled into a greater variety of lattices than traditional FCC, BCC lattices with lower levels of stimulus required to achieve such phase transitions (Mock & Zukoski, 2007; Gerbode *et al.*, 2008). To achieve assembly of these anisotropic particles into ordered lattices or other microstructures, a variety of processing strategies are being considered involving concentrated suspensions of particles subject to shear flows, sedimentation, pressure filtration, draining film flows, and convective assembly (Hosein & Liddell, 2007). Under these conditions, hydrodynamic interactions among the particles may play an important role in determining the dynamics of the microstructure development in the suspension.

Given the interest in processing suspensions of these novel particles, it is important to develop algorithms for the accurate and efficient computation of hydrodynamic interactions among particles of non-spherical shape. Over the past two decades, Stokesian dynamics techniques has been employed successfully to model the hydrodynamic interactions in suspensions for a variety of particles including spheres, spheroids and slender fibers (Brady & Bossis, 1988; Claeys & Brady, 1993a; Sierou & Brady, 2001; Butler & Shaqfeh, 2002; Saintillan *et al.*, 2005). In this work, we will extend the Stokesian dynamics technique to dicolloidal particles, which can be modelled as two fused spheres of varying radii and center-to-center separation (see Figure 2.1). For previous implementations of Stokesian dynamics, theoretical solutions for the one body hydrodynamics have been available in terms of fundamental singularities (spheres)or prescribed distributions of singularities along the particle

axis (spheroids, slender bodies). In the present effort, a distributed singularity method will be developed for the one-body solution in a given flow. The one body solution forms an integral part of the computation of far-field many-body interactions in Stokesian dynamics. In addition, we develop modified representations for the near field lubrication interactions based on asymptotic expressions for spheres and numerically determined correction factors for the dicolloidal particle geometries.

The distributed singularity approach used to construct solutions for the one body hydrodynamics of non-spherical particles in this effort follows an approach which has been common in the literature on low Reynolds number flows. Examples include the slender body theory of Batchelor (1970) utilizing a line distribution of Stokeslets along the axis of body, and the exact solutions for spheroidal particles by Chwang & Wu (1975) using a continuous distribution of low order singularities (Stokeslet, Stokes Doublet,Potential Dipole and Potential Quadrupole) along the major axis for uniform and linear flows. Later, Wu (1984) employed distributed high order Sampson's spherical singularities along the axis of a general axisymmetric body, and found their coefficients by satisfying the no-slip boundary condition at properly chosen collocation points. Zhou & Pozrikidis (1995) used a similar approach with an adaptive algorithm to optimize both the strengths and the locations of singularities, so as to satisfy the boundary conditions with the highest accuracy. These authors used Stokeslet, Potential dipole, and a rotlet (antisymmetric Stokes Doublet) to represent the disturbance velocity in ambient flows of up to linear order for spherical and other non spherical particles like spheroids. A more detailed account of this and other related methods may be found in the extensive review article by Weinbaum & Ganatos (1990).

Several authors have adapted the distributed singularity method for use with the Stokesian dynamics technique. Claeys & Brady (1993a) used the exact singularity solutions developed by Chwang & Wu (1975) for approximating the far-field term in their Stokesian dynamics technique on spheroids, while asymptotic lubrication theory for arbitrary convex particles (Claeys & Brady, 1989) was used for the near field interactions. The method was used to compute transport properties of spheroidal suspensions including the diffusivity, resistivity and viscosity. Two types of particle configurations were studied - statistically homogeneous suspensions (Claeys & Brady, 1993b) and crystalline ordered suspensions (Claeys & Brady,

1993c), however no dynamic simulations were performed. Butler & Shaqfeh (2002) and Saintillan *et al.* (2005) used the slender body theory developed by Batchelor (1970) for approximating the far-field interactions in their Stokesian dynamics technique for fibers. Again, for the lubrication correction, they used the asymptotic formulas developed by Claeys & Brady (1989). The method was used to study the sedimentation of fibers. Meng & Higdon (2008a) developed Stokesian dynamics for plate-like particles by modelling them as rigid planar assemblages of spheres. This technique, which in effect involves constrained motion of spheres, allowed for the use of singularity solutions for spheres in the far-field term and the classic lubrication results for spheres in the near-field interactions. Meng & Higdon (2008b) extended their approach to incorporate Brownian interactions and employed these algorithms to investigate the effect of aspect ratio, Brownian motion, and shear on suspensions of plate-like particles describing the microstructure, orientation correlation, and viscosity.

The primary goal of the present work is to extend the Stokesian dynamics technique to dicolloidal particles. However, the algorithm presented here may be easily adapted to particles of more complex shape. Here, we will focus on four specific examples of particle shape including spheres and three different dicolloids. In this article, we will restrict our efforts to investigating instantaneous properties of homogeneous suspensions, while dynamic simulations for microstructure and rheology of dicolloidal suspensions in shear flows will be discussed in a subsequent article. The organization of this article is as follows: in Section (2.2) we present the problem formulation as relates to hydrodynamic interactions. Section 2.3 provides details of the singularity solution method for the one body problem, while development of the far-field many-body interactions is presented in Section 2.4. Near-field terms are considered in Section 2.5, and the overall algorithm for PME Stokesian dynamics with an efficient O(N ln N) implementation is given in Section 2.6. Results from the numerical simulations are presented in Section 2.7 followed by concluding remarks in Section 2.8. Additional details concerning the determination of coefficients in the singularity solution procedure are given in the Appendix.

2.2 Formulation

The motion of small non-Brownian particles in a viscous fluid can be described by Newton's second law written as

$$\mathbf{m} \cdot \frac{d\mathbf{U}}{dt} = \mathbf{F}^H + \mathbf{F}^P, \tag{2.1}$$

where $\mathbf{m}$ is the mass/moment of inertia tensor of the particles, $\mathbf{U}$ is the generalized velocity/angular velocity vector, while $\mathbf{F}^H$ and $\mathbf{F}^P$ are the generalized force/torque vectors arising from the hydrodynamic stress in the fluid and from the interparticle interactions respectively. Here the vectors $\mathbf{U}$, $\mathbf{F}^H$ and $\mathbf{F}^P$ are $6N$ vectors where N is the number of particles in the system; and the mass/moment of inertia $\mathbf{m}$ is a $6N$ square block diagonal matrix where each 6×6 block consists of the mass and moment of inertia tensor of each individual particle. We assume that the particle size is small, and the inertial effects are negligible on the time scales of interest to us. With this assumption, the left hand side of (2.1) is zero, and the sum of the forces and torques on each individual particle must be zero at every instant of time. Fluid motion around the particles is governed by the continuity and steady Stokes equation

$$\begin{aligned} \boldsymbol{\nabla} \cdot \mathbf{u} &= 0 \\ -\boldsymbol{\nabla} p + \mu \nabla^2 \mathbf{u} &= 0 \end{aligned} \tag{2.2}$$

where p represents the pressure in the fluid while $\mathbf{u}$ is its velocity.

In low Reynolds number flow, the hydrodynamic force on each particle is a linear function of the fluid velocity and may be determined from the solution of the above equations for a specified set of particle configurations, particle velocities and of a prescribed undisturbed flow field. The linear relationship may be expressed in terms of a configuration dependent N body resistance tensor $\mathbf{R}$ as follows

$$\begin{pmatrix} \mathbf{F}^H \\ \mathbf{S}^H \end{pmatrix} = \mathbf{R} \cdot \begin{pmatrix} \mathbf{u}^\infty - \mathbf{U} \\ \mathbf{E}^\infty \end{pmatrix} \tag{2.3}$$

In this equation, a homogeneous undisturbed linear flow is assumed which determines the generalized velocity/angular velocity $\mathbf{u}^\infty$ evaluated at the center of each particle and the

uniform rate of strain tensor denoted by $\mathbf{E}^{\infty}$. $\mathbf{F}^{H}$ is the usual force/torque $6N$ vector and $\mathbf{S}^{H}$ denotes the stresslets on the particle, the symmetric part of the first moment of the force on each particle, and can be expressed by a $5N$ vector.

For specified external and interparticle forces, the velocity and angular velocity may be calculated as the solution of a linear system as defined in section (2.6) below. The particle positions and orientations may then be integrated over time to trace the dynamics of the particle suspension. The primary computational challenge is to compute the configurational dependent N body resistance tensor at each time step. Alternatively, iterative solutions techniques may be employed which avoid the computation of the full resistance matrix at each step. In our simulations, the hydrodynamic interactions are calculated using a method similar to the Stokesian dynamics algorithm for spheres, appropriately modified for non-spherical dicolloidal particles. In Stokesian dynamics, the total resistance tensor $\mathbf{R}$ in equation (2.3) is expressed by the following approximation

$$\mathbf{R} \approx \mathbf{R}^{MB} + \mathbf{R}^{LB} \tag{2.4}$$

where $\mathbf{R}^{MB}$ is a many-body resistance tensor accurate for widely separated particles. When particles come near contact however, the small particle gaps lead to strong interactions with $\mathbf{R}$ diverging at contact. The many body resistance tensor cannot capture this singular behavior due to the truncated multipole expansion employed in its calculation (see section 2.4), hence, a correction term is added to account for the missing terms. This correction tensor denoted by $\mathbf{R}^{LB}$ is based on asymptotic lubrication theory for nearly touching particles. Unlike $\mathbf{R}^{MB}$, $\mathbf{R}^{LB}$ is a sparse matrix as the lubrication interactions affect only near neighbors, and most importantly, the asymptotic lubrication contributions are pairwise additive as the interaction is highly localized around the point of contact.

2.3 Singularity Solution for Dicolloidal Particles - Single Particle Flows

Given an undisturbed fluid flow field $\boldsymbol{u}^{\infty}(\boldsymbol{x})$, the disturbance velocity $\boldsymbol{u}^{D}(\boldsymbol{x})$ is that velocity induced by the presence of the particle which yields a total velocity which satisfies the no-slip boundary condition on the surface of the particle. The total velocity is defined as

$$\boldsymbol{u}(\boldsymbol{x}) = \boldsymbol{u}^{D}(\boldsymbol{x}) + \boldsymbol{u}^{\infty}(\boldsymbol{x}) \tag{2.5}$$

For rigid particles, velocity on the surface of the particle is given by

$$\boldsymbol{u}_p(\boldsymbol{x}_s) = \boldsymbol{U}_p + \boldsymbol{\Omega}_p \times \boldsymbol{x}_s \tag{2.6}$$

where $\boldsymbol{U}_p$ and $\boldsymbol{\Omega}_p$ are the velocity and angular velocity of the particle respectively.

The no-slip boundary condition then requires

$$\boldsymbol{u}(\boldsymbol{x}_s) = \boldsymbol{u}_p(\boldsymbol{x}_s) \tag{2.7}$$

for every point $\boldsymbol{x}_s$ on the surface of the particle.

The challenge in any solution procedure in Stokes flow is to develop an efficient representation for the disturbance velocity $\boldsymbol{u}^{D}(\boldsymbol{x})$ which satisfies the no-slip boundary condition to a reasonable standard of precision. Singularity solutions are ideal for this purpose as they induce strong velocity fields near the location of the singularity and decay at large distances thereby preserving the proper boundary conditions at infinity. In this article, we choose a small collection of singularities placed in the interior of the particles and choose the locations of the singularities to assure an accurate velocity field with a small number of singularities. Recall that the collection of singularities required to represent the exact solution for a sphere translating with arbitrary velocity and angular velocity in a linear undisturbed flow includes the Stokeslet, Stokes doublet, Potential Dipole and Potential Quadrupole with all singularities located at the center of the sphere. Here, for dicolloidal particles, we choose the same collection of singularities, but include independent sets located at N different positions $\boldsymbol{x}_l$

along the symmetry axis of the particle.

We define the kernels for the Stokeslet, Stokes Doublet, Potential Dipole and Potential Quadrupole respectively as

$$\begin{aligned} S_{ij}(\boldsymbol{x}) &= \frac{\delta_{ij}}{r} + \frac{x_i x_j}{r^3} \\ SD_{ijk}(\boldsymbol{x}) &= \frac{\partial S_{ij}(\boldsymbol{x})}{\partial x_k} \\ PD_{ij}(\boldsymbol{x}) &= \nabla^2 S_{ij}(\boldsymbol{x}) \\ PQ_{ijk}(\boldsymbol{x}) &= \nabla^2 \frac{\partial S_{ij}(\boldsymbol{x})}{\partial x_k} \end{aligned} \tag{2.8}$$

and let their strengths be represented by coefficients $\boldsymbol{p}$, $\boldsymbol{q}$, $\boldsymbol{s}$, and $\boldsymbol{t}$ respectively.

The disturbance velocity represented by the collection of singularities at the different points $\boldsymbol{x}_l$ is then written

$$\begin{aligned} u_i^D(\boldsymbol{x}) = \sum_{l=1}^{l=N} & p_j^l S_{ij}(\boldsymbol{x} - \boldsymbol{x}_l) \; + \; q_{jk}^l SD_{ijk}(\boldsymbol{x} - \boldsymbol{x}_l) + \\ & s_j^l PD_{ij}(\boldsymbol{x} - \boldsymbol{x}_l) \; + \; t_{jk}^l PQ_{ijk}(\boldsymbol{x} - \boldsymbol{x}_l) \end{aligned} \tag{2.9}$$

Our goal is to determine the unknown coefficients of the singularities in eq (2.9) which yields the best approximation of the exact velocity field. Early researchers using singularity methods chose to satisfy the boundary condition at a collection of collocation points leading to a linear system or linear least squares problem to solve for the coefficients. The collocation points were usually distributed according to some heuristic reasoning based on particle geometry. Here we avoid such issues and require that the coefficients be chosen to minimize the L_2 norm of the velocity error over the surface of the particle. A similar approach was employed by Zhou & Pozrikidis (1995). We let $\hat{\boldsymbol{u}}(\boldsymbol{x}_s) = \boldsymbol{u}_p(\boldsymbol{x}_s) - \boldsymbol{u}(\boldsymbol{x}_s)$ represent the point-wise error in the velocity on the boundary and the L_2 norm of the error is then defined as

$$||\hat{\boldsymbol{u}}||^2_{(\partial D)} = \int_{\partial D} \hat{\boldsymbol{u}}.\hat{\boldsymbol{u}} dS \tag{2.10}$$

With an appropriate choice of numerical quadrature formula for the integration, this may be written in discretized form as

$$||\hat{\boldsymbol{u}}||^2_{(\partial D)} = \sum_\alpha w_\alpha \hat{\boldsymbol{u}}_\alpha . \hat{\boldsymbol{u}}_\alpha \tag{2.11}$$

where the summation extends over N_Q quadrature points α and w_α is the appropriate weight based on the quadrature formula and surface element dS. For any well conditioned quadrature formula, w_α is positive for all α.

Equation 2.11 leads directly to a standard linear least squares problem for the unknown coefficients which may be efficiently solved using standard algorithms in linear algebra. Briefly, assemble the velocity components at all of the quadrature points into a vector u_i of length $3N_Q$. Assemble all of the unknown coefficients $\boldsymbol{p}$, $\boldsymbol{q}$, $\boldsymbol{s}$, and $\boldsymbol{t}$ into a vector z_j of length N_C. With the linear relationship between velocity and the unknown coefficients, the velocity may be written as $u_i = A_{ij} z_j$. Let the components of the particle velocities evaluated at the quadrature points be assembled into a $3N_Q$ vector b. The boundary condition at each quadrature point is then written $A_{ij} z_j = b_i$. The discrete form of the L_2 norm 2.11 may now be written as

$$||\hat{\boldsymbol{u}}||^2_{(\partial D)} = (A_{ij} z_j - b_i)(A_{ik} z_k - b_i) \equiv (A\boldsymbol{z} - \boldsymbol{b})^T (A\boldsymbol{z} - \boldsymbol{b}) \tag{2.12}$$

In writing this equation, for simplicity we have absorbed the quadrature weights into the definitions of A and b, i.e. multiplied each row of A and each component of b by $w^{1/2}$. Since w is strictly positive, this presents no problems. Finally we differentiate 2.12 with respect to z to minimize the norm and find the standard least square equation in normal form

$$A^T A\boldsymbol{z} = A^T \boldsymbol{b} \tag{2.13}$$

To summarize, we find that choosing to minimize the L_2 norm of the velocity error over the particle surface leads to a discretized form equivalent to using a finite collection of collocation points. The difference lies in the fact that the location of the quadrature points is dictated by an efficient choice of numerical quadrature and the weighting of the equations in the linear

least squares expression is dictated by the associated weights in the quadrature formula. As the number of quadrature points is increased, the solution is guaranteed to converge for any well conditioned quadrature formula. Note that the placement of all singularities in the interior of the particle guarantees continuity of the fluid velocity and all of its derivatives over the particle surface.

A few words concerning the choice of quadrature formulas for dicolloid particles may be helpful. Each dicolloid consists of the combined surfaces of two intersecting spheres, hence the union of two spherical caps. Since the slope is discontinuous at the junction of the two spheres, it proves convenient to divide the L_2 integral into separate integrals over each spherical cap represented by ∂D_1 and ∂D_2 respectively. The integral on each cap may be written in a local spherical coordinate system (r, θ, ϕ) based on its respective center with the z axis along the particle symmetry axis

$$||\hat{\boldsymbol{u}}||^2_{L_2(\partial D)} = a^2 \int_{\partial D_1} (\hat{\boldsymbol{u}}.\hat{\boldsymbol{u}}) \sin\theta \; d\theta d\phi \; + \; b^2 \int_{\partial D_2} (\hat{\boldsymbol{u}}.\hat{\boldsymbol{u}}) \sin\theta \; d\theta d\phi \tag{2.14}$$

where a and b are the radii of the two spherical caps forming the dicolloidal particle. On each integral, we now have smooth, infinitely differentiable integrands. Gauss-Legendre quadrature is used for θ integrations, while the rectangle rule is used in ϕ owing to the periodicity in the ϕ coordinate. Note that the ϕ dependence of the term with the highest wavenumber in the integrand varies as $\cos^p(\phi)\sin^q(\phi)$ with $p+q=6$, which comes from the square of the $x_i x_j x_k$ term in the Stokes doublet or Potential quadrupole. Therefore a 7 point rectangle rule is sufficient to integrate exactly the ϕ part of the integrand above. For integration in θ coordinate, Guass-Legendre quadrature was used which gives an exponential convergence to the final solution with increasing number of quadrature points. As an example, the convergence of the predicted force, torque and stresslets with the number of θ quadrature points are shown in Figure 2.3 which clearly shows exponential convergence. We emphasize that these integrations for the least squares problem need be done only once for each particle shape in each of the standard velocity fields (uniform translation, rotation, linear straining field). The result of the least squares procedure is the selection of the one body singularity coefficients $\boldsymbol{p}$, $\boldsymbol{q}$, $\boldsymbol{s}$, and $\boldsymbol{t}$ for a given particle shape. These coefficients are the only quantities

required for the Stokesian dynamics algorithm, and the detailed procedure for computing the coefficients does not enter the computational cycle for Stokesian dynamics simulations.

With the general approach now established, we turn our attention to details of the approach which lead to optimal solutions for dicolloid particles. Specifically, one must choose the number of singularity collections and their specific positions in the interior of the particle. As shown in the results below, we find it sufficient to employ singularity collections at just two positions S_1 and S_2 with the singularities placed along the axis of the particle as shown in Figure 2.1. This leaves two independent parameters (the positions of the the singularities relative to center of the particle) to be determined before we solve for the coefficients via the linear least squares procedure above. In principle, these parameters could be selected to further minimize the norm of the residual $\hat{\boldsymbol{u}}$, however this constitutes a non-linear problem (Zhou & Pozrikidis, 1995). The solution for optimal positions is a function not only of particle shape, but of the specific combination of elementary flow fields constituting the undisturbed flow. This makes the further optimization step unsuitable for Stokesian dynamics simulations. Instead, we seek a single specification for the singularity positions which is optimized for a given particle shape, but which performs acceptably for all imposed flow fields. From a series of numerical tests, we find that the solution for particles immersed in a uniform flow is more accurate and less sensitive to the positions of the singularities than for particles in linear flow fields. Thus, if one optimizes the positions to minimize the error in linear flow fields, the same choice will be satisfactory for uniform flows, and the errors for uniform flows will remain smaller than those for the linear flows. Further numerical tests show that the linear flows subject to the largest errors are those associated with dominant velocity components normal to the particle axis. In particular, if the z axis is aligned with the particle axis, then for linear flows $u_i = G_{ij}x_j$, errors are usually largest for flows with non-zero coefficients $G_{11}, G_{12}, G_{21}, G_{22}$. Based on these results, we chose to optimize the location of singularities based on the simple straining field $G_{11} = 1, G_{22} = -1$, and results presented below show that this gives excellent accuracy for all imposed flow fields.

Results for the optimal locations for the singularities may be divided into two classes depending on the relative size of the two constituent spheres. For heteronuclear dicolloidal particles with spheres of different radii, we consider first the case where the smaller sphere

occupies less than a hemisphere, e.g. small bump particles (Figure 2.2). We find good accuracy is achieved by placing one group of singularities at the origin of the larger sphere. For the second group of singularities let d_s specify the distance from the surface of the small sphere (see Figure 2.1). We find that d_s is well correlated with d_w the radius of the circle at the intersection of the spheres. Figure 2.4 shows the optimal positions plotted versus d_w together with a simple polynomial fit to the data. This choice works well for all small bumps from a hemisphere down to an infinitesimal perturbation. For homonuclear particles (with spheres of equal radius), the optimal locations of the singularities maintain fore-aft symmetry consistent with the symmetry of the particles. For such particle shapes, the optimal location in each sphere lies between the sphere center and the particle surface. We define the $\Delta C = (C_1 - S_1)$ as the displacement from the center as shown in Figure 2.1. Figure 2.5 shows the optimal ΔC plotted versus center to center spacing c together with a simple correlation of the position data. Note that all lengths in correlations have been non-dimensionalized by the radius of the larger sphere denoted by 'a' in this work. The final positions for the flow singularities for the dicolloid shapes pictured in Figure 2.2 are listed in Table 2.1.

The force, torque and stresslet for dicolloidal particles in general translation, rotation and linear straining fields have been computed for the three sample particle shapes shown in Figure 2.2. To assess the accuracy of the results, we compared the computed force moments with values computed with the spectral boundary element method (Muldowney & Higdon, 1995), a high order boundary element algorithm capable of extremely high precision. Spectral BEM predictions for all force/torque/stresslets were computed to 6 significant figures. Comparison of the results for the two-point singularity method with the spectral BEM results are given in Tables 2.2, 2.3 and 2.4 for a homonuclear, small-bump and fused-dumbbell particles respectively. The various moments and undisturbed flow fields specified in the table are defined in the Appendix. For homonuclear particles, relative errors are less than 1% in all cases. For small bump particles, relative errors are less than 3% in all cases except for a stresslets or forces associated with cross-couplings (e.g. stresslet-velocity or force-straining field) and the magnitude of these couplings themselves is negligible (order 10^{-2}). For fused dumbbell particles, all errors are less than 2% except for a single stresslet-strain coupling

whose error is less than 4%. In summary, the two-point singularity method gives excellent accuracy for the one body resistance functions for the dicolloid particles in flow fields involving translation, rotation and general linear flows. The computational cost of employing the two-point singularity method in Stokesian dynamics is merely twice that required for spherical particles.

2.4 Far-Field Many-Body Interactions

Far-field many-body interactions in Stokesian Dynamics are computed using an extension of the multipole-moment method. This method requires expressions for the disturbance velocity and force-moments on a single particle in a prescribed flow field. These have been computed in section 2.3 above. Here, we develop the procedure for computing many-body interactions, beginning with the presentation of Faxén's laws for particles represented by two-point singularity solutions. The method of reflections approach, an iterative technique to compute hydrodynamic interactions using the multipole-moment method follows at the end of the section.

2.4.1 Faxén's laws for Non-Spherical Particles

Computation of the force moments (force, torque, stresslet) on a particle in a specifed ambient flow is an important step in the Stokesian Dynamics technique. For spherical particles, these moments are given by the well known Faxén's law (see, e.g., Kim & Karrila (2005)). Kim & Lu (1987) generalized Faxén's law to any particle shape where the disturbance velocity associated with the particle in a given ambient field can be represented by a collection of Stokes-singularities inside the particle. In particular, for an arbitrary flow field, there exists a Faxén's law relating the force and the singularity solution in a uniform flow, for the torque and the singularity solution in a rotational flow, and for the stresslet and the singularity solution in a linear straining flow. Referring to the form of disturbance velocity expressed in equation (2.9), we shall append a superscript u, ω or e to the coefficients $\boldsymbol{p}$, $\boldsymbol{q}$, $\boldsymbol{s}$, and $\boldsymbol{t}$ to designate solutions relative to a uniform flow, rotational flow or linear straining field.

For example, the singularity solution giving the disturbance velocity for a particle in a uniform flow $\boldsymbol{U}$ is written

$$\begin{aligned} u_i(\boldsymbol{x}) - U_i = \sum_{l=1}^{l=N} p_j^{ul} S_{ij}(\boldsymbol{x}-\boldsymbol{x}_l) \; + \; q_{jk}^{ul} SD_{ijk}(\boldsymbol{x}-\boldsymbol{x}_l) + \\ s_j^{ul} PD_{ij}(\boldsymbol{x}-\boldsymbol{x}_l) \; + \; t_{jk}^{ul} PQ_{ijk}(\boldsymbol{x}-\boldsymbol{x}_l) \end{aligned} \tag{2.15}$$

The Faxén's law for the force on the particle $\boldsymbol{F}$ in an arbitrary ambient flow $\boldsymbol{v(x)}$ satisfies

$$\boldsymbol{U}.\boldsymbol{F} = -8\pi\mu \sum_{l=1}^{l=N} \left(p_j^{ul} + s_j^{ul}\nabla^2\right) v_j(\boldsymbol{x}_l) \; + \left(\; q_{jk}^{ul} + t_{jk}^{ul}\nabla^2\right) \frac{\partial v_j(\boldsymbol{x}_l)}{\partial x_k} \tag{2.16}$$

Similarly, if the singularity solution in a rotational flow $\boldsymbol{\Omega}$ is given by the following equation

$$\begin{aligned} u_i(\boldsymbol{x}) - \epsilon_{ijk}\Omega_j x_k = \sum_{l=1}^{l=N} p_j^{\omega l} S_{ij}(\boldsymbol{x}-\boldsymbol{x}_l) \; + \; q_{jk}^{\omega l} SD_{ijk}(\boldsymbol{x}-\boldsymbol{x}_l) + \\ s_j^{\omega l} PD_{ij}(\boldsymbol{x}-\boldsymbol{x}_l) \; + \; t_{jk}^{\omega l} PQ_{ijk}(\boldsymbol{x}-\boldsymbol{x}_l) \end{aligned} \tag{2.17}$$

then the torque on the particle $\boldsymbol{T}$ in an arbitrary ambient flow $\boldsymbol{v(x)}$ satisfies

$$\boldsymbol{\Omega}.\boldsymbol{T} = -8\pi\mu \sum_{l=1}^{l=N} \left(p_j^{\omega l} + s_j^{\omega l}\nabla^2\right) v_j(\boldsymbol{x}_l) \; + \left(\; q_{jk}^{\omega l} + t_{jk}^{\omega l}\nabla^2\right) \frac{\partial v_j(\boldsymbol{x}_l)}{\partial x_k} \tag{2.18}$$

where $\boldsymbol{T}$ is about the same point about which $\boldsymbol{\Omega}$ is defined.

Similarly, if the singularity solution in a straining field $\boldsymbol{E}$ is given by the following equation

$$\begin{aligned} u_i(\boldsymbol{x}) - E_{ij}x_j = \sum_{l=1}^{l=N} p_j^{el} S_{ij}(\boldsymbol{x}-\boldsymbol{x}_l) \; + \; q_{jk}^{el} SD_{ijk}(\boldsymbol{x}-\boldsymbol{x}_l) + \\ s_j^{el} PD_{ij}(\boldsymbol{x}-\boldsymbol{x}_l) \; + \; t_{jk}^{el} PQ_{ijk}(\boldsymbol{x}-\boldsymbol{x}_l) \end{aligned} \tag{2.19}$$

then the stresslet on the particle $\boldsymbol{S}$ in an arbitrary ambient flow $\boldsymbol{v(x)}$ satisfies

$$\boldsymbol{E} : \boldsymbol{S} = -8\pi\mu \sum_{l=1}^{l=N} \left(p_j^{el} + s_j^{el}\nabla^2\right) v_j(\boldsymbol{x}_l) \; + \left(\; q_{jk}^{el} + t_{jk}^{el}\nabla^2\right) \frac{\partial v_j(\boldsymbol{x}_l)}{\partial x_k} \tag{2.20}$$

where $\boldsymbol{S}$ is about the same point about which $\boldsymbol{E}$ is defined.

In all, we require the singularity solutions for the single particle in 11 independent flows

(3 uniform velocities, 3 rotational velocities and 5 straining fields). With the coefficients $\boldsymbol{p}$, $\boldsymbol{q}$, $\boldsymbol{s}$, and $\boldsymbol{t}$ from the solutions for these 11 reference flow fields, we may determine all components of $\boldsymbol{F}$, $\boldsymbol{T}$ and $\boldsymbol{S}$ on a particle in an arbitrary flow field $\boldsymbol{v}(\boldsymbol{x})$ utilizing equations (2.16), (2.18), and (2.20) respectively.

2.4.2 Disturbance velocity for particle in an arbitrary flow

The method of reflections requires two complementary steps in order to calculate the many body interactions among a collection of particles. The first is the computation of the force, torque, stresslet (and higher force moments if desired) for the given particle in an arbitrary flow field. This is accomplished using the Faxén's laws in the section above. The second step is to determine the disturbance flow field associated with the moments and propagate that disturbance flow field out to all other particles. For the singularity method of the current effort, the disturbance velocity field is represented by the collection of singularities employed in the least squares one body solution for a particle embedded in a specified linear flow $\boldsymbol{U}, \boldsymbol{\Omega}, \boldsymbol{E}$. For a given set of force moments $\boldsymbol{F}, \boldsymbol{T}, \boldsymbol{S}$, there is a unique set of linear flow parameters $\boldsymbol{U}, \boldsymbol{\Omega}, \boldsymbol{E}$ in the one body solution with the corresponding force moments. These are given by

$$\begin{pmatrix} \boldsymbol{U} \\ \boldsymbol{\Omega} \\ \boldsymbol{E} \end{pmatrix} = \boldsymbol{R}_{1B}^{-1} \begin{pmatrix} \boldsymbol{F} \\ \boldsymbol{T} \\ \boldsymbol{S} \end{pmatrix} \tag{2.21}$$

where $\boldsymbol{R}_{1B}$ is the one body resistance tensor determined from the one body singularity solutions.

Given $\boldsymbol{U}, \boldsymbol{\Omega}, \boldsymbol{E}$, the singularity coefficients may be determined immediately from the pre-computed reference solutions following the procedure described in the Appendix. Schematically we represent the steps in this process as

$$\begin{pmatrix} \boldsymbol{F} \\ \boldsymbol{T} \\ \boldsymbol{S} \end{pmatrix} \rightarrow \begin{pmatrix} \boldsymbol{U} \\ \boldsymbol{\Omega} \\ \boldsymbol{E} \end{pmatrix} \rightarrow \begin{pmatrix} \boldsymbol{p} \\ \boldsymbol{q} \\ \boldsymbol{s} \\ \boldsymbol{t} \end{pmatrix} \tag{2.22}$$

With the singularity coefficients given, we may then propagate the disturbance velocity out to all other particles and complete one stage of operations for the method of reflections.

Finally, we summarize the steps in the method of reflections for computing many body interactions. A detailed description of the method of reflections can be found in standard monographs on low Reynolds number flow (Happel & Brenner, 1991; Kim & Karrila, 2005). In this iterative method, we suppose a collection of particles with known velocity U and angular velocity Ω are immersed in a linear straining field E. The initial estimate of the force, torque and stresslet on each particle is given by the one body solution as embodied in the resistance tensor $\boldsymbol{R}_{1B}$. The disturbance velocity associated with the singularities from the one body solution is propagated to the singularity locations of all other particles in the system. The total disturbance velocity at each singularity location is computed and the resulting velocity field is employed to compute the correction to the force, torque and stresslet on each particle using Faxén's laws. This completes one reflection step in the method of reflections. The process continues with the new (F, T, S) corrections leading to new disturbance velocities and new corrections again via Faxén's laws. The iterative method of reflections is equivalent to a Jacobi iterative solution of the system of equations

$$\begin{pmatrix} \mathbf{F}^H \\ \mathbf{S}^H \end{pmatrix} = (\mathbf{I} - \mathcal{R})^{-1} \mathbf{R}_{1B} \begin{pmatrix} \mathbf{u}^\infty - \mathbf{U} \\ \mathbf{E}^\infty \end{pmatrix} \tag{2.23}$$

where the many body resistance tensor is defined as $\mathbf{R}^{MB} = (\mathbf{I} - \mathcal{R})^{-1}\mathbf{R}_{1B}$ and $\mathcal{R}$ is the reflection operator (Kim & Karrila, 2005), which represents one reflection step. If one wishes to compute the many body tensor directly, it requires the inversion of the matrix $(\mathbf{I} - \mathcal{R})$ which is computationally intensive. Fortunately, efficient iterative solution of the resistance equations are possible and no direct inversion is necessary. It should be noted that the Jacobi

iterative solution of equation (2.23) embodied in the method of reflections may be slow to converge or completely fail to converge for concentrated suspensions with large numbers of particles. However, more robust iterative algorithms can be used successfully even in those cases.

2.5 Near Field Lubrication interaction

In the method of reflections, we make use of a truncated multipole expansion for the disturbance velocity to compute the force, torque and stresslet on each particle. While this far field expansion yields good accuracy for particles which are well separated, it cannot capture the strong lubrication forces that can arise due to flows between two particles separated by a small gap. These asymptotic lubrication terms depend only on the pairwise interaction of two particles and may be added as a pairwise correction term to the results from the method of reflection as in equation (2.4). We require the following conditions for the lubrication correction term: (i) it must capture the singular asymptotic force and force moments when particles are separated by vanishingly small gaps, (ii) it must preserve the accuracy of $\boldsymbol{R}^{MB}$ in the far field.

To illustrate the procedure for computing $\boldsymbol{R}^{LB}$, we shall first consider the case of spheres and focus on the submatrix of $\boldsymbol{R}$ for the force-velocity coupling, while noting that all other submatrices are defined in similar fashion. The force F on a given particle moving toward a second particle with speed U along the line of centers is given in terms of the scalar resistance X^A as

$$F = -X^A U \tag{2.24}$$

Similar relationships exist for motion perpendicular to the line of centers and similarly for the second particle. Detailed expressions for X^A are known for spheres in terms of far field expansion, asymptotic lubrication approximations and uniformly accurate composite expansions (Jeffrey & Onishi, 1984). Here we note that only the asymptotic lubrication expansion is needed for our present purposes. Let R be the distance between the particle centers, a be the radius of one sphere, $\beta = b/a$ be the ratio of the sphere radii and $s =$

$2R/(a+b)$ be the dimensionless distance between centers. The dimensionless gap between particle is $\xi = s - 2$. The asymptotic expression for X^A for spheres may now be written

$$X^A_\xi = g_1(\beta)\xi^{-1} + g_2(\beta)\ln\xi^{-1} + g_3(\beta)\xi\ln\xi^{-1} + O(1) \tag{2.25}$$

The functions $g_1(\beta)$, $g_2(\beta)$ and $g_3(\beta)$ are known functions which can be found in Kim & Karrila (2005) or Jeffrey & Onishi (1984). Owing to the logarithm term, this asymptotic expression is unbounded at large distance. Following Jeffrey & Onishi (1984), we introduce an auxiliary variable η which scales as ξ for small gaps and approaches 1 as $\xi \to \infty$. Specifically, we set $\eta = 1 - 4/s^2$. This choice has the desired asymptotic properties and is amenable to Taylor series expansion in the far field for large s. See Viera (2002) for additional details. Now, we write the asymptotic lubrication term as

$$X^A_\eta = g_1(\beta)\eta^{-1} + g_2(\beta)\ln\eta^{-1} + g_3(\beta)\eta\ln\eta^{-1} \tag{2.26}$$

Note these two asymptotic lubrication expressions agree to $O(1)$. Adding this asymptotic expression X^A_η to the many body resistance result will give the correct singular behavior for near field interactions, with bounded behavior at infinity, however it will not preserve the desired far field behavior. To accomplish this task, we write a far field Taylor series expansion in $2/s$ for (2.26) as

$$X^A_\eta = \sum_{k=0}^{\infty} h_{2k}(\beta)\left(\frac{2}{s}\right)^{2k} \tag{2.27}$$

We then construct the proper form of the lubrication interaction by adding the singular asymptotic form (2.26) and subtracting a truncated non-singular far field expansion (2.27). This guarantees that (i) the proper singular asymptotic form is captured and (ii) the terms from the two expressions (2.26) and (2.27) cancel in the far field up to the accuracy of $\boldsymbol{R}^{MB}$, thereby preserving the accuracy of the latter in the far field. The far field expansion of (2.27) is truncated at the same level of approximation as the truncation in the many body

calculation. Thus we write

$$X^A_{LB} = X^A_\eta(\eta) - \sum_{k=0}^{2} h_{2k}(\beta) \left(\frac{2}{s}\right)^{2k} \tag{2.28}$$

This gives the desired behavior for the singular lubrication corrections to the many body calculations. The improvement associated with the lubrication correction is illustrated in Figure 2.6 for the squeezing motion of two spheres. In the classic Stokesian dynamics approach for spheres, one may go a step further. While we have the correct singular behavior at small gaps, the many body calculation generally leads to an error of $O(1)$ for particles near contact owing to the truncation of the reflection operator at the force dipole level. When the exact form of the resistance tensor is available (e.g. spheres), this error may be corrected by subtracting off an appropriate polynomial approximation with proper asymptotic form (Viera, 2002). This has the desirable effect of effectively preserving the full exact resistance tensor for two body interactions.

We turn now to the implementation for dicolloid particles. The many body contribution to the resistance tensor is computed as described in the previous section. The contributions needed for the lubrication correction are exactly as given by equations (2.25), (2.27) and (2.28), because the pairwise lubrication interactions are simply the additive contributions of lubrication between the constitutive spheres. For smooth convex particles of any prescribed shape, equivalent lubrication expressions may be calculated using standard asymptotic analysis (Cox, 1974; Claeys & Brady, 1989). While the correct near field singular behavior and far field asymptotic behavior is readily achieved for dicolloid particles , the final $O(1)$ correction available for spheres is not achievable. The reason for this difficulty stems from the fact that the complete specification of the geometry for a pair of dicolloidal particles requires four parameters (prescribing separation and orientations) as against one parameter (separation) for spheres. The $O(1)$ errors in the many body calculation for closely spaced paricles would have to be tabulated as a function of 4 variables with appropriate polynomial approximations constructed for a large number of functions. Thus, in the present effort, we shall be satisfied with the correct singular behavior for closely spaced particles and the correct far field behavior for widely spaced particles. In fact, this is not a significant compromise. Clas-

sic Stokesian dynamics gives exact two body results, however with three particles in near proximity, a three body near field term arises which cannot be computed by the pairwise lubrication corrections. Thus the classic Stokesian dynamics approach for spheres will have comparable errors to those arising here whenever concentrated suspensions are studied.

To complete the specification of the lubrication tensor $\boldsymbol{R^{LB}}$ expressions similar to those above are written for all scalar resistances arising in the specification of the lubrication interaction, namely Y^A_{LB}, Y^B_{LB}, X^C_{LB}, Y^C_{LB}, X^G_{LB}, Y^G_{LB}, Y^H_{LB}, X^M_{LB}, Y^M_{LB}, and Z^M_{LB}. These scalar resistances are as given for spherical particles in (Kim & Karrila, 2005). Note that no exact two-body solution were required in the calculation of the lubrication correction for dicolloid particles. Only the asymptotic lubrication forms are needed.

For a pair of dicolloidal particles, the total lubrication interaction is found by summing lubrication interactions between all the spherical node pairs formed between the two particles. For example, given the pair of dicolloidal particles shown in Figure 2.7, the total lubrication interaction is written as the sum of the pairwise interactions between the following spherical node pairs: $(S1A, S2A)$, $(S1A, S2B)$, $(S1B, S2A)$, and $(S1B, S2B)$. This lubrication calculation requires the individual velocities/angular velocities of the constituent spheres. These are related to the velocity/angular velocity of the colloidal particle by :

$$\begin{aligned} (\boldsymbol{u}^\infty - \boldsymbol{U})_{sp} &= (\boldsymbol{u}^\infty - \boldsymbol{U}) + (\boldsymbol{\omega}^\infty - \boldsymbol{\Omega}) \times (\boldsymbol{x}_{sp} - \boldsymbol{x}_c) + \boldsymbol{E}^\infty (\boldsymbol{x}_{sp} - \boldsymbol{x}_c) \\ (\boldsymbol{\omega}^\infty - \boldsymbol{\Omega})_{sp} &= (\boldsymbol{\omega}^\infty - \boldsymbol{\Omega}) \\ \boldsymbol{E}_{sp} &= \boldsymbol{E}^\infty \end{aligned} \tag{2.29}$$

where the subscript 'sp' refers to the center of the spherical node while the subscript 'c' refers to the center of the colloidal particle. The velocities on the RHS correspond to the dicolloidal particle, while the velocities on the LHS correspond to the individual spherical nodes. The lubrication interactions may now be computed for the force moments on the individual spheres. These moments are translated back into moments on the full particles

by summing the contributions from the constituent spheres

$$\begin{aligned} \boldsymbol{F} &= \sum \boldsymbol{F}_{sp} \\ \boldsymbol{T} &= \sum (\boldsymbol{T}_{sp} + (\boldsymbol{x}_c - \boldsymbol{x}_{sp}) \times \boldsymbol{F}_{sp}) \\ \boldsymbol{S} &= \sum (\boldsymbol{S}_{sp} + [(\boldsymbol{x}_c - \boldsymbol{x}_{sp})\boldsymbol{F}_{sp} + \boldsymbol{F}_{sp}(\boldsymbol{x}_c - \boldsymbol{x}_{sp})]/2) \end{aligned} \tag{2.30}$$

2.5.0.1 Correction Factor for Dicolloids

In the above section, we used asymptotic results for complete spheres to compute the lubrication interaction between a pair of spherical nodes. One concern with this approach is the possible overestimation of the interaction when the point of closest approach lies very near the circle of intersection of the two constituent spheres. In this case, each of the spherical nodes is truncated and will not experience the full lubrication force. In order to correct this overestimation, we employ a semi-empirical correction factor which takes into account the incomplete spherical geometry involved in each of these pairwise interactions. Our basic premise in the calculation of the correction factor is that the stress fields are weaker when incomplete spherical geometries are involved compared to the case involving two complete spheres. To estimate the correction factor, consider the example of the interaction between spherical node pair $(S1B, S2A)$ in Figure 2.7. Let the radius of spherical node $S1B$ be ba and that of $S2A$ be a, and let h_0 be the gap between these two spherical components. Now, for a squeezing motion between these two components, the dominant source of interaction is the pressure that builds in between the two particles required to squeeze the fluid out. From asymptotic analysis, the pressure field is strong only in a circular region around the line of centers whose radius scales as $\sqrt{a_m h_0}$, where $a_m = (2ab)/(a+b)$. This circular region, whose radius is taken as $r_c = \alpha\sqrt{a_m h_0}$ ($\alpha = 0.5$ works well), is denoted as the circle of influence in Figure 2.7. If the projection of this circle onto each spherical node is a complete circle, no correction is needed. If the projection of the circle of influence onto the surface of spherical nodes is truncated owing to their incomplete spherical geometry, then a correction is needed. We define the correction factor as the ratio of a weighted area of the truncated circle of influence to that of the complete circle of influence. Since our primary goal here

is to accurately estimate the dominant squeeze interaction, the weighting function for the area calculation is chosen as the corresponding pressure field for squeezing motion. Thus, the correction factor C_F becomes

$$C_F = \int_{C_1} p(r)\, dS / \int_{C_2} p(r) dS \tag{2.31}$$

where C_1 refers to the region contained in the truncated circle, C_2 refers to region contained in the complete circle, and $p(r)$ refers to the pressure field in a squeezing type motion given by

$$p(r) = \frac{3\mu a_m U}{2(h_0 + r^2/a_m)^2} \tag{2.32}$$

In the above equation U is arbitrary as it appears both in the numerator and in the denominator of equation (2.31). With this correction factor, the corrected lubrication moments are

$$\boldsymbol{F}^{LB}_{corr} = C_F \boldsymbol{F}^{LB} \tag{2.33}$$

where $\boldsymbol{F}$ is a vector containing force, torque, and stresslets on each of the spherical nodes. The effect of using the lubrication correction factor is shown in Table 2.5 for a pair of homonuclear particles with parallel axes being squeezed with velocity perpendicular to the axes. There are four lubrication contacts between the two particles. (See configuration 1 in Figure 2.9.) In this table, high precision results from spectral boundary element computations are compared with the Stokesian dynamics results both with and without the lubrication correction. A major improvement in the prediction of force moments is observed when the correction factor from (2.31) is employed.

Similar tests were performed for a number of other particle shapes and flow fields, and the results compared with the solutions from the spectral boundary element method. A selection of specific test geometries for dicolloid particles is shown in Figure 2.9. An error under 10% was obtained in almost all cases, with most cases giving under 5% error.

Comparison for force on fused-dumbbell particles in configuration 1 (Figure 2.9) are tabulated in Table 2.6. Under 10% error is obtained at all separations, and the error is in fact negligible at large and very small separations. The worst performing case among all the test

cases was for two fused dumbbells in configuration 3 (Figure 2.9), which essentially has two fused-dumbbells arranged symmetrically in a cross. The comparison of force for this test case is tabulated in Table 2.7. In this case, an error as high as 45% was obtained for the smallest gap that was investigated here. We expect the error to go down as we go to even smaller gaps, as was demonstrated in the previous example, but that could not be verified due to computational cost of resolving four small gaps as against two in the previous example (see Muldowney & Higdon (1995) for a discussion on resolving small gaps). Instead, we solved a similar test case with complete dumbbells instead of fused-dumbbells, which essentially involves four spheres. Comparison of force with the spectral BEM solution for this particular case is tabulated in Table 2.8. Note that for this comparison, we have used both the modified lubrication developed in this work, and the classic lubrication for spheres which would result in zero error in the resistance tensor for a two sphere system. In this context, the full dumbbell system is interesting as it yields the exact same error as arises with classic Stokesian dynamics when there are 3 or more bodies in close proximity. As could be seen in Table 2.8, an error as high as 30% is obtained at the smallest gap investigated here.

In conclusion, we again emphasize that the errors in two-body solution is usually less than 10% except for certain particle configurations with intermediate size gaps where lubrication forces are not a dominant contribution to the overall resistance.

2.6 PME Stokesian Dynamics for Dicolloids

In previous sections, we have developed a approximation for the overall resistance tensor for dicolloidal particles via a Stokesian dynamics approach. With this approach, we obtain the classic system of resistance equations

$$\begin{pmatrix} \mathbf{F}^H \\ \mathbf{S}^H \end{pmatrix} = \left((\mathbf{I} - \mathcal{R})^{-1} \mathbf{R}_{1B} + \mathbf{R}_{LB} \right) \begin{pmatrix} \mathbf{u}^\infty - \mathbf{U} \\ \mathbf{E}^\infty \end{pmatrix}. \tag{2.34}$$

This system may be employed to follow the dynamics of a collection of N particles in an infinite fluid,; or extended to infinite periodic systems with the use of periodic singularities (Hasimoto, 1959) in the reflection operator. The calculation of lubrication interactions is an $O(N)$ operation, as it involves only those neighboring particles within close proximity to a given particle. The direct evaluation of the reflection operator is an $O(N^2)$ operation, which may be expensive for large systems. To circumvent this difficulty for periodic systems, Guckel (1999) developed a particle-mesh-Ewald (PME) Stokesian dynamics method which accurately reproduces the classic result in $O(N \ln N)$ operations. Sierou & Brady (2001) and Viera (2002) utilized Guckel's PME far field algorithm to achieve an $O(N \ln N)$ operation count, but incorporated alternative iterative solution algorithms to yield considerably improved performance in their PME Stokesian dynamics implementations. Our approach for dicolloid particles follows that of Viera.

Briefly, in the classic Ewald summation approach, Hasimoto showed that the infinite Fourier series for the periodic Green's function (Stokeslet) could be represented as the combination of rapidly decaying real space and wave space sums (Hasimoto, 1959). The real space sum captures the sharp singular velocity near the location of the Stokeslet using singular functions which decay exponentially with distance according to a length scale l, while the wave sum employs a Fourier series to capture the smooth long range behavior with Fourier coefficients which decay exponentially with wave number scaling as l^{-1}. This length scale l (related to Hasimoto's shift parameter α as $l^2 = \alpha$) determines the relative number of terms required to evaluate accurately the real space and wave space sums. In the limit as l approaches zero, the contribution of the real space sum approaches zero, and the wave sum returns to the form of the original slowly convergent Fourier series. In the limit as l approaches infinity, the wave space sum vanishes, and the real space sum approaches an infinite lattice sum of slowly decaying Stokeslet singularities. In the classic Ewald approach, the length scale l is chosen to yield rapid convergence in each sum with approximately equal number of terms required in each summation. Hasimoto shows that the appropriate choice for l scales as $V^{1/3}$ based on the volume of the unit cell.

In the PME method, the length scale l is chosen to be small such that the exponentially decaying real sum terms are negligible beyond a few sphere radii. This yields an $O(N)$

computation for the real sum, however, as a consequence many terms are needed in the wave sum. To accelerate the wave sum computation, Guckel (1999) showed that Fast Fourier Transforms could be employed in place of direct evaluation of the wave sum. First, the singularities at all sphere locations are replaced by an equivalent set of singularities on a uniform rectangular grid. The evaluation of the fluid velocity at every grid point then takes the form of a three dimensional Fourier transform which may be evaluated via FFT's. The velocity field and derivatives at sphere locations are then evaluated by local interpolation from the grid velocity. The number of FFT points N_{FFT} for a specified accuracy is a function of the shift parameter length scale l. With the optimal choice of this length scale l, the entire computation may be completed in $O(N \ln N)$ operations.

In his original algorithm, Guckel employed an iterative method of reflections approach which is analogous to Jacobi iteration of the resistance equation (2.34). Sierou & Brady (2001) and Viera (2002) replaced this step with efficient preconditioned iterative solvers which dramatically accelerated the algorithm. For example, Viera demonstrated that hydrodynamic interactions in individual realizations could be resolved for up to 1,000,000 particles in a Monte Carlo configuration.

For dynamic simulations, the resistance equation (2.34) can be solved to obtain the velocity of spheres given the force/torque on each sphere. Solving this equation directly requires two nested iterations, where each iteration for the resistance equation requires a full iterative solution for the term involving the inverse of the reflection operator $(\mathbf{I}-\mathcal{R})^{-1}$. This method is not effective for large systems due to the expensive $O(N \ln N)$ operations for the reflection operator. To develop a more efficient technique, Viera suggested an approach which he called the *pseudo-resistance method* to eliminate the nested iterations.

In this approach, Viera introduced intermediate variables $\hat{\mathbf{F}}$ and $\hat{\mathbf{S}}$ which represent the force/torque and stresslet which satisfy just the many body form of the resistance equations without lubrication. These may be computed by multiplying (2.23) by the inverse of its system matrix giving

$$\begin{pmatrix} \mathbf{u}^{\infty} - \mathbf{U} \\ \mathbf{E}^{\infty} \end{pmatrix} = \mathbf{R}_{1B}^{-1} \left(I - \mathcal{R} \right) \begin{pmatrix} \hat{\mathbf{F}} \\ \hat{\mathbf{S}} \end{pmatrix}. \tag{2.35}$$

With this definition, we substitute for the velocity and strain rate in the resistance equation (2.34) and find,

$$\begin{pmatrix} \mathbf{F}^H \\ \mathbf{S}^H \end{pmatrix} = \left(I + \mathbf{R}_{LB} \cdot \mathbf{R}_{1B}^{-1} \cdot (\mathbf{I} - \mathcal{R}) \right) \begin{pmatrix} \hat{\mathbf{F}} \\ \hat{\mathbf{S}} \end{pmatrix} \tag{2.36}$$

If the velocities and strain rate were known for every particle (e.g. a resistance problem), the system (2.35) may be solved for the terms $\hat{\mathbf{F}}$ and $\hat{\mathbf{S}}$. By contrast, if the force/torque and stresslet were known for every particle (e.g. a mobility problem), then (2.36) may be solved for $\hat{\mathbf{F}}$ and $\hat{\mathbf{S}}$. As it is, we know the force/torque on every particle as well as the strain rate at the location of every particle, which gives a mixed problem. The appropriate system of equations is obtained by a partition of the system matrices in (2.35) and (2.36). We take the first $6N$ equations from (2.36) which involve the known force/torques $\mathbf{F}^H$ and the last $5N$ equations from (2.35) which involve the known strain rates. This gives a system of $11N$ equations for the $11N$ unknowns $\hat{\mathbf{F}}$ and $\hat{\mathbf{S}}$. This system is amenable to iterative GMRES solution with no nested iterations.

Once the intermediate variables $\hat{\mathbf{F}}$ and $\hat{\mathbf{S}}$ have been determined, the true velocity and stresslets on the spheres may be computed via a post-processing operation involving simple matrix vector products using the remaining equations from the systems (2.35) and (2.36). In particular, the velocity is computed using the first $6N$ equations from (2.35), while the stresslet is computed from the last $5N$ equations of (2.36).

The pseudo-resistance equations are solved by using the generalized minimum residual (GMRES) method. At high volume fractions, the strong lubrication interactions between nearly touching particles result in very large eigenvalues for the matrix, which makes the GMRES method converge slowly. To improve the convergence, we developed a physically motivated preconditioner similar in spirit to that employed by Viera for spheres. This preconditioner matrix is build using an approximation for the singular lubrication interactions only. The resulting preconditioned system requires the solution of an auxiliary system of equations with a symmetric positive definite system matrix of size $3N \times 3N$. This system is solved using the MINRES method with a computational cost of less than 10% of the overall cost of the main iterative solution. With this lubrication preconditioner, a system with 1000

particles requires less than 20 GMRES iterations of (2.35), (2.36) to obtain a solution with a relative error of 10^{-3}. Lower iteration counts are possible if a good initial guess is available, e.g. from an earlier time step. A detailed description of the preconditioner similar to the one employed here can be found in Meng & Higdon (2008a).

Figure 2.10 illustrates the performance of the preconditioned iterative solver for a system of 1000 particles. The figure show results suspensions at volume fractions of $\phi = .10$ and $\phi = .50$. For each suspension, results for two different configurations are shown. First, a test system is generated by a Monte Carlo initialization yielding a near equilibrium distribution with a minimal number of very small particle gaps and a moderate condition number. Second a test system is generated by performing a dynamic simulation for a sheared suspension which exhibits a large number of very small gaps and a large condition number. With no preconditioner, the systems show modest convergence for Monte Carlo systems and slow convergence for dynamic configurations. At $\phi = .50$, extrapolation shows that the dynamic system with no preconditioner would require perhaps 600 iterations to reach a relative error of 10^{-3}. With the preconditioner, for all configurations, this same standard of error is reached is less than 10 iterations at $\phi = .10$ and between 20 and 28 iterations at $\phi = .50$.

With these results, we conclude that the PME Stokesian dynamics algorithm for dicolloid particles provides an efficient tool for studying hydrodynamic interactions in concentrated suspensions of non-spherical particles.

2.7 Results

Using the algorithms developed in this work, we investigate the transport properties of concentrated suspensions with four different particle shapes. These include spheres and three different dicolloids identified as homonuclear, small-bump, and fused-dumbbell as illustrated in Figure 2.2. The parameters defining the particle shapes and the locations of singularities employed in our simulations are reported in Table 2.1. In the present effort, we examine suspensions whose microstructure is obtained by a Monte Carlo initialization procedure. In a separate article, we consider the microstructure and rheology of suspensions in dynamic simulations . Here, we begin by characterizing the microstructure obtained from Monte

Carlo simulations for dicolloid particles.

2.7.1 Microstructure

The equilibrium microstructure for suspensions of hard spheres exhibits a fluid like state below $\phi = 0.494$ (freezing transition) and a face centered cubic (FCC) solid state above $\phi = 0.545$ (melting transition). Between these two volume fractions, coexisting fluid and solid phases may exist, however simulations generally lead to a fluid like state below the melting transition $\phi = 0.545$ (Woodcock, 1981; Speedy, 1997). In our Monte Carlo initializations, all simulations for hard spheres yield fluid like states for $\phi \leq 0.5$. To quantify the microstructure, the pair distribution functions (PDF) are shown in Figure 2.11 for $\phi = .10$ and $\phi = .50$ with two dimensional slices presented for $g(x, y)$. As noted, a fluid like state is seen for spheres in both cases.

Microstructure of hard dicolloids has been studied by several authors (Singer & Mumaugh, 1990; Vega *et al.*, 1992b,a). Vega *et al.* (1992a) characterized the phase transitions in these systems showing the existence of orientationally disordered FCC plastic crystals at high volume fractions. For our present investigation however, fluid like states are predicted for all particle shapes in Figure 2.2 from $\phi = 0$ to $\phi \leq 0.5$. Our Monte Carlo simulations confirm this behavior with pair distribution functions illustrated in Figure 2.11.

2.7.2 Viscosity

We begin this section by considering the viscosity of dicolloid suspensions in the dilute limit and compute the intrinsic viscosity $[\mu]$

$$[\mu] = \lim_{\phi \to 0} \frac{\mu_r - 1}{\phi} \tag{2.37}$$

The intrinsic viscosity is a function of the particle shape with a value of 2.5 for spheres. In a dynamic simulation, for axisymmetric non-spherical particles in a shear flow, the intrinsic viscosity may be a function of initial orientation and a periodic function of time as the particles execute Jeffery's orbits (Jeffery, 1922). Here, for simplicity we assume a homogeneous

orientation distribution of particles in the suspension, and compute the intrinsic viscosity from single particle simulations yielding values 2.4977 for homonuclear particle, 2.5029 for small-bump particles and 2.5378 for fused-dumbbell particles. The intrinsic viscosities are close to that of spheres not surprisingly given the relatively small degree of anisotropy. It is interesting to note that the intrinsic viscosity for homonuclear particles is slightly less than 2.5 with the difference being less than the the error tolerance of the method. Nonetheless, an intrinsic viscosity less than 2.5 is not totally surprising, as certain orientations of the particle (near the vorticity axis) make a contribution to intrinsic viscosity at a rate less than 2.5.

In non-dilute suspensions, viscosity depends strongly on hydrodynamic interactions between particles. In dynamic simulations, particle interactions determine the microstructure which develops in the suspension. Here we consider a prescribed microstructure provided by the Monte Carlo initialization for which the computed viscosity gives the infinite frequency viscosity of the suspension. We compute the viscosity for suspensions of each of the particle shapes at volume fractions over a range from $\phi = 0$ to .50. Results are shown in Figure 2.12(a) and tabulated in Table 2.9. For comparison, we have also plotted results for spheres from Sierou & Brady (2001) and for spheroids with aspect ratio 3 from Claeys & Brady (1993b). Our results for spheres are in excellent agreement with the results of Sierou & Brady (2001) and other literature values cited by those authors. For dicolloid particles, viscosities are quite close to those of spheres, but show a consistent monotonic deviation with increasing volume fraction. The deviation can be seen more clearly by plotting the ratio of the dicolloid viscosity to that of spheres at the same ϕ as shown in Figure 2.12b. The viscosity for homonuclear and small-bump particles are found to be higher than those of spheres, while that for for fused-dumbbells is lower than for spheres. It is interesting to observe that at any volume fraction ϕ, the viscosity is a non-monotonic function of particle aspect ratio (see Figure 2.13 a). The viscosity ratio begins at 1 for spheres, increases for homonuclear particles, then decreases for fused dumbbells. Note that the shape transition from homonuclear particles ($c/a = .2$) to fused dumbbells ($c/a = 1.0$) may be achieved through continuous variation of the center to center spacing c/a. Thus one may anticipate a continuous but non-monotonic dependence of viscosity as a function of c/a. At high degree

of anisotropy, it is well known from previous works (Claeys & Brady, 1993b; Mackaplow & Shaqfeh, 1996) that the viscosity is higher for particles with larger aspect ratio at equal volume fractions. Therefore, the viscosity likely shows at least one local maximum and minimum before reaching its large aspect ratio limit. We confirm these local minimum and maximum by computing the viscosity for a full dummbbell (tangent spheres c/a=2.0) which shows higher viscosity than that of spheres or homonuclear particles (Figure 2.13a). To explore further the non-monotonic trends of viscosity as a function of particle shape, we consider a simple equation to fit the viscosity data with correct intrinsic viscosity at low ϕ and divergent viscosity at some maximum volume fraction ϕ_m. For this purpose, we use a simple Eiler equation (Krieger, 1973)

$$\mu_r = \left(1 + \frac{[\mu]\phi}{2(1-\phi/\phi_m)}\right)^2 \tag{2.38}$$

where ϕ_m is employed as an adjustable parameter to fit our data over the range $0 < \phi \leq 0.5$. Values of the parameters needed for this equation are given in Table 2.10. For reference, values for close packed volume fractions (ϕ_{cp}) and random close packed volume fractions (ϕ_{rcp}) are also included in the table. We found that the Eiler's equation based on a fit to the viscosity data below the freezing volume fraction ($\phi \approx 0.5$) does a reasonable job of fitting the data in Figure 2.12(a) and also of extrapolating the data up to $\phi = 0.60$ from Sierou & Brady (2001) for spheres, however it doesn't match their data as one approaches the divergence at the random close-packed fraction of $\phi_{rcp} \approx 0.64$. (See Figure 2.13 b.) Sierou & Brady (2001) employed metastable fluid states for their viscosity calculation and hence a divergence at ϕ_{rcp} is perhaps expected.

It is interesting to examine the predictions for ϕ_m from the Eiler equation and to compare, at least qualitatively, with known values for ϕ_{cp} or ϕ_{rcp}. Of course, one should not attempt to push too far with the results of comparisons with semi-empirical equations. Values of ϕ_m from Eiler fits along with ϕ_{cp} and ϕ_{rcp} as function of particle shape is tabulated in Table 2.10. Both ϕ_{cp} and ϕ_{rcp} give a maxima for a particle shaped like a fused-dumbbell, which is similar to the behavior shown by ϕ_m. But neither ϕ_{cp} nor ϕ_{rcp} predict a local maximum in the viscosity vs. c/a plot in Figure 2.13. In general, the maxima in the packing fraction

(random or close) is associated with the slowest divergence in viscosity of fused-dumbbell particle suspensions with volume fraction.

2.7.3 Short time self-diffusivity

The short-time self-diffusivity is related to the mobility of the particle. If $M_{UF} = R_{FU}^{-1}$ is the full $6N \times 6N$ mobility tensor of the N particle system, then the translational and rotational short-time self-diffusivity, denoted here by D_s and D_s^r respectively, are given by

$$D_s = kT\langle (M_{uF})_{ii} \rangle = \frac{kT}{3N} \langle \text{trace}(M_{uF}) \rangle \tag{2.39a}$$

$$D_s^r = kT\langle (M_{\omega T})_{ii} \rangle = \frac{kT}{3N} \langle \text{trace}(M_{\omega T}) \rangle \tag{2.39b}$$

where M_{uF} and $M_{\omega T}$ denote $3N \times 3N$ block sub-matrices of M_{UF} representing the (velocity, force) and (angular velocity, torque) coupling respectively and $\langle \cdot \rangle$ represents an ensemble average. To compute these quantities exactly for a given configuration is computationally intensive, as it requires $O(N)$ distinct simulations with the $O(N \ln N)$ algorithm. Sierou & Brady (2001) gave an efficient algorithm to compute the short-time translational and rotational diffusivity using a sampling technique with uncorrelated random numbers. We follow their approach here. In short, an external generalized force/torque vector $\mathbf{F}^e$ of length $6N_p$ is applied on the system of particles, with $\mathbf{F}^e$ satisfying: $\langle \mathbf{F}^e \rangle = 0$ and $\langle F_i^e F_j^e \rangle = \delta_{ij}$. The resulting velocity/angular velocity $\mathbf{U}^e$ of the force-free particles satisfies

$$U_i^e = (M_{UF})_{ij} F_j^e \tag{2.40}$$

The ensemble average of the dot product $\langle \mathbf{U}^e \cdot \mathbf{F}^e \rangle$ therefore satisfies

$$\langle U_i^e F_i^e \rangle = \langle (M_{UF})_{ii} \rangle \tag{2.41}$$

To extract the translational and rotational diffusivity, the dot product in the above equation is restricted to the components representing (velocity, force) and (angular velocity, torque)

respectively.

The convergence of diffusivity in this random sampling process depends upon both the number of random force/torque vectors employed per Monte Carlo configuration, and the number of Monte Carlo configurations employed. The convergence behavior for both sampling parameters is illustrated in Figure 2.14 for a volume fraction of $\phi = 0.5$ and two different system sizes with $N = 64$ and $N = 1000$ particles. The thin lines in the figure show the convergence in the translational diffusivity with the number of random force/torque vectors employed per configuration, while the thick line shows the same quantity averaged over all the individual configurations in the figure. From the theory of the variance in the mean of random uncorrelated numbers, the difference between the true mean and the computed mean is expected to decay as $N_R^{-1/2}$, where N_R is the number of realizations and applies both to the number of random force/torque vectors employed per configuration and the number of Monte Carlo configurations employed for computing the mean. To better quantify the convergence behavior, we computed the coefficient of the $N_R^{-1/2}$ decay term. These are $(.112, .032)$ and $(.031, .004)$ for the 64 and 1000 particle system respectively, where the first number in parenthesis corresponds to the convergence with number of force/torque vectors employed, while the second number in the parenthesis corresponds to the convergence with the number of Monte Carlo configurations. The above numbers reveal that the convergence with the number of random force/torque vectors is almost an order of magnitude slower than the convergence with the number of Monte Carlo configurations. In addition, as expected, the convergence is faster for larger system size. For lower volume fractions, the convergence was found to be faster than the $\phi = 0.5$ case discussed here. In this work, we obtained the diffusivity by averaging over one hundred independent configurations, with ten random force/torque vectors $\mathbf{F}^e$ employed per configuration. The above analysis shows that equal accuracy might be achieved with fewer configurations and more random force/torque vectors per configuration.

At infinite dilution, the Stokes-Einstein equation gives the diffusivity for spheres: $D_{so} = kT/(6\pi\mu a)$ and $D^r_{so} = kT/(8\pi\mu a^3)$ with the subscript o designating infinite dilution. Corresponding infinite dilution diffusivity for the dicolloid particles have been computed and are tabulated in Table 2.11. The translational and rotational diffusivity in the table have been non-

dimensionalized by $kT/(6\pi\mu a_{eq})$ and $kT/(8\pi\mu a_{eq}^3)$ respectively, where a_{eq} is the radius of the sphere with the same volume (see Table 2.1). For comparison, we have also tabulated the diffusivity for spheroids having the same aspect ratio as the corresponding dicolloidal particles, where the aspect ratio was defined as the ratio of the length of the particle to its maximum width. Diffusivity for spheroids were computed from the analytically known translational and rotational resistance (Shimizu, 1962). Infinite dilution diffusivity for the dicolloids are comparable to the diffusivity of the respective spheroid, though it is slightly smaller for dicolloids (homonuclear particle is an exception), and is clearly smaller than that of a sphere with the same volume.

In a periodic suspension, the interaction between periodic images causes the diffusivity to be smaller than would be obtained from a random suspension of infinite system size. Fortunately, D_s shows a clear trend with system size (Phillips *et al.*, 1988; Ladd, 1990). Ladd (1990) suggested the following expression to correct for system size

$$D_s = D_s(N) + D_{\text{corr}}(N) \tag{2.42}$$

where D_s in the above equation represents the limit for infinite system size, $D_s(N)$ represents the system size dependent self-diffusivity, while $D_{\text{corr}}(N)$ is the system size dependent correction given by

$$D_{\text{corr}}(N) = \left(1.7601(\phi/N)^{1/3} - \phi/N\right) D_{so} \tag{2.43}$$

This correction was found to work well at low volume fraction, but at high volume fraction the required correction was found to be smaller than (2.43) due to the more effective screening of periodic images by neighboring particles. Ladd (1990) suggested using the suspension viscosity μ_r as a measure of the screening, thereby leading to the following equation for the infinite limit D_s

$$D_s = D_s(N) + D_{\text{corr}}/\mu_r \tag{2.44}$$

We found excellent system size corrections with this method when using the classic definition of the lubrication interaction for spheres; however, for simulations with the simpler asymptotic lubrication term in this article (see section 2.5), stronger screening of the peri-

odic images was observed. This is because the modified lubrication interactions in this work (denoted by SP) are slightly stronger than the corresponding *classic* definition of lubrication interactions (denoted by SP*). The simplified asymptotic lubrication formula has negligible impact on the viscosity in suspensions, because of the dominant role of the near singular lubrication interactions. For mobility/diffusivity/permeability calculations, lubrication forces are not as dominant and larger errors occur. We found that equation (2.44) still describes the system size correction well if the μ_r is replaced by a different screening function $\chi = \chi(\phi)$ as follows:

$$D_s = D_s(N) + D_{\text{corr}}/\chi(\phi) \tag{2.45}$$

The χ which gave the best agreement between the data and the above model is plotted in Figure 2.15(a). It clearly shows that χ grows much more rapidly than the suspension viscosity μ_r. The variation of the diffusivity with system size at various volume fractions are shown in Figures 2.15b for SP* and 2.15c for SP, which clearly confirms the stronger screening effect in the latter. Finally, the infinite system limit for the translational diffusivity obtained from both the lubrication models are compared with various literature values in Figure 2.15d. Results with SP* show an excellent agreement with various other simulation results. Results obtained from the modified lubrication (SP) gives slightly lower values. Experimental results lie mostly in between the two values.

The correction for finite system size in suspensions of non-spherical particles can be similarly derived as an extension of the procedure for spheres. To compute the periodic correction, one takes the collection of flow singularities used in the one body solution (Stokeslet, Stokes-Doublet, Potential Dipole and Potential Quadrupole) and computes the velocity field at the particle location due to the periodic images of these singularities. Faxen's laws for the given particle shape are applied to this velocity field. Corrected particle velocity and angular velocity are computed to maintain the balance of forces and torques on the particle. The leading order change in the particle mobility $O((\phi/N)^{1/3})$ comes from the velocity induced at the center of the particle due to the Stokeslet images in the lattice. This term is the same as in suspensions of spheres. The $O(\phi/N)$ term requires the corrected velocity field due to Stokeslets and higher order singularities. Owing to the displaced positions of singularities

along the particle symmetry axis in the dicolloids, it proves convenient to express their cumulative effect as a multipole expansion about the particle center. This leads to an effective Stokes-doublet and Stokes quadrupole in the far field with higher order singularities having lower order effects. Thus the Faxen's law is applied to a combined velocity field due to an effective Stokelet, Stokes-doublet and Stokes-Quadrupole. In this work, all of the these terms were numerically computed and an orientationally averaged change in mobility was found. We non-dimensionalize the change in mobility with the orientatinally averaged mobility of the particle (Table 2.11), to obtain D_{corr} as

$$D_{\text{corr}} = \lambda \left(1.7601 \left(\frac{\phi}{N} \right)^{1/3} - \alpha \frac{\phi}{N} \right) D_{so} \tag{2.46}$$

where

$$D_{so} = \left(\frac{kT}{6\pi\mu a_{eq}\lambda} \right) \tag{2.47}$$

is the infinite dilution diffusivity for the dicolloid particle; a_{eq} is the equivalent sphere radius with volume equal to that of the particle. The correction factor λ depends only on the one body mobility coefficients for the given particle shape. Values of λ for the dicolloid shapes in the present effort are $\lambda = 1.0020$, 1.0004 and 1.0206 for small-bump, homonuclear and fused-dumbbell particles resepctively. Computed values for α are $\alpha = 1.0082$, 1.0040 and 1.102 for small bump, homonuclear and fused-dumbbell particles respectively. With values $\lambda = 1$ and $\alpha = 1$, this equation reduces to the Ladd result for spheres. The diffusivity for non-spherical particles corrected for system size can now be written by an equation similar to (2.45) with D_{corr} given by (2.46) . In order to verify the system size dependence presented above, we plot the translational diffusivity as a function of $f(\phi/N) = D_{\text{corr}}/D_{so}$ for fused-dumbbells at two different volume fractions, $\phi = 0.01$ and $\phi = 0.5$, in Figure 2.16. The close linear relationship between the self-diffusivity and $f(\phi/N)$ confirms the validity of the finite system size correction, while the magnitude of the slope at each volume fraction provides the inverse of the screening function $1/\chi(\phi)$. Results for $\chi(\phi)$ for all particle shapes are presented in Figure 2.17(a), where $\chi(\phi)$ is defined in equation (2.45), and the form of D_{corr} used is given in equation (2.46). The screening function was found to be approximately the

same for all particle shapes, though at intermediate volume fractions it was slightly lower for spheres. The ratio of screening function to viscosity also shows a similar trend with volume fraction for all particle shapes, which is shown in Figure 2.17(b). This ratio seems to plateau at high volume fractions.

Data for short time translation self-diffusivity presented here have been extrapolated to an infinite system using the procedure described above. These results are are shown in Figure 2.18(a) and tabulated in Table 2.12. The diffusivities for all particles shapes were found to decrease in a similar fashion with volume fraction. For comparison, in the above figure, we have also plotted the diffusivity of prolate spheroids with aspect ratio 6, which shows a slower decrease at all volume fractions. It is worth noting that this decay is even slower than the SP* result in Figure 2.15(d), which was for spheres with the classic definition of lubrication. To better distinguish the variation in diffusivity with volume fraction for different particle shapes, we plot the diffusivity as a ratio to that of spheres at the same volume fraction in Figure 2.18(b). Some interesting features are apparent in the figure. For homonuclear and small-bump particles, the diffusivity at high ϕ decays relative to that of spheres. On the other hand, the diffusivity for fused-dumbbells is very close to that of spheres accept for a sharp uptick at high ϕ. This uptick is expected owing to the higher value of ϕ_{cp} for the fused-dumbbells. Finally, following Claeys & Brady (1993b), we also computed the translational diffusivity parallel and perpendicular to the axis of symmetry. The variation of these components with volume fraction were found to be very similar to the overall diffusivity, hence they are not reported here.

Rotational diffusivity was found to be almost independent of system size which is consistent with previous works (Phillips *et al.*, 1988; Claeys & Brady, 1993b). Also the form of the lubrication interaction, as discussed above in the context of translational diffusivity, was found to have a very little impact on rotational diffusivity. Rotational diffusivity for all particle shapes are shown in Figure 2.19(a) and tabulated in Table 2.13. In addition, rotational diffusivity for dicolloids plotted as a ratio to that of spheres at the same volume fraction is shown in Figure 2.19(b). A clear trend is perceptible in this case as the rotational diffusivity for dicolloids was found to decrease more strongly in a monotonic fashion with volume fraction. Among dicolloids, the rotational diffusivity was found to be the lowest for

fused-dumbbells, intermediate for homonuclear particles and highest for small-bump particles. Also plotted in Figure 2.19(a) is the rotational diffusivity for prolate spheroids of aspect ratio 6 from Claeys & Brady (1993b), which shows a slower decrease with volume fraction than any of the particles considered here. We also computed the rotational diffusivity parallel and perpendicular to the axis of symmetry (Claeys & Brady, 1993b). For particles with small degree of anisotropy (homonuclear and small-bump), the two components showed a similar trend with volume fraction as compared to the overall rotational diffusivity. But for fused-dumbbell particles, the two components showed a perceptible difference, which is shown in Figure 2.20. As could be seen, the diffusivity for rotations perpendicular to the axis of symmetry shows a stronger decrease with volume fraction as compared to the diffusivity for rotations along the axis of symmetry, which is not surprising. Also note that the diffusivity for rotations parallel to the axis of symmetry varies almost identically to that of spheres, which again is not surprising given that the particle cross-section is very similar to that of a sphere. In the figure, we also plot the corresponding components of rotational diffusivity for spheroids of aspect ratio 6 from Claeys & Brady (1993b). This shows that the diffusivity for rotations perpendicular to the axis of symmetry in spheroids decays almost identically to that of the corresponding component for fused-dumbbell particles, but the component for rotation parallel to the axis of symmetry decays slowly, thereby leading to slower decay of its overall rotational diffusivity in Figure 2.19(a).

2.8 Conclusions

A PME Stokesian dynamics algorithm has been developed for non-spherical dicolloidal particles. The singularity solution for a dicolloid in a given flow was represented by a distribution of Stokes-singularities along the axis of symmetry. For linear flows, two singularity locations with low order Stokes singularities (Stokeslet, Stokes-doublet, Potential dipole, and Potential quadrupole) were found to be sufficiently accurate with optimized strengths and locations. The knowledge of the one-body singularity solutions in linear flows completely defines the far-field many-body term in Stokesian dynamics. For the lubrication interaction, a modified lubrication tensor was developed for dicolloid particles which does not require the exact

Table 2.1: Parameters for dicolloid geometry and numerical solution: See Figure (2.1) for illustration of terms. S_1 and S_2 refer to the location of singularities, while C_1 and C_2 refer to centers of spherical nodes along the axis of symmetry, with the center of mass taken as the origin. Also given is the effective radius of the sphere which has the same volume as the particle (a_{eq}). All distances are non-dimensionalized by a, the radius of the largest spherical node forming the dicolloid.

Particle	b	c	S_1	S_2	C_1	C_2	a_{eq}
fused dumbbell	1.0	1.0	-0.580	0.580	-0.5	0.5	1.1905
homonuclear	1.0	0.2	-0.165	0.165	-0.1	0.1	1.0475
small-bump	0.8	0.4	-0.053	0.588	-0.053	0.347	1.0192

two-body solution. The lubrication tensor was used in conjunction with a semi-empirical correction factor to predict the near field interactions between a pair of dicolloids. The accuracy of the method developed here was tested against high precision numerical solutions from the spectral boundary element method with accuracy agreement comparable that for spheres in the classic Stokesian dynamics approach. The new algorithm was used to study viscosity and self-diffusivity of homogeneous suspensions of dicolloidal particles. The viscosity was shown to be a non-monotonic function of particle aspect ratio, with a local maximum at aspect ratio 1.1 (homonuclear), a minimum at aspect ratio 1.5 (fused-dumbbells) and a monotonic increase for larger aspect ratio. A similar trend was observed for the translational diffusivity. The non-monotonic trend in viscosity was shown to correlate well with the maximum close-packed volume fraction of the particles. The rotational diffusivity was found to decrease monotonically with increasing aspect ratio.

Table 2.2: Accuracy: Single Homonuclear particle in various flows. Comparison of moments from singularity solution and from spectral boundary element (BEM) method. See Appendix for the definitions of flows. All moments have been non-dimensionalized by $8\pi\mu$, with the flows defined as above and radius of the largest spherical node a=1.

Field	Moment	Singularity	BEM	% Error
$\boldsymbol{u}_1$	F_1	7.9105E-01	7.9118E-01	0.017
$\boldsymbol{u}_3$	F_3	7.7691E-01	7.7719E-01	0.036
$\boldsymbol{\omega}_1$	T_1	1.1764E+00	1.1777E+00	0.110
$\boldsymbol{\omega}_3$	T_3	1.1073E+00	1.1103E+00	0.270
$\boldsymbol{e}_3$	S_{12}	9.3295E-01	9.3639E-01	0.367
$\boldsymbol{e}_4$	S_{13}	9.6567E-01	-9.6765E-01	0.205
$\boldsymbol{e}_6$	S_{11}	9.6500E-01	9.6677E-01	0.183
$\boldsymbol{e}_6$	S_{33}	-9.9705E-01	-9.9715E-01	0.010

Table 2.3: Accuracy: Single Small-bump particle in various flows. Comparison of moments from singularity solution and from spectral boundary element (BEM) method. See Appendix for the definitions of flows. All moments have been non-dimensionalized by $8\pi\mu$, with the flows defined as above and radius of the largest spherical node a=1.

Field	Moment	Singularity	BEM	% Error
$\boldsymbol{u}_1$	F_1	7.7086E-01	7.7124E-01	0.049
$\boldsymbol{u}_1$	S_{13}	6.7439E-03	6.9218E-03	2.571
$\boldsymbol{u}_3$	F_3	7.5612E-01	7.5650E-01	0.051
$\boldsymbol{u}_3$	S_{11}	5.1109E-03	4.6216E-03	-10.587
$\boldsymbol{u}_3$	S_{33}	-1.0222E-02	-9.2433E-03	-10.585
$\boldsymbol{\omega}_1$	T_1	1.0913E+00	1.0936E+00	0.207
$\boldsymbol{\omega}_3$	T_3	1.0201E+00	1.0230E+00	0.282
$\boldsymbol{e}_3$	S_{12}	8.5545E-01	8.5998E-01	0.526
$\boldsymbol{e}_4$	F_1	1.3604E-02	1.3844E-02	1.728
$\boldsymbol{e}_4$	S_{13}	1.5638E+00	-1.5894E+00	1.607
$\boldsymbol{e}_6$	F_3	1.5262E-02	1.3865E-02	-10.072
$\boldsymbol{e}_6$	S_{11}	8.7774E-01	8.8208E-01	0.492
$\boldsymbol{e}_6$	S_{33}	-9.0002E-01	-9.0418E-01	0.459

Table 2.4: Accuracy: Single fused-dumbbell particle in various flows. Comparison of moments singularity solution and from spectral boundary element (BEM) method. See Appendix for the definitions of flows. All moments have been non-dimensionalized by $8\pi\mu$, with the flows defined as above and radius of the largest spherical node a=1.

Field	Moment	Singularity	BEM	% Error
$\boldsymbol{u}_1$	F_1	9.3521E-01	9.3815E-01	0.312
$\boldsymbol{u}_3$	F_3	8.6790E-01	8.7150E-01	0.412
$\boldsymbol{\omega}_1$	T_1	2.0718E+00	2.0872E+00	0.739
$\boldsymbol{\omega}_3$	T_3	1.4657E+00	1.4937E+00	1.874
$\boldsymbol{e}_3$	S_{12}	1.2576E+00	1.3053E+00	3.655
$\boldsymbol{e}_4$	S_{13}	1.5638E+00	1.5894E+00	1.607
$\boldsymbol{e}_6$	S_{11}	1.5323E+00	1.5563E+00	1.542
$\boldsymbol{e}_6$	S_{33}	1.8071E+00	1.8073E+00	0.015

Table 2.5: Numerical tests for lubrication correction factor: Homonuclear particles in configuration 1 (see figures (2.2) and (2.9) and Table (2.1)) with $\boldsymbol{u}^{p1} = (0, 1, 0)$ and $\boldsymbol{u}^{p2} = (0, 0, 0)$. Comparison of the force $(-F_y^1/(8\pi\mu a))$ obtained from the spectral boundary element (BEM) method with that from the Stokesian dynamics technique, both with (SD + LB) and without (SD)the lubrication correction, is shown. δ represents the smallest gap between the two particles which occurs at two locations in this configuration.

δ/a	BEM	SD + LB	SD
2.00	0.9417	0.9582	0.9440
1.00	1.1234	1.2457	1.1465
0.70	1.2720	1.5423	1.3187
0.40	1.6285	2.3611	1.7256
0.20	2.4478	4.3238	2.5967
0.10	4.1635	8.0752	4.3074
0.01	44.3133	58.2027	39.9709

Table 2.6: Accuracy: Two fused dumbbell particles in configuration 1 with $\boldsymbol{u}^{p1} = (0, 1, 0)$ and $\boldsymbol{u}^{p2} = (0, 0, 0)$. Comparison of the force $(-F_y^1/(8\pi\mu a))$ obtained from the spectral boundary element method (BEM) with that from the Stokesian dynamics (SD) technique. δ represents the smallest gap between the two particles which occurs at two locations in this configuration.

δ/a	SD	BEM
5.00	1.0058	1.0095
4.00	1.0336	1.0374
3.00	1.0832	1.0868
2.50	1.1248	1.1277
2.00	1.1890	1.1902
1.50	1.2989	1.2952
1.00	1.5206	1.5046
0.50	2.1416	2.1181
0.20	3.6574	3.8517
0.10	5.8089	6.3064
0.01	40.3725	41.7200

Table 2.7: Accuracy: Two fused dumbbell particles in configuration 3 with $\boldsymbol{u}^{p1} = (0, 1, 0)$ and $\boldsymbol{u}^{p2} = (0, 0, 0)$. Comparison of the force $(-F_y^1/(8\pi\mu a))$ obtained from the spectral boundary element method (BEM) with that from the Stokesian dynamics technique (SD). δ represents the smallest gap between the two particles which occurs at four locations in this configuration.

δ/a	SD	BEM
2.06	1.1790	1.1890
1.08	1.4795	1.4948
0.88	1.6196	1.6426
0.5	2.2111	2.3300
0.45	2.5826	2.5288
0.29	3.5348	3.7027
0.14	6.2566	8.2716
0.06	12.9363	23.7980

Table 2.8: Accuracy: Two full dumbbells (effectively a 4 sphere system) in configuration 3 with with $\boldsymbol{u}^{p1} = (0, 0, 0)$ and $\boldsymbol{u}^{p2} = (0, 1, 0)$. Comparison of the force $(F_y^1/(8\pi\mu a))$ obtained from the spectral boundary element method (BEM) with that from the Stokesian dynamics technique using the modified lubrication (SD) and using the classic lubrication for spheres (SD*). δ represents the smallest gap between the two particles which occurs at four locations in this configuration.

δ	SD	SD*	BEM
5.14	0.1725	0.1725	0.1754
4.16	0.2043	0.2042	0.2080
3.20	0.2519	0.2516	0.2570
2.24	0.3330	0.3317	0.3410
1.32	0.5115	0.5043	0.5278
0.45	1.1983	1.1405	1.3702
0.29	1.6148	1.5260	2.0389
0.14	2.6168	2.4826	3.7833
0.06	4.5185	4.3550	6.4162

Table 2.9: Relative viscosity for all particle shapes in a Monte Carlo configuration (1000 particles).

ϕ	Homonuclear	Small-Bump	Fused-dumbbell	Sphere
0.05	1.1381	1.1383	1.1399	1.1380
0.10	1.3129	1.3119	1.3158	1.3102
0.20	1.8250	1.8145	1.8049	1.8029
0.30	2.7627	2.7179	2.6518	2.6798
0.40	4.6142	4.5018	4.2503	4.3861
0.50	8.6860	8.3217	7.5742	8.0731

Table 2.10: Parameters for viscosity model (Eiler): c/a, $[\mu]$, ϕ_m, ϕ_{cp}, ϕ_{rcp} for particles composed of equal sized components. ϕ_{cp} is taken from Vega *et al.* (1992b), while ϕ_{rcp} is taken from Donev *et al.* (2004) for the same aspect ratio spheroid.

Particle	c/a	$[\mu]$	ϕ_m	ϕ_{cp}	ϕ_{rcp}
Sphere	0	2.50	0.755	0.7405	0.640
homonuclear	0.2	2.4977	0.734	0.7587	0.670
fused dumbbell	1.0	2.5378	0.782	0.7870	0.716
dumbbell	2.0	2.9862	0.776	0.7405	0.706

Table 2.11: Infinite dilution diffusivity (translational and rotational) non-dimensionalized by $kT/6\pi\mu a_{eq}$ and $kT/8\pi\mu a_{eq}^3$ respectively, where a_{eq} is the radius of sphere with the same volume (Table 2.1). For comparison, corresponding diffusivity for a spheroid ($D_{so}(R)$ and $D_{so}^r(R)$) with the same aspect ratio R is also tabulated. Aspect ratio was taken to be the ratio of the length of the particle to its maximum breadth (1.1 for homonuclear and small-bump, 1.5 for fused-dumbbell).

Particle	D_s	$D_{so}(R)$	D_{so}^r	$D_{so}^r(R)$
Small-Bump	0.9980	0.9992	0.9928	0.9964
Homonuclear	0.9996	0.9992	0.9973	0.9964
Fused-dumbbell	0.9798	0.9854	0.9267	0.9421

Table 2.12: Translational diffusivity: $D_s(\phi)/D_{so}$ for all particle shapes in a Monte Carlo configuration extrapolated to an infinite system size.

ϕ	Homonuclear	Small-Bump	Fused-dumbbell	Sphere
0.01	0.9592	0.9646	0.9631	0.9710
0.05	0.8412	0.8440	0.8541	0.8480
0.10	0.6973	0.7015	0.7114	0.7149
0.20	0.4703	0.4781	0.4910	0.4986
0.30	0.3128	0.3248	0.3344	0.3426
0.40	0.2026	0.2095	0.2192	0.2242
0.50	0.1247	0.1305	0.1400	0.1387

Table 2.13: Rotational diffusivity: $D_s^r(\phi)/D_{so}^r$ for all particle shapes in a Monte Carlo configuration extrapolated to an infinite system size.

ϕ	Homonuclear	Small-Bump	Fused-dumbbell	Sphere
0.01	0.9912	0.9908	0.9882	0.9932
0.05	0.9644	0.9649	0.9643	0.9675
0.10	0.9206	0.9214	0.9192	0.9242
0.20	0.8163	0.8202	0.8139	0.8318
0.30	0.6978	0.7025	0.6894	0.7241
0.40	0.5699	0.5755	0.5577	0.6024
0.50	0.4422	0.4471	0.4233	0.4774

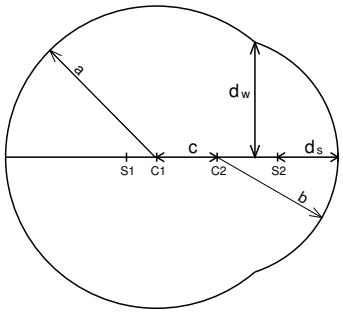

Figure 2.1: Dicolloidal particle showing parameters: C1 and C2 are the centers of the two spherical nodes forming the dicolloid. S1 and S2 are the singularity positions. c is the center to center separation, d_w is the maximum width of the bump; d_s is the smallest distance of the singularity S2 from the surface of the particle. a, b are radii of the two spheres ($a \geq b$).

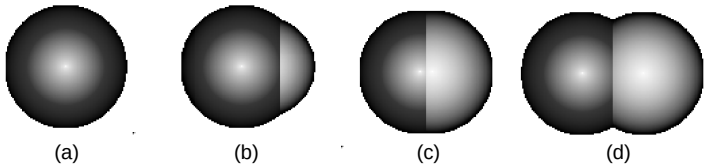

Figure 2.2: All particle shapes: (a) Sphere, (b) Small-Bump, (c) Homonuclear, (d) Fused-dumbbell. See table (2.1) for geometry parameters for these particles as defined in Figure (2.1).

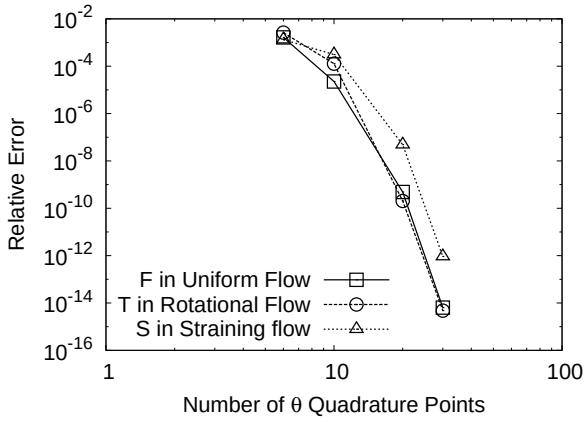

Figure 2.3: Convergence in computed moments with number of θ quadrature points in integral for norm of the error in boundary condition (sec 2.3) for a fused-dumbbell particle.

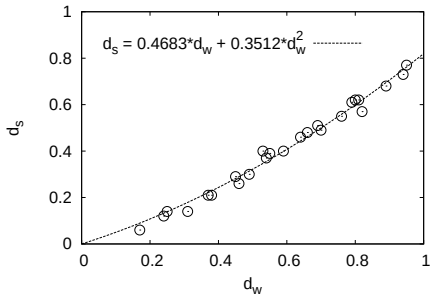

Figure 2.4: d_s as a function of d_w for hetero-nuclear particles with bumps smaller than a hemisphere

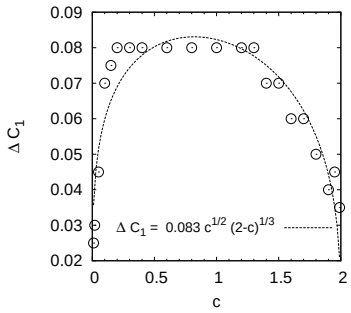

Figure 2.5: Displacement of Singularities from the respective centers for homo-nuclear particles. Displacement is in the direction away from the the two centers

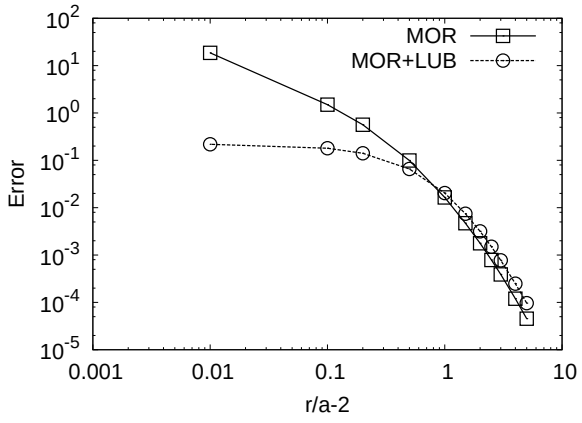

Figure 2.6: Error in force $(F - F_{exact})$ for two spheres undergoing a squeezing motion. The method of reflection result (MOR) and corrected lubrication result $(MOR{+}LUB)$ compared with the spectral boundary element result. Error in the $MOR + LUB$ term plateaus as the gap goes to zero, while MOR error is unbounded.

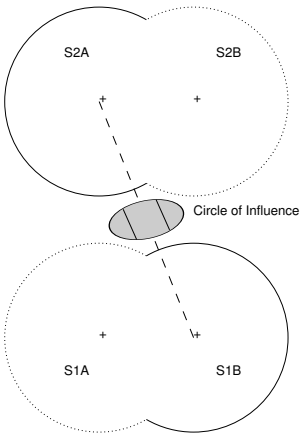

Figure 2.7: Lubrication Correction Factor: Figure showing the complete and the truncated circle of influence

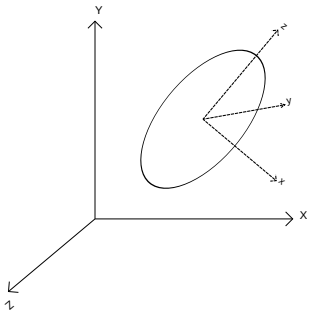

Figure 2.8: Illustration showing the local particle frame and global frame. Origins of two frames have been displaced for clarity.

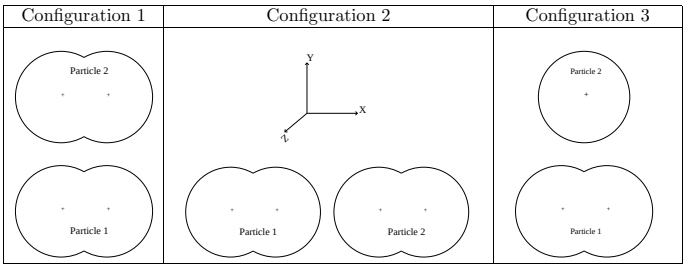

Figure 2.9: Geometry for configurations used as test cases for comparison with solutions from spectral boundary method. The coordinate axis shown in configuration 2 is the same for configurations 1 and 3.

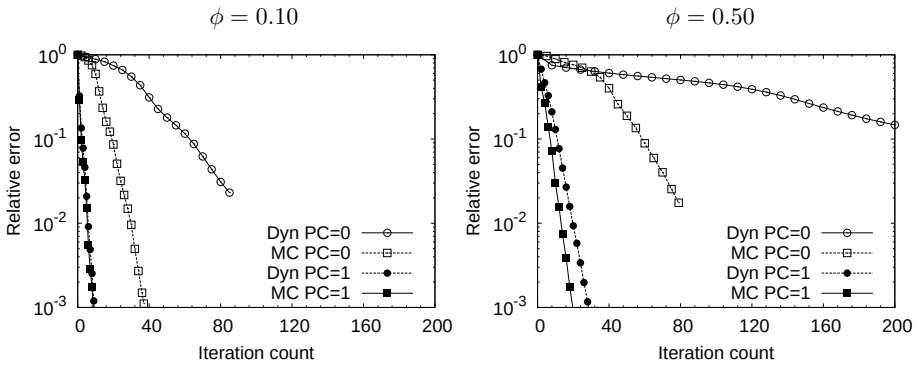

Figure 2.10: Convergence of relative error (L_2 norm of the error in solution non-dimensionalized by its initial value) with number of GMRES iterations in suspensions of fused-dumbbell particles. Results with the preconditioner are denoted by PC=1 and those without a preconditioner are denoted by PC=0. Convergence behavior is shown for two different volume fractions ($\phi = 0.1$ and $\phi = 0.5$) and for two different configuration types: Monte Carlo configurations (MC) and Dynamic sheared configurations (Dyn). The latter has a characteristic minimum gap of $10^{-3}\times$ radius of a spherical node.

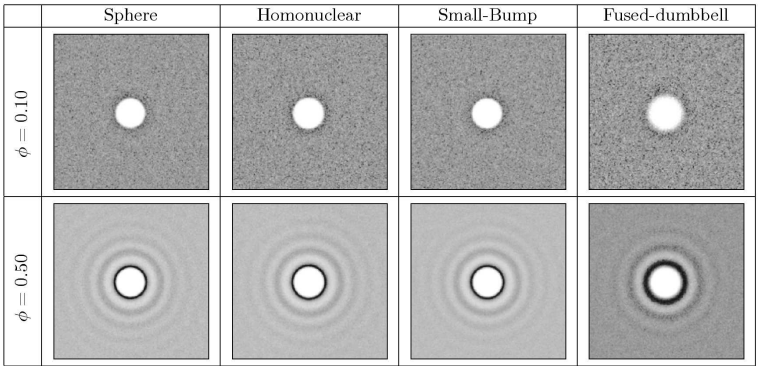

Figure 2.11: Pair distribution functions for two representative volume fractions: $\phi = 0.1$ and $\phi = 0.5$. Particles are in a Monte Carlo configuration. For dicolloids, pair distribution functions are computed for the center of mass of the particles.

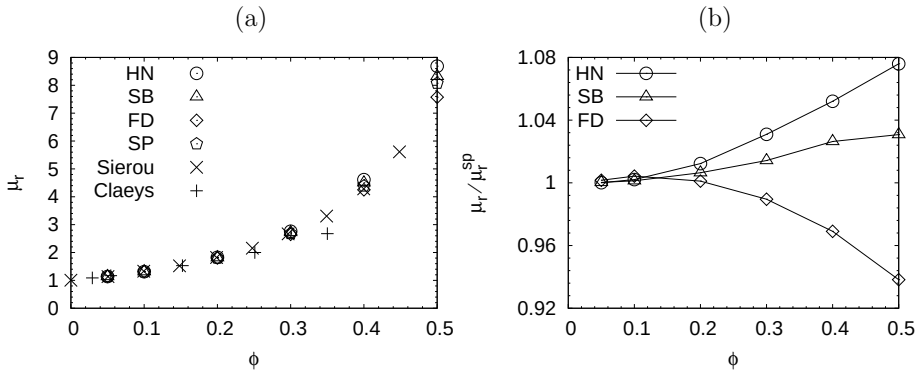

Figure 2.12: Viscosity for suspensions with different particle shapes in a Monte Carlo configuration. (a) HN, SB, FD, and SP refer to homonuclear, small-bump, fused-dumbbell and sphere respectively. Sierou refers to simulation data for spheres from (Sierou & Brady, 2001) while Claeys refers to simulation data for spheroids with aspect ratio 3 from (Claeys & Brady, 1993b). (b) Viscosity of dicolloids expressed as a ratio with that of spheres at the same volume fraction.

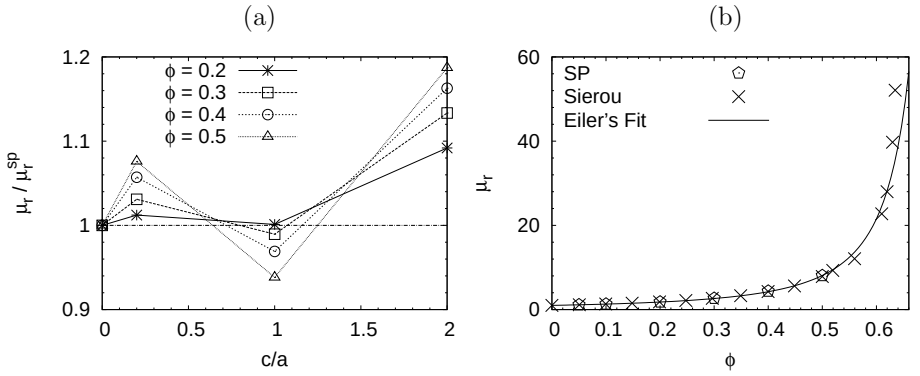

Figure 2.13: (a) Viscosity at four volume fractions as a function of c/a. $c/a = 0.2$ is homonuclear, $c/a = 1.0$ is fused-dumbbell, $c/a = 2.0$ is full dumbbell (tangent spheres), (b)viscosity data fit to semi-empirical Eiler's equation (2.38). SP refers to data from this work, while Sierou is taken from Sierou & Brady (2001).

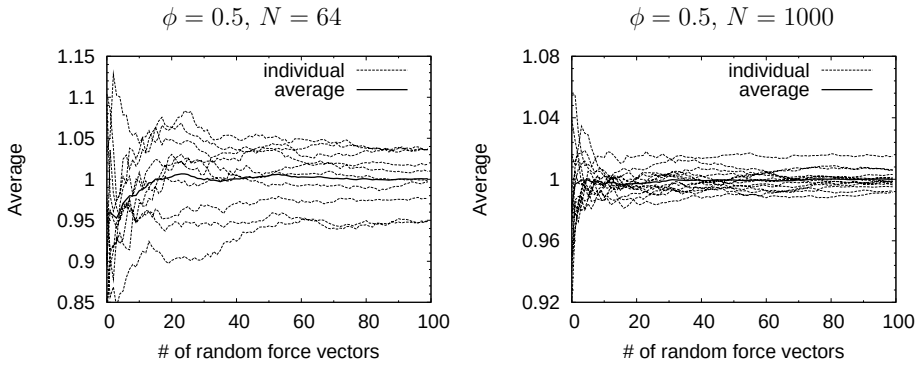

Figure 2.14: Thin lines: Convergence of diffusivity with the number of random force/torque vectors employed for a single Monte Carlo configuration. Thick line: Corresponding average over all the Monte Carlo configurations in the figure. All values have been non-dimensionalized by the final converged average shown by the thick line in corresponding plots.

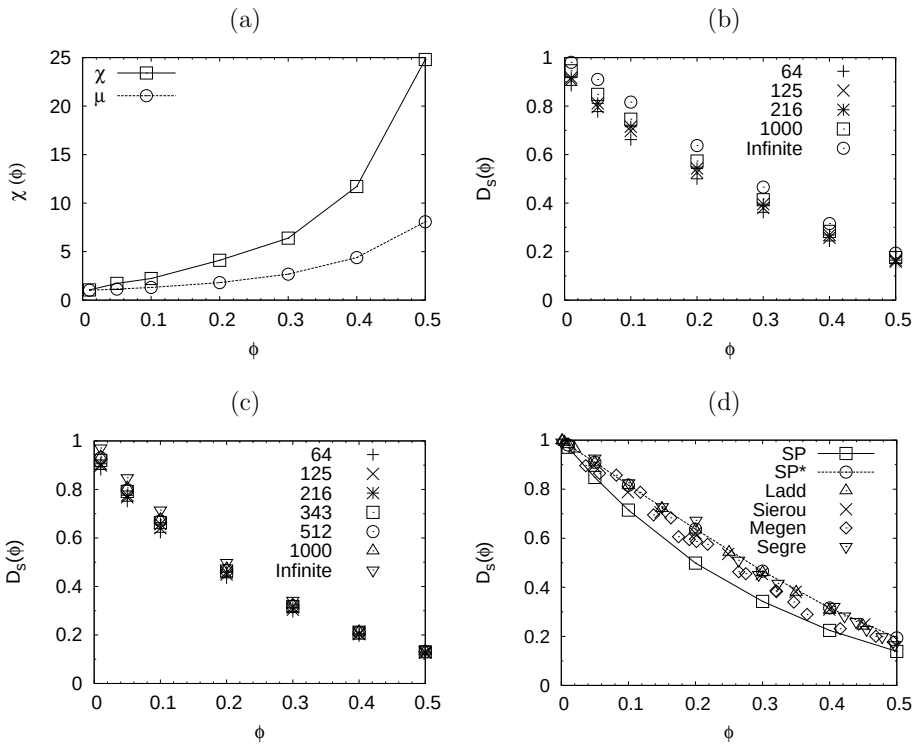

Figure 2.15: Diffusivity parameters for spheres. (a) Screening function χ as defined in (2.45) compared with suspension viscosity μ. (b) Effect of system size on short-time self-diffusivity with classic form of lubrication (SP*) correction . (c) Effect of system size on short-time self-diffusivity with modified definition of lubrication correction (SP). (d) Comparison of extrapolated short-time self-diffusivity with literature. SP and SP* are values obtained in this work with SP using the modified lubrication, while SP* using the classic lubrication form. For literature values: Ladd and Sierou refers to simulation data from Ladd (1990) and Sierou & Brady (2001) respectively, while Megen and Segre refers to experimental data from van Megen & Underwood (1989) and Segré *et al.* (1995) respectively.

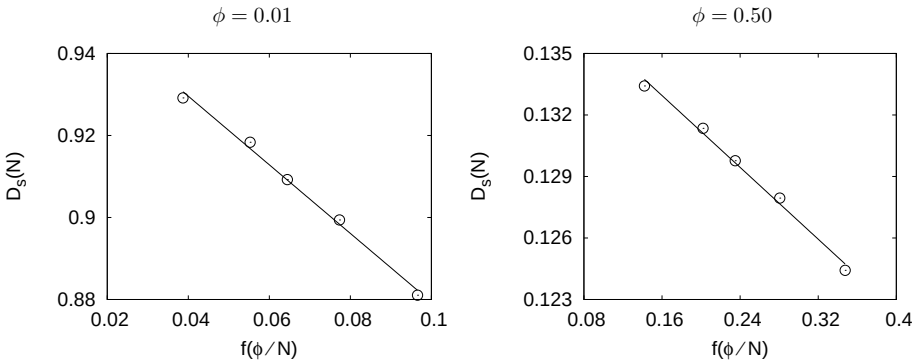

Figure 2.16: Short time translational diffusivity for fused dumbbells as a function of $f(\phi/N) = D_{\text{corr}}/D^s_{so}$ (see equation 2.46). Two representative volume fractions are shown: $\phi = 0.01$ and $\phi = 0.5$

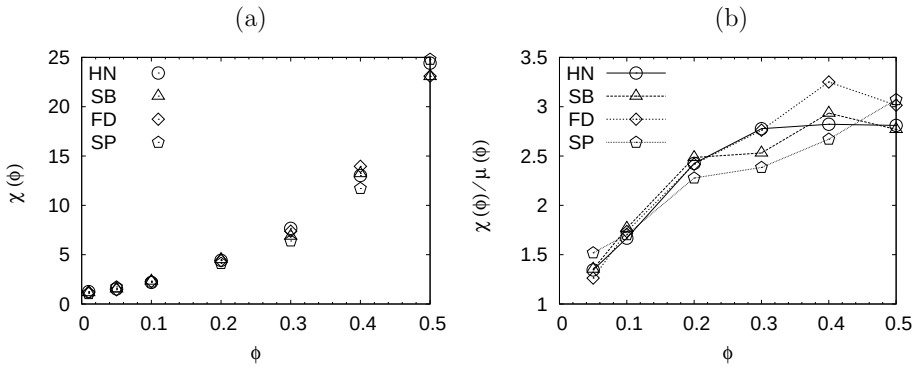

Figure 2.17: (a)Screening function χ as defined in equation (2.45) for all particle shapes. (b) Ratio of the screening function and suspension viscosity for all particle shapes. See Figure (2.12) for legends for particle shapes.

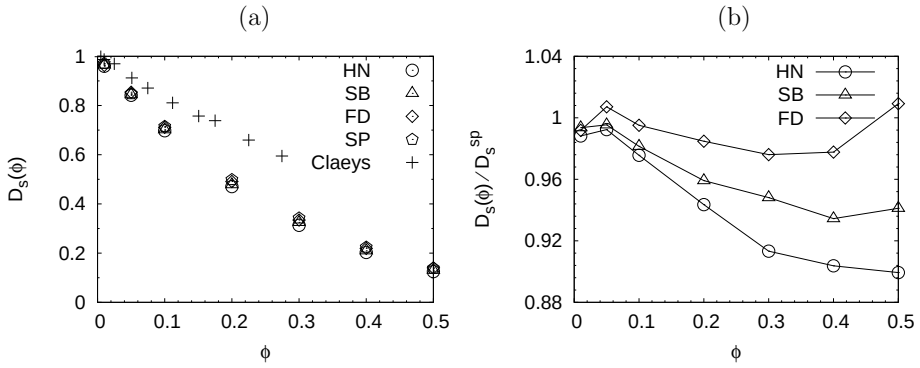

Figure 2.18: Short time translational diffusivity for different particles in Monte Carlo configuration. Diffusivity data extrapolated to infinite system size. $D_s(\phi)$ non-dimensionalized by the corresponding infinite dilution values. (a) HN, SB, FD and SP refer to homonuclear, small-bump, fused-dumbbell and sphere suspension respectively. Claeys refers to short-time self diffusivity for spheroids with aspect ratio 6 taken from Claeys & Brady (1993b). (b) Same as (a) with the diffusivity scaled by value for spheres (SP) at same volume fraction.

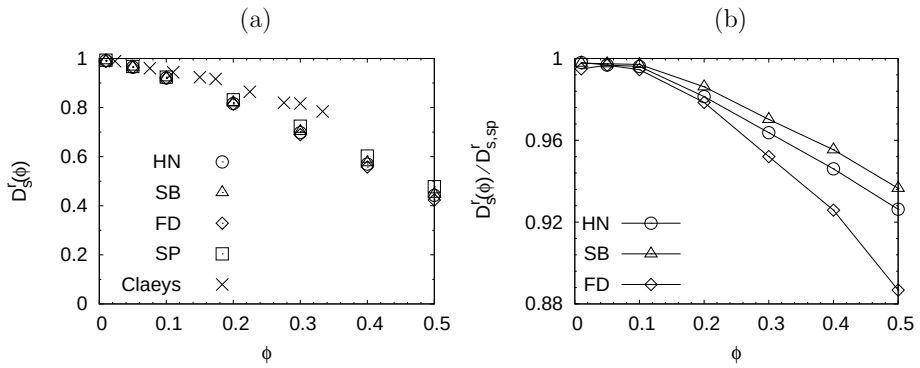

Figure 2.19: (a) Short time rotational diffusivity for all particle shapes in a Monte Carlo configuration. $D_s^r(\phi)$ non-dimensionalized by the corresponding infinite dilution values. See Figure (2.18) for notation. (b) Same as (a) with the diffusivity scaled by that of spheres (SP) at the same volume fraction.

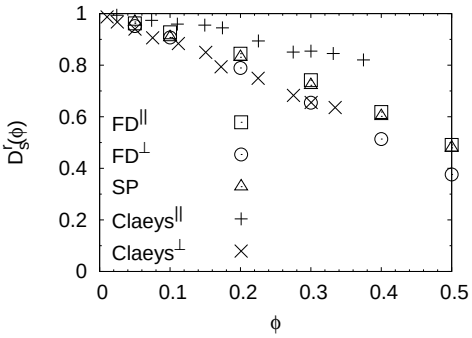

Figure 2.20: Short time rotational diffusivity parallel ($\|$) and perpendicular ($\perp$) to the axis of symmetry. See Figure (2.18) for notation.

References

Batchelor, G.K. 1970. Slender-body theory for particles of arbitrary cross-section in Stokes flow. *Journal of Fluid Mechanics*, **44**, 419–440.

Brady, J.F., & Bossis, G. 1988. Stokesian Dynamics. *Annual Review of Fluid Mechanics*, **20**(1), 111–157.

Butler, J.E., & Shaqfeh, E.S.G. 2002. Dynamic simulations of the inhomogeneous sedimentation of rigid fibres. *Journal of Fluid Mechanics*, **468**, 205–237.

Chwang, A.T., & Wu, T.Y. 1975. Hydromechanics of low-Reynolds-number flow. Part 2. Singularity method for Stokes flows. *Journal of Fluid Mechanics*, **67**, 787–815.

Claeys, I.L., & Brady, J.F. 1989. Lubrication singularities of the grand resistance tensor for two arbitrary particles. *Physico Chem. Hydrodyn.*, **11**, 261–293.

Claeys, I.L., & Brady, J.F. 1993a. Suspensions of prolate spheroids in Stokes flow. Part 1. Dynamics of a finite number of particles in an unbounded fluid. *Journal of Fluid Mechanics*, **251**, 411–442.

Claeys, I.L., & Brady, J.F. 1993b. Suspensions of prolate spheroids in Stokes flow. Part 2. Statistically homogeneous dispersions. *Journal of Fluid Mechanics*, **251**, 443–477.

Claeys, I.L., & Brady, J.F. 1993c. Suspensions of prolate spheroids in Stokes flow. Part 3. Hydrodynamic transport properties of crystalline dispersions. *Journal of Fluid Mechanics*, **251**, 479–500.

Cox, R.G. 1974. The motion of suspended particles almost in contact. *International Journal of Multiphase Flow*, **1**, 343–371.

Donev, A., Cisse, I., Sachs, D., Variano, E.A., Stillinger, F.H., Connelly, R., Torquato, S., & Chaikin, P.M. 2004. Improving the Density of Jammed Disordered Packings Using Ellipsoids. *Science*, **303**(5660), 990–993.

Gerbode, S.J., Lee, S.H., Liddell, C.M., & Cohen, Itai. 2008. Restricted Dislocation Motion in Crystals of Colloidal Dimer Particles. *Physical Review Letters*, **101**, 058302.

Glotzer, S.C., & Solomon, M.J. 2007. Anisotropy of building blocks and their assembly into complex structures. *Nature Materials*, **6**, 557–562.

Guckel, E.K. 1999. *Large Scale Simulations of Particulate Systems using the PME Method*. Ph.D. thesis, University of Illinois at Urbana-Champaign.

Happel, John, & Brenner, Howard. 1991. *Low Reynolds Number Hydrodynamics: With Special Applications to Particulate Media*. Springer.

Hasimoto, H. 1959. On the periodic fundamental solutions of the stokes equations and their application to viscous flow past a cubic array of spheres. *Journal of Fluid Mechanics*, **5**, 317–328.

Hosein, I.D., & Liddell, C.M. 2007. Convectively Assembled Asymmetric Dimer-Based Colloidal Crystals. *Langmuir*, **23**, 10479–10485.

Jeffery, G.B. 1922. The Motion of Ellipsoidal Particles Immersed in a Viscous Fluid. *Proceedings of the Royal Society of London. Series A*, **102**(715), 161–179.

Jeffrey, D.J., & Onishi, Y. 1984. Calculation of the resistance and mobility functions for two unequal rigid spheres in low-Reynolds-number flow. *Journal of Fluid Mechanics*, **139**, 261–290.

Johnson, P.M., van Kats, C.M., & van Blaaderen, A. 2005. Synthesis of Colloidal Silica Dumbbells. *Langmuir*, **21**(24), 11510–11517.

Kim, J.W., Larsen, R.J., & Weitz, D.A. 2006. Synthesis of nonspherical colloidal particles with anisotropic properties. *Journal of American Chemical Society*, **128**(44), 14374–14377.

Kim, S., & Lu, S.Y. 1987. The Functional Similarity between Faxen Relations and Singularity Solutions for Fluid-Fluid, Fluid-Solid, and Solid-Solid Dispersions. *Internation Journal of Multiphase Flow*, **13**(6), 837–844.

Kim, Sangtae, & Karrila, Seppo J. 2005. *Microhydrodynamics: Principles and Selected Applications*. Dover Publicatons.

Krieger, I.M. 1973. Rheology of monodisperse latices. *Advances in Colloid and Interface Science*, **3**, 111–136.

Ladd, A.J.C. 1990. Hydrodynamic transport coefficients of random dispersions of hard spheres. *Journal of Chemical Physics*, **93**(5), 3484–3494.

Mackaplow, M.B., & Shaqfeh, E.S.G. 1996. A numerical study of the rheological properties of suspensions of rigid, non-Brownian fibres. *Journal of Fluid Mechanics*, **329**, 155–186.

Meng, Q., & Higdon, J.J.L. 2008a. Large scale dynamic simulation of plate-like particle suspensions. Part I: Non-Brownian simulation. *Journal of Rheology*, **52**, 1–36.

Meng, Q., & Higdon, J.J.L. 2008b. Large scale dynamic simulation of plate-like particle suspensions. Part II: Brownian simulation. *Journal of Rheology*, **52**, 37–65.

Mitragotri, S., & lahann, J. 2008. Physical approaches to biomaterial design. *Nature Materials*, **8**, 15–23.

Mock, E.B., & Zukoski, C.F. 2007. Determination of Static Microstructure of Dilute and Concentrated Suspensions of Anisotropic Particles by Ultra-Small-Angle X-ray Scattering. *Langmuir*, **23**, 8760–8771.

Mock, E.B., Bruyn, H. De, Hawkett, B.S., Gilbert, R.G., & Zukoski, C.F. 2006. Synthesis of Anisotropic Nanoparticles by Seeded Emulsion Polymerization. *Langmuir*, **22**(9), 4037–4043.

Muldowney, G.P., & Higdon, J.J.L. 1995. A spectral boundary element approach to three-dimensional Stokes flow. *Journal of Fluid Mechanics*, **298**, 167–192.

Phillips, R.J., Brady, J.F., & Bossis, G. 1988. Hydrodynamic transport properties of hard-sphere dispersions. I. Suspensions of freely mobile particles. *Physics of Fluids*, **31**(12), 3462–3472.

Saintillan, D., Darve, E., & Shaqfeh, E.S.G. 2005. A smooth particle-mesh Ewald algorithm for Stokes suspension simulations: The sedimentation of fibers. *Physics of Fluids*, **17**(3), 033301.

Segré, P.N., Behrend, O.P., & Pusey, P.N. 1995. Short-time Brownian motion in colloidal suspensions: Experiment and simulation. *Physical Review E*, **52**(5), 5070–5083.

Shimizu, H. 1962. Effect of molecular shape on nuclear magnetic relaxation. *Journal of Chemical Physics*, **37**(4), 765–778.

Sierou, A., & Brady, J.F. 2001. Accelerated Stokesian Dynamics simulations. *Journal of Fluid Mechanics*, **448**, 115–146.

Singer, S.J., & Mumaugh, R. 1990. Monte Carlo study of fluid-plastic coexistence in hard dumbbells. *Journal of Chemical Physics*, **93**(2), 1278–1286.

Speedy, R.J. 1997. Pressure of the metastable hard-sphere fluid. *Journal of Physics Condensed Matter*, **9**(41), 8591–8599.

van Megen, W., & Underwood, S.M. 1989. Tracer diffusion in concentrated colloidal dispersions. III. Mean square displacements and self-diffusion coefficients. *Journal of Chemical Physics*, **91**(1), 552–559.

Vega, C., Paras, E.P.A., & Monson, P. A. 1992a. On the stability of the plastic crystal phase of hard dumbbell solids. *Journal of Chemical Physics*, **97**(11), 8543–8548.

Vega, C., Paras, E.P.A., & Monson, P.A. 1992b. Solid-fluid equilibria for hard dumbbells via Monte Carlo simulation. *Journal of Chemical Physics*, **96**(12), 9060–9072.

Viera, M.N. 2002. *Large Scale Simulation of Brownian Suspensions*. Ph.D. thesis, University of Illinois at Urbana-Champaign.

Weinbaum, S., & Ganatos, P. 1990. Numerical multipole and boundary integral equation techniques in Stokes flow. *Annual Review of Fluid Mechanics*, **22**, 275–316.

Woodcock, L.V. 1981. Glass Transition in the Hard-Sphere Model and Kauzmann's paradox. *Annals of the New York Academy of Sciences*, **371**, 274–298.

Wu, W.Y. 1984. A new approach of treating the stokes flow of nonslender prolate arbitrary axisymmetrical body. *Scientia Sinica Series A*, **27**, 731–744.

Zhou, H., & Pozrikidis, C. 1995. Adaptive Singularity Method for Stokes Flow Past Particles. *Journal of Computational Physics*, **117**, 79–89.

Chapter 3

Microstructure, Orientation, and Rheology in Sheared Suspensions of Non-spherical Dicolloidal Particles by Stokesian Dynamics Simulations

Synopsis

The orientation, microstructure and rheology in non-Brownian shear flow was studied for suspensions of dicolloidal particles using a novel PME Stokesian Dynamics algorithm for anisotropic particles. Four different particle shapes were studied with dicolloids modeled as the union of two intersecting spheres. Dynamic simulations were conducted for periodic systems of 1000 particles for volume fractions $\phi = 0.05$ to 0.55. The suspension microstructure was disordered for all particle shapes at $0 \leq \phi \leq 0.50$, with some systems showing ordered microstructure at $\phi = 0.55$. The viscosity in the disordered state was similar for all particle shapes at equal volume fraction. Negative first and second normal stress differences were found for $\phi \leq 0.5$, but positive values were observed for certain ordered systems at $\phi = 0.55$. Complex orientation behavior was observed as a function of volume fraction and particle shape. All particles showed a orientation shift toward the vorticity axis for $\phi \geq 0.10$. Certain shapes showed a shift away from the vorticity axis for $\phi \leq 0.10$. The high ϕ orientation dynamics were consistent with predictions based on the mobility tensor $\mathbf{M}^{\omega S}$ relating the angular velocity to particle stresslet. The orientation dynamics were dominated by the second normal stress differences. The shift away from the vorticity axis for small ϕ was induced by migration away from orientations with large orientation fluctuations.

3.1 Introduction

Suspensions of spherical particles have seen extensive investigation over the last several decades, from which a detailed picture of the microstructure and bulk properties has emerged

(see Vermant & Solomon (2005) and Morris (2009) for recent reviews). Suspensions of high aspect ratio fibers have also seen significant research however the understanding of suspension dynamics has not reached the same level as spheres. By comparison, suspensions of non-spherical particles with modest anisotropy have received relatively little attention in the literature. Recently, new synthesis techniques in the materials science community have lead to a plethora of new particle shapes (van Blaaderen, 2006; Yang *et al.*, 2008) with precise non-spherical particle structure. An interesting class among these new particles are dicolloidal particles (Johnson *et al.*, 2005; Mock *et al.*, 2006; Kim *et al.*, 2006), whose geometry is closely approximated by the union of two intersecting spheres of varying radii and center to center separation (see Fig. 3.1). A significant feature of this class of particles is its low aspect ratio (AR) with an upper bound of 2.0. Owing to this low aspect ratio, mildly aspherical dicolloids often exhibit microstructural and rheological behavior similar to that in suspensions of spheres. However, in addition to the positional microstructure of spheres, suspensions of dicolloids possess distinct orientational microstructure. The orientation of the particles is of significant interest as it may affect optical, electrical and mechanical properties of the suspension. Changes in orientation may lead to phase changes and order-disorder transitions in the suspensions with significantly lower stimulus than for positional re-ordering. These characteristics and their exploitation for novel materials have provided significant impetus for the synthesis of novel particle geometries. In the present article, we seek to analyze the orientational behavior of dicolloids in sheared suspensions as a first step in developing an overall understanding of the dynamics of these novel particles in different processing flows. In the remainder of this section, we review previous studies on the orientational behavior in suspensions of non-spherical particles under shear.

In the absence of non-hydrodynamic effects (such as Brownian motion or electrical fields), Jeffery (1922) showed that a single spheroid (or more generally an ellipsoid) in a linear shear flow would rotate indefinitely in a single parameter family of closed orbits, commonly known as the Jeffery orbits. The parameter characterizing an orbit is called the orbit constant C (see Sec. 3.3.3) whose value varies from $C = 0$ for particle director aligned with the vorticity axis to $C = \infty$ for particle alignment in the velocity-gradient plane. Later, Bretherton (1962) showed that most axisymmetric bodies in a shear flow would rotate in Jeffery orbits with

period equivalent to that of an effective spheroid. In a suspension of particles, hydrodynamic interactions between particles provide a mechanism for the particles to change their orbits. At steady state, the orientation distribution may be expected to be independent of its initial distribution.

The majority of prior work in this area has focused on large aspect ratio particles typically having an effective aspect ratio greater than ten. Early work of Anczurowski & Mason (1967) noted that the orbits of fibers (aspect ratio 18.4) at the lowest concentration in the dilute regime showed a shift towards lower orbit constants compared to the orbit distribution that would be expected from an isotropic initial distribution. At higher concentrations, still in the dilute regime, a shift towards higher orbit constants was observed by the above authors. Stover *et al.* (1992) reported orbit distributions in the semi-dilute regime and found very little variation with volume fraction. However, the orbit distribution was found to be shifted to higher orbit constants in comparison to the observations of Anczurowski & Mason (1967) in the dilute regime. Like Anczurowski & Mason (1967), Rahnama *et al.* (1995) measured orientation of fibers in the dilute regime and found that the shift to lower orbits in the dilute regime was not as dramatic as observed in the previous work. Summarizing these early observations, one may expect that: (i) in the dilute regime, a shift to lower orbit constants may be expected in a sheared system relative to an isotropic distribution, (ii) with increasing volume fractions a shift to higher orbit constant is expected. More recent experiments by Petrich *et al.* (2000) in semi-dilute to semi-concentrated suspensions of high aspect ratio fibers ($AR \geq 50$) suggest a different behavior. These authors found a shift towards lower orbit constants with increasing concentrations. Owing to this observation, it appears that some uncertainty remains concerning the variation of orientation behavior with concentration in suspensions of high aspect ratio fibers. In very recent studies, Egres *et al.* (2006) measured flow alignment in suspensions of ellipsoids of comparatively lower aspect ratios (between 2 and 7). This study showed that the flow alignment (parallel to velocity axis, with high orbit constant) was preferred at all shear rates with the maximum in flow alignment coinciding with the onset of shear thickening. At higher shear rates, a decrease in flow alignment was observed. Their studies also indicated an increased flow alignment with higher particle loadings and higher aspect ratios. No information about the distribution into

Jeffery's orbits was reported. In general, no conclusion about orbital drift can be inferred from their study as increased flow alignment can be caused by a decrease in the rate of particle flipping without any orbital drift. In other words, for particles with fixed orbit constant, increased flow alignment will result due to particles spending greater time aligned with the flow relative to Jeffery 's solution.

There have been a number of theoretical and numerical studies on the orientation behavior in suspensions of fibers and other non-spherical particles under shear. Rahnama *et al.* (1995) developed a theory to predict the orbital drift of large aspect ratio fibers in sheared suspensions. To leading order, the disturbance velocity due to uncorrelated motion of a collection of particles leads to a change in the average rate of rotation of a particle but no change in its orbital constant. In order to obtain an orbital drift, it was necessary to consider correlated motion of particles, restricted to a pairwise interactions in their work. The authors showed that the net effect could be represented as the action of a hydrodynamically induced rotary diffusivity. The rotary diffusivity tensor was shown to be anisotropic and dependent on the orientation of the particle relative to the flow. The theory predicts a shift to higher orbit constants with increasing concentration consistent with some observations reported above, though the experiments lack a consensus. The analysis was restricted to high aspect ratio fibers, and no equivalent theory exists for particles with small degree of anisotropy. Sundararajakumar & Koch (1997) performed simulations on fibers interacting only via a non-hydrodynamic contact force. A shift to higher orbit constants with increasing concentrations was observed in these simulations. Fan *et al.* (1998) performed simulations with full hydrodynamic interactions and reported a similar trend of increasing orbit constants with increasing concentration. Particles with small aspect ratio have been studied by Pozrikidis (2005) who analyzed the orientation distribution in two dimensional suspensions of ellipsoids with aspect ratios between 2 & 4. Full hydrodynamic interactions were included via boundary element computations. An increased flow alignment was observed with increasing aspect ratio and increasing volume fraction, however these 2D simulations provide no information concerning orientation statistics relative to the vorticity direction. Meng & Higdon (2008) studied concentrated suspensions of plate-like particles (AR between 3 and 7) with hydrodynamic interactions computed via an extension of the Stokesian Dy-

namics technique. They modeled the plate-like particles as an assemblage of spheres. Their studies showed a strong correlation between the orientation of different particles (a measure of nematic character), which was found to increase with increasing aspect ratio and volume fractions. The increased orientation correlation was found to be accompanied by the formation of distinct local ordering consisting of sliding layers of particles in the velocity-vorticity plane or particle stacks translating and rotating as a rigid body.

While the studies above have considered suspensions of particles in a Newtonian fluid, there has also been significant interest in particle orientation in shear flows of non-Newtonian fluids. For dilute suspensions in a viscoelastic fluid, Leal (1975) presented a theory for large aspect ratio fibers in a second order non-Newtonian fluid. His analysis showed that an isolated fiber in a second order fluid would drift towards vorticity alignment in a shear flow. A negative second normal stress difference (more precisely, normal stress difference coefficient of the suspending fluid) was shown to be necessary to observe such a behavior. Experiments (see e.g. Gunes *et al.* (2008)) on non-spherical particles of varying aspect ratio have qualitatively reproduced the predictions of Leal's theory. Brunn (1979) investigated the orientation behavior of slightly deformed spheres in a second order fluid. The linear perturbation for the particle geometry is a reasonable first approximation for dicolloids studied in this work. Brunn showed that an orbital drift is expected for perturbed spheres with first and second normal stress differences as well as particle shape parameters affecting the orbital drift. Depending on the normal stresses and geometrical parameters, orbital drift in either direction (higher or lower orbit constants) may be experienced.

In the present effort, we will conduct numerical simulations for the dynamics of sheared suspensions of dicolloids with accurate hydrodynamic interactions. We employ a novel approach with a recently developed PME (Particle Mesh Ewald) Stokesian Dynamics algorithm extended to compute hydrodynamic interactions in suspensions of dicolloidal particles (Kumar & Higdon, 2009). The PME simulation technique is employed to study sheared suspensions over a wide range of volume fractions ($0 \leq \phi \leq 0.55$) for three different dicolloidal particle shapes (Fig.3.1, 3.2). The particles are called homonuclear, small-bump, and fused-dumbbell particles as illustrated in Fig.3.2. Results for spheres are included for comparison purposes. The main goal of this work is to investigate the orientational dynamics

of dicolloidal particles in sheared suspensions over a range of volume fractions. We seek to characterize the variation in behavior among particles of different shape and to determine the underlying mechanisms responsible for the observed behavior. The organization of this article is as follows. In Sec. (3.2) we present the governing equations and briefly discuss the Stokesian Dynamics technique for the computation of the hydrodynamic interactions. Next, in Sec. (3.3.1), we present results for the microstructure in sheared suspensions for each particle shape as a function of volume fraction, followed by the characterization of the rheological properties in Sec. (3.3.2). The orientation behavior is presented in Sec. (3.3.3). This is followed by a detailed analysis of the orientational micromechanics in Sec. (3.4) where a micromechanical model is developed to determine the mechanisms responsible for the observed orientation statistics. Concluding remarks are presented in Sec. (3.5).

3.2 Formulation

The motion of small non-Brownian particles in a viscous fluid can be described by Newton's second law written as

$$\mathbf{m} \cdot \frac{d\mathbf{U}}{dt} = \mathbf{F}^H + \mathbf{F}^P, \tag{3.1}$$

where $\mathbf{m}$ is the mass/moment of inertia tensor of the particles, $\mathbf{U}$ is the generalized velocity/angular velocity vector, while $\mathbf{F}^H$ and $\mathbf{F}^P$ are the generalized force/torque vectors arising from the hydrodynamic stress in the fluid and from the interparticle interactions respectively. Here the vectors $\mathbf{U}$, $\mathbf{F}^H$ and $\mathbf{F}^P$ are $6N$ vectors where N is the number of particles in the system; and the mass/moment of inertia $\mathbf{m}$ is a $6N$ square block diagonal matrix where each 6×6 block consists of the mass and moment of inertia tensor of each individual particle. We assume that the particle size is small, and the inertial effects are negligible on the time scales of interest to us. With this assumption, the left hand side of (3.1) is zero, and the sum of the forces and torques on each individual particle must be zero at every instant of time. Fluid motion around the particles is governed by the continuity equation and the steady Stokes equations. In these low Reynolds number flows, the hydrodynamic force on each particle is a linear function of the fluid velocity and may be determined from the solution of the

governing equations for a specified set of particle configurations, particle velocities and of a prescribed undisturbed flow field. The linear relationship may be expressed in terms of a configuration dependent N body resistance tensor $\mathbf{R}$ as follows

$$\begin{pmatrix} \mathbf{F}^H \\ \mathbf{S}^H \end{pmatrix} = \mathbf{R} \cdot \begin{pmatrix} \mathbf{U}^\infty - \mathbf{u} \\ \mathbf{E}^\infty \end{pmatrix} \tag{3.2}$$

In this equation, a homogeneous undisturbed linear flow is assumed which determines the generalized velocity/angular velocity $\mathbf{U}^\infty$ evaluated at the center of each particle and the uniform rate of strain tensor denoted by $\mathbf{E}^\infty$. $\mathbf{F}^H$ is the usual force/torque $6N$ vector and $\mathbf{S}^H$ denotes the stresslets on the particle, the symmetric part of the first moment of the force on each particle, and can be expressed by a $5N$ vector.

For specified external and interparticle forces and specified linear flow $\mathbf{U}^\infty$, the velocity and angular velocity may be calculated as the solution of a linear system from Eq. (3.2). The particle positions and orientations may then be integrated over time to trace the dynamics of the particle suspension. The primary computational challenge is to compute the configurational dependent N body resistance tensor at each time step. Alternatively, iterative solutions techniques may be employed which avoid the computation of the full resistance matrix at each step. In our simulations, the hydrodynamic interactions are calculated using a novel method similar to the Stokesian Dynamics algorithm for spheres, appropriately modified for non-spherical dicolloidal particles. In Stokesian Dynamics, the total resistance tensor $\mathbf{R}$ in Eq. (3.2) is expressed by the following approximation

$$\mathbf{R} \approx \mathbf{R}^{MB} + \mathbf{R}^{LB} \tag{3.3}$$

where $\mathbf{R}^{MB}$ is a many-body resistance tensor accurate for widely separated particles. When particles come near contact however, the small particle gaps lead to strong interactions with $\mathbf{R}$ diverging at contact. The many body resistance tensor cannot capture this singular behavior due to the truncated multipole expansion employed in its calculation, hence, a correction term is added to account for the missing terms. This correction tensor denoted by $\mathbf{R}^{LB}$ is based on asymptotic lubrication theory for nearly touching particles. Unlike $\mathbf{R}^{MB}$,

$\mathbf{R}^{LB}$ is a sparse matrix as the lubrication interactions affect only near neighbors, and most importantly, the asymptotic lubrication contributions are pairwise additive as the interaction is highly localized around the point of contact.

We recently extended the Stokesian Dynamics technique (Bossis & Brady, 1984), to model hydrodynamic interactions in suspensions of dicolloidal particles (Kumar & Higdon, 2009). Briefly, the calculation of the many body contribution to the resistance tensor requires the solution for a single particle in a general linear flow which gives the single particle resistance tensor plus the disturbance velocity induced by the particle. This solution combined with the appropriate generalization of Faxen's law for that particle shape provides all the information required to compute the many body interactions. These quantities are know in exact form for spheres, but must be computed in a suitable approximate analytical form for other particle shapes to allow efficient Stokesian Dynamics simulations. In Kumar & Higdon (2009), we showed that the one-body solutions for dicolloids in linear flows could be accurately approximated by placing Stokes-singularities at two optimized positions along the symmetry axis of the particle. With this choice, it was sufficient to employ a collection of singularities including the Stokeslet, Stokes-doublet, Potential dipole, and Potential quadrupole - the same as required for the exact solution for a sphere. The strengths and locations of the singularities were optimized by minimizing the norm of the no-slip boundary condition for all independent linear flows. For a particle of general shape, there are eleven independent flows, (three uniform flows, three rotational flows, and five straining flows), however for a axisymmetric body this reduces to 7 independent flows. (Kumar & Higdon, 2009). For a periodic suspension with N particles, the many body interactions can then be computed in $O(N \log N)$ operations by employing the particle-mesh-Ewald method for Stokesian Dynamics. (Guckel, 1999; Sierou & Brady, 2001; Viera, 2002; Meng & Higdon, 2008). The one body solutions for dicolloids are computed only once for a given particle shape to determine the singularity strengths for the independent flow fields. There is no need for recomputation, and thus the total computational effort for the many body interactions of dicolloidal particles requires merely twice that of the effort for spheres. The lubrication interaction between a pair of dicolloidal particles was found by summing pairwise the lubrication interactions between all spherical node pairs formed between the two particles. For

each of the spherical node pairs, we used the asymptotic solutions for spheres with a correction to account for the truncated spherical geometry inherent for dicolloidal particles. The combined far-field and near field terms were found to give accurate solutions for a pair of dicolloids at all separations and orientations; the error was usually less than 10% as validated by the spectral boundary element method of Muldowney & Higdon (1995) (see Kumar & Higdon (2009) for details of the comparison).

The interparticle force $\mathbf{F}^P$ employed in this work is a short range repulsive force which can be summed pairwise (Meng & Higdon, 2008)

$$\frac{\mathbf{F}^P}{8\pi\mu a^2\dot{\gamma}} = \begin{cases} C^P\left(\frac{\delta_{min}}{\delta}\right)\left(\eta - \frac{1}{2}\eta^2\right)^3 \mathbf{d} & \text{if} \quad \delta < \delta_{min} \\ \mathbf{0} & \text{if} \quad \delta \geq \delta_{min} \end{cases} \tag{3.4}$$

where δ is the gap between two spheres, $\eta = 1 - \delta/\delta_{min}$, $\mathbf{d}$ is the unit vector along the line of centers of the spheres and $C^P = 10$ is a constant. In this work, the value of δ_{min} was fixed at 10^{-3} of a sphere radius. For gaps smaller than a specified numerical tolerance δ_{num}, both the hydrodynamic force and interparticle force are capped by evaluating at δ_{num}. The tolerance for all simulations presented here was set at $\delta_{num} = 10^{-5}$ of a sphere radius. The interparticle force between a pair of dicolloids was computed as the sum of pairwise forces between the spherical nodes comprising the particles.The above form of the repulsive force gives a near hard sphere behavior with non-zero repulsive interaction only when the gap between a pair of particles becomes less than 10^{-3} of a sphere radius.

At each time step, the unknown particle velocities are found from a linear system based on Eq. (3.2). Efficient iterative solutions are obtained using the modified system presented in the pseudo resistance method as described in Meng & Higdon (2008); Kumar & Higdon (2009). The system of equations are solved using the GMRES algorithm with a physics based preconditioner to accelerate the convergence (Kumar & Higdon, 2009). With a particle's velocity and angular velocity known, its position and orientation is evolved in time using a third order explicit Runge-Kutta method. The time-step Δt employed in this study typically varied between $\dot{\gamma}\Delta t = 10^{-2} - 10^{-3}$ depending on the volume fraction where $\dot{\gamma}$ is the shear rate of the imposed flow field.

For each time-step, the bulk stress tensor $\mathbf{\Sigma}$ (ignoring isotropic pressure) is computed as

$$\mathbf{\Sigma} = 2\mu_f \mathbf{E}^\infty + \mathbf{\Sigma}_p \tag{3.5}$$

where μ_f is viscosity of the fluid, $\mathbf{E}^\infty$ is the bulk rate of strain tensor, and $\mathbf{\Sigma}_p$ is the extra contribution due to the presence of particles written as

$$\mathbf{\Sigma}_p = \frac{1}{V}\left(\sum_i^N \mathbf{S}_i + \frac{1}{2}\sum_i^N \sum_{j,\, j\neq i}^N (\mathbf{x}_j - \mathbf{x}_i)\mathbf{F}_{ij}^R\right) \tag{3.6}$$

Here $\mathbf{S}$ is the stresslet of the particle given by

$$\mathbf{S} = \mathbf{R}_{SU} \cdot (\mathbf{U}^\infty - \mathbf{u}) + \mathbf{R}_{SE} : \mathbf{E}^\infty \tag{3.7}$$

where V is the volume of the periodic unit cell.

Note that the stresslet $\mathbf{S}$ in Eq. 3.6 is the total stresslet defined as the symmetric part of the first moment of the stress distribution integrated over the surface of the particle. Returning to Eq. (3.6), the second term on the right is the direct contribution of the repulsive force to the stress tensor which is summed pairwise; $\mathbf{F}_{ij}^R$ is simply the repulsive force on particle i due to the pairwise repulsive interaction between particles i and j. For later use, we also define a single particle's contribution (say particle i) to the overall stress tensor as

$$\mathbf{\Sigma}_{p,i} = \frac{1}{V}\left(\mathbf{S}_i + \frac{1}{2}\sum_{j,\, j\neq i} (\mathbf{x}_j - \mathbf{x}_i)\mathbf{F}_{ij}^R\right) \tag{3.8}$$

We define the relative viscosity of the suspension, which is computed from the overall stress tensor $\mathbf{\Sigma}$ defined above as

$$\mu = 1 + \frac{\Sigma_{xy}}{\dot{\gamma}\mu_f} \tag{3.9}$$

The first and the second normal stress differences are obtained as

$$N_1 = \Sigma_{xx} - \Sigma_{yy} \tag{3.10a}$$

$$N_2 = \Sigma_{yy} - \Sigma_{zz} \tag{3.10b}$$

One can similarly define a single particle's contribution to the overall viscosity or either of the normal stress differences by replacing $\boldsymbol{\Sigma}$ by $\boldsymbol{\Sigma}_{p,i}$ in the above equations.

3.3 Results

3.3.1 Microstructure

We begin by reviewing the equilibrium microstructure for particle suspensions in quiescent conditions, which establishes a standard for comparison for the microstructure in sheared suspensions. Suspensions of spheres in a quiescent system at equilibrium exist in a fluid like state below $\phi = 0.494$ and in a face centered cubic (FCC) state above a volume fraction of $\phi = 0.545$. The volume fraction $\phi = 0.494$ is commonly known as the freezing point, while the volume fraction $\phi = 0.545$ is known as the melting point. Between these two volume fractions, coexisting fluid and FCC phases are found. The equilibrium microstructure for hard-dicolloids with fore-aft symmetry has been characterized via numerical simulations (Vega *et al.*, 1992). The freezing and melting transitions for dicolloids with $c/a = 0.2$ (homonuclear) were found to occur at approximately $\phi = 0.4945$ and $\phi = 0.543$ respectively, while for dicolloids with $c/a = 1.0$ (fused-dumbbell), the same two transitions were found to occur at approximately $\phi = 0.6013$ and $\phi = 0.6463$. Moreover, the ordered phase at the freezing transition is orientationally disordered (plastic crystal) in suspensions of dicolloids with $c/a = 0.2$, while it is orientationally ordered in suspensions of dicolloids with $c/a = 1.0$. In simulations, the ordered phase is typically observed at volume fractions above the melting transition (Speedy, 1997). The maximum volume fraction investigated in the present work is $\phi = 0.55$, hence the equilibrium microstructure is expected to be disordered in fused-dumbbell particle suspensions at all volume fractions studied here, while an ordered microstructure is expected in suspensions of spheres and homonuclear particles at $\phi = 0.55$.

When a suspension of spheres is sheared, its microstructure goes through a series of transitions as characterized by Chow & Zukoski (1995). At high shear rates where Brownian

effects are negligible, a disordered state is typically obtained in suspensions of spheres (Chow & Zukoski, 1995) comparable to the non-Brownian systems studied in this work. Very little is known about the microstructure of dicolloids under shear. Mock & Zukoski (2007) studied charge-stabilized dicolloids at low shear rates for volume fraction of $\phi = 0.42$, where all dicolloids had a small degree of anisotropy ($\leq$ homonuclear). They observed a series of microstructural transitions with increasing shear rate analogous to the results for suspensions of spheres with comparable electrostatic potential. These authors did not study the high shear limit, however a disordered state is expected comparable to the results for spheres.

We turn to the present results for the microstructure of suspensions for four different particle shapes - spheres, homonuclear, small-bump and fused-dumbbell dicolloids. To characterize the microstructure, we employ pair distribution functions (PDF) in the three planes of interest, designated as front view (flow-gradient plane $\equiv g(x, y)$), top view (flow-vorticity plane $\equiv g(x, z)$) and end view (vorticity-gradient plane $\equiv g(z, y)$) (See Fig. 3.3). As an example, the two dimensional function, $g(x, y)$ is obtained from the full three dimensional PDF $g(x, y, z)$ by integrating over a slice of one particle diameter along the z direction as

$$g(x, y) = \int_{-a}^{+a} g(x, y, z)dz \tag{3.11}$$

For all volume fractions below $\phi \leq 0.5$ studied in this work, a disordered state was obtained for all particle shapes. This is similar to the behavior at equilibrium, though the detailed characteristics of the microstructure are quite different. The PDF's for the front view for all four particle shapes are shown in Fig.3.4 for two representative volume fractions: $\phi = 0.1$ and $\phi = 0.5$. For dicolloidal particles, the PDF is computed from the correlations between the center-of-mass of the particles. At low volume fractions (e.g. $\phi = 0.1$), a disordered state is obvious from the PDFs. As the volume fraction is increased, features of weak string like ordering begin to emerge in suspensions of spheres and dicolloids with small degree of anisotropy (small-bump and homonuclear) for $\phi > 0.4$. The presence of weak string like characteristic in the microstructure is clearly seen in the PDFs (Fig.3.4) at $\phi = 0.5$, though no long range order is present at that volume fraction. For fused-dumbbells, no significant sign of string like ordering is observed. An interesting feature

of the PDF is the lack of fore-aft symmetry, which can be attributed to the presence of non-hydrodynamic interactions - short range repulsive forces in this study (Brady & Morris, 1997). In a suspension with purely hydrodynamic interactions, the reversibility of Stokes flow combined with the fore-aft symmetry of the geometry and imposed flow field leads to fore-aft symmetric pair distribution function (Sundararajakumar & Koch, 1997). The presence of non-hydrodynamic interactions break the reversibility and consequently may lead to fore-aft asymmetric PDF with rheological consequences, i.e. non-Newtonian effects (Brady & Morris, 1997).

Moving to higher volume fraction, we present the microstructure for $\phi = 0.55$. At this volume fraction, a one-dimensional long range string like ordering was observed for spherical, homonuclear, and small-bump particle suspensions. Marginal hints of layering are observed for fused-dumbbells, however the suspensions are primarily disordered. The string like nature for the ordered systems is shown in the PDF's shown in Fig.3.5. In the front and top views, horizontal bands can be seen, where the central band corresponds to the home string of the reference particle. The two PDF's show no correlation between particle positions in different bands, which is characteristic of strings and rules against the presence of ordered layers. In the end view, hexagonal packing of the strings can be seen. Sierou & Brady (2002) observed similar string like ordering in their Stokesian Dynamics simulations of non-Brownian spheres at $\phi = 0.55$. As noted earlier, in experiments at high shear rates where the effect of Brownian or interparticle interactions are negligible (except in a thin boundary layer (Brady & Morris, 1997)), a disordered state is usually obtained. In some experiments, the microstructure at high volume fractions and at high shear rates has been shown to fluctuate with time with the appearance and disappearance of well defined maxima in scattering patterns (Chen *et al.*, 1994). Similarly, (Butera *et al.*, 1996), a metastable crystalline state has been observed after the cessation of shear from a shear thickened disordered state ($\phi = 0.48$). This led to the suggestion of latent order in the shear thickened state which is not readily apparent in scattering measurements. Both these experimental observations are consistent with the observation of order in the present numerical simulations. Finally, the disordered microstructure in the fused-dumbbell suspensions at $\phi = 0.55$ is consistent with equilibrium results which require much higher volume fractions ($\phi > 0.6$) for freezing or

melting transitions.

3.3.2 Rheology

3.3.2.1 Viscosity

The viscosity for all particle shapes as a function of volume fraction is plotted in Fig.3.6 and tabulated in Tables 3.3 and 3.4. The figure also shows the viscosity for suspensions of spheres reported for Stokesian Dynamics simulations by Sierou & Brady (2002). Our results are in excellent agreement with the earlier study though a different algebraic form of interparticle force is used the two studies. The range of the interparticle force is approximately equal ($10^{-3}\times$radius). In comparison to experimental values, omitted here for clarity, the simulated values are smaller at high volume fractions (Sierou & Brady, 2002). However, as noted in the earlier study, this discrepancy can be attributed to the range and strength of the interparticle force employed in the simulation. The contribution to viscosity from interparticle forces for suspensions of spheres is tabulated in Table 3.3(b). As can be seen, this contribution is negligible in comparison to the overall viscosity. Nonetheless, the distribution of smallest gaps in the system is strongly affected by the interparticle force, which in turn affects the hydrodynamic contribution to viscosity. In general, a greater hydrodynamic viscosity is expected when the range of interparticle interaction is reduced, as that leads to smaller gaps and larger lubrication forces (Viera, 2002).

Fig.3.6 provides an interesting comparison of viscosity for different particle shapes. At the lowest volume fractions, the fused-dumbbells have the highest viscosity, which can be attributed to higher intrinsic viscosity (Table 2, Kumar & Higdon (2009)). In non-dilute suspensions ($0.2 \leq \phi \leq 0.5$) however, the fused-dumbbells show the smallest viscosity (see Tables 3.3 & 3.4). A similar trend was observed in the infinite frequency viscosity for these particles (Kumar & Higdon, 2009). The slower divergence in viscosity with volume fraction can be attributed to a higher value for random close-packed volume fraction (RCP). To first approximation, RCP for dicolloids may be estimated by considering values for spheroids with the same aspect ratio. Donev *et al.* (2004) showed that a prolate spheroid with an

aspect ratio of approximately 1.5 has the largest RCP with this maxima being $\phi_{RCP} \approx 0.71$ (compared to $\phi_{RCP} \approx 0.64$ in suspensions of spheres). The fused-dumbbell particle with an approximate aspect ratio of 1.5 may be expected to have the highest RCP among dicolloids studied here. A larger RCP implies a slower divergence of viscosity with more free volume at a given volume fraction. Note that the divergence of the infinite shear viscosity does not necessarily occur at ϕ_{RCP}. Flow induced microstructural distortions may lead to divergence at higher volume fractions as in the results of van Der Werff & Kruif (1989) for spheres. While a strict correspondence may not always be inferred, a general trend is observed with higher volume fraction for viscosity divergence associated with increasing ϕ_{RCP}. As a final point of interest in Fig.3.6, at $\phi = 0.55$, all particles except fused-dumbbells exhibit a slight decrease in viscosity with increasing ϕ. This is associated with the string-like ordered microstructure.

3.3.2.2 Normal Stress Differences

In suspensions with statistically symmetric microstructure and purely hydrodynamic interactions, normal-stress differences are expected to be zero. This follows from the symmetry of the imposed flow, the particle distribution function, and the reversibility of Stokes flow (Sundararajakumar & Koch, 1997). The presence of the repulsive force breaks the reversibility condition and leads to a microstructure lacking fore-aft symmetry as was shown in section (3.3.1). In addition to the positional asymmetry, an asymmetry in the orientational distribution function is also expected (Sundararajakumar & Koch, 1997). Asymmetry in the orientational distribution function of non-spherical particles may lead to non-zero mean normal stress differences at the single particle level, however these may be insignificant for particles with small degree of anisotropy.

We begin by presenting normal stress data for our numerical simulations for suspensions of spheres in Table 3.3. At $\phi \leq 0.5$ where the microstructure is disordered, both the first and the second normal stress differences are negative. We have compared the normal-stress differences in this study with other numerical and experimental works in Fig. 3.7 and Fig. 3.8 for the first and second normal stress differences respectively. Each figure includes normal stress data plotted on both linear and logarithmic axes. Results for dicolloid particles are

also included in these figures. Normal stress differences in this work agree well with the numerical results of Sierou & Brady (2002). Good agreement for the first normal-stress difference is obtained with the experimental work of Singh & Nott (2003), but the numerical simulations give second normal stress differences a factor of two smaller than experiments. Sierou & Brady (2002) attributed this difference to the presence of friction, while Singh & Nott (2003) attributed this to the effect of the interparticle force used in simulations. The definitive explanation for this consistent discrepancy between simulations and experiments remains elusive. In the normal stress Table 3.3, we include the specific contributions due to interparticle forces in suspensions of spheres. These show that the direct contribution is negligible for volume fractions up to $\phi = 0.5$ where the microstructure is disordered. However, the interparticle forces have an indirect effect by breaking the reversibility of Stokes flow and by controlling the distribution of small interparticle gaps where large hydrodynamic lubrication forces play a major role. At $\phi = 0.55$, an ordered microstructure arises and both the normal stress differences become positive. A change to positive first normal stress difference is typically observed in experiments at high volume fractions and high shear rates in conjunction with a rapid increase in viscosity indicating an approach to jamming (Lootens *et al.*, 2005). While no jamming is observed here, the ordered microstructure is highly anisotropic leading to the change of sign in the normal stress differences. It is interesting to note that the interparticle force contribution to normal stress differences can be significant in the ordered states at $\phi = 0.55$ (Table 3.3).

Results for normal stress differences in suspensions of dicolloidal particles are presented in Table 4 and plotted in Figures 3.7 and 3.8 discussed above. Similar to the results for spheres, both the first and second normal stress differences were negative for $\phi \leq 0.5$. The magnitudes of the normal stress differences were typically close to those of spheres. In terms of absolute value, the first normal stress difference was typically higher in homonuclear particle suspensions, while the second normal stress difference was typically higher in fused-dumbbell particle suspensions. For fused-dumbbells, note that the second normal stress difference can be several times higher than the first normal stress difference at high volume fractions (e.g. $\phi = 0.5$). This is in contrast to the behavior observed in suspensions of spheres and other dicolloids where the two are of comparable magnitude. At the highest

volume fraction ($\phi = 0.55$), the first normal stress difference changes sign and becomes positive for homonuclear and small-bump particles similar to the result for spheres. This is likely due to the ordering transition in these suspensions. For fused-dumbbells, the first normal stress difference remains negative at $\phi = 0.55$; it decreases in magnitude over the corresponding value at $\phi = 0.5$. This shows a shift towards positive values which is similar to that for other particle shapes in this work and for experimental results at high volume fractions and high shear rates noted above (Lootens *et al.*, 2005).

3.3.3 Orientation

In this section, we begin with a discussion of orientation distributions in suspensions of anisotropic particles at infinite dilution; then follow with discussion of the effects of particle interactions in suspensions at finite volume fractions.

3.3.3.1 Orientation at infinite dilution

Jeffery (1922) showed that a spheroid in a shear flow at low Reynolds number would rotate in a periodic orbit whose period and geometry depends on its initial orientation. The Jeffery orbits comprise an infinite family of orbits characterized by a single parameter "C" (see Eq. 3.12b below). In an extension of Jeffery's result, Bretherton (1962) showed that axisymmetric bodies of more general shape execute Jeffery orbits similar to spheroids with an effective aspect ratio r_e replacing the aspect ratio r_p of the spheroid. For high aspect ratio cylindrical fibers, the ratio r_e/r_p decreases with increasing particle aspect ratio r_p. Typical values of r_e/r_p lie between $0.6 - 0.7$ for $r_p < 100$ (Petrich *et al.*, 2000). Effective aspect ratios for dicolloidal particles are presented below.

For an arbitrary axisymmetric body, its orientation may be specified by spherical coordinates (φ, θ) where θ measures the angle between the particle axis and z axis and φ is angle measured from the x axis in the xy plane. The evolution of the orientational angles (φ, θ)

in shear flow with time t is given by (see Fig. 3.9)

$$\tan\varphi = r_e \tan\left(\frac{\dot{\gamma}t}{r_e + 1/r_e} + \kappa\right) \tag{3.12a}$$

$$\tan\theta = \frac{Cr_e}{\sqrt{r_e^2\cos^2\varphi + \sin^2\varphi}} \tag{3.12b}$$

Here κ denotes the initial phase and C is the orbit constant. Two limiting values are $C = 0$ for particles aligned with the vorticity axis of the flow (z) and $C = \infty$ for particles aligned in the velocity-gradient plane ($x - y$). Both C and κ are completely determined by the initial orientation. The period of rotation T in the Jeffery's orbit follows from Eq. (3.12a) and is given by

$$T = \frac{2\pi}{\dot{\gamma}}\left(r_e + \frac{1}{r_e}\right) \tag{3.13}$$

Note that the orbit period depends solely on particle geometry and is independent of the orbit constant. For dicolloidal particles, numerical simulations were conducted to determine the orbit periods and hence to find the effective aspect ratio r_e using Eq. (3.13). These computations yield an effective aspect ratio of 1.0868, 1.0967, and 1.5075 for the homonuclear, small-bump, and fused-dumbbell particles respectively (Table 3.2). By comparison, the aspect ratios based purely on geometry give 1.1, 1.1 and 1.5 respectively, quite close to the values obtained from the Jeffery's orbit calculation.

To characterize the statistical distribution of particle orientations in a suspension, we define an orientational order parameter relative to each coordinate axis i as the average over all particles of

$$S_{ii} = \frac{3}{2}n_i n_i - \frac{1}{2} \tag{3.14}$$

Here n_i designates the component of the unit vector along the particle symmetry axis (the director $\mathbf{n}$) with i taking values x, y, z. For a random dispersion $S_{ii} = 0$; for perfect alignment of particles with axis i, $S_{ii} = 1.0$; and for particles aligned in the plane perpendicular to i, $S_{ii} = -0.5$. Even in the absence of particle interactions, a particle immersed in a shear flow exhibits preferred average orientation due to the non-uniform rate of rotation in the orbits. In particular, particles spend a greater portion of the orbital period aligned near the

velocity-vorticity plane compared with the gradient-vorticity plane.

To compute the orientational order parameter for a suspension at infinite dilution, one must specify the initial distribution of particles into orbits as specified by C. There are two simple ways which can be used to compute this initial distribution. In the first scheme, one assumes that the director of the particle is initially uniformly distributed in the (φ, θ) space, which then dictates the statistical distribution of C as determined from Eq. (3.12b). Alternatively, in the presence of an asymptotically weak rotary diffusivity, an arbitrary initial distribution will evolve into a determinate distribution of orbit constants as given by Leal & Hinch (1971). For the modest particle aspect ratios investigated in this work, the two methods lead to nearly identical distributions; hence for simplicity, we assume an initially isotropic distribution. The time average distribution yields the probability distribution shown in Fig.3.10. For convenience, we define a normalized orbit constant C_b

$$C_b = \frac{C}{C+1} \tag{3.15}$$

where C_b varies between 0 and 1 as C varies from 0 to ∞. The value $C_b = 0$ corresponds to alignment with the vorticity axis, while $C_b = 1$ corresponds to alignment in the velocity-gradient plane. In Fig.3.10, $p(C_b)$ gives the probability of finding a particle with a given C_b with normalization:

$$\int_0^1 p(C_b) dC_b = 1 \tag{3.16}$$

For later use, we define the mean orbit constant C_b^m as follows

$$C_b^m = \int_0^1 p(C_b)\, C_b\, dC_b \tag{3.17}$$

which is the first moment of the probability distribution function $p(C_b)$. This parameter will prove most useful in characterizing the distribution of particle orientations.

For suspensions at infinite dilution, each particle executes a Jeffery orbit with specified orbit constant C_b. Once the distribution into orbits $p(C_b)$ is specified, the overall mean orientational order parameter (3.14) is easily obtained by time averaging over the period of the orbit for each C_b and averaging over the distribution of orbit constants. The mean

order parameters are tabulated in Table 3.2 for all particle shapes considered in this study. Dicolloids with small degree of anisotropy, i.e. homonuclear and small-bump particles, show a modest increase in the orientational order parameter in the flow direction S_{xx}, primarily at the expense of the orientational order parameter in the gradient direction S_{yy}. By comparison, fused-dumbbells show a significant increase in S_{xx} (alignment with velocity axis) which is expected due to its larger degree of anisotropy. We note that the orientational order parameter for the vorticity axis S_{zz} is negligibly affected by rotations in Jeffery's orbit for particles considered here.

3.3.3.2 Orientation distribution at finite concentration

In this section, we present the main computational results of this study for average orientation distributions in sheared suspensions of dicolloidal particles at finite concentrations. We focus on average distributions here and investigate dynamics and micromechanics in the next section 3.4. To characterize the statistical distribution of particle orientations in the suspensions, we choose two measures based on the definitions of the section 3.3.3.1 above. The first is the mean orientation order parameter S_{ii} which gives a direct measure of the degree of particle orientation relative to the velocity-gradient-vorticity axes. The second measure is based on the mean orbit constant C_b^m as a measure of the probability distribution function $p(C_b)$. At finite volume fraction, particles no longer execute perfect Jeffery's orbits owing to particle interactions. Nonetheless, we may use the orbit parameter C_b to characterize a particle's instantaneous orientation and compute the rate of change of orbit parameter to characterize the effect of particle interactions. Previously, we have computed the mean orbit constant C_b^m for infinite dilution, and we now define ΔC_b^m as the difference of mean orbit constant relative to infinite dilution. Positive values of ΔC_b^m indicate an increase in C_b^m and a net shift of orientation away from the vorticity axis and toward the velocity-gradient plane. Negative values of C_b^m indicate a shift in orientation toward the vorticity axis. As this quantity is defined relative to infinite dilution, it captures the net influence of particle interactions, in effect measuring the departure from the non-uniform probability distribution shown in Fig.3.10 associated with the single particle Jeffery orbit. Fig.3.11 shows ΔC_b^m as a

function of volume fraction for each of the three dicolloid particle shapes. Fig.(3.12) shows the corresponding orientation order parameters S_{xx}, S_{yy}, S_{zz} as a function of volume fraction for each of the three particle shapes.

We begin our discussion of these figures by considering the results for homonuclear particles. By definition, $\Delta C_b^m = 0$ at infinite dilution. At low volume fractions up to ($\phi = 0.05$), there is a clear increase in the mean orbit constant with positive ΔC_b^m. This reflects a net change in orientation moving away from the vorticity axis. This is accompanied by an increase in the orientational order parameter along the x and y axis with a corresponding decrease in orientational order along the z direction. With increasing volume fraction above $\phi = 0.05$, there is a monotonic decrease in ΔC_b^m with increasing ϕ representing a shift in orientation toward the vorticity axis. This is reflected in the monotonic increase in order parameter S along z axis. The overall behavior of homonuclear particles is intriguing as it shows that particle interactions initially favor movement away from the vorticity axis but shift at higher volume fraction and favor movement toward the vorticity axis.

Next, we turn our attention to small bump particles. In contrast to the homonuclear particles, there is negligible change in C_b^m up to $\phi = 0.10$. This is confirmed by the plots for the orientational order parameters. For higher volume fractions, the small bump particles exhibit orientation behavior similar to the homonuclear particles; that is they show a negative ΔC_b^m and a shift toward the vorticity axis. On the other hand, despite a shift toward the vorticity axis and increase in S_{zz} at higher volume fractions, the orientational order parameter S_{xx} shows little change with even a modest increase above $\phi = .30$. These increase alignments come at the expense of orientation along the gradient axis S_{yy} which implies that the particles aren't flipping as often as would be expected in Jeffery's orbits.

The behavior of fused-dumbbells is qualitatively similar to homonuclear particles in the low to moderate volume fraction region, but with significantly exaggerated effects. At $\phi = 0.05$, a dramatic shift towards higher orbit constants is seen with large positive ΔC_b^m. Upon further increase in volume fraction, a gradual shift towards the vorticity axis (negative ΔC_b^m) is observed. But, unlike the previous particle shapes, the shift toward the vorticity axis and lower orbit constants was found to essentially plateau for $0.2 \leq \phi \leq 0.4$. There is negligible variation in the orientational order parameter along any of the three axes, which is consistent

with the leveling out of ΔC_b^m. At $\phi \geq 0.5$, there is an increase in the orientational order along the x axis which comes at the expense of the orientational order along the y axis. As suggested above, this implies that the particles at high volume fractions aren't flipping as often as expected in Jeffery's orbits.

3.4 Micromechanics of particle orientation

In this section, we investigate the micromechanics which governs the orientation behavior of anisotropic particles in concentrated suspensions under shear. Our goal is to determine the specific mechanisms for the orientation distributions observed in the previous section. In particular, three important characteristics of orientation dynamics were observed: (i) at small finite volume fraction, homonuclear and fused-dumbbell particles with fore-aft symmetry showed a shift towards higher orbit constants with increased alignment toward the velocity-gradient plane; small bump particles lacking fore-aft symmetry exhibited negligible change in orientation relative to dilute systems; (ii) with increasing volume fraction $\phi > 0.1$, all particle shapes showed a shift towards lower orbit constants with increased alignment with the vorticity axis; and (iii) homonuclear and small bump particles with small anisotropy showed a monotonic increase in vorticity alignment with increasing volume fraction, while fused-dumbbells with high anisotropy showed a plateau in vorticity alignment at modest volume fraction ($\phi \sim 0.2$). Distinct mechanisms responsible for each of these phenomena will be presented in the discussion below.

For an arbitrary system of particles in low Reynolds flow, the linearity of the equations of motion guarantees that the force and force moments (torque, stresslet) on a particle may be related to the kinematics (particle velocities, angular velocities and undisturbed flow field) through a linear relationship embodied in the N body resistance tensor $\mathbf{R}$. Specifically, the force and force moments (torque, stresslet) on each particle may be written as

$$\begin{pmatrix} \mathbf{F} \\ \mathbf{T} \\ \mathbf{S} \end{pmatrix} = \mathbf{R} \cdot \begin{pmatrix} \mathbf{U}^\infty - \mathbf{u} \\ \boldsymbol{\Omega}^\infty - \boldsymbol{\omega} \\ \mathbf{E}^\infty \end{pmatrix} \tag{3.18}$$

where $\mathbf{F}$ and $\mathbf{T}$ are $3N_p$ force and torque vectors, $\mathbf{S}$ is the $5N_p$ stresslet written in vector form; $\mathbf{u}$ and $\mathbf{U}^\infty$ are $3N_p$ particle velocity and fluid velocity vectors, $\boldsymbol{\omega}$ and $\boldsymbol{\Omega}^\infty$ are $3N_p$ angular velocity vectors for the particle and for the undisturbed fluid velocity respectively, while $\mathbf{E}^\infty$ is a $5N_p$ rate of strain tensor for the fluid velocity field. Here the fluid velocities for each particle are those of the undisturbed velocity field evaluated at the particle center. In a simple shear flow, $\boldsymbol{\Omega}^\infty$ and $\mathbf{E}^\infty$ are spatially uniform and hence equal to a constant for all particle positions.

The N body resistance tensor may be inverted to obtain expressions for the particle velocity, angular velocity and local strain rate as

$$\begin{pmatrix} \mathbf{U}^\infty - \mathbf{u} \\ \boldsymbol{\Omega}^\infty - \boldsymbol{\omega} \\ \mathbf{E}^\infty \end{pmatrix} = \mathbf{M} \cdot \begin{pmatrix} \mathbf{F} \\ \mathbf{T} \\ \mathbf{S} \end{pmatrix} \tag{3.19}$$

where $\mathbf{M}$ is now the N body mobility matrix.

In principle, this equation shows that knowledge of the force and force moments on every particle is sufficient to completely determine the kinematics of particle motion. However, for most common experiments, we know the force and torque on every particle and the strain rate imposed by the undisturbed flow. The stresslet is not known *a priori* Thus, neither the resistance formulation (3.18) nor the mobility formulation (3.19) is used directly, but rather the equations are rearranged to form a linear system from which we solve for the unknown particle velocity, angular velocity and stresslet. This leads to the classic definition of a mobility matrix for a mixed problem (see section 5.3, Kim & Karrila (2005)) with

$$\begin{pmatrix} \mathbf{U}^\infty - \mathbf{u} \\ \boldsymbol{\Omega}^\infty - \boldsymbol{\omega} \\ \mathbf{S} \end{pmatrix} = \mathcal{W} \cdot \begin{pmatrix} \mathbf{F} \\ \mathbf{T} \\ \mathbf{E}^\infty \end{pmatrix} \tag{3.20}$$

where $\mathcal{W}$ is now the N body mobility matrix for the mixed problem.

Our purpose in the present section is to interpret the results of the detailed numerical simulations and thereby to identify the underlying physical mechanisms. In pursuit of this

goal, we shall focus on the mobility formulation (3.19). As our primary interest here is in the orientation of the particles, we take the angular velocity from (3.19) and rewrite in the compact form

$$\boldsymbol{\omega} = \boldsymbol{\Omega}^{\infty} - \mathbf{M}^{\omega F} \cdot \mathbf{F} - \mathbf{M}^{\omega T} \cdot \mathbf{T} - \mathbf{M}^{\omega S} \cdot \mathbf{S} \tag{3.21}$$

where the superscripts designate the appropriate couplings in the $\mathbf{M}$ submatrices taken from the full mobility matrix. The force and torque on all particles is given in the specification of experiments or simulations, and we have computed the individual stresslets on all particles in the simulations. Mean values for the stresslets may be inferred from the results in the previous section for the effective viscosity and normal stress differences. Given this information, we may employ (3.21) to determine the individual contributions to ω from the force, torque and individual stresslet components.

In systems for which the external force and torque are identically zero, Eq. 3.21 reduces to

$$\boldsymbol{\omega} = \boldsymbol{\Omega}^{\infty} - \mathbf{M}^{\omega S} \cdot \mathbf{S} \tag{3.22}$$

With this equation the mobility tensor $\boldsymbol{\omega}$ may be used to explore the effect of particle stresslets on the angular velocity and hence orientation dynamics of all particles in the suspension. Moreover in the absence of external forces and torques, the mean particle stresslet may immediately be inferred from the bulk stress in the suspension from Eq. (3.5).

In the present work, the force and torque on each particle is identically zero except for particles in near contact for which a short range repulsive force has been assumed to assist in preventing particle overlaps. With a simple modification, we find that the mobility tensor ω in Eq. (3.22) may also be used to interpret results in our simulations. Using the mobility tensor $\mathcal{M}$ from the mixed problem in Eq. (3.20), the total stresslet $\mathbf{S}$ on the particles may be written as s

$$\mathbf{S} = \mathbf{S}^{\mathbf{F}} + \mathbf{S}^{\mathbf{T}} + \mathbf{S}^{\dot{\gamma}} \tag{3.23}$$

representing the contributions to the stresslet arising from the force, torque and straining

field respectively. Substituting into Eq. (3.21) we have

$$\boldsymbol{\omega} = \boldsymbol{\Omega}^{\infty} - \mathbf{M}^{\omega F} \cdot \mathbf{F} - \mathbf{M}^{\omega T} \cdot \mathbf{T} - \mathbf{M}^{\omega S} \cdot (\mathbf{S}^{\mathbf{F}} + \mathbf{S}^{\mathbf{T}} + \mathbf{S}^{\dot{\gamma}}) \tag{3.24}$$

or regrouping

$$\boldsymbol{\omega} = \boldsymbol{\Omega}^{\infty} - \left[\ \mathbf{M}^{\omega F} \cdot \mathbf{F} - \mathbf{M}^{\omega T} \cdot \mathbf{T} - \mathbf{M}^{\omega S} \cdot (\mathbf{S}^{\mathbf{F}} + \mathbf{S}^{\mathbf{T}}) \ \right] \ - \ \mathbf{M}^{\omega S} \cdot S^{\dot{\gamma}} \tag{3.25}$$

Detailed simulation results show that the contributions in square brackets due to net forces and torques on the particles have negligible direct contributions to the angular velocity in (3.25), and we thus we arrive at the simple form

$$\boldsymbol{\omega}^{\dot{\gamma}} = \boldsymbol{\Omega}^{\infty} - \mathbf{M}^{\omega S} \cdot \mathbf{S}^{\dot{\gamma}} \tag{3.26}$$

where the superscript $\dot{\gamma}$ emphasizes that the origin of the stresslets and the resulting angular velocity is the imposed shear flow with shear rate $\dot{\gamma}$. Even in the presence of external forces and torques in our simulation, the mean particle stresslets $\mathbf{S}^{\dot{\gamma}}$ may be inferred directly from the bulk stress in the suspension using Eq. (3.6). For very small particle gaps where the short range repulsive forces are active, the direct particle stress in Eq. (3.6) cancels the associated stresslets $\mathbf{S}^{\mathbf{F}} + \mathbf{S}^{\mathbf{T}}$ nearly exactly, and the net contribution to the bulk stress is negligible. Thus the particle stresslets $\mathbf{S}^{\dot{\gamma}}$ represent the major contribution to the bulk stress, and their mean values may be obtained from the rheological results in Table 4 and in Figs. 3.6, 3.7 and 3.8.

A brief comment is in order. While the direct contribution of the short range repulsive forces to the bulk stress and orientation dynamics is negligible, these forces have a significant effect on the particle-particle gaps and the overall microstructure which in turn affect the stresslets. Thus there is a significant indirect effect whose influence is included through the effect on $\mathbf{S}^{\dot{\gamma}}$. In our focus on the effect of particle stresslets on the orientation dynamics, we do not delve into detailed analysis of the origin of particular stresslet components. Certainly the stresslets arise from particle interactions and are most strongly affected by hydrodynamic lubrication forces and short range repulsive forces. The stresslets are a function of the

full N body microstructure and are strongly affected by the orientation of the individual particle and its near neighbors. The stresslets exhibits large fluctuations about the mean among individual particles and as a function of time. A detailed analysis and predictive model for the individual stresslets at each instant of time is beyond the scope of the present study. Rather, we shall take the computational results for both mean and individual time dependent particle stresslets as given and focus on the mechanisms by which these imposed stresslets affect the orientation dynamics. By focusing on the impact of particle stresslets on the orientational dynamics, we are following an approach similar to that which has proved useful in the study of orientation of particles in viscoelastic fluids (Leal, 1975). In these fluids, the effect of the viscoelasticity is to perturb the particle's velocity from the corresponding Newtonian solution yielding a distinct equilibrium orientation distribution. The changes in orientation associated with viscoelastic effects are typically characterized in terms of the normal stress coefficients of the fluid. In a similar fashion, we shall examine the relationship between the angular velocity of the particles and the normal and shear stresses and show how changes in this relationship explain the differences in observed orientation behavior for different particle shapes and volume fractions.

In the sections below, we will explore the interaction between the particle stresslets and orientation dynamics through a sequence of models based on different physical mechanisms. First , we will examine the mobility of a single axisymmetric particle in an infinite Newtonian fluid and show how the mobility changes as a function of orientation of the particle relative to the imposed shear flow. Next we will examine diagonal blocks of the mean mobility tensor evaluated numerically from configurations generated by the dynamic simulations for suspensions at finite volume fraction. The diagonal blocks represent the angular velocity of an individual particle due to its own stresslet. We will determine the extent to which the orientation dependence of these self terms in the simulations is well modeled by the theoretical one body results. We then consider a simple model for pairwise interactions and examine how this model captures qualitatively the mean simulation results for particle interactions. In section 3.4.2, we will turn to direct measures of the correlation between a particle's orientation dynamics and its individual stresslet. If a particle's motion can be predicted solely by its own stresslet, there is a perfect correlation between its stresslet and its angular velocity.

This implies that (i) the mean effect of particle stresslets on neighboring particles cancel out on average or (ii) the particle stresslets on neighboring particles are themselves strongly correlated with the self stresslet, such that their collective action is well correlated with the self particle stresslet. For weaker overall correlations of single stresslet-angular velocity, additional stresslets must play a more important role in determining the angular velocity. These may be contributions from other stresslet components on the individual particle or contributions owing to variations in the stresslets on neighboring particles. We shall examine the quality of the one body correlations as a function of particle orientation and of volume fraction. The statistical analysis of these sections is based on a deterministic mechanism in which there is a direct linear relationship (mobility tensor) between the stresslets on a particle (or a collection of neighboring particles) and its angular velocity. These mechanisms are significant when there are strong normal stresses in the suspension at moderate to high volume fractions. In the final section 3.4.3 we shall examine how stresslet fluctuations lead to rotational hydrodynamic diffusion even in the absence of significant mean normal stresses. These diffusive fluctuations prove to be the dominant mechanism for suspensions at low volume fractions.

3.4.1 Mobility Matrix $\mathbf{M}^{\omega S}$

3.4.1.1 Single axisymmetric particle

Consider a single axisymmetric particle immersed in an infinite Newtonian fluid. For a single particle with zero force and zero torque, the N body mobility equation (3.26) reduces to the single body result

$$\omega_i = \Omega_i^{\infty} + M_{ijk}^{\omega S} \cdot S_{jk} \tag{3.27}$$

where the third rank tensor $M_{ijk}^{\omega S}$ is a function only of the particle shape and orientation. For axisymmetric bodies, the director $\mathbf{p}$ (unit vector along symmetry axis) provides the sole specification of orientation, and the general form for the third rank mobility tensor $M_{ijk}^{\omega S}$ is

$$M_{ijk}^{\omega S} = \mathcal{M}_0(\epsilon_{ijl}\, p_k p_l \; + \; \epsilon_{ikl}\, p_j p_l) \tag{3.28}$$

where $\mathcal{M}_0$ is a positive scalar mobility coefficient. An axisymmetric particle placed in a linear shear flow will experience instantaneous normal stress differences from the hydrodynamic stresses induced by the shear flow. These perturb its angular velocity relative to Ω^∞ as specified in (3.27) and will lead to exact agreement with the Jeffery orbit equations. The normal stress differences averaged over the period of the orbit are zero and there is no change in the orbit constant C_b.

Now for the present discussion, we are interested in the angular velocity which results from an arbitrarily prescribed stresslet for a particle with director $\mathbf{p}$, i.e if the stresslet experienced by the particle is *not* due solely to hydrodynamics of single particle motion in a simple shear flow. The exact origin of this arbitrary stresslet is not important for discussion here. In certain applications, it might arise from a distribution of charge over a particle, or as in the present study, a stresslet may arise owing to particle interactions. Independent of the origin of the stresslet, we are interested in the angular velocity which would result if the particle were immersed in an infinite Newtonian fluid with the mobility tensor given by (3.28). In effect, we seek to clarify the particle dynamics by analyzing the *response* of a particle to an imposed stresslet independent of the source the stresslet. In particular, we are interested in the effect of individual stresslet components on the direction of orbital drift of the particle, i.e. whether the stresslet pushes the particle axis toward the velocity-gradient plane ($\dot{C}_b > 0$) or toward the vorticity axis ($\dot{C}_b < 0$). In the following discussion, we focus solely on the contributions in (3.27) due to the stresslet. In the absence of external stresslets, the constant angular velocity Ω_i^∞ yields no net drift averaged over the period of rotation.

In evaluating the effect of different stresslet components, we wish to focus on three terms - the first and second normal stress differences $N_1 = S_{11} - S_{22}$, $N_2 = S_{22} - S_{33}$, and the shear stress $\tau_{12} = S_{12}$. For independent contributions to these three terms, we choose reference stresslet tensors:

$$\mathbf{S}^{N_1} = S_0 \begin{pmatrix} 2/3 & 0 & 0 \\ 0 & -1/3 & 0 \\ 0 & 0 & -1/3 \end{pmatrix} \quad \text{for } N_1 \tag{3.29a}$$

$$\mathbf{S}^{N_2} = S_0 \begin{pmatrix} 1/3 & 0 & 0 \\ 0 & 1/3 & 0 \\ 0 & 0 & -2/3 \end{pmatrix} \quad \text{for } N_2 \tag{3.29b}$$

$$\mathbf{S}^{\tau_{12}} = S_0 \begin{pmatrix} 0 & 1 & 0 \\ 1 & 0 & 0 \\ 0 & 0 & 0 \end{pmatrix} \quad \text{for } \tau_{12} \tag{3.29c}$$

where S_0 is arbitrary coefficient characterizing the strength of the stresslet. The angular velocity of the particle associated with a given reference is then written as

$$\omega_i = M^{\omega S}_{ijk} \cdot S_{jk} \tag{3.30}$$

With the angular velocity $\boldsymbol{\omega}$ specified by (3.30), we may compute the orbit drift rate $\dot{C}_b$, and we discuss details of that procedure below. Before presenting quantitative results for the mobility tensors for the three components N_1, N_2 and τ_{12}, it is useful to consider simple model flows which give a qualitative understanding of these mobilities. In the mobility formulation expressed by Eq. (3.30), it is important to note that the physical origin of the stresslet is not important, any system which leads to the specified $\mathbf{S}$ gives the correct contribution to $\boldsymbol{\omega}$ from the $\mathbf{M}^{\omega\mathbf{S}}$ coupling.

Perhaps the simplest examples which lead to the stresslets analogous to those in Eq. (3.29) are to consider uniform straining fields with constant strain rate tensors $\mathbf{E}$. We define a diagonal strain rate tensors $\mathbf{E_1}$ with diagonal elements $(2/3, -1/3, -1/3)\, e$, and $\mathbf{E_2}$ with diagonal elements $(1/3, 1/3, -2/3)\, e$. We define $\mathbf{E}_\tau$ analogous to $\mathbf{S}^{\tau_{12}}$ with the sole non-zero elements $e_{12} = e$, $e_{21} = e$. For spheres, the stresslets arising from these reference straining fields are exactly those specified in Eq. (3.29) for the respective fields $\mathbf{E_1}$, $\mathbf{E_2}$ and $\mathbf{E}_\tau$. For particles with modest anisotropy studied here, the anisotropic resistance tensor yields additional stresslet terms from each of these straining fields, however the dominant stresslet for each will be the associated $\mathbf{S}$ in Eq. (3.29. Hence, study of these straining fields provides an excellent qualitative interpretation for the effect of a stresslet S on orientational changes induced through the mobility tensor $\mathbf{M}^{\omega\mathbf{S}}$.

For $\mathbf{E_1}$, we have an axisymmetric uniaxial straining field drawing all particles toward the x axis. For a particle subject to the associated stresslet, it will experience angular velocity $\boldsymbol{\omega}$ exactly as if it were immersed in this straining field. A negative strain rate e and negative normal stress difference N_1 would thus push all particles away from the x axis. All particles in the xz plane will experience a net push toward the z axis, while all particle in the xy plane will experience a net push toward the y axis. Owing to the axisymmetry, all intermediate positions will experience a positive push toward the y and z axes. The respective components p_y and p_z of the particle director $\mathbf{p}$ will increase at a rate proportional to $sin\beta$ and $cos\beta$ respectively where β is the angle measured from z axis in the yz plane. Thus all particles experience a net change $\dot{p_y} \geq 0$ and $\dot{p_z} \geq 0$ independent of orientation.

For $\mathbf{E_2}$, we have an axisymmetric uniaxial straining field drawing all particles away from the z axis. A negative e and associated negative N_2 thus draws all particles toward the z axis with a rate $\dot{p_z}$ independent of φ . We should thus expect $\dot{C}_b < 0$ with nearly uniform strength independent of φ. For $\mathbf{E_{12}}$, we have a 2D straining field in the xy plane. Averaged over all angles φ this would yield zero average effect for $\dot{C}_b$. From consideration of these effective straining fields, we expect $-N_2$ to have a strong uniform effect on orbital drift rate, with $-N_1$ having a variable effect though always pushing toward the vorticity axis, and τ_{12} to have an oscillating effect with zero mean.

To obtain quantitative values for $\dot{C}_b$, we first compute $\dot{\mathbf{p}}$ from

$$\dot{\mathbf{p}} = \boldsymbol{\omega} \times \mathbf{p} \tag{3.31}$$

The time derivatives $\dot{\varphi}$ and $\dot{\theta}$ of the spherical coordinates (Fig. 3.9) are then

$$\dot{\varphi} = \dot{\mathbf{p}} \cdot \frac{\mathbf{e}_\varphi}{\sin\theta} \tag{3.32a}$$

$$\dot{\theta} = \dot{\mathbf{p}} \cdot \mathbf{e}_\theta \tag{3.32b}$$

where $\mathbf{e}_\varphi$ and $\mathbf{e}_\theta$ are the standard unit vectors along φ and θ directions respectively. One can then compute $\dot{C}_b$ as

$$\dot{C}_b = \frac{\partial C_b(\theta,\varphi)}{\partial\theta}\,\dot{\theta} + \frac{\partial C_b(\theta,\varphi)}{\partial\varphi}\,\dot{\varphi} \tag{3.33}$$

We denote the mobility coefficient relating $\dot{C}_b$ to each of the prescribed stresses as M_{N_1}, M_{N_2}, and $M_{\tau_{12}}$ respectively. For example, for an imposed normal stress difference N_2 given by (3.29b), we write

$$\dot{C}_b = M_{N_2} S_0 \tag{3.34}$$

As seen in Eq. (3.32) and (3.33) , $\dot{C}_b$ is a function of the particle's orientation, $\dot{C}_b = \dot{C}_b(\theta, \varphi)$, and consequently, M_{N_1}, M_{N_2}, and $M_{\tau_{12}}$ are also functions of θ and φ. It proves useful to focus on the variation of these mobility coefficients with respect to a single variable θ or φ, which we achieve defining an average over the other variable. For example, $M_{N_2}(\varphi)$ and $M_{N_2}(\theta)$ are defined from $M_{N_2}(\theta, \varphi)$ as follows

$$M_{N_2}(\varphi) = \frac{1}{2} \int_0^{\pi} M_{N_2}(\theta, \varphi) \, \sin\theta \, d\theta \tag{3.35a}$$

$$M_{N_2}(\theta) = \frac{1}{2\pi} \int_0^{2\pi} M_{N_2}(\theta, \varphi) \, d\varphi \tag{3.35b}$$

Here the averaged quantities are identified by the single argument, and we choose not to further complicate the notation by introducing a new symbol for the average.

We define the norm for these mobility coefficients based on the average over all orientations, e.g.:

$$\|M_{N_2}\| = \left(\frac{1}{4\pi} \int_0^{2\pi} \int_0^{\pi} \left(M_{N_2}(\theta, \varphi)\right)^2 \sin\theta \, d\theta \, d\varphi \right)^{1/2}. \tag{3.36}$$

With these preliminaries completed, we consider the orientation dependence of the mobility coefficients, showing the variation of M_{N_1}, M_{N_2}, $M_{\tau_{12}}$ with φ and with θ in Fig.3.13. Focusing on the variation with φ, we see a net positive contribution to $\dot{C}_b$ from both N_1 and N_2 with the latter showing a stronger and almost uniform contribution for all φ. By contrast, the net contribution from τ_{12} averages to zero over the range of φ. (i.e. $M_{\tau_{12}}$) is zero. These features are confirmed by examining M_{N_1}, M_{N_2}, $M_{\tau_{12}}$ averaged over φ and plotted versus θ. From these figures, one concludes that the net effect of positive single particle first and second normal stress differences is to induce an orbital drift towards the velocity-gradient plane ($\dot{C}_b > 0$).

3.4.1.2 Suspension of particles

Having seen a clear relationship between $\dot{C}_b$ and particle normal stress differences for a single particle, we turn our attention to the mobility tensors for suspensions of particles. Beginning with (3.19), we rewrite the angular velocity of a particle "a" and separate the diagonal self-contributions "aa" and the non-self contributions "ab" in the form

$$\boldsymbol{\omega^a} = \boldsymbol{\Omega}^{\infty} - \mathbf{M}^{aa} \cdot \mathbf{S}^a - \sum_{b \neq a} \mathbf{M}^{ab} \cdot \mathbf{S}^b \tag{3.37}$$

For simplicity we have omitted the superscript ωS used previously for this mobility coupling. For concentrated suspensions, particle interactions contribute to the mobility tensors, and it is not possible to reduce to simple forms based on a single director as in (3.28). In this section, we explore simple models which might approximate the mobility tensors $\mathbf{M}^{aa}$ and $\mathbf{M}^{ab}$ and hence capture the dominant physical contributions from these terms.

First, we briefly note the procedure for computing the mobility matrix from simulation data. In the Stokesian Dynamics technique, the N particle resistance tensor is never explicitly computed as that is expensive and not necessary. Nonetheless, for a given configuration, it is straightforward to compute the full resistance tensor which may then be inverted to give the mobility matrix $\mathbf{M}$ defined in (3.19). The size of this mobility matrix $\mathbf{M}$ in (3.19) is $11N \times 11N$. One can then extract the relevant $3N \times 5N$ $\mathbf{M}^{\omega S}$ submatrix from the $\mathbf{M}$ matrix. We have computed the full mobility matrix for one realization for each volume fraction considered here. Since each configuration has information about 1000 particles, reasonable averages may be achieved by averaging over all the particles in a single configuration. From the $\mathbf{M}^{aa}$ blocks obtained from the simulation, we compute the couplings M_{N_1} and M_{N_2}, where M_{N_1} and M_{N_2} have been defined above. Smoother data could be achieved by averaging over more realizations.

Given a collection of mean mobility data from the numerical simulations, we consider simple models which may capture the dominant character of these tensors. For the $\mathbf{M}^{aa}$ self tensor, the simplest approach is to assume that the given particle behaves the same as a single axisymmetric particle in an isotropic medium. In other words, one might assume

that to leading order, the mean effect of particle interactions is to produce an isotropic hindrance for the mobility. Under this assumption, the single particle-single director form (3.28) applies. Given the full block mobility tensors M_{ijk} for the diagonal self contributions, we multiply by the reference stresslets (3.29) to compute M_{N_1} and M_{N_2} and average these self contributions for all particles in the system.

We show mobilities M_{N_1} and M_{N_2} computed from the simulation configurations as a function of φ in Fig.3.14 for fused-dumbbell particles and in Fig.3.15 for homonuclear particles. In each figure, we also plot the profile for the corresponding single particle axisymmetric result presented in section 3.4.1 above. For fused-dumbbells (Fig.3.14), the single particle model offers a very good approximation at $\phi = 0.05$, and a good qualitative fit at $\phi = 0.5$ though the magnitude is significantly reduced. Homonuclear particles, which have a smaller degree of anisotropy than fused-dumbbells, showed a similar variation with φ though the magnitude of this coupling is greatly reduced, being approximately 1/5 of the corresponding single body result (Fig.3.15). For both particles, note that the single particle model predicts a nearly uniform contribution from N_2. The data are in reasonable agreement with this prediction though with significant fluctuations. Overall, these results provide credence to the use of the single axisymmetric body result to describe the average $\mathbf{M}^{aa}$ tensor, at least qualitatively.

For the interparticle mobility $\mathbf{M}^{ab}$, we consider a simple model in which we compute the interaction between two dicolloids based purely on the interaction between their constituent spheres, and we include only the effect of the pair of spheres with the smallest interparticle gap. (See Fig. 3.16). Under this approximation, there is a single director characterizing the interaction - the vector along the line of centers of the two closest spheres. In such a case, the mobility tensor for both the "aa" and "ab" coupling take a form similar to that given in (3.28) with $\mathbf{p}$ being replaced by $\mathbf{d}$. With this model, we write the $\mathbf{M}^{aa}$ and $\mathbf{M}^{ab}$ tensors as

$$M^{ab}_{ijk} = \mathcal{M}^{ab}_0(\epsilon_{ijl}\, d_k d_l \,+\, \epsilon_{ikl}\, d_j d_l) \tag{3.38a}$$

$$M^{aa}_{ijk} = \mathcal{M}^{aa}_0(\epsilon_{ijl}\, d_k d_l \,+\, \epsilon_{ikl}\, d_j d_l) \tag{3.38b}$$

Note that the self term $\mathbf{M}^{aa}$ includes particle interactions, because it measures the effect of a stresslet on particle "a" on the angular velocity of "a" in the presence of particle "b".

Using the above model, one can predict the contribution to $\dot{C}_b$ for particle "a" based on the stresslet on all particles "b". This prediction may be compared to the correct value obtained from the numerically computed (many body) mobility tensor obtained from the simulation. We show such a comparison for the N_2 coupling in homonuclear particle suspensions at volume fractions $\phi = 0.1$ and $\phi = 0.5$ in Fig.3.17. A strong linear relationship can be seen at $\phi = 0.1$, which was found to degrade at $\phi = 0.5$. The slope of the best fit line in the figure can be interpreted as $\mathcal{M}_0^{ab}$ in Eq. (3.38a). $\mathcal{M}_0^{ab}$ is expected to be a function of the separation between the spherical components, and it is straightforward to incorporate this dependence to refine the quality of fit here, though, that is not our goal here. Our main objective is to provide a model to interpret the "ab" interparticle interactions. Similar to the N_2 mobility shown above, the N_1 mobility coupling (not shown here) showed good agreement between the simple interparticle model and the exact mobility tensor data. Similar results were obtained for fused-dumbbell particles. Finally, one can also compare the model and exact mobility data for the $\mathbf{M}^{aa}$ tensor. We generally saw poor agreement for this comparison which may be attributed to the fact that the exact $\mathbf{M}^{aa}$ tensor includes the single particle self effect as well as the sum of contributions from all its near neighbors. The expression above in (3.38b) models the contribution from just a single neighbor and hence it is not surprising that it performs poorly.

In addition to providing data for comparison with the simple one particle and two particle models, the exact mobility tensors from simulations provide important information concerning the relative importance of single particle terms and two particle interaction terms. We compute the norm of the $\mathbf{M}^{aa}$ coupling and the $\mathbf{M}^{ab}$ coupling for different volume fractions and plot the results in Fig. 3.18a and Fig. 3.18b for fused-dumbbell and homonuclear particles respectively.

For the fused-dumbbells, the "aa" self coupling is consistently stronger than "ab" at all volume fractions (within the noise of the data). The opposite is true for homonuclear particles. This is not surprising given that the fused-dumbbell with large anisotropy is expected to be dominated by the isolated body mobility. For the homonuclear particle which

is nearly spherical, contributions from interparticle interaction are expected to dominate. For a sphere, the single particle term is identically zero. An "ab" coupling was included in the above plot only when the minimum gap between the particles was less that $0.5a$, a being the radius of the spherical component forming the particle. Also note that each particle has multiple "ab" couplings present, corresponding to each of the nearest neighbors.

3.4.2 Analysis of Orientation Dynamics

In the section above, we have examined the N body mobility tensor for the particle configurations which develop in dynamic simulations. We have seen that simple models based on single particle mobility tensors and pairwise particle interactions capture the essential features of the mean mobility for the ωS components of the mobility tensor. The mean mobility tensor for the M_{N_1}, M_{N_2} components predicts a net average drift toward the vorticity axis when the mean normal stresses N_1 and N_2 are negative consistent with the data presented in the Results section above. While the product of the *mean* mobility and the *mean* normal stresses yields results consistent with overall observations of particle orientation, the particle interactions in concentrated suspensions lead to strong fluctuations in both the particle mobility and individual particle stresslets. These fluctuations are due to fluctuations in configuration. In the present section, we will examine the dynamics and investigate the relationship between the instantaneous orbital drift $\dot{C}_b$ and the instantaneous particle stresslets.

The first tool which we employ to study the orientation dynamics is a conditional average $\langle \dot{C}_b \rangle$ defined as the ensemble average taken over all particles with a specified particle stresslet averaged over long interval of time. Thus we define $\langle \dot{C}_b(N_1) \rangle$, $\langle \dot{C}_b(N_2) \rangle$ and $\langle \dot{C}_b(\tau_{12}) \rangle$. To compute these conditional averages, we divide the full range of stresslet values into a number of small intervals and sort all particles into bins based on their respective stresslet values. The orbital drift rate $\langle \dot{C}_b \rangle$ is then computed as the average over all particles in that bin.

The second tool which we use to study the dynamics is a direct correlation between the orbital drift rate $\dot{C}_b$ and different components of the particle stresslets – N_1, N_2, and τ_{12}. Because we are concerned primarily with the effect of fluctuations about the mean, we will

focus on correlations between the fluctuations in $\dot{C}_b$ and fluctuations in N_1, N_2 and τ_{12}.

For any particle function f which is a function of time and particle number, we define the mean $\bar{f}$ and fluctuation f' by

$$\bar{f} = \frac{1}{N_r}\sum_{i=1}^{N_r} f_i \;\; ; \;\; f_i' = f_i - \bar{f} \tag{3.39}$$

The norm of the fluctuation f' is defined as

$$\|f'\| = \left(\frac{1}{N_r}\sum_{i=1}^{N_r} f_i'^2\right)^{1/2} \tag{3.40}$$

Given two particle functions f and g, we define normalized correlations of the functions $\Psi[f,g]$ as

$$\Psi[f,g] = \frac{1}{N_r}\left(\sum_{i=1}^{N_r} f'_i\, g'_i\right) / \, \|f'\|\,\|g'\| \tag{3.41}$$

By definition, any correlation Ψ lies between -1 and 1. If the two quantities are perfectly correlated, then $\Psi[f,g] = 1$. On the other hand, if the quantities are perfectly anti-correlated (e.g. $f = -g$), then $\Psi[f,g] = -1$. Lastly, if the two functions are uncorrelated, then $\Psi[f,g] = 0$. With these tools defined, we proceed to analyze the orientation dynamics by considering detailed results from the numerical simulations.

3.4.2.1 Conditional averages $\langle \dot{C}_b \rangle$

In Fig.3.19, we show $\langle \dot{C}_b(N_1) \rangle$ and $\langle \dot{C}_b(N_2) \rangle$ for a suspension of fused-dumbbell particles at $\phi = 0.1$ and at $\phi = 0.5$. For $\phi = 0.1$, $\langle \dot{C}_b(N_2) \rangle$ shows a near linear relationship with N_2, while $\langle \dot{C}_b(N_1) \rangle$ is nearly independent of N_1. $\langle \dot{C}_b(N_1) \rangle$ is omitted in later plots; similarly $\langle \dot{C}_b(\tau 12) \rangle$ is not shown as it nearly independent of τ_{12}. This last result is expected based on single particle results shown earlier. Overall, the weak correlations for N_1 and τ_{12} suggest that the second normal stress difference N_2 is the dominant feature in orientation dynamics for fused dumbbells at $\phi = 0.10$. At $\phi = 0.50$, the fused-dumbbells show a linear relationship for $\langle \dot{C}_b(N_2) \rangle$ vs N_2 for small values of N_2, but $\langle \dot{C}_b(N_2) \rangle$ plateaus at large values of the

particle stresslet $|N_2|$. Note that the distribution of the particle level N_2 was found to be non-Gaussian about the mean, with a significantly higher probability for negative values. For this reason the abscissa extends to greater negative values in the figure. The plateau in $\langle \dot{C}_b(N_2) \rangle$ can be attributed to strong particle interactions which are the source of the large N_2 stresslets and the large fluctuations in this range. These particle interactions lead to strong hindrance in the particle's rotational mobility $\mathbf{M}^{\omega S}$ and hence limit the magnitude of $\langle \dot{C}_b(N_2) \rangle$.

Next, we turn our attention to homonuclear particles, and plot $\langle \dot{C}_b(N_2) \rangle$ in Fig. 3.20 for $\phi = 0.1$ and $\phi = 0.5$. At $\phi = 0.10$, there is a linear relationship between $\langle \dot{C}_b(N_2) \rangle$ and N_2 similar to the result for fused-dumbbells, but with a much smaller slope. In addition, the homonuclear particles show larger fluctuations at low volume fraction relative to the fused-dumbbells. Both of these results are consistent with the results for the mobility tensor which showed a smaller rotational ωS mobility for the homonuclear particles with larger statistical variation. For $\phi = 0.5$, the homonuclear particles show a clear linear relationship over the entire range of N_2 with no sign of the hindrance plateau observed for fused-dumbbells. This is not surprising, as the small aspect ratio of the homonuclear allows much easier rotation and less hindrance than the fused-dumbbells. Another interesting feature observed in Fig. 3.20b is the appearance of a significant effect of particle shear stress with a negative slope for $\langle \dot{C}_b \rangle$. The origin of this behavior is discussed later in this section.

3.4.2.2 Correlations: orbital drift rate and stresslets

The conditional averages $\langle \dot{C}_b \rangle$ presented above provide a complete and detailed description for the orientation drift rate as a function of the strength of the different particle stresslets at two different volume fractions. As a further characterization of these interactions, we consider the overall correlations $\Psi[\dot{C}_b, N_1]$, $\Psi[\dot{C}_b, N_2]$ and $\Psi[\dot{C}_b, \tau_{12}]$ as defined above. The correlations for all particle shapes are plotted as a function of volume fraction in Fig.3.21. We focus first on the results for homonuclear particles. The correlation $\Psi[\dot{C}_b, N_2]$ is the strongest and is found to increase monotonically with increasing volume fraction. This is consistent with the increased vorticity alignment observed in suspensions of homonuclear particles with

increasing volume fractions. Larger negative N_2 found at high volume fractions would imply a greater negative $\dot{C}_b$ and consequently a greater vorticity alignment.

In contrast to the N_2 correlation, $\dot{C}_b$ shows very little correlation with N_1, while $\Psi[\dot{C}_b, \tau_{12}]$ shows a slightly negative correlation at high volume fraction. The correlation results for small bump particles mimic those for homonuclear particles. In contrast to the homonuclear particles, the fused-dumbbell particles show the opposite trend with increasing volume fraction. The correlation $\Psi[\dot{C}_b, N_2]$ is again the strongest, however it peaks at $\phi = 0.10$ and decreases monotonically with increasing volume fraction. This decay in correlation with N_2 is consistent with the plateau in vorticity alignment S_{zz} at volume fraction $\phi = 0.2$ seen for fused-dumbbells in Fig.3.12. Correlations of $\dot{C}_b$ with N_1 and τ_{12} remains statistically negligible in suspensions of fused-dumbbells at all volume fractions.

3.4.2.3 Shape effects on orientation dynamics

The micromechanical origins of the orientation dynamics observed in our simulations are now clear. For all particle types, the primary driving forces for orbital drift are the normal stress differences which arise from particle interactions. In section (3.3.2.2), we saw that the normal stress differences are negative with magnitude monotonically increasing as a function of volume fraction for all particle shapes at all volume fractions up to $\phi = 0.50$. The magnitude of the mean normal stress differences is insensitive to particle shape and shows little difference from spheres for volume fractions in the range $0 \leq \phi \leq 0.50$. With increasing volume fraction, particles experience more interactions with smaller particle gaps leading to stronger interactions and an overall increase in normal stresses. The origin of the opposite trends in correlation seen for fused-dumbbells and homonuclear particles follow directly from our earlier observations for the mobility tensors of these two particle shapes. In Sec. (3.4.1), we developed two models for the ωS mobility tensor in concentrated suspensions. The first model was based on a mobility tensor proportional to the single particle mobility tensor with a coefficient of proportionality representing an isotropic hindrance function. The second model was based on the pairwise interaction between neighboring particles. We saw that the single particle model was more important for fused-dumbbells, while the effect of

the particle interactions was more pronounced for homonuclear particles. The difference between these two mobilities is largely responsible for differences in the overall orientational dynamics as well as the opposite trends seen for correlations for the two particle types with increasing volume fraction.

Briefly, for fused-dumbbells, the single particle mobility model dominates. For a single particle, the fused dumbbell shows a large $\mathbf{M}^{\omega\mathbf{S}}$ mobility while the $\mathbf{M}^{\omega\mathbf{S}}$ mobility for a sphere is identically zero, and homonuclear particles with their small anisotropy show small single particle mobility. The mobilities computed from simulation configurations for fused-dumbbells show good agreement with the one body results subject to isotropic hindered mobility associated with particle interactions. With increasing volume fraction, there are stronger particle interactions leading to stronger hindrance for the higher aspect ratio fused-dumbbells. The degree of mobility hindrance can be estimated from the slope of $\langle \dot{C}_b \rangle$ versus N_2 in Fig.3.19. From $\phi = 0.10$ to $\phi = 0.50$, we see a 25 fold reduction in the slope and hence in the hindered mobility of the fused-dumbbells. This estimate is based on the slope over the small linear region at $\phi = 0.50$. In fact, $\langle \dot{C}_b \rangle$ plateaus near $N_2 = 5$ with negligible increase up to $|N_2| = 30$. The non-linear behavior with larger N_2 shows that the hindered single particle mobility model breaks down with stronger interaction. Nonetheless, a rough estimate of hindered mobility for this region gives a 100 fold decrease in mobility relative to $\phi = 0.10$ The breakdown of the single particle approximation and the non-linear plateau for strong particle interactions is responsible for the observed decrease in the normalized correlation for $\Psi[\dot{C}_b, N_2]$ in Fig. 3.21 at high volume fraction .

For homonuclear particles, the single particle ωS mobility is quite small, and the components of the ωS mobility tensor are primarily due to particle interactions. The homonuclear mobility is less sensitive to increasing volume fraction as may be seen in Fig. 3.20. Here, the slopes at $\phi = 0.10$ and $\phi = 0.50$ show mobilities at the two different volume fractions with roughly a 7 fold decrease, in contrast to the 25-100 fold decrease for fused dumbbells. With increasing volume fraction, there are an increasing number of particle interactions with increasing strength, and the $\Psi[\dot{C}_b, N_2]$ correlation for homonuclear particles increases monotonically with increasing ϕ. With an excellent linear fit over the entire range of N_2 , there is no decrease or plateau in the correlations over the range from $\phi = 0.10$ to $\pi = 0.50$

Note that the changes in the magnitude of the mobility as reflected by the slopes in Figs. 3.21 and 3.20 have a significant effect on the overall orientational dynamics. These effects do not appear in the correlations owing to the normalization with $\|\dot{C}_b\|$. For all particles, the magnitude of the normal stresses increases with increasing ϕ. For homonuclear particles, the increased driving force represented by the normal stresses combined with the increasing correlation $\Psi[\dot{C}_b, N_2]$ and the comparable mobility coefficients leads to the monotonic increase in orientation function S_{zz} with increasing volume fraction in Fig. 3.12a. For fused dumbbells, the orientation function S_{zz} plateaus in Fig. 3.12c with little change from $\phi = 0.20$ to $\phi = 0.50$. In this case, the increased normal stresses at higher volume fraction are offset by the 25-100 fold decrease in mobility and by the breakdown in the linear model for large normal stresses reflected in the decrease in $\Psi[\dot{C}_b, N_2]$ at large ϕ.

3.4.2.4 Correlations: orientation effects

In order to gain additional insight into the correlations presented above, it proves useful to evaluate the correlations as a function of orientation of the particle, here specified by the spherical coordinate φ. To evaluate the angular dependence, all particle are sorted into bins over narrow ranges of φ, and the summation in the correlation is restricted to particles in the given bin. The correlations $\Psi[\dot{C}_b, N_1]$, $\Psi[\dot{C}_b, N_2]$ and $\Psi[\dot{C}_b, \tau_{12}]$ for fused-dumbbell particles as a function of φ are shown in Fig.3.22. One may compare these to the similar variations in φ shown previously for the mobility tensor for fused-dumbbells (see Fig.3.14). The N_1 correlation shows a shape similar to that for N_1 mobility tensor, however the former is shifted more towards negative values. As a result, the N_1 correlation vanishes when averaged over φ. The τ_{12} correlation shows similar shape and position to that of the τ_{12} mobility tensor. The curve for the N_2 correlation from the numerical simulation data shows a deeper minimum than that for the mobility tensor. The reduced overall N_2 correlation for suspensions of fused-dumbbells at high volume fractions in this figure is consistent with the micromechanics discussed above. In addition, we see additional features based on particle orientation. There is a substantial reduction in $\Psi[\dot{C}_b, N_2]$ for particles which are aligned in the extensional quadrant ($0 < \varphi < \pi/2$), while there is considerably less reduction in $\Psi[\dot{C}_b, N_2]$ for particles

aligned in the compression quadrant ($\pi/2 < \varphi < \pi$). To explain the microstructural origins for this, we examine the pair distribution function for particles with axes aligned in the compression quadrant and in the extension quadrant respectively. Fig. 3.23 shows pair distribution contour plots for these two cases. Particles aligned in the extensional quadrant show more particles (darker ring) in the near contact region compared with particles aligned in the compression quadrant. The kinematics responsible for this disparity may be traced by observing detailed particle trajectories in the simulations. We omit a detailed discussion here. Briefly, for approaching particles, the combination of approach velocity, direction, angular velocity and particle orientation favors a higher concentration of particles for those aligned with symmetry axes in the compression quadrant.

Next, we consider correlations as a function of φ for homonuclear particles. Correlations for $\Psi[\dot{C}_b, N_1]$, $\Psi[\dot{C}_b, N_2]$ and $\Psi[\dot{C}_b, \tau_{12}]$ as functions of φ are shown in Fig.3.24. All correlations show increasing magnitude with increasing volume fraction consistent with the micromechanics discussed above. An additional effect revealed by the variation of correlations with φ is that there is an enhanced correlation with τ_{12} for particles in the compression quadrant $\pi/2 \leq \varphi \leq \pi$ relative to particles in the extension quadrant. The microstructural origin of this behavior is seen in the pair distribution functions for particles with symmetry axes in the respective quadrants (Fig. 3.25). Careful examination shows that the pair distribution function for the compression quadrant shows a greater degree of fore-aft asymmetry. The increased fore-aft asymmetry can be shown to lead to enhanced correlation using simple arguments consistent with the pairwise particle interaction model presented in Section 3.4.1.2.

3.4.3 Fluctuation effects on orientation dynamics

For concentrated suspensions, we have conducted a detailed analysis of the relationship between the particle stresslets with associated normal stress differences and the orientational dynamics of the different particle shapes. We have seen how changes in the character of the $\mathbf{M}^{\omega S}$ mobility tensor for different particles leads to the observed changes in the orientation correlation functions and distribution of orbital constants. The sole remaining question

concerns the low volume fraction behavior where at $\phi = 0.05$ both the fused-dumbbells and the homonuclear particles show an orientational drift away from the vorticity axis toward the velocity-gradient plane. The rheological results show negligible mean normal stress differences at this low volume fraction (roughly an order of magnitude smaller than the values at $\phi = 0.10$), and the $\mathbf{M}^{\omega S}$ mobility coupling of the previous section would have negligible effect. Indeed, the observed orbital drift is in the opposite sense to the predicted mobility coupling. Instead, we must look elsewhere for the explanation of this low ϕ behavior.

In studies of orientation behavior of anisotropic particles in low Reynolds number flows, it is well known that particles tend to drift away from axial alignments which are subject to large orientation fluctuations and toward alignments with smaller orientation fluctuations. As a result of the anisotropic fluctuation distribution, non-uniform equilibrium orientation distributions may arise. A detailed discussion of these phenomena is given by Shaqfeh & Koch (1988). In the present study, we seek to assess the influence of non-uniform orientation dependent fluctuations on the orbital drift behavior of the anisotropic particles in our study.

As noted, for suspensions at low volume fraction, the mean normal stress differences are quite small, however the instantaneous normal stresslets on a particle during a close interaction with another particle may be significant. The associated orientation fluctuation may also be significant. For spherical particles in a purely hydrodynamic pairwise interaction in a simple shear flow, symmetry and reversibility dictate that the mean particle normal stress differences and orbital drift are identically zero. For non-zero net contributions from particle interactions, one must look for a mechanism to break the symmetry of the encounter. For interactions between anisotropic axisymmetric particles, the symmetry may be broken by particles approaching with different orientations relative to the axes of the shear flow. Particles may thus experience a net change in orbital constant with each particle interaction, and particles at distinct orientations (or orbit constants $\dot{C}_b$) may experience larger or smaller orientation fluctuation. Thus collisions of this type may induce a non-uniform distribution in the strength of the orientation fluctuation. (Here the term collision may involve purely hydrodynamic interactions or may include contributions from short range repulsive forces.) This is exactly the non-uniformity required leading to non-uniform equilibrium orientation distribution. For the present study, with anisotropic particles immersed in a simple shear

flow, it implies a perturbation of the orientation distribution relative to the unperturbed Jeffery orbits.

To probe this hypothesis, we investigate the relationship between the magnitude of orientation fluctuations and the strength of particle interactions in a "collision" event. We characterize the magnitude of orientation fluctuations by the magnitude of the orbital drift rate $|\dot{C}_b|$ and the strength of the collision by the magnitude of the normal stress differences (e.g. $|N_2|$) or alternatively by the magnitude of the short range repulsive force (e.g. $|F_x|$) for collisions with extremely small gaps of $O(10^{-3})$ particle radius. We compute normalized correlations as defined previously and consider two examples $\Psi[\,|\dot{C}_b|, |N_2|\,]$ and $\Psi[\,|\dot{C}_b|, |F_x|\,]$. To assess the orientation dependence of these quantities, we proceed analogous to previous cases. We divide the range of C_b into a number of small intervals and bin particles according to their orbit constants. We then evaluate Ψ correlations by summing over all particles in a given bin. We begin by considering suspensions of fused-dumbbells and plot $\Psi[\,|\dot{C}_b|, |N_2|\,]$ and $\Psi[\,|\dot{C}_b|, |F_x|\,]$ as a function of C_b for two distinct volume fractions $\phi = 0.05$ and $\phi = 0.50$ (Fig.3.26). At $\phi = 0.05$, the particles show a distinctly non-uniform correlation of fluctuations with respect to orbit constant C_b. Particles near the vorticity axis ($C_b \sim 0$) show a large positive correlation, while particles near the velocity-gradient plane ($C_b \sim 1$) show negligible correlation. The behavior is similar for correlations with N_2 and F_x though the decay is more rapid for the F_x correlation. At $\phi = 0.05$, the presence of larger orientation fluctuations during collision events at small C_b would predict a statistical migration away from the vorticity axis exactly as observed for the numerical simulations in Fig.3.12 at $\phi = 0.05$. At large $\phi = 0.5$, Fig.3.26 shows nearly uniform correlations as a function of C_b suggesting negligible impact on the orientation distribution at higher volume fraction.

We now briefly consider the case of homonuclear and small bump particles and show $\Psi[\,|\dot{C}_b|, |N_2|\,]$ for each particle in Fig.3.27. We omit the other correlations for these particles as the results show similar behavior. At low volume fraction, the results for the homonuclear particles show large correlation at $C_b \sim 0$ and rapid decay for higher C_b qualitatively similar to the behavior for fused-dumbbells. This is consistent with the migration of particles away from the vorticity axis observed for homonuclear particles in numerical simulations in

Fig.3.12. At high volume fraction, the homonuclear particles show uniform correlation as a function of C_b with negligible migration effect again matching the correlations observed for fused-dumbbells. By contrast, the small bump particles show different behavior. Here, the correlation is nearly uniform at low volume fraction with a narrow region of lowered correlation near $C_b = 0$. The broadly uniform correlation would predict no significant change in orbit constant for the small bump particles consistent with observations in the numerical simulations. One might infer that the lowered correlation near the vorticity axis would predict migration toward that region, however the region is such a small slice of orientation space that the flux of particles into the region is likely to be small. The large volume fraction results for small bump particles show uniform correlations consistent with the other particle shapes.

We have seen that the strong non-uniform fluctuations explain the observed migration away from the vorticity axis for homonuclear and fused-dumbbell particles at small ϕ. We have noted that the more uniform fluctuations at higher volume fraction would not lead in and of themselves lead to non-uniform orientation distributions. This does not mean that the uniformly distributed fluctuations play no role in governing the orientation of particles in the system. The strong fluctuations occurring at high ϕ introduce a strong rotary hydrodynamic diffusivity into the system. In the overall population balance equation for orientation, the strong forcing induced by the normal stress/mobility mechanism of sections 3.4.1 and 3.4.2 is balanced by rotary hydrodynamic diffusivity to yield the steady state orientation distributions shown in Fig.3.11. In the absence of the rotary hydrodynamic diffusivity, the strong normal stress/mobility forcing would push all particles toward perfect alignment with the vorticity axis at high ϕ .

In the end, both the forcing terms and the hydrodynamic diffusive terms arise from particle interactions and may be analyzed in a precise manner through consideration of the dynamically evolving mobility and resistance tensors in the numerical simulations. There is a wealth of information in these tensors, however owing to the temporally evolving dependence on the orientation and positions of all particles in the N body system the elucidation of clear microscale physical mechanisms remains a formidable challenge.

3.5 Conclusion

In this study, we have investigated the microstructure, orientation, and rheology in suspensions of dicolloidal particles over a wide range of volume fractions ($0 \leq \phi \leq 0.55$). We have seen that the basic microstructure and rheological properties for mildly anisotropic homonuclear and small-bump particles closely follow the related properties for suspensions of spheres. The more highly anisotropic fused-dumbbells show similar behavior at low volume fraction, but exhibit significant departures above $\phi = 0.50$. It is in the orientation dynamics that suspensions of anisotropic colloids show the true complexity associated with their interactions in a sheared suspension at finite concentration. We have seen that features such as aspect ratio, fore-aft symmetry and suspension volume fraction lead to a complex pattern of system response. Despite this complexity, we have seen that elucidation of the individual microscale physical mechanisms can indeed provide a clear explanation of the observed behavior. At this time, the microscale models can provide qualitative predictions of the system behavior though quantitative model predictions remain for future efforts.

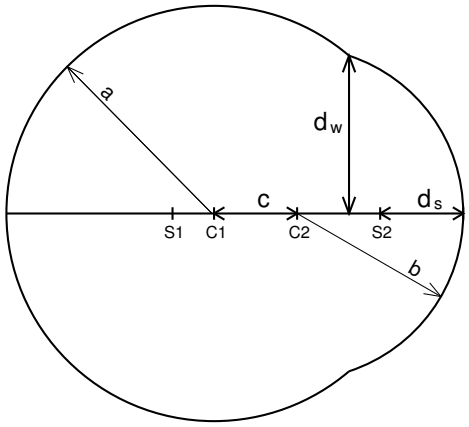

Figure 3.1: A cartoon of a dicolloidal particle showing various parameters. In the figure, C1 and C2 refer to the centers of the two spherical nodes forming the dicolloid. S1 and S2 refer to the location where singularities are placed. c is the center to center separation, d_w is the maximum width of the bump, while d_s is the smallest distance of the singularity S2 from the surface of the particle.

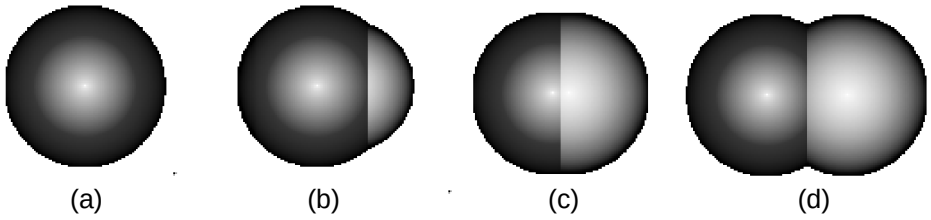

Figure 3.2: All particle shapes studied in this work: (a) Sphere, (b) Small-Bump, (c) Homonuclear, (d) Fused-dumbbell. See table (3.1) for some of the parameters for these particles as defined in figure (3.1).

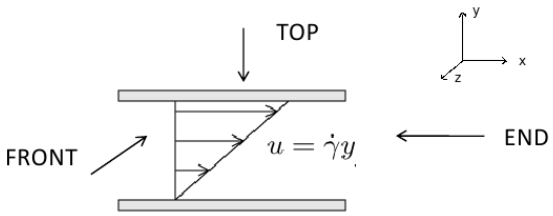

Figure 3.3: Cartoon defining front (flow-gradient), top (flow-vorticity), and end (vorticity-gradient) views. These definitions are used in presenting the pair distribution functions.

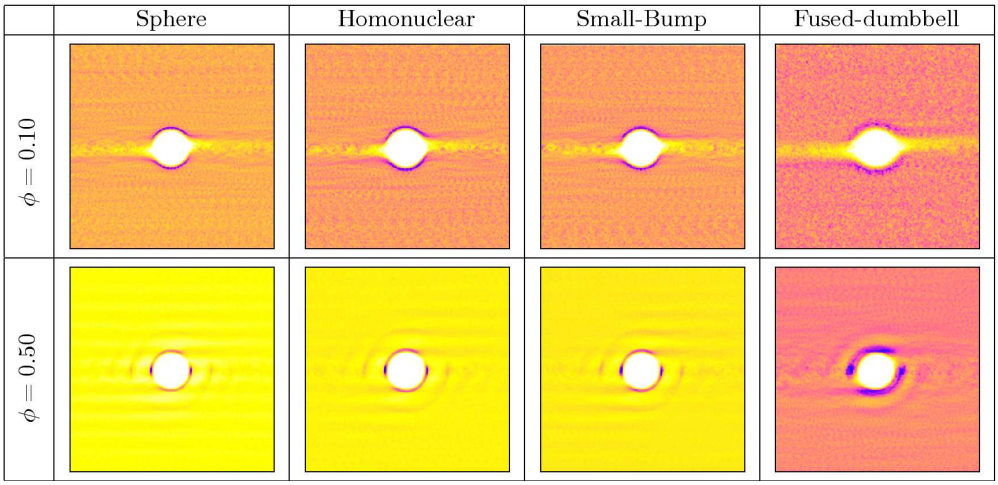

Figure 3.4: Pair distribution functions (PDF) for all particle shapes in the front view at $\phi = 0.10$ and $\phi = 0.50$. Centroid of the particles were used in computing the PDF for all particle shapes.

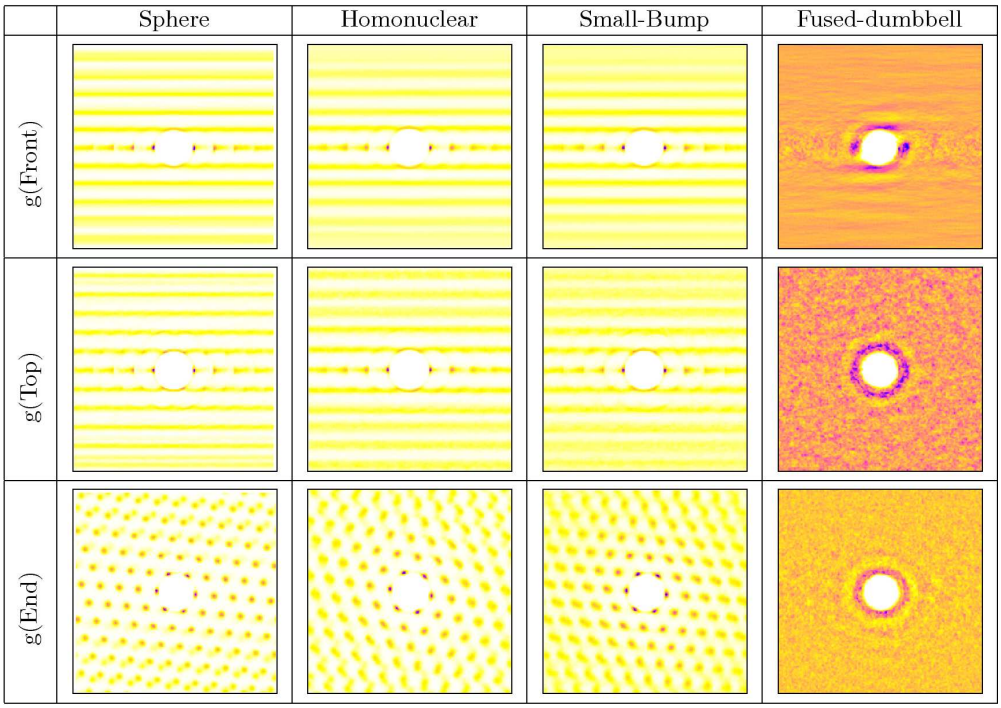

Figure 3.5: Pair distribution functions in front, top, and end views for all particle shapes at $\phi = 0.55$. Centroid of the particles were used in computing the PDF for all particle shapes.

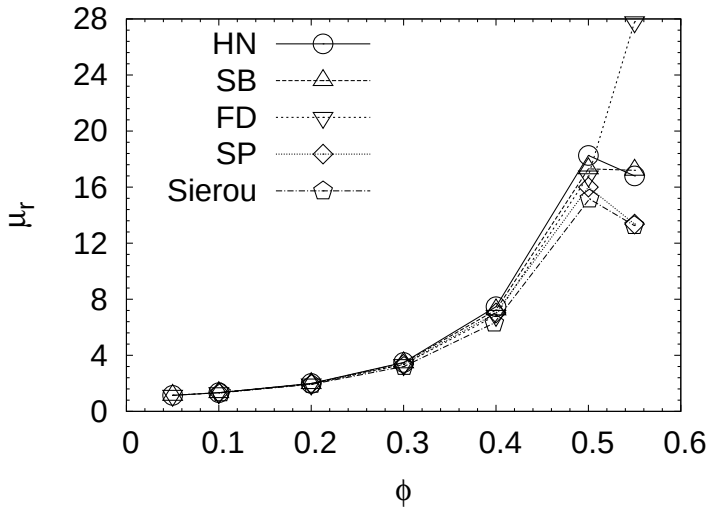

Figure 3.6: Relative viscosity (μ_r) for all particle shapes as function of volume fraction (ϕ). In the plot, data for homonuclear, small-bump, fused-dumbbell, and spherical particles are denoted by HN, SB, FD, and SP respectively. Sierou refers to simulation data from Sierou & Brady (2002).

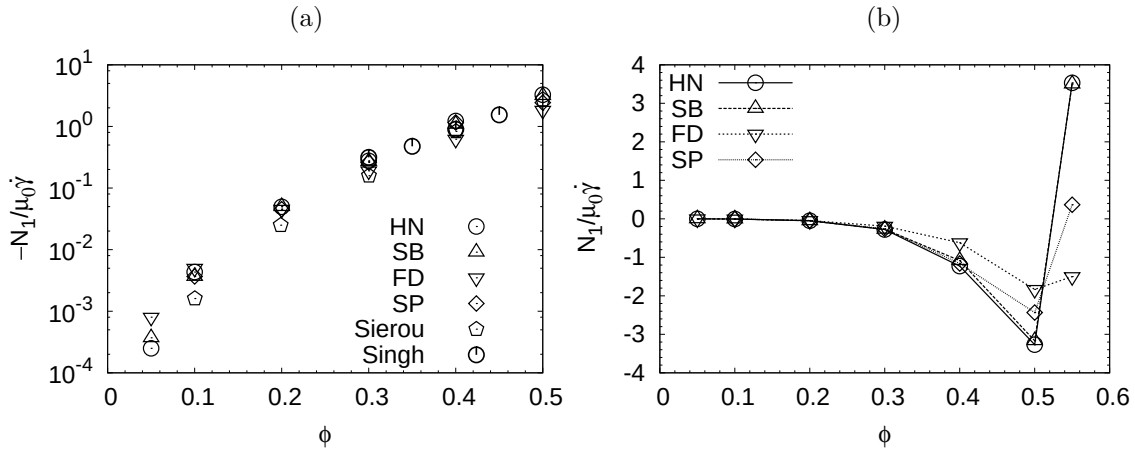

Figure 3.7: First normal stress difference N_1 as function of volume fraction ϕ. (a) $-N_1/\mu_0\dot{\gamma}$ as a function of ϕ where the y-axis is on a log scale (b) $N_1/\mu_0\dot{\gamma}$ as a function of ϕ where the y-axis is on a linear scale. μ_0 in the plot refers to the suspending fluid viscosity. Data for homonuclear, small-bump, fused-dumbbell, and spherical particles are respectively denoted by HN, SB, FD, and SP in the plot. Sierou refers to simulation data from Sierou & Brady (2002) while Singh refers to experimental data from Singh & Nott (2003).

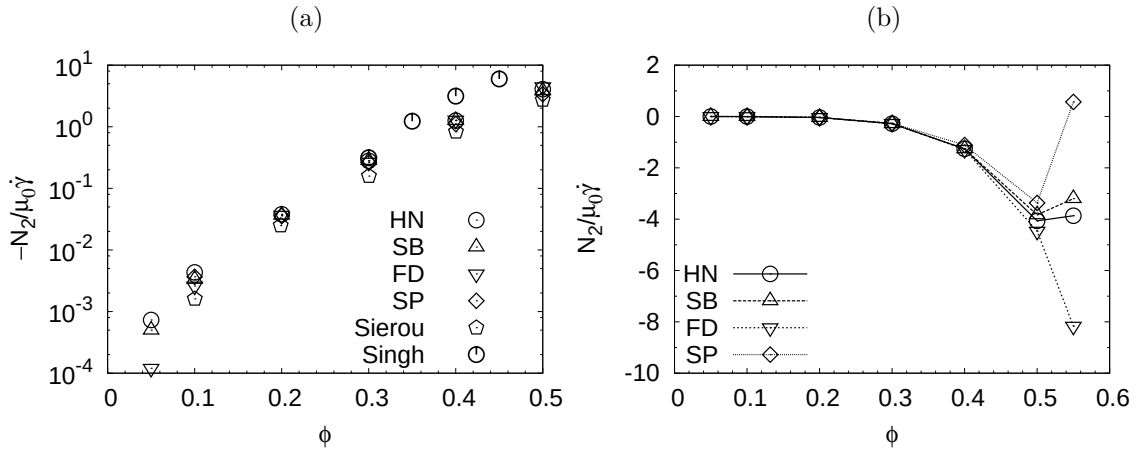

Figure 3.8: Second normal stress difference N_2 as function of volume fraction ϕ. (a) $-N_2/\mu_0\dot{\gamma}$ as a function of ϕ where the y-axis is on a log scale (b) $N_2/\mu_0\dot{\gamma}$ as a function of ϕ where the y-axis is on a linear scale. μ_0 in the plot refers to the suspending fluid viscosity. Data for homonuclear, small-bump, fused-dumbbell, and spherical particles are respectively denoted by HN, SB, FD, and SP in the plot. Sierou refers to simulation data from Sierou & Brady (2002) while Singh refers to experimental data from Singh & Nott (2003).

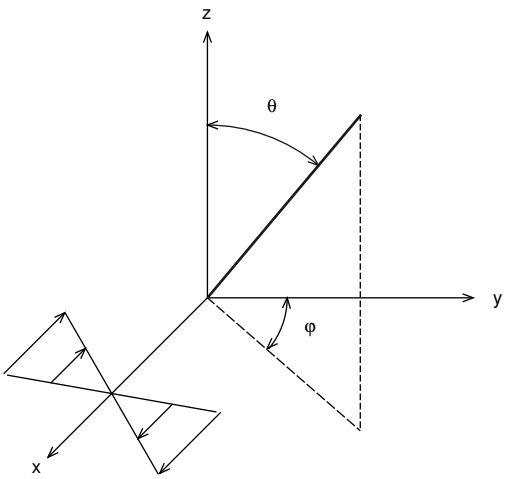

Figure 3.9: Definition of spherical coordinates θ and φ used in this study. As shown, θ is the angle made by the axis of the particle with the z axis, while φ is the angle made by the projection of the symmetry axis on the $x-y$ plane with the y axis.

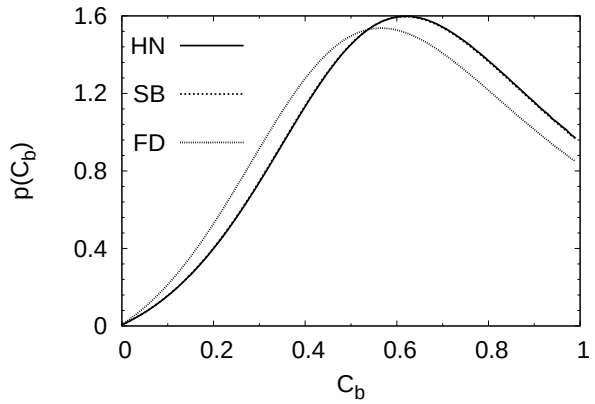

Figure 3.10: Probability $p(C_b)$ of finding a particle with a given orbit constant C_b for homonuclear (HN), small-bump (SB), and fused-dumbbell (FD) particles. It was computed assuming an isotropic initial distribution of the symmetry axis of the particle. Infinite dilution distribution was assumed to be given by this distribution.

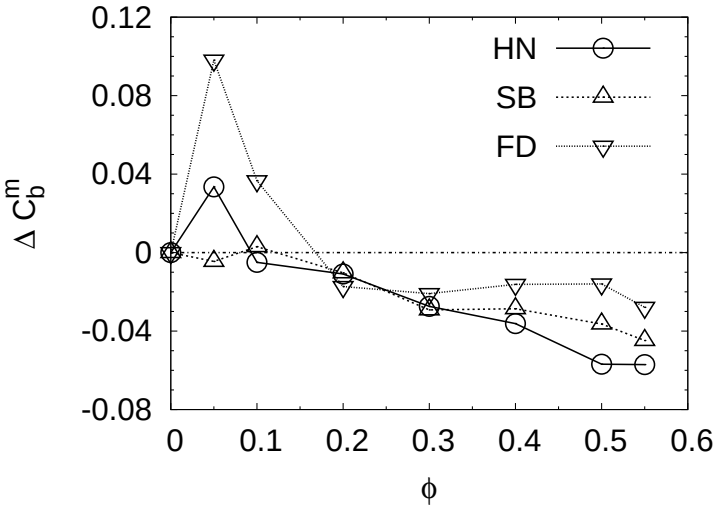

Figure 3.11: Change in mean orbit constant ΔC_b^{m} at volume fraction ϕ over the corresponding infinite dilution value: $\Delta C_b^{\mathrm{m}} = C_b^{\mathrm{m}}(\phi) - C_b^{\mathrm{m}}(\phi \to 0)$. Figure shows data for homonuclear (HN), small-bump (SB), and fused-dumbbell (FD) particle suspensions. The mean orbit constant at infinite dilution corresponding to the distribution in Figure (3.10) were: $C_b^{\mathrm{m}} = 0.6105$ for homonuclear, $C_b^{\mathrm{m}} = 0.6096$ for small-bump, and $C_b^{\mathrm{m}} = 0.5828$ for fused-dumbbell particles.

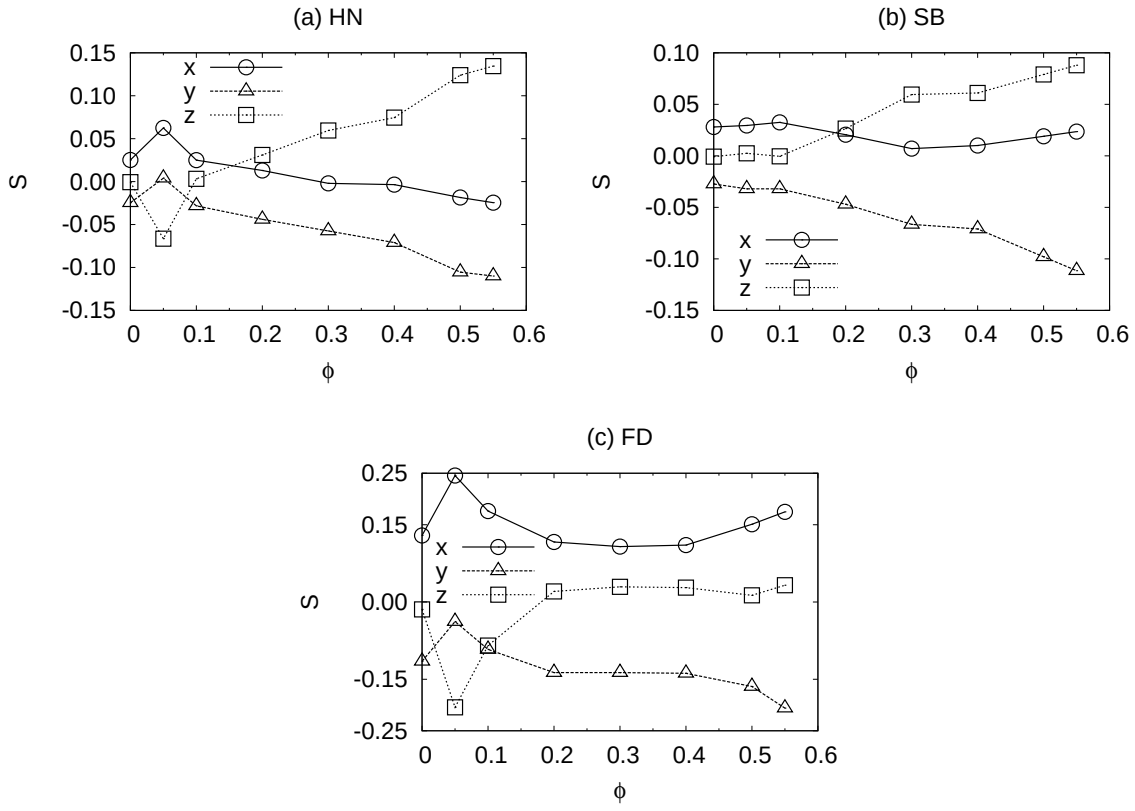

Figure 3.12: Orientational order parameter S (see Eq. 3.14) along the three coordinate axes for (a) homonuclear (HN), (b) small-bump (SB), and (c) fused-dumbbell particles (FD).

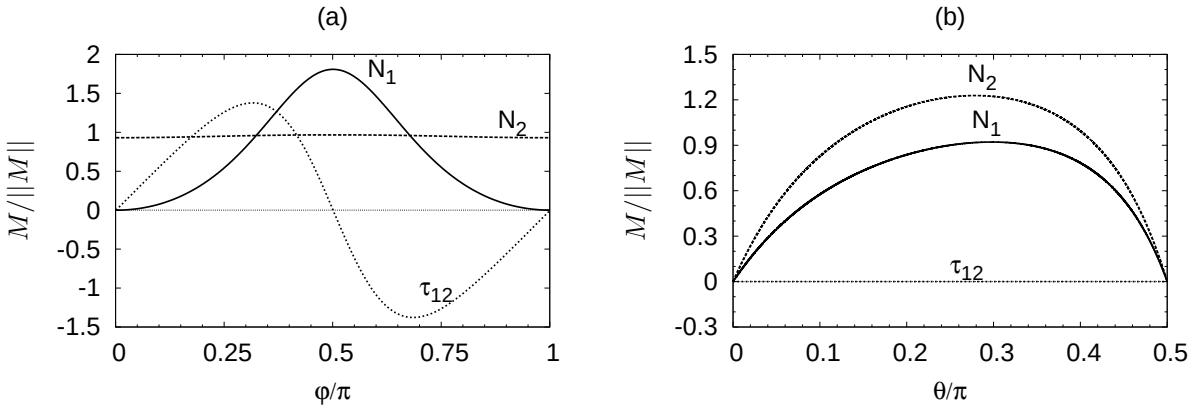

Figure 3.13: Various mobility couplings M for a single axisymmetric particle. Plots show $M_{N_1}/||M_{N_1}||$, $M_{N_2}/||M_{N_2}||$, and $M_{\tau_{12}}/||M_{\tau_{12}}||$ denoted respectively by N_1, N_2, and τ_{12} as a function of (a) φ and (b) θ. Data is shown for an axisymmetric particle with an effective aspect ratio equal to that of fused-dumbbells. Note that these couplings are equivalent to the 'aa' couplings described in the text.

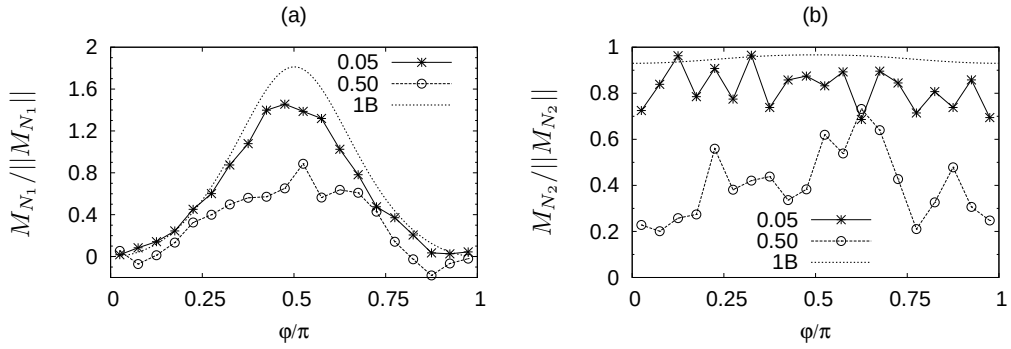

Figure 3.14: Fused Dumbbell particles: Mobility couplings $M^{aa}_{N_1}$ and $M^{aa}_{N_2}$ normalized by their respective norms as a function of φ for two different volume fractions: $\phi = 0.05$ and $\phi = 0.50$. These were computed numerically and have been averaged over all particles in a single configuration as described in the text. Also shown is the single axisymmetric body result denoted by '1B' in the figures.

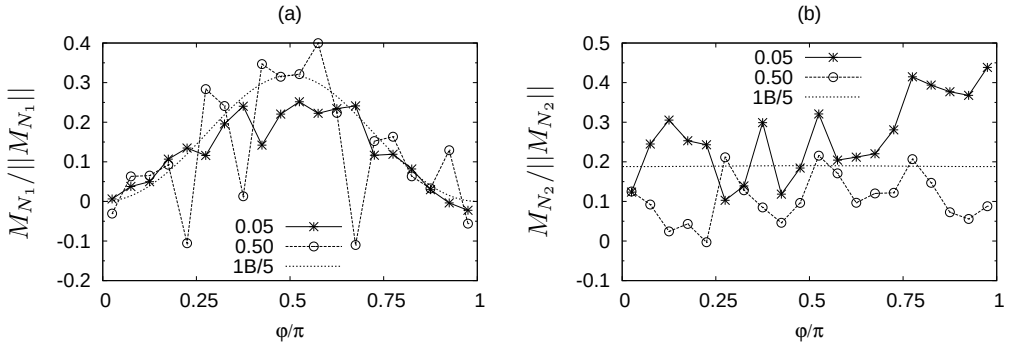

Figure 3.15: Homonuclear particles: Mobility couplings $M^{aa}_{N_1}$ and $M^{aa}_{N_2}$ normalized by their respective norms as a function of φ for two different volume fractions: $\phi = 0.05$ and $\phi = 0.50$. These were computed numerically and have been averaged over all particles in a single configuration as described in the text. Also shown is the single axisymmetric body result scaled by 1/5 and is denoted by '1B/5' in the figures.

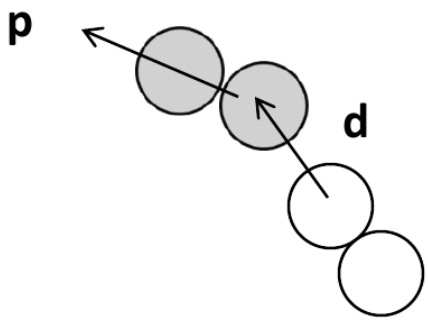

Figure 3.16: Cartoon showing definition of **d** and **p**

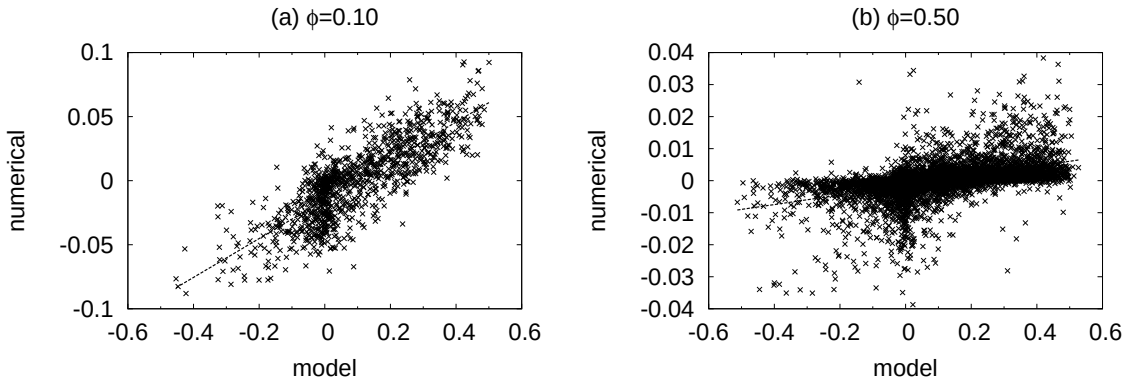

Figure 3.17: Homonuclear particles: $M_{N_2}^{ab}$ coupling at two different volume fractions: $\phi = 0.10$ and $\phi = 0.50$. Numerically computed values from simulation are compared with the corresponding values obtained from the model (Eq. 3.38a with $\mathcal{M}_0^{ab} = 1$). A $M_{N_2}^{ab}$ coupling was included for calculation only when the minimum gap between the pair 'ab' was less than $\delta/a < 0.5$. The solid straight line in figures is the linear best fit to the data.

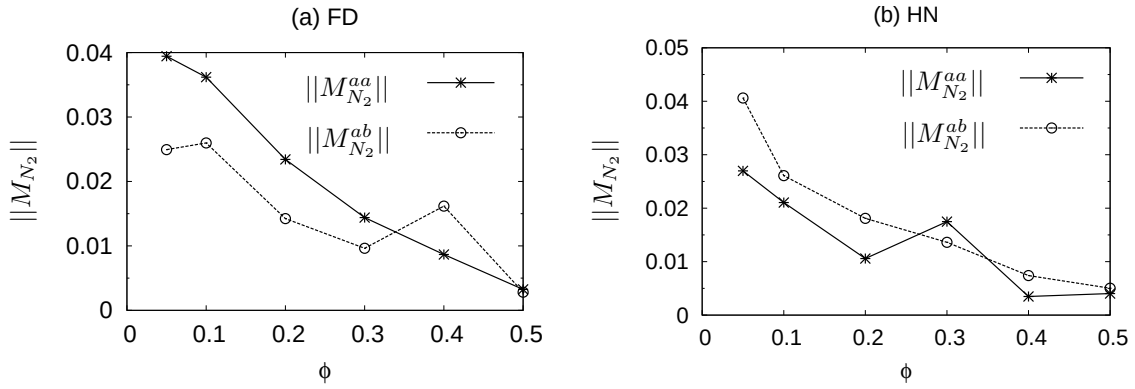

Figure 3.18: Norm of couplings $||M^{aa}_{N_2}||$ and $||M^{ab}_{N_2}||$ as a function of volume fraction for (a) fused-dumbbell particles (FD) and (b) homonuclear particles (HN). The norm is normalized by $(8\pi\mu_0 a^3)^{-1}$, where a is the radius of the spherical component forming the dicolloid, while μ_0 is the viscosity of the suspending fluid. Note that a $M^{ab}_{N_2}$ coupling was included for calculation only when the minimum gap between the pair 'ab' was less than $\delta/a < 0.5$.

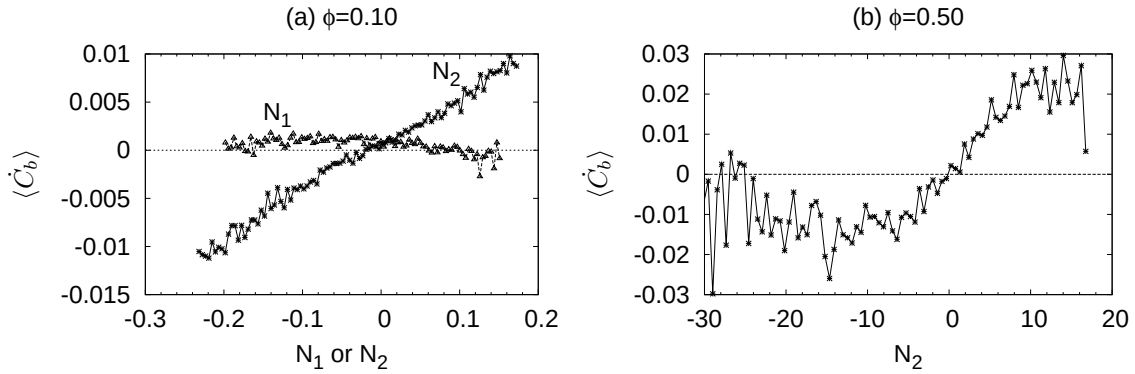

Figure 3.19: Fused-dumbbell: Mean rate of a particle's orbital drift $\langle \dot{C}_b \rangle$ as a function of the particle's contribution to N_1 or N_2 at (a) $\phi = 0.10$ and (b) $\phi = 0.50$ (only $\langle \dot{C}_b \rangle$ vs. N_2 shown). Note that the particle's contribution to N_1 or N_2 has been multiplied by the number of particles N in the system ($N = 1000$).

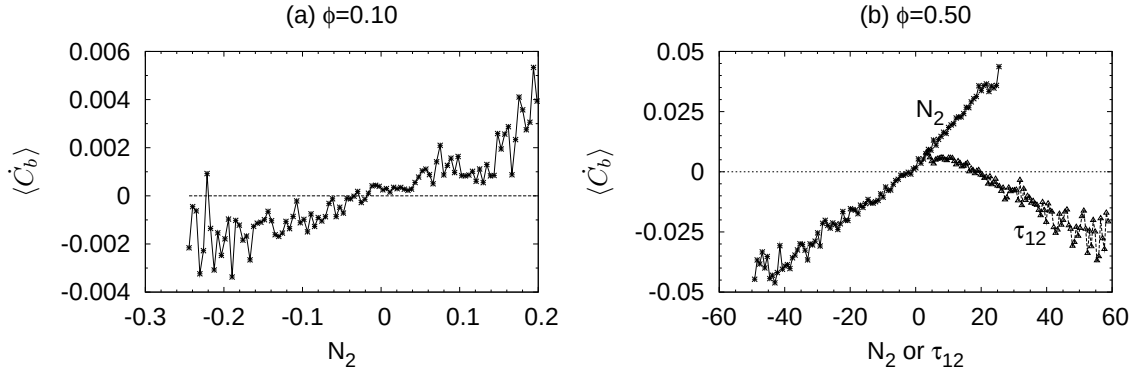

Figure 3.20: Homonuclear ($\phi = 0.5$): Mean rate of a particle's orbital drift $\langle \dot{C}_b \rangle$ as a function of the particle's contribution to N_2 or τ_{12} at (a) $\phi = 0.10$ (only $\langle \dot{C}_b \rangle$ vs. N_2 shown) and (b) $\phi = 0.50$. Note that the particle's contribution to N_2 or τ_{12} has been multiplied by the number of particles N in the system ($N = 1000$).

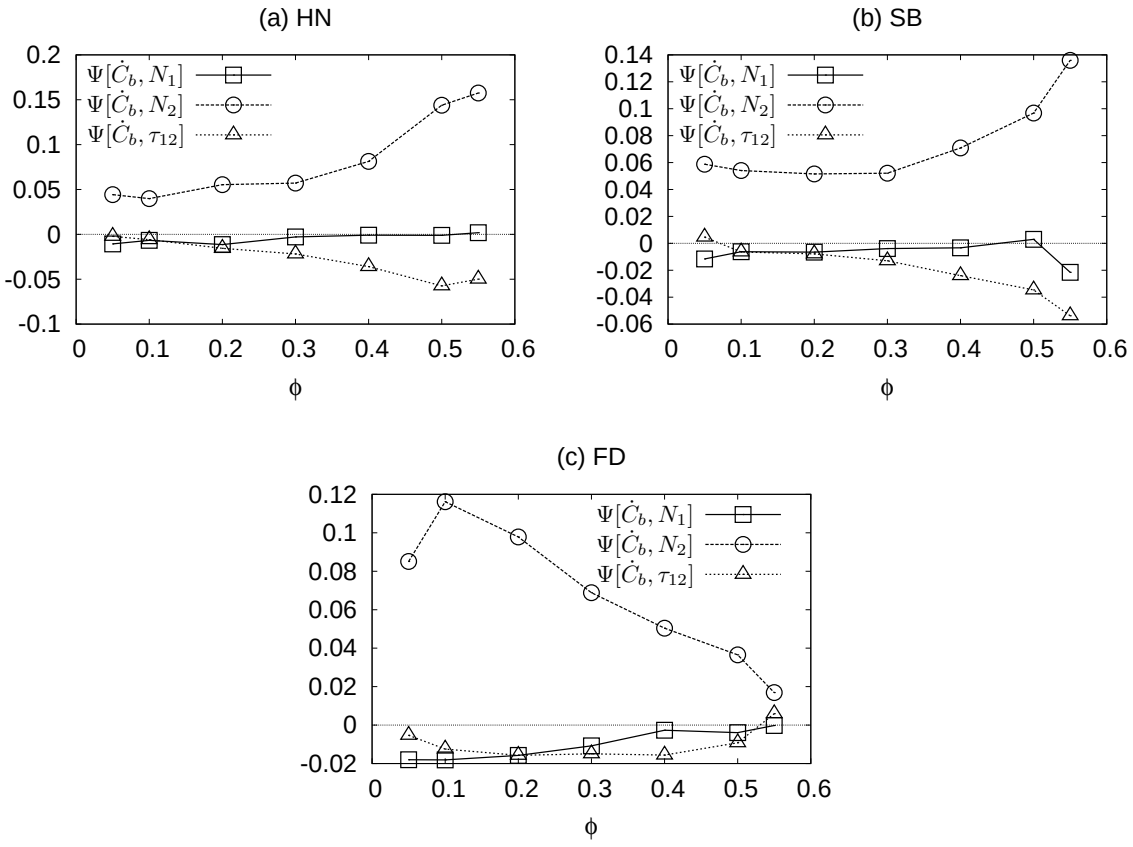

Figure 3.21: Correlations $\Psi[\dot{C}_b, N_1]$, $\Psi[\dot{C}_b, N_2]$, and $\Psi[\dot{C}_b, \tau_{12}]$ as a function of volume fraction for (a) homonuclear particles, (b) small-bump particles, and (c) fused-dumbbell particles. Correlations are defined in Eq. 3.41

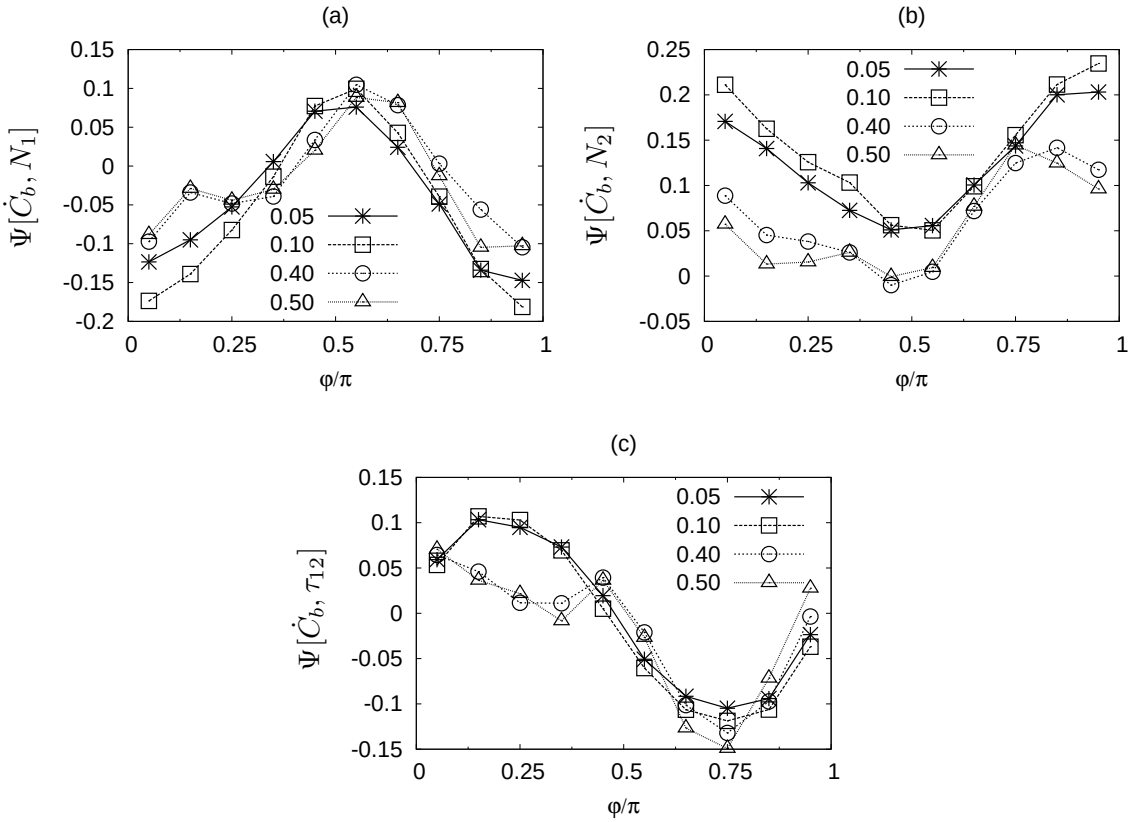

Figure 3.22: Fused-dumbbell particles: Correlations $\Psi[\dot{C}_b, N_1]$, $\Psi[\dot{C}_b, N_2]$, and $\Psi[\dot{C}_b, \tau_{12}]$ as a function of the particle's φ at four different volume fractions: $\phi = 0.05$, $\phi = 0.10$, $\phi = 0.40$, and $\phi = 0.50$.

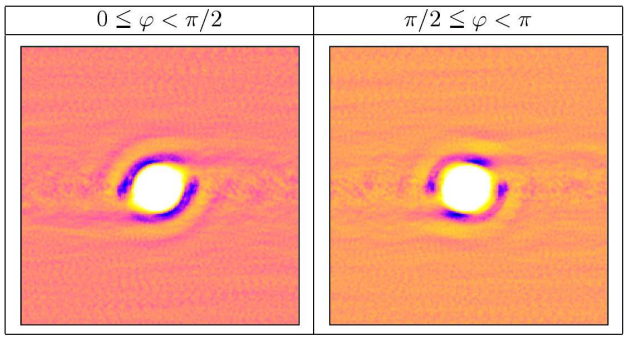

Figure 3.23: Fused-dumbbell particles ($\phi = 0.5$): Pair distribution function in the front view between centroids as a function of the particle's orientation. Left: Reference particle oriented in the extension quadrants ($0 \leq \varphi < \pi/2$). Right: Reference particle oriented in the compression quadrant ($\pi/2 \leq \varphi < \pi$).

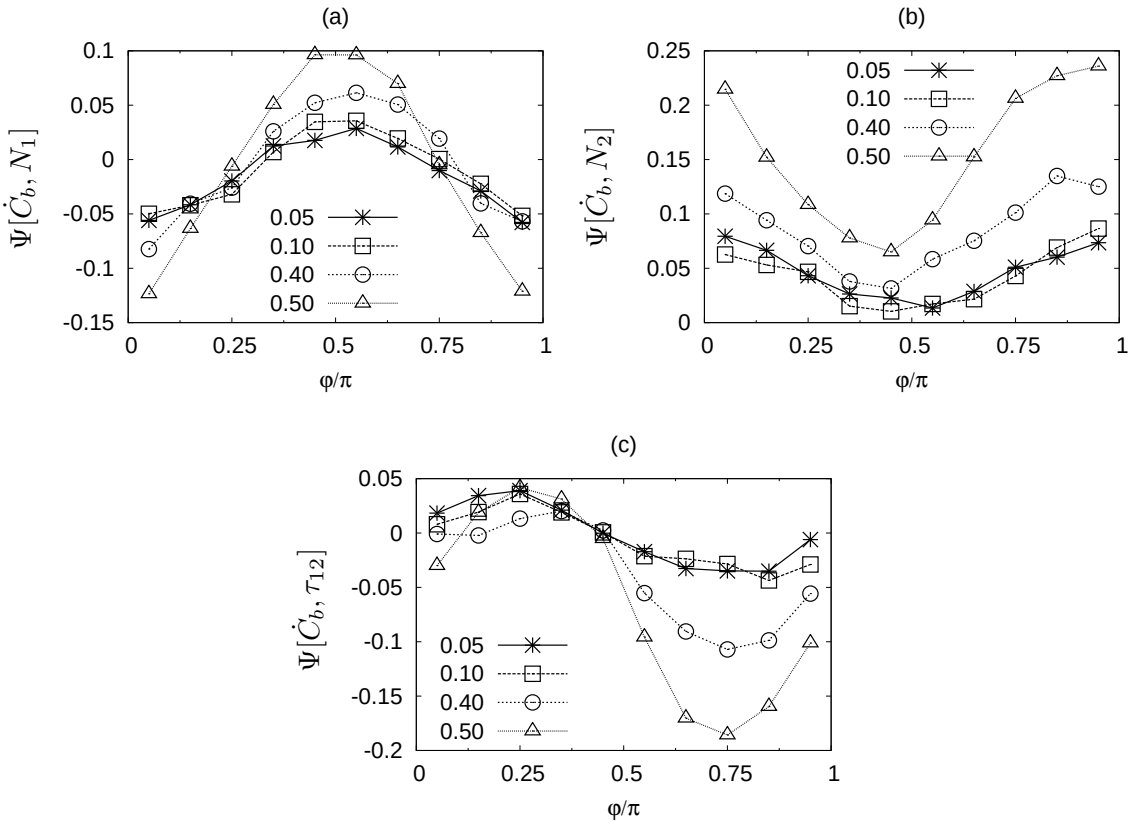

Figure 3.24: Homonuclear particles: Correlations $\Psi[\dot{C}_b, N_1]$, $\Psi[\dot{C}_b, N_2]$, and $\Psi[\dot{C}_b, \tau_{12}]$ as a function of the particle's φ at four different volume fractions: $\phi = 0.05$, $\phi = 0.10$, $\phi = 0.40$, and $\phi = 0.50$.

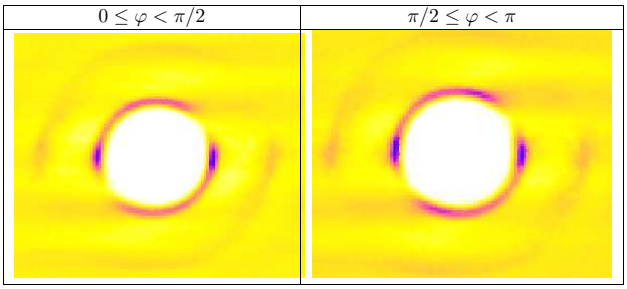

Figure 3.25: Homonuclear particles ($\phi = 0.5$): Pair distribution function between center of constituent spheres as a function of particle orientation. Left: Reference particle oriented in the extension quadrant ($0 \leq \varphi < \pi/2$). Right: Reference particle oriented in the compression quadrant ($\pi/2 \leq \varphi < \pi$).

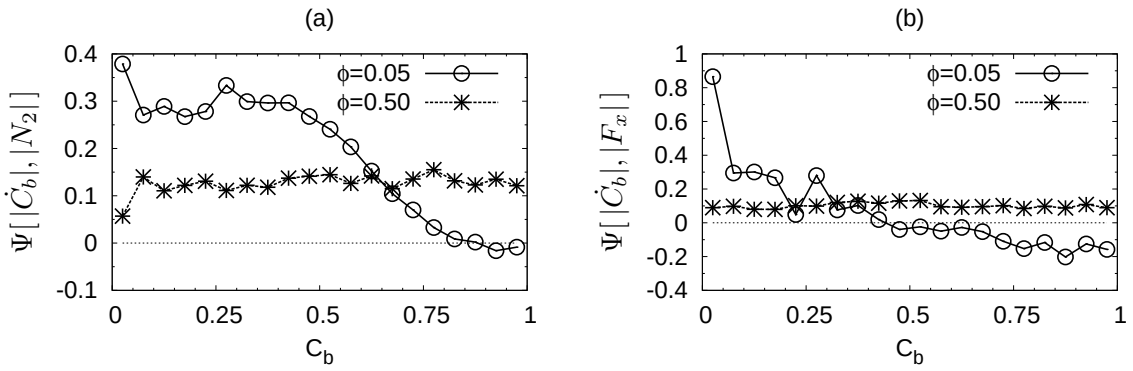

Figure 3.26: Fused-dumbbell particles: Correlations $\Psi[\,|\dot{C}_b|, |N_2|\,]$ and $\Psi[\,|\dot{C}_b|, |F_x|\,]$ as a function of particle's orbit constant C_b at two different volume fractions: $\phi = 0.05$ and $\phi = 0.50$.

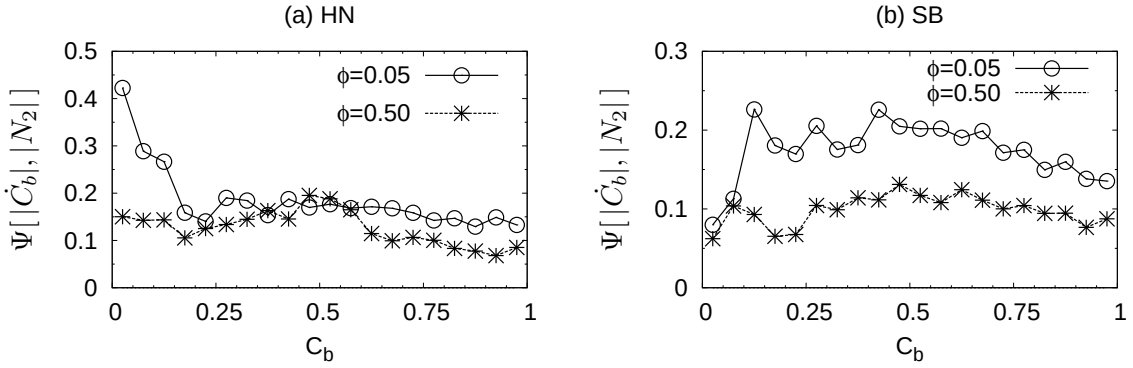

Figure 3.27: Correlations $\Psi[\,|\dot{C}_b|, |N_2|\,]$ for (a) homonuclear particles and (b) small-bump particles as a function of particle's orbit constant C_b at two different volume fractions: $\phi = 0.05$ and $\phi = 0.50$.

Table 3.1: Parameters (geometrical and numerical): See Fig. (3.1) for pictorial depiction of various terms. S_1 and S_2 refer to the location of singularities, while C_1 and C_2 refer to centers of spherical nodes along the axis of symmetry, with the center of mass taken as the origin. Also given is the effective radius of the sphere which has the same volume as the particle. All distances have been non-dimensionalized by a, the radius of the largest spherical node forming the dicolloid.

Particle	b	c	S_1	S_2	C_1	C_2	a_{eff}
fused dumbbell	1.0	1.0	-0.580	0.580	-0.5	0.5	1.1905
homonuclear	1.0	0.2	-0.165	0.165	-0.1	0.1	1.0475
small-bump	0.8	0.4	-0.053	0.588	-0.053	0.347	1.0192

Table 3.2: Effective aspect ratio r_e obtained from Jeffery's orbit time period, orientational order parameter S_{ii} along the three coordinate axis at infinite dilution, and intrinsic viscosity for all particle shapes.

Particle	r_e	S_{xx}	S_{yy}	S_{zz}	$[\mu]$
Small-Bump	1.0967	0.0252	-0.0247	-0.0006	2.5029
Homonuclear	1.0868	0.0280	-0.0274	-0.0008	2.4977
Fused-dumbbell	1.5075	0.1291	-0.1151	-0.0143	2.5378

Table 3.3: Viscosity and normal stresses for spherical particle suspension. Both the total as well as the interparticle force contributions to the corresponding components are given.

(a) Total

ϕ	μ_r	$N_1/(\mu\dot{\gamma})$	$N_2/(\mu\dot{\gamma})$
0.10	1.334	-3.67E-3	-3.50E-3
0.20	1.965	-4.53E-2	-3.56E-2
0.30	3.363	-2.60E-1	-2.62E-1
0.40	7.020	-1.16	-1.11
0.50	16.000	-2.43	-3.37
0.55	13.360	3.66E-1	5.67E-1

(b) Interparticle

ϕ	μ_r	$N_1/(\mu\dot{\gamma})$	$N_2/(\mu\dot{\gamma})$
0.10	1.6E-5	2.3E-5	-2.5E-5
0.20	2.9E-4	2.5E-4	-2.8E-4
0.30	2.8E-3	1.2E-3	-1.8E-3
0.40	1.9E-2	7.5E-5	-5.9E-3
0.50	1.0E-1	-1.5E-2	-4.4E-3
0.55	6.9E-2	3.4E-2	2.3E-1

Table 3.4: Viscosity and normal stresses for all particle shapes

(a) Homonuclear

ϕ	μ_r	$N_1/(\mu\dot{\gamma})$	$N_2/(\mu\dot{\gamma})$
0.05	1.143	-0.00025	-0.00073
0.10	1.337	-0.00433	-0.00433
0.20	1.991	-0.04967	-0.03800
0.30	3.490	-0.27667	-0.28000
0.40	7.470	-1.22667	-1.26000
0.50	18.260	-3.26667	-4.06667
0.55	16.800	3.53333	-3.86667

(b) Fused-dumbbell

ϕ	μ_r	$N_1/(\mu\dot{\gamma})$	$N_2/(\mu\dot{\gamma})$
0.05	1.148	-0.00080	-0.00012
0.10	1.336	-0.00500	-0.00260
0.20	1.959	-0.04533	-0.03667
0.30	3.338	-0.19000	-0.26667
0.40	6.850	-0.62000	-1.28333
0.50	16.800	-1.83333	-4.46667
0.55	27.800	-1.50000	-8.16667

(c) Small-Bump

ϕ	μ_r	$N_1/(\mu\dot{\gamma})$	$N_2/(\mu\dot{\gamma})$
0.05	1.142	-0.00037	-0.00050
0.10	1.334	-0.00367	-0.00333
0.20	1.977	-0.05000	-0.03667
0.30	3.456	-0.27000	-0.28333
0.40	7.240	-1.08333	-1.26000
0.50	17.300	-3.16667	-3.83333
0.55	17.200	3.50000	-3.20000

References

Anczurowski, E. & Mason, S.G. 1967 The kinetics of flowing dispersions iii. equilibrium orientations of rods and discs (experimental). *Journal of Colloid and Interface Science* **23**, 533–546.

van Blaaderen, A. 2006 Colloids get complex. *Nature* **439**, 545–546.

Bossis, G. & Brady, J.F. 1984 Dynamic simulation of sheared suspensions. i. general method. *Journal of Chemical Physics* **80** (10), 5141–5154.

Brady, J.F. & Morris, J.F. 1997 Microstructure of strongly sheared suspensions and its impact on rheology and diffusion. *Journal of Fluid Mechanics* **348**, 103–139.

Bretherton, F.P. 1962 The motion of rigid particles in a shear flow at low reynolds number. *Journal of Fluid Mechanics* **14**, 284–304.

Brunn, P. 1979 The motion of slightly deformed sphere in a viscoelastic fluid. *Rheological Acta* **18**, 229–243.

Butera, R.J., Wolfe, M.S., Bender, J. & Wagner, N.J. 1996 Formation of a highly ordered colloidal microstructure upon flow cessation from high shear rates. *Physical Review Letters* **77**, 2117–2120.

Chen, L.B., Chow, M.K., Ackerson, B.J. & Zukoski, C.F. 1994 Rheological and microstructural transitions in colloidal crystals. *Langmuir* **10**, 2817–2829.

Chow, M.K. & Zukoski, C.F. 1995 Nonequilibrium behavior of dense suspensions of uniform particles: Volume fraction and size dependence of rheology and microstructure. *Journal of Rheology* **39** (1), 33–59.

van Der Werff, J.C. & Kruif, C.G. De 1989 Hard-sphere colloidal dispersions: The scaling of rheological properties with particle size, volume fraction, and shear rate. *Journal of Rheology* **33** (3), 421–454.

Donev, A., Cisse, I., Sachs, D., Variano, E.A., Stillinger, F.H., Connelly, R., Torquato, S. & Chaikin, P.M. 2004 Improving the density of jammed disordered packings using ellipsoids. *Science* **303** (5660), 990–993.

Egres, R.G., Nettesheim, F. & Wagner, N.J. 2006 Rheo-sans investigation of acicular-precipitated calcium carbonate colloidal suspensions through the shear thickening transition. *Journal of Rheology* **50**, 685–709.

Fan, X., Phan-Thien, N. & Zheng, R. 1998 A direct simulation of fibre suspensions. *Journal of Non-Newtonian Fluid Mechanics* **74**, 113–135.

Guckel, E.K. 1999 Large scale simulations of particulate systems using the pme method. PhD thesis, University of Illinois at Urbana-Champaign.

Gunes, D.Z., Scirocco, R., Mewis, J. & Vermant, J. 2008 Flow-induced orientation of non-spherical particles: Effect of aspect ratio and medium rheology. *Journal of Non-Newtonian Fluid Mechanics* **155**, 39–50.

Jeffery, G.B. 1922 The motion of ellipsoidal particles immersed in a viscous fluid. *Proceedings of the Royal Society of London. Series A* **102** (715), 161–179.

Johnson, P.M., van Kats, C.M. & van Blaaderen, A. 2005 Synthesis of colloidal silica dumbbells. *Langmuir* **21** (24), 11510–11517.

Kim, J.W., Larsen, R.J. & Weitz, D.A. 2006 Synthesis of nonspherical colloidal particles with anisotropic properties. *Journal of American Chemical Society* **128** (44), 14374–14377.

Kim, Sangtae & Karrila, Seppo J. 2005 *Microhydrodynamics: Principles and Selected Applications*. Dover Publicatons.

Kumar, A. & Higdon, J.J.L. 2009 Pme stokesian dynamics simulations of non-spherical dicolloidal particles. Submitted to Journal of Fluid Mechanics.

Leal, L.G. 1975 The slow motion of slender rod-like particles in a second-order fluid. *Journal of Fluid Mechanics* **69**, 305–337.

Leal, L. G. & Hinch, E. J. 1971 The effect of weak brownian rotations on particles in shear flow. *Journal of Fluid Mechanics* **46**, 685–703.

Lootens, D., van Damme, H., Hemar, Y. & Hebraud, P. 2005 Dilatant flow of concentrated suspensions of rough particles. *Physical Review Letters* **95**, 268302.

Meng, Q. & Higdon, J.J.L. 2008 Large scale dynamic simulation of plate-like particle suspensions. part i: Non-brownian simulation. *Journal of Rheology* **52**, 1–36.

Mock, E.B., Bruyn, H. De, Hawkett, B.S., Gilbert, R.G. & Zukoski, C.F. 2006 Synthesis of anisotropic nanoparticles by seeded emulsion polymerization. *Langmuir* **22** (9), 4037–4043.

Mock, E.B. & Zukoski, C.F. 2007 Investigating microstructure of concentrated suspensions of anisotropic particles under shear by small angle neutron scattering. *Journal of Rheology* **51** (3), 541–559.

Morris, J.F. 2009 A review of microstructure in concentrated suspensions and its implications for rheology and bulk flow. *Rheological Acta* **48**, 909–923.

Muldowney, G.P. & Higdon, J.J.L. 1995 A spectral boundary element approach to three-dimensional stokes flow. *Journal of Fluid Mechanics* **298**, 167–192.

Petrich, M.P., Koch, D.L. & Cohen, C. 2000 An experimental determination of the stressmicrostructure relationship in semi-concentrated fiber suspensions. *Journal Non-Newtonian Fluid Mechanics* **95**, 101–133.

Pozrikidis, C. 2005 Orientation statistics and effective viscosity of suspensions of elongated particles in simple shear flow. *European Journal of Mechanics B/Fluids* **24**, 125–136.

Rahnama, M., Shaqfeh, E.S.G. & Koch, D.L. 1995 The effect of hydrodynamic interactions on the orientation distribution in a fiber suspension subject to simple shear flow. *Physics of Fluids* **7**, 487–506.

Shaqfeh, E. S. G. & Koch, D. L. 1988 The effect of hydrodynamic interactions on the orientation of axisymmetric particles flowing through a fixed bed of spheres or fibers. *Physics of Fluids* **31** (4), 728–743.

Sierou, A. & Brady, J.F. 2001 Accelerated stokesian dynamics simulations. *Journal of Fluid Mechanics* **448**, 115–146.

Sierou, A. & Brady, J.F. 2002 Rheology and microstructure in concentrated noncolloidal suspensions. *Journal of Rheology* **46**, 1031–1056.

Singh, A. & Nott, P.R. 2003 Experimental measurements of the normal stresses in sheared stokesian suspensions. *Journal of Fluid Mechanics* **490**, 293–320.

Speedy, R.J. 1997 Pressure of the metastable hard-sphere fluid. *Journal of Physics Condensed Matter* **9** (41), 8591–8599.

Stover, C.A., Koch, D.L. & Cohen, C. 1992 Observations of fiber orientation in simple shear flow of semi-dilute suspensions. *J. Fluid Mech.* **238**, 277–296.

Sundararajakumar, R.R. & Koch, D.L. 1997 Structure and properties of sheared fiber suspensions with mechanical contacts. *Journal of Non-Newtonian Fluid Mechanics* **73**, 205–239.

Vega, C., Paras, E.P.A. & Monson, P. A. 1992 On the stability of the plastic crystal phase of hard dumbbell solids. *Journal of Chemical Physics* **97** (11), 8543–8548.

Vermant, J. & Solomon, M.J. 2005 Flow-induced structure in colloidal suspensions. *Journal of Physics: Condensed Matter* **17**, R187–R126.

Viera, M.N. 2002 Large scale simulation of brownian suspensions. PhD thesis, University of Illinois at Urbana-Champaign.

Yang, S., Kim, S., Lima, J. & Yi, G. 2008 Synthesis and assembly of structured colloidal particles. *Journal of Materials Chemistry* **18**, 2177–2190.

Chapter 4

Microstructure and Orientation in Brownian Suspensions of Spherical and Dicolloidal Particles

Synopsis

Microstructural and orientational transitions are investigated for spherical and anisotropic Brownian particle suspension under shear using computer simulations. The class of anisotropic particles studied here can be modeled by two intersecting spheres of varying radii and center to center separation. Hydrodynamic interactions were approximated with a modified lubrication model. Results are reported for two different volume fractions, $\phi = 42\%$ & $\phi = 55\%$ and three different particle shapes: spheres, homonuclear, and fused-dumbbell. The 42% sample had repulsive electrostatic interaction while the 55% sample had hard-sphere type interaction. Particles with small degree of anisotropy (homonuclear) showed microstructural transitions similar to that of spheres. Particles with relatively larger degree of anisotropy (fused-dumbbell) showed a significantly different microstructural behavior from that shown by spherical particles. In both the homonuclear and fused-dumbbell particle suspensions, an orientationally disordered state is observed at low shear rates. An increase in flow alignment is seen as the shear rate is further increased reaching a maxima between $Pe = 1$ and $Pe = 20$ depending on particle shape. Upon further increase in shear rate an increase in vorticity alignment is seen. The degree of was anisotropy and volume fraction was found to have a significant effect on extent of increase in flow or vorticity alignment.

4.1 Introduction

Microstructure of a colloidal suspension plays a very important role in determining its macroscopic properties. Perhaps the best example of this is the effect of microstructure on rhe-

ological properties, which has been the focus of many previous studies. In recent times, many modern applications have been envisioned based on an ordered microstructure. These include photonic band gap materials, optical microlenses, physical masks for evaporation and etching, templates for generating other specialized materials, etc (Xia *et al.*, 2000). Anisotropic particles can play an important role in such applications as they may form ordered structures which cannot be formed from spherical particles (Lu *et al.*, 2001) ,(Glotzer *et al.*, 2004). There have been several efforts in the recent past to synthesize various types of anisotropic particles. Examples include ellipsoidal particles, rod shaped particles, peanut shaped particles, and polyhedral shaped particles formed from simple spheres (Lu *et al.*, 2001), (Glotzer *et al.*, 2004). In this work, we will restrict our attention to anisotropic particles called dicolloids. These particles can be modeled as two fused spheres of varying radii and center to center separation. Such particles have been synthesized recently by several groups (Johnson *et al.*, 2005), (Mock *et al.*, 2006), (Kim *et al.*, 2006). These kinds of particles can be produced in bulk with great control over their shape. Also their degree of anisotropy can be varied from extremely small to large. All these attributes makes this an exciting class of anisotropic particles which may show very interesting properties.

A large body of experimental work exists on microstructural characterization of spherical suspensions. We review some of the important microstructural transitions documented in the literature. At rest, hard sphere suspensions undergo a disorder-order transition at a volume fraction of $\phi = 0.494$, when face-centered cubic (FCC) crystals begins to form (Russel *et al.*, 1989), although experiments can show random stacking (Pusey *et al.*, 1989). Charge stabilized suspensions of spherical particles can show similar disorder-order transition, forming either body-centered cubic (BCC), or FCC crystal depending on the screening length of the repulsive interaction, and also the volume fraction (Sirota *et al.*, 1989). Roughly, if the screening length is large compared to the diameter of the particles, BCC crystal forms, otherwise FCC crystal forms (Xia *et al.*, 2000). Shearing the suspension can bring about several microstructural transitions depending on the shear rate, particle size, volume fraction and charge. At low rates of shear, the suspension maintains a crystalline structure, and shearing is achieved by hopping from one close packed site to its twin (Ackerson, 1990). This results in a zig-zag hopping kind of motion, which is also the path of minimum energy (Stevens

& Robbins, 1993). As the shear rate is further increased, a polycrystalline microstructure results which has been described as crystals with smaller domain sizes and lack of crystal orientation (Chen *et al.*, 1994b),(Chen *et al.*, 1994a). High volume fraction suspensions were found to transition to polycrystalline structure directly without going through the strained crystalline structure (Chen *et al.*, 1994a), (Chow & Zukoski, 1995). As the shear rate is further increased, a sliding layer microstructure results, where a row of particles in a layer is centered between the two rows of particles in the neighboring layers (Ackerson, 1990). This allows for easier slipping of layers. With further increase in shear rate, a string like structure develops (Ackerson, 1990),(Yan & Dhont, 1993). At very high rates of shear, an amorphous structure is obtained due to shear induced melting (Ackerson, 1990), (Chow & Zukoski, 1995). Another interesting feature of microstructure of suspensions under shear is the presence of metastable states. For lower volume fraction suspensions, metastable strained crystalline microstructure can exist, which eventually transitions to the stable polycrystalline microstructure (Chen *et al.*, 1994b). For higher volume fraction suspensions, a metastable state with polycrystalline microstructure is reported to exist, which eventually transitions to a mixture of polycrystalline and sliding layer microstructure (Chen *et al.*, 1992). These transitions have been studied in detail in chapter (5).

Many computer simulations have characterized the microstructural transitions in spherical suspensions. For example, molecular dynamics simulation predicts the melting of equilibrium FCC crystals with shear, which then form a reentrant solid at higher rates of shear having a sliding layer microstructure (Stevens & Robbins, 1993). Non-equilibrium Brownian dynamics (NEBD) simulations have predicted the formation of sliding layer microstructure (Rastogi *et al.*, 1996) and string like microstructure (Foss & Brady, 2000). Stokesian dynamics simulation on charge stabilized non-Brownian spheres (Gray & Bonnecaze, 1998) has predicted the low-shear zig-zag motion and high shear rate straight trajectory (sliding layer) motion. Stokesian Dynamics simulation on hard sphere, non-Brownian suspension (Sierou & Brady, 2002) have shown the effect of volume fraction on ordering. Their simulations showed a disordered state for $\phi < 0.5$, a string like state for $\phi = 0.52$ and $\phi = 0.55$, and again a disordered state for $\phi = 0.6$ suspension. Simulations with only the dominant squeeze lubrication have also been reported (Ball & Melrose, 1995), (Catherall *et al.*, 2000).

Their investigation showed that charge stabilized spheres which were disordered at rest were caused to order upon shearing, which again disordered with further increase in the shear rate (Catherall *et al.*, 2000).

Several works have focused on microstructural and orientational analysis for anisotropic particles. Experiments on fiber suspensions under shear reveal that they spend most of the time aligned along the flow direction as they would in a Jeffery's orbit (Stover *et al.*, 1992). Plate like particles have also been studied under shear (Jogun & Zukoski, 1999). Particle alignment with flow was found to increase with shear rate, but was found to be independent of the volume fraction in the range studied. Extensive simulations have also been performed on spherocylinders at rest, completely mapping its phase diagram (Bolhuis & Frenkel, 1997). These authors found that for $L/D < 0.35$, the first ordered phase formed is a plastic crystal, which at higher volume fractions transitions to an orientationally ordered phase. On the other hand for $L/D > 0.35$, fluid freezes directly into an orientationally ordered phase. Similar results were reported for hard dumbbells (dicolloids) at rest by Vega *et al.* (1992b). They found that for $L/D = 0.3$, fluid freezes into a plastic crystal, while for $L/D = 0.6$, fluid freezes into an orientationally ordered base-centered monoclinic structure. Recently, experimental studies were done on various charge stabilized dicolloidal particles by Mock & Zukoski (2007). They found that for heteronuclear particles with mild degree of anisotropy, the microstructural transitions were similar to those for spheres. At rest, they showed close packed structure with random stacking. With further increase in shear a polycrystalline structure was formed. Unlike spheres, no strained crystalline microstructure was observed for heteronuclear dicolloids under the shear rates investigated. Upon further increase in shear rate, the polycrystalline microstructure transitioned to a sliding layer microstructure. On the other hand, homonuclear particle ($L/D = 0.1$) showed a different set of microstructural transitions with shear rate. It was found to be polycrystalline at rest, which then transitioned to a sliding layer microstructure at higher shear rates. Upon further increase in shear rate, it was found to disorder. At this point, it must be mentioned that the surface potential of homonuclear particles was much smaller (-0.35mV) in comparison to that of heteronuclear particles (-11mV). This could be the likely cause for the difference in their microstructural transitions with shear rate.

4.2 Formulation

4.2.1 Governing Equation

The motion of colloidal particles, suspended in a fluid, is governed by the Langevin equation

$$m\frac{d\mathbf{U}}{dt} = \mathbf{F}^H + \mathbf{F}^B + \mathbf{F}^P \tag{4.1}$$

which is the relevant form of the Newton's second law for a colloidal particle. In the above equation m is the mass/moment of inertia of the particle, $\mathbf{U}$ is the generalized velocity/angular velocity vector, and $\mathbf{F}^H$, $\mathbf{F}^B$, and $\mathbf{F}^P$ are the generalized force/torque vectors due to the hydrodynamic interaction, thermal fluctuations (Brownian motion), and inter-particle interaction respectively. Each of the vectors $\mathbf{U}$, $\mathbf{F}^H$, $\mathbf{F}^B$, and $\mathbf{F}^P$ have $6N_p$ elements, where N_p is the number of particles in the system. In the above equation, inertia of the particles, $m\frac{d\mathbf{U}}{dt}$, is usually negligible, and is therefore taken as zero in our simulations. With this simplification, the governing equation for the particle's motion becomes

$$\mathbf{F}^H + \mathbf{F}^B + \mathbf{F}^P = 0 \tag{4.2}$$

which was the form used in all our simulations. In the following sections, we discuss in detail the estimation of each of the above three interactions, i.e., $\mathbf{F}^H$, $\mathbf{F}^B$, and $\mathbf{F}^P$.

4.2.2 Hydrodynamic Interaction ($\mathbf{F}^H$)

Colloidal particles are very small, usually having a characteristic length smaller than $10^{-6}m$. Due to its small size, Reynolds number for the fluids motion around the particle is usually negligible, and hence the linear Stokes equation may be used. In Stokes flow, the hydrodynamic force on a particle is a linear function of the fluid velocity, and this linear relationship is usually expressed in the form of a resistance tensor $\mathbf{R}$. In this work, we will restrict ourselves to forces/torques $\mathbf{F}$, and stresslets $\mathbf{S}$ on the particles in a linear ambient flow, which is customarily broken into uniform velocities/angular velocities $\mathbf{U}^\infty$, and a rate of strain tensor $\mathbf{E}^\infty$. Then by definition of the resistance tensor, we have the following relationship between

the aforementioned quantities

$$\begin{pmatrix} \mathbf{F} \\ \mathbf{S} \end{pmatrix} = \mathbf{R} \begin{pmatrix} \mathbf{U}^{\infty} - \mathbf{U} \\ \mathbf{E}^{\infty} \end{pmatrix} \tag{4.3}$$

where $\mathbf{U}$, refer to the velocities/angular velocities of the particles. In this work, we will use a modified version of the algorithm presented by Ball & Melrose (1997). In our algorithm, which will be presented in detail in chapter (6), we express the resistance tensor as

$$\mathbf{R} = \mathbf{R}_0 + \mathbf{R}_{\delta} \tag{4.4}$$

where $\mathbf{R}_0$ is an additional term added to the $\mathbf{R}_{\delta}$ term in (Ball & Melrose, 1997). $\mathbf{R}_0$ is a diagonal tensor representing an isotropic resistance, which in some ways is a simplification of the many-body hydrodynamic resistance commonly used in Stokesian dynamics method (Bossis & Brady, 1984). In our method, the isotropic resistance depends only on the volume fraction and is obtained by matching the short-time self-diffusivity D_s^s of a hard-sphere suspension with that from Stokesian dynamics technique. These isotropic resistances for various couplings $F-U$, $T-\Omega$, and $S-E$ have been fitted to a second order polynomial in ϕ, and are given by the following equation

$$\begin{aligned} R_0^{FU} &= 1 + 2.725\phi - 6.583\phi^2 \\ R_0^{T\Omega} &= 1 + 0.749\phi - 2.469\phi^2 \\ R_0^{SE} &= 1 + 3.643\phi - 6.951\phi^2 \end{aligned} \tag{4.5}$$

4.2.2.1 Dicolloidal Particles

In this section, we develop Fast Lubrication Dynamics for dicolloidal particles. A generic dicolloidal particle has been shown in figure (4.1). For simplicity, we have used the same value of $\mathbf{R}_0$ tensor as in the case of spheres. For particles with small degree of anisotropy this is a fair assumption, though a small error can be expected at larger degree of anisotropy. Note that the largest aspect ratio investigated in this work was approximately 1.5. Next,

we outline the computation of the lubrication interaction for these dicolloidal particles. As noted earlier, these dicolloidal particles are made of spherical components. A lubrication interaction between two particles can, therefore, be modeled as a sum of one, or more interactions between spherical components as shown in Fig (4.2). Note that in the limit of very small gap, the asymptotic analysis will give the same result as for spherical particles for most relative positions and orientations. So, this technique will model the important asymptotic limit correctly for most cases. Now our goal is to find $\mathbf{F}$, $\mathbf{T}$ and $\mathbf{S}$ on the particle given $\mathbf{U}^\infty - \mathbf{U}$, $\boldsymbol{\Omega}^\infty - \boldsymbol{\omega}$, and $\mathbf{E}^\infty$ about the center of the dicolloidal particle. For this a two step procedure is employed. First $\mathbf{U}^\infty - \mathbf{U}$, $\boldsymbol{\Omega}^\infty - \boldsymbol{\omega}$, and $\mathbf{E}^\infty$ about the center of the particle is transformed to $\mathbf{U}_{sp}$, $\boldsymbol{\Omega}_{sp}$, and $\mathbf{E}_{sp}$ about the center of the spherical component. These can be obtained using the following equations

$$\begin{aligned} \mathbf{U}_{sp} &= (\mathbf{U}^\infty - \mathbf{U}) + (\boldsymbol{\Omega}^\infty - \boldsymbol{\omega}) \times (\mathbf{x}_{sp} - \mathbf{x}_c) + \mathbf{E}^\infty(\mathbf{x}_{sp} - \mathbf{x}_c) \\ \boldsymbol{\Omega}_{sp} &= (\boldsymbol{\Omega}^\infty - \omega) \\ \mathbf{E}_{sp} &= \mathbf{E}^\infty \end{aligned} \tag{4.6}$$

Next, the lubrication interaction between the spherical components is found as usual, using velocities found above, and using $\mathbf{R}_\delta$ for a spherical pair, to obtain $\mathbf{F}_{sp}$, $\mathbf{T}_{sp}$ and $\mathbf{S}_{sp}$. Note that these moments are about the center of the spherical components, and need to be transformed back to the center of the particles to obtain $\mathbf{F}$, $\mathbf{T}$ and $\mathbf{S}$ as follows

$$\begin{aligned} \mathbf{F} &= \mathbf{F}_{sp} \\ \mathbf{T} &= \mathbf{T}_{sp} + (\mathbf{x}_c - \mathbf{x}_{sp}) \times \mathbf{F}_{sp} \\ \mathbf{S} &= \mathbf{S}_{sp} + [(\mathbf{x}_c - \mathbf{x}_{sp})\mathbf{F}_{sp} + \mathbf{F}_{sp}(\mathbf{x}_c - \mathbf{x}_{sp})]/2 \end{aligned} \tag{4.7}$$

Note in the equations above, subscript '*sp*' and '*c*' stands for the center of the spherical node and the center of the particle respectively.

4.2.2.2 Lubrication Pairs

As discussed in the previous section, we find lubrication interaction between two particles by considering the interaction between spherical node pairs formed between the two particles.

So, a pair of dicolloidal particles can form up to four spherical node pairs. In our algorithm, we don't necessarily consider all four pairs. This depends on the cutoff separation, and what we call the inter-visibility. By having inter-visibility, we mean that a spherical node sees the surface of the other spherical node. More precisely, if the line joining the centers of the two spherical nodes passes through each of their surfaces, then that pair is considered for interaction, provided that the separation is less than the cutoff separation. This prevents double counting which would have happened otherwise. Similar procedures have been used in the past for finding interparticle potential between patchy particles (see, e.g., Kern & Frenkel (2003)).

4.3 Brownian Force

Brownian force and torque can be found using the fluctuation-dissipation theorem and the equipartition of energy (Russel *et al.*, 1989), the application of which gives the following relationships

$$< \mathbf{F}^B >= \mathbf{0} \tag{4.8}$$

$$< \mathbf{F}^B \mathbf{F}^B >= \frac{2kT\mathbf{R}_{FU}}{\Delta t} \tag{4.9}$$

where $\mathbf{F}^B$ is the generalized force/torque vector due to the Brownian motion. The above equations can be satisfied using random numbers with special properties. Basically, we write $\mathbf{F}^B$ as

$$\mathbf{F}^B = \sqrt{\frac{2kT}{\Delta t}}[\mathbf{A}\psi + \mathbf{B}\phi] \tag{4.10}$$

where ψ, and ϕ are vectors, whose elements are random numbers (say γ_i) satisfying the following two properties

$$\begin{aligned} < \gamma_i >= 0 \\ < \gamma_i \gamma_j >= \delta_{ij} \end{aligned} \tag{4.11}$$

With the random numbers satisfying the above properties, we only need to satisfy the

following two equations to obtain the agreement of eq (4.10) with eq (4.8), and eq (4.9)

$$\begin{aligned} \mathbf{A}\mathbf{A}^T &= \mathbf{R}_0^{FU} \\ \mathbf{B}\mathbf{B}^T &= \mathbf{R}_\delta^{FU} \end{aligned} \tag{4.12}$$

So, in essence we need to find the square root of the above two matrices on the right. We refer the reader to chapter (6) for details on computing the generalized Brownian force.

4.4 Interparticle Interaction

The interparticle force considered in this work for all suspensions at a volume fraction of $\phi = 0.42$ is the electrostatic repulsion between charged particles. The suspending medium, due to the presence of electrolytes, complicates the governing equation. In fact, no analytical solution exists even for a pair of spherical particles (Russel *et al.*, 1989). Hence various approximations are used to arrive at a solution. The approximation used in this work is the linear superposition approximation, which works well in the case of thin double layers, i.e. $\kappa a \gg 1$, where κ^{-1} is called the Debye screening length (eq. 4.14), and a is the radius of the particle. Under this approximation, interparticle potential and corresponding repulsive force is given by (Bell *et al.*, 1970)

$$\begin{aligned} U^P &= \epsilon V_1 V_2 \left(\frac{a_1 a_2}{R}\right) e^{-\kappa(R-a_1-a_2)} \\ F^P &= \epsilon V_1 V_2 (1+\kappa R) \left(\frac{a_1 a_2}{R^2}\right) e^{-\kappa(R-a_1-a_2)} \end{aligned} \tag{4.13}$$

where $\epsilon = \epsilon_0 \epsilon_r$ is the dielectric constant, V_1 and V_2 are the surface potential of the two spherical particles, R is the separation between the centers, while a_1 and a_2 are the radii of the two particles. κ^{-1} is the Debye screening length given by

$$\kappa^{-1} = \sqrt{\frac{\epsilon k T}{2 N_A e^2 I}} \tag{4.14}$$

where e is the electronic charge, N_A is the Avogadro constant, and I is the ionic strength

given by ($\frac{mol}{m^3}$ in SI units)

$$I = \frac{1}{2}\sum_{k=1}^{k=N} c_k z_k^2 \tag{4.15}$$

where c_k and z_k is the concentration and charge number respectively of the ionic species k in the electrolyte.

For simplicity we will write the repulsive force in eq. (4.13) as

$$F^P = F_0(1+\kappa R)\left(\frac{a_1 a_2}{R^2}\right) e^{-\kappa(R-a_1-a_2)} \tag{4.16}$$

For non-spherical dicolloidal particles, we use pairwise sums over spherical node pairs, each of which uses the result for a pair of spherical particles. Again, the concept of inter-visibility and cutoff distance is used to turn the interaction on or off for a spherical node pair. Note that these forces are about the center of the spherical node, $\mathbf{F}_{sp}$, which should be transformed to the $\mathbf{F}$, $\mathbf{T}$, and $\mathbf{S}$, which is about the center of the particle. This is done just as in the case of lubrication interaction, which is already discussed.

4.5 Iterative Methods and Time Stepping

As noted in section (4.2.1), the net force and torque on a particle should be zero at any instant as given by eq (4.2). So, with known particle positions and orientations, along with the known ambient velocity field, one can solve for the generalized velocities $\mathbf{U}$ of the particles from the following equation

$$\mathbf{R}_{FU}(\mathbf{U}^\infty - U) = -(\mathbf{F}^P + \mathbf{F}^B) - \mathbf{R}_{FE}\mathbf{E}^\infty \tag{4.17}$$

which is the same as eq (4.2) with $\mathbf{F}^H$ replaced by its value in terms of the resistance tensor. Also $\mathbf{F}^P$ and $\mathbf{F}^B$ are assumed to be known as they depend only on the known particle configuration. Equation (4.17) can be solved by inverting $\mathbf{R}_{FU}$, but direct inversion is computationally expensive both in terms of CPU and memory requirements. So, instead of inverting $\mathbf{R}_{FU}$, we make use of an iterative technique to find the solution. Since $\mathbf{R}_{FU}$

is symmetric positive definite, we use conjugate gradient iterative technique (Saad, 2003) which works efficiently both in terms of memory usage and computation time. The solution of eq (4.17) gives the velocity and angular velocity of each particle, which is used to find the new particle positions and orientations. For time stepping, we use 2^{nd} order midpoint method at low shear rates ($Pe < 10$) and 3^{rd} order Runge-Kutta method at higher shear rates ($Pe \geq 10$) for evolving both the position and orientation.

4.6 Artificial Repulsive Force

During time stepping, due to integration errors, small gaps or overlaps between particles can occur. To overcome this, we make use of an artificial repulsive force whenever the gap becomes smaller than a specified minimum gap δ_{min}. The following form was used for the artificial repulsive force

$$F^P = \begin{cases} C^P(\frac{\delta_{min}}{\delta})(\eta - \frac{1}{2}\eta^2) & \text{if } \delta < \delta_{min} \\ 0 & \text{if } \delta > \delta_{min} \end{cases} \tag{4.18}$$

where δ is the gap between two spheres, $\eta = 1 - \delta/\delta_{min}$, $\mathbf{d}$ is the unit vector pointing from one sphere to the other, and C^P is a constant. We have used $\delta_{min} = 10^{-3}$ in our simulations. We also used a numerical minimum gap, $\delta_{num} = 10^{-2}\delta_{min}$, to cap off any gaps smaller than it. This prevents extremely strong repulsive force due to small gaps, and also provides a meaningful gap for overlapping particles that can be used in computing the artificial repulsive force. In this work, the artificial repulsive force was used only in suspensions of (near) hard-spheres or (near) hard-dicolloids at a volume fraction of $\phi = 0.55$.

4.7 Simulation Parameters

In this section, we discuss some of important parameters in our simulation. These include shear rate, volume fraction, repulsive force parameters, system size, and particle shape among others. Perhaps the most important among these is the rate of shear, which is represented

in our simulations by the non-dimensional Peclet number (Pe). Pe is defined as

$$Pe = \frac{\dot{\gamma} a^2}{D_0} \tag{4.19}$$

where $\dot{\gamma}$ is the rate of shear, a is the radius of the sphere, and $D_0 = kT/6\pi\mu a$ is the diffusivity of an isolated particle. In case of dicolloids, for simplicity, we have defined $D_0 = kT/6\pi\mu a$, where a is the radius of the constituent sphere. As should be clear from the above equation, Pe represents the ratio of convective mass transport to diffusive mass transport. In this work, the effect of Pe was investigated over a large range $0 \leq Pe \leq 100$.

Volume fraction, ϕ, is another important parameter in our simulations. All of our simulations were done at either a volume fraction of 42%, or at a volume fraction of 55%. Suspensions at the volume fraction of 42% were charge stabilized, such that the repulsive force can be modeled by equation (4.16). The repulsive force has two variable parameters in its definition, the strength of interaction F_0 and the range of interaction κ^{-1}. Suspensions at a volume fraction of 55% had a hard-sphere type interaction and a repulsive force was used only when the gap between a pair of particles fell below $\delta_{min} < 10^{-3}$ as was discussed in section (4.6).

System size is another important parameter in our simulations. The systems in our simulation were 3-dimensional with periodic boundaries. An appropriate measure of the system size in our simulations is the number of particles in a periodic box. Most of our simulations were done with 1000 particles, but some simulations were also performed with 8000 particles. Larger is the system size, more realistic will be the prediction. System size is essentially limited by the computational cost.

Particle shape constitutes another important parameter in this work. The class of particles studied in this work can be modeled by two fused spheres of varying radii and center to center separation. This kind of particles have been named as dicolloidal particles in the literature (Mock & Zukoski, 2007). In this work, we have studied three different particle shapes: sphere, homonuclear, and fused-dumbbell. The shape parameters for these particles are given in table (4.2). Note that the shape of these dicolloidal particles are completely specified by two parameters, b/a, and c/a (figure 4.1).

4.8 Results

4.8.1 Microstructural Transitions in Spherical Suspensions with Shear Rate

4.8.1.1 Charged Spherical Suspension at a Volume Fraction of 42%

At a volume fraction of 42%, a hard sphere suspension is expected to be disordered at rest. For charge stabilized suspensions, order can be obtained at an appropriate strength of repulsive interaction. Note the repulsive force contains two parameters: strength F_0 and range κ^{-1} (eq 4.16). To obtain order, we kept the range (κ^{-1}) fixed at $0.092a$, while the strength of interaction (F_0) was varied. The effect of this on the microstructure is shown in Fig (4.3), which shows the pair distribution function in the front view. $F_0/8\pi\mu D_0 = 15$ is estimated to be the minimum strength of repulsion required at this screening length to obtain order at rest. We performed all simulations, both at rest and under shear, at this strength of interaction. We report the microstructure in suspensions of spheres at this strength of interaction below. All simulations at non-zero shear rate were started with the ordered microstructure at rest.

Static microstructure ($Pe = 0$): Suspensions are normally presheared to speed up the crystallization process. Shearing orients the close packed planes in the flow-vorticity plane, with one of its close-packed directions parallel to the flow (Ackerson, 1990). At high rates of shear there is little registration between different layers, but on the cessation of shear, the layers try to relax to the minimum energy state, thereby registering themselves along the gradient direction. The registration process is usually slow and is found to increase with time (Versmold *et al.*, 2000). Thus, under normal experimental time frames randomly registered layers are usually observed. This is particularly true when there are no long range interactions in the system, which serves as a driving force to attain a particular stacking sequence (Loose & Ackerson, 1994). Similar behavior was observed in our simulations. Pair distribution functions for the microstructure are shown in Fig(4.4), (4.5), and (4.6), which are in the front, top and end view respectively. The reader is referred to chapter (B.2) for details on computing the pair distribution function. Hexagonally close packed planes can

be seen in the top view pair distribution function at $Pe = 0$. Front, top, and end view pair distribution functions in conjunction proves the 3-dimensional (crystalline) ordering, as distinct maxima spots can be seen in each of these. Investigating the structure factor is also useful as many previous research efforts have established the relationship between microstructure and structure factor (Ackerson, 1990), (Chen *et al.*, 1992), (Chow & Zukoski, 1995), (Loose & Ackerson, 1994). Structure factors from our simulations are reported in Fig (4.7), which at rest shows six-fold maxima in the primary ring indicating a 3-dimensional close packed ordering. Information on the exact stacking sequence can be obtained from the modulation in intensity along k_y for any of these peaks (tubes). Modulation in intensity for $q_1(k_y)$ is shown in Fig(4.8), where $q_1(k_y)$ has been defined in appendix B.3.2. At rest a broad maxima around 0.61 can be seen which indicates a random stacking.

Low shear rates ($Pe = 0.01$): At low rates of shear, the suspension maintains a 3-dimensional ordering. This can be seen in the front, top and end view pair distribution functions (Fig 4.4, 4.5, 4.6), each of which show distinct maxima spots. Particles shear by hopping from one close packed site to its twin (Ackerson, 1990). For example, a sequence of two layers stacked as AB could undergo a transition to AC, where A,B, and C refer to close packed sites (Fig B.1). Such a microstructure is usually characterized as strained crystals.

Intermediate rates of shear ($0.1 \leq Pe \leq 1$): At these shear rates, the system showed very sluggish behavior. We found that a simulation started with an ordered initial state, maintained its order even after hundreds of strains. The same was true for a simulation started with a disordered initial state. This can be attributed to the energy barrier to the creation of an interface between ordered and disordered regions (Stevens & Robbins, 1993). We have already discussed this behavior in detail in chapter (5). In this chapter, we will restrict our focus to the ordered phase only. The ordering in this regime was found to be in the form of a 2-dimensional (liquid crystalline) sliding layer microstructure. A layer still retains its hexagonally close packed structure as can be seen in the top view pair distribution function (Fig 4.5), though there is negligible correlation between different layers. Loss of correlation between different layers is clearly seen in the front view where distinct peaks at equilibrium give way to horizontal bands (Fig 4.4). In the end view, where each horizontal row corresponds to a layer, a centering of layers is evident as a string of particles in a given

layer is located midway between two strings of particles in its two neighboring layers (Fig 4.6). The loss of intensity in the top and the bottom peaks in the structure factor is also consistent with this sliding layer microstructure (Ackerson (1990)).

High Shear rates ($10 \leq Pe \leq 20$): Upon further increase in shear rate, the sliding layer structure transitions to a string like structure. At these shear rates, there is little correlation between different strings in a given layer as could be seen in the top view PDF (Fig 4.5), and hence is appropriately characterized as strings. The structure factor (Fig 4.7) shows much broader vertical bands which indicates a progression towards a string like microstructure.

Very high shear rates ($Pe \geq 50$): With further increase in shear rate, a completely disordered state was observed (Fig 4.4, 4.5, 4.6). At high shear rates, the strength of repulsive interaction should be scaled with the shear rate. Consequently as the shear rate increases, the effective strength decreases which leads to this order to disorder transition.

4.8.1.2 Hard Sphere Suspensions at a Volume Fraction of 55%

A hard sphere suspension at a volume fraction of 55% is known to order in a FCC lattice at rest. Our results are consistent with that behavior. Front, top, and end view pair distribution functions (Fig 4.9, 4.10, 4.11) with distinct maxima spots prove the crystalline ordering at rest. A similar conclusion could be reached from the structure factor (not shown here). The stacking sequence remains random as revealed by the modulation in $q_1(k_y)$ (Fig 4.8), which shows a broad maxima around 0.61. As the suspension is sheared it goes through the same series of transitions as was reported above for suspensions of charged stabilized suspensions at $\phi = 0.42$. Briefly, we observe the strained crystal microstructure at $Pe = 0.01$, sliding layer structure for Pe in the range $0.1 \leq Pe \leq 1$ and string like microstructure for $Pe > 10$. Of course, all transitions are gradual. No disordering transition (shear melting) was observed with increasing shear rate at this volume fraction. This is consistent with the result of Stokesian Dynamics simulation for non-Brownian (near) hard-sphere suspensions at $\phi = 0.55$ which was presented in chapter (3).

4.9 Microstructural transition in suspensions of dicolloids

In suspensions of homonuclear particles we observed a very similar series of microstructural transitions with shear rate as was presented above in the context of spheres. The pair distribution function in suspensions of homonuclear particles at a volume fraction of $\phi = 0.42$ are shown in figures (4.12), (4.13), and (4.14) in the front, top, and end views respectively. The same three pair distribution functions for homonuclear particles at a volume fraction of $\phi = 0.55$ are shown in figures (4.15), (4.16), and (4.17). Due to the similarity of the microstructural transitions in suspensions of spheres and homonuclear particles with shear rate, we refer the reader to the section above on spheres for a detailed discussion. We do note, however, that the modulation in intensity of $q_1(k_y)$ (Fig 4.8), shows a sharp peak around 0.61 in the homonuclear particle suspension at $\phi = 0.42$. This indicates that the stacking sequence at rest in this case is HCP.

In contrast to microstructure reported above in suspensions of homonuclear particles, microstructure in suspensions of fused-dumbbells were found to be disordered at all shear rates at both the volume fractions ($\phi = 0.42$ and $\phi = 0.55$). The pair distribution functions in suspensions of fused-dumbbell particles at a volume fraction of $\phi = 0.42$ are shown in figures (4.12), (4.13), and (4.14) in the front, top, and end views respectively, while the same three pair distribution functions at a volume fraction of $\phi = 0.55$ are shown in figures (4.15), (4.16), and (4.17). It's obvious from these pair distribution functions that the microstructure is disordered at all shear rates. This behavior is not entirely surprising as previous research has shown that, in hard-dicolloids, the volume fraction required to undergo a disorder to order transition at equilibrium is higher for a fused-dumbbell particle suspension than for a suspension of spheres or homonuclear particles (Vega *et al.*, 1992a). To summarize their result, the freezing and melting transitions in suspensions of homonuclear dicolloids were found to occur at approximately $\phi = 0.4945$ and $\phi = 0.543$ respectively, while in suspensions of fused-dumbbell dicolloids the same two transitions were found to occur at approximately $\phi = 0.6013$ and $\phi = 0.6463$. In suspensions of hard-spheres, the well known result for these two transitions are $\phi = 0.494$ (freezing) and $\phi = 0.545$ (melting). Moreover, at the freezing transition, the ordered phase in homonuclear suspensions is orientationally

disordered, while it is orientationally ordered in fused-dumbbell particle suspensions. Under shear, the inherent rotational motion present in such flows will cause the particle to rotate which may prove further disruptive to the formation of positional ordering. Note that the above argument is made with respect to the aspect ratios under consideration here and not with respect to, e.g., large aspect ratio fibers which can give a very high degree of flow alignment under shear, thereby promoting a nematic like ordering.

4.10 Orientation Behavior

To characterize the orientational distribution, we would make use of distribution into Jeffrey's orbit and orientational order parameter. These have been defined earlier in chapter (3). We would only summarize the key points here. For an arbitrary axisymmetric body of effective aspect ratio r_e, in the absence of non-hydrodynamic effects, the evolution of the orientational angles (φ, θ) in shear flow with time t is described by (see Fig. 4.24 for notation)

$$\tan\varphi = r_e \tan\left(\frac{\dot{\gamma}t}{r_e + 1/r_e} + \kappa\right) \tag{4.20a}$$

$$\tan\theta = \frac{Cr_e}{\sqrt{r_e^2\cos^2\varphi + \sin^2\varphi}} \tag{4.20b}$$

where κ denotes the initial phase, while C is a parameter which is a constant in each of the Jeffery's orbits and is commonly known as the orbit constant. Two representative values of C are: $C = 0$ when the axis of symmetry is aligned with the vorticity direction (z) and $C = \infty$ when it is aligned in the shear plane $(x - y)$. In this work, we would express the orbit constant C by the scaled orbit constant C_b given by

$$C_b = \frac{C}{C+1} \tag{4.21}$$

In contrast to C, C_b has the favorable property that it lies between 0 and 1. Further, we express the probability of finding a particle in a given orbit by $p(C_b)$ with the following

normalization

$$\int_0^1 p(C_b) dC_b = 1 \tag{4.22}$$

Most of the features of the probability distribution $p(C_b)$ can be captured by the mean orbit constant C_b^m defined as

$$C_b^m = \int_0^1 C_b \; p(C_b) \; dC_b \tag{4.23}$$

In this chapter, we would present all our results in terms of C_b^m.

Next, we define the orientational order parameter S along each of the coordinate axis i as

$$S_{ii} = \frac{3}{2} n_i n_i - \frac{1}{2} \tag{4.24}$$

where n_i is the component of the director $\mathbf{n}$ in the direction i (could be $\mathbf{x}$, $\mathbf{y}$, or $\mathbf{z}$). Note that S above is really a tensor, but here we are focusing only on its diagonal components. For a random dispersion $S_{ii} = 0$, $S_{ii} = 1.0$ if the director is aligned with axis i, while $S_{ii} = -0.5$ if the director is perpendicular to the axis i.

With mean orbit constant C_b^m and orientation order parameter S defined, we now report these quantities for both homonuclear and fused-dumbbell particle suspensions at both the volume fractions ($\phi = 0.42$ and $\phi = 0.55$). Figure (4.25a) shows ΔC_b^m for homonuclear particle suspensions at $\phi = 0.42$, while figure (4.25b) shows the orientational order parameter S along each of the three coordinate axes. Note that ΔC_b^m is obtained by subtracting the mean orbit constant in the suspension with the mean orbit constant obtained by assuming an isotropic distribution (see chapter 3 for details). The mean orbit constant doesn't show any significant changes with Pe (Fig. 4.25a), though it does show slight drift towards lower orbit constants at higher shear rates ($Pe > 20$). This is consistent with the behavior observed in the non-Brownian suspensions of homonuclear particles. The orientational order parameters at low Pe is close to zero due to strong randomizing effects of Brownian rotations (Fig. 4.25b). With increasing shear rates there is an increase in S_{xx} accompanied with a comparable decrease in S_{yy}. This change is comparable to the change in orientational order parameter due to rotations into Jeffery's orbit alone. The corresponding Jeffrey's orbit orientational order parameter is tabulated in table (4.1). The orientational order parameter

at $Pe = 20$ is very close to the isolated body result. This implies that this change in orientational order parameter is attributable to the decreasing influence of the Brownian motion and also that the particle rotation is not strongly hindered at this volume fraction. At even higher shear rates ($Pe > 20$), the drift towards lower orbit constant causes an increase in S_{zz} which is accompanied with a corresponding decrease in S_{xx}.

Next, we present results for homonuclear particle suspensions at a volume fraction of $\phi = 0.55$ in figures (4.26a) and (4.26b) which respectively show ΔC_b^m and S_{ii}. The low Pe behavior is similar to the $\phi = 0.42$ suspension and doesn't warrant further discussion. As the shear rate is increased, though, there is a dramatic shift to higher orbit constant and shows an apparent maxima at $Pe = 20$. Note that this transition in orientational ordering is accompanied by the positional ordering to a string like microstructure. It seems that the constrained motion in the string like structure is promoting this increased alignment of the particle in the flow-gradient plane. At higher shear rates, a drift towards lower orbit constant is observed which is consistent with the behavior shown by non-Brownian suspensions of the same particles (chapter 3). The orientational order parameter is consistent with the analysis presented above. In particular, increase in S_{xx} and S_{yy} around $Pe = 20$ is consistent with the increase in the mean orbit constant, while at higher shear rates an increase in S_{zz} is consistent with the drift towards lower orbit constants. We also briefly note that the maxima in S_{xx} in figure (4.26b) at $Pe = 20$ is much larger than S_{xx} in Jeffrey's orbit (table 4.1).

For fused-dumbbell particle suspensions at $\phi = 0.42$, we present ΔC_b^m in figure (4.27a) and S_{ii} in figure (4.27b). At low Pe, again, we see that ΔC_b^m and S_{ii} are all close to zero, which can be attributed to strong Brownian effects. As the shear rate is further increased, there is first a small drift towards higher orbit constants around $Pe = 1$ which is then followed by a small drift towards lower orbit constants. The orientational order parameter along the x axis shows an increase with increasing shear rate and shows a maxima around $Pe = 1$, with this value being comparable to that observed for an isolated particle in Jeffery's orbit (table 4.1). Therefore, it seems likely that this increased flow alignment is due to rotations in Jeffery's orbit combined with the decreasing influence of Brownian rotations. At high shear rates, there is a slight decrease in S_{xx} accompanied by an equivalent increase in S_{yy}, which either implies that the particles are flipping more often or that the particles are spending

more time at orientations with higher projection along the gradient direction. The latter seems more likely. Lastly, we report the orientation in suspensions of fused-dumbbells at a volume fraction of $\phi = 0.55$. Figure (4.28a) shows ΔC_b^m with Pe in such suspensions, while figure (4.28b) shows the orientational order parameter S along each of the three coordinate axes for the same. In this case too, the trend in both ΔC_b^m and S_{ii} are nearly the same as above for suspensions of fused-dumbbell particles at $\phi = 0.42$. We note that in both the $\phi = 0.42$ and $\phi = 0.55$ suspension the orientational order parameter along the vorticity axis S_{zz} at high shear rates is nearly zero which is similar to that observed in non-Brownian suspensions (chapter 3), though the orientational order parameter S_{xx} is smaller here than in those simulations (or S_{yy} is larger here).

4.11 Conclusions

We investigated the microstructure and orientation in Brownian suspensions of spheres and dicolloids using Fast Lubrication Dynamics. Two different dicolloids were studied in this work: homonuclear and fused-dumbbell. Results were presented for two different volume fractions: $\phi = 0.42$ and $\phi = 0.55$. The $\phi = 0.42$ suspension was charge stabilized while the $\phi = 0.55$ suspension had a very short range repulsive interaction. In simulations on spheres, we observed a series of microstructural transitions commonly reported in the experimental literature. These transitions led to the following microstructures with increasing rate of shear: hexagonal close packed structure, strained crystals, sliding layers, strings, and amorphous structure. A high shear rate amorphous state was only observed only in the $\phi = 0.42$ suspension. In suspensions of homonuclear particles, which has mild degree of anisotropy, microstructural transitions similar to that of spheres were observed. In fused-dumbbell particle suspensions, which a relatively larger degree of anisotropy, a disordered microstructure was observed at all shear rates. Suspensions of all particle shapes showed nearly an isotropic orientation distribution at low shear rates. As the shear rate was increased, an increase in flow alignment was observed, while with further increase in the rate of shear an increase in vorticity alignment was observed. The degree of increase in flow or vorticity alignment was found to be a strong function of the degree of anisotropy as well as the volume fraction.

Possible mechanisms for the observed orientation behavior were presented.

Table 4.1: Effective aspect ratio r_e obtained from Jeffery's orbit time period, orientational order parameter S_{ii} along the three coordinate axis at infinite dilution, and intrinsic viscosity for all particle shapes.

Particle	r_e	S_{xx}	S_{yy}	S_{zz}	$[\mu]$
Homonuclear	1.0868	0.0280	-0.0274	-0.0008	2.4977
Fused-dumbbell	1.5075	0.1291	-0.1151	-0.0143	2.5378

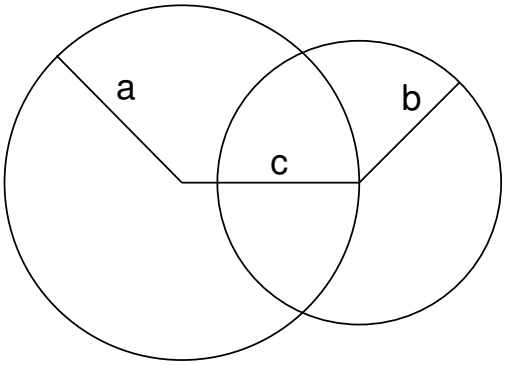

Figure 4.1: Shape of generic dicolloidal particle. Two dimensionless parameter b/a and c/a completely defines the particles

Table 4.2: Particle shape parameters b/a and c/a for all particles

Illustration	Name	b/a	c/a
	Sphere	1.0	0.0
	Homonuclear	1.0	0.2
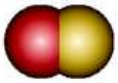	Fused-Dumbbell	1.0	1.0

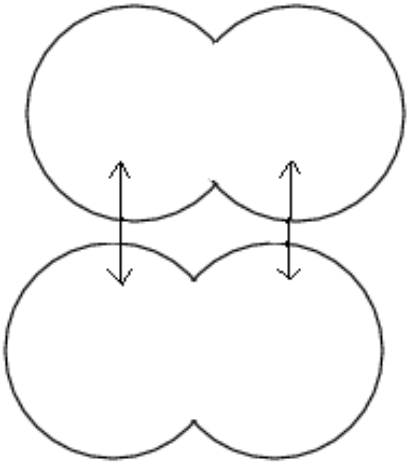

Figure 4.2: Figure showing multiple contacts between a pair of dicolloidal particles

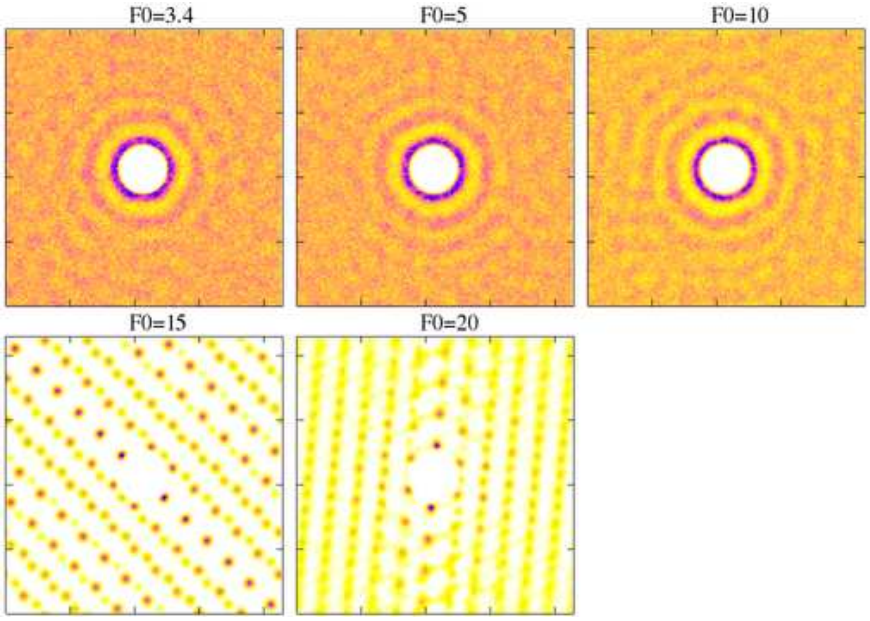

Figure 4.3: Front view pair distribution at Pe = 0 for different strengths of repulsive interactions. This is for a $\phi = 42\%$ spherical suspension which wasn't presheared. Actual F_0 in eq (4.16) is non-dimensionalized by $8\pi\mu D_0$. Non-dimensionalized F_0 is presented in this figure.

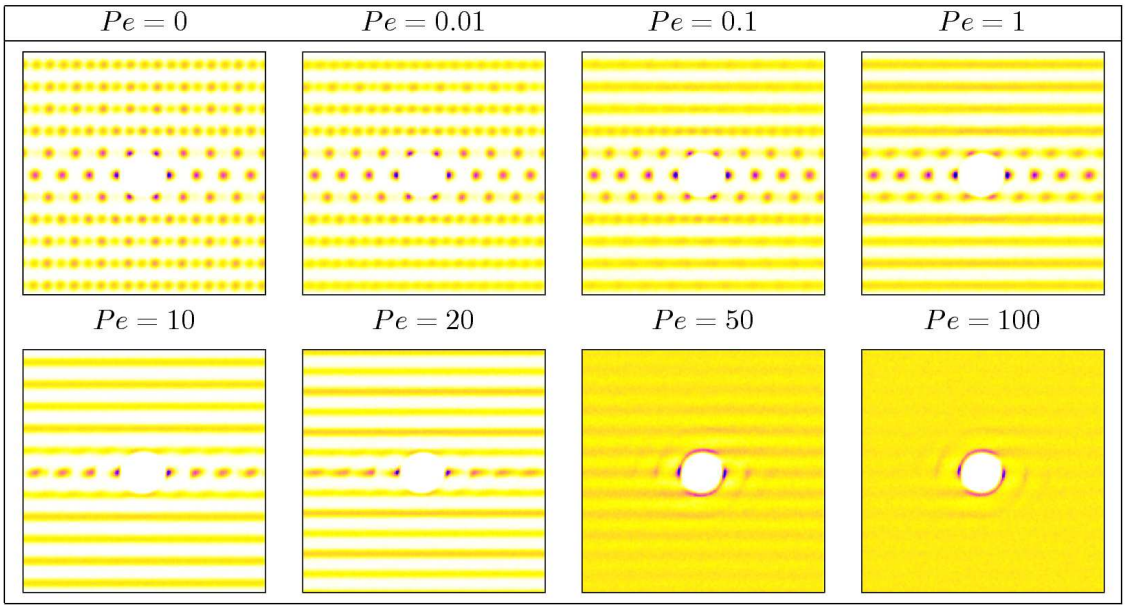

Figure 4.4: Front view pair distribution functions in suspensions of spherical particles at $\phi = 0.42$ as a function of Pe.

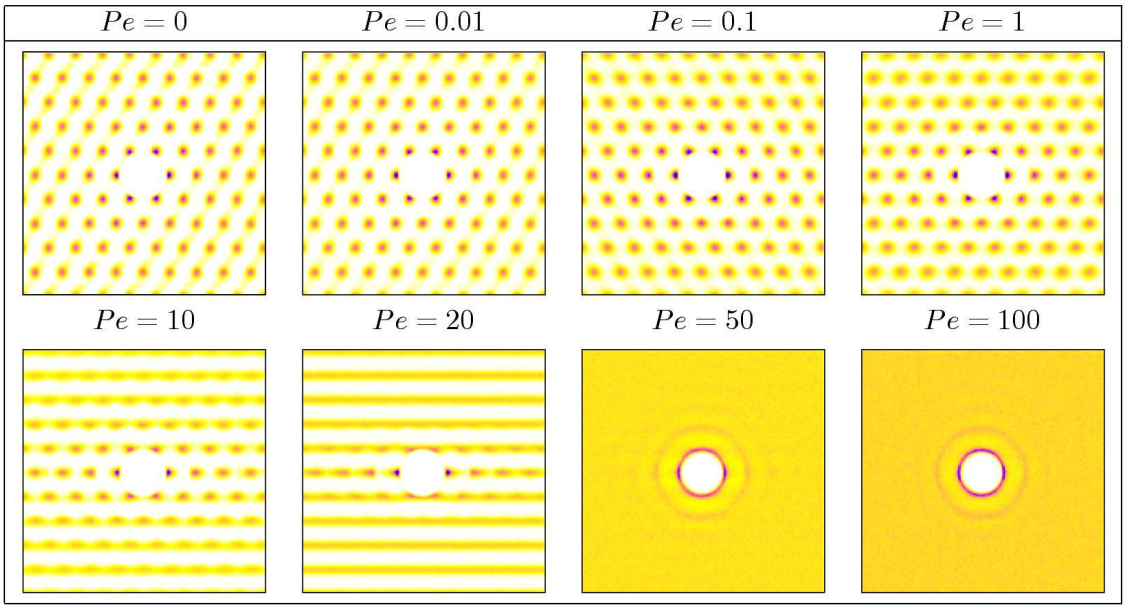

Figure 4.5: Top view pair distribution function in a suspension of spherical particles at $\phi = 0.42$ as a function of Pe.

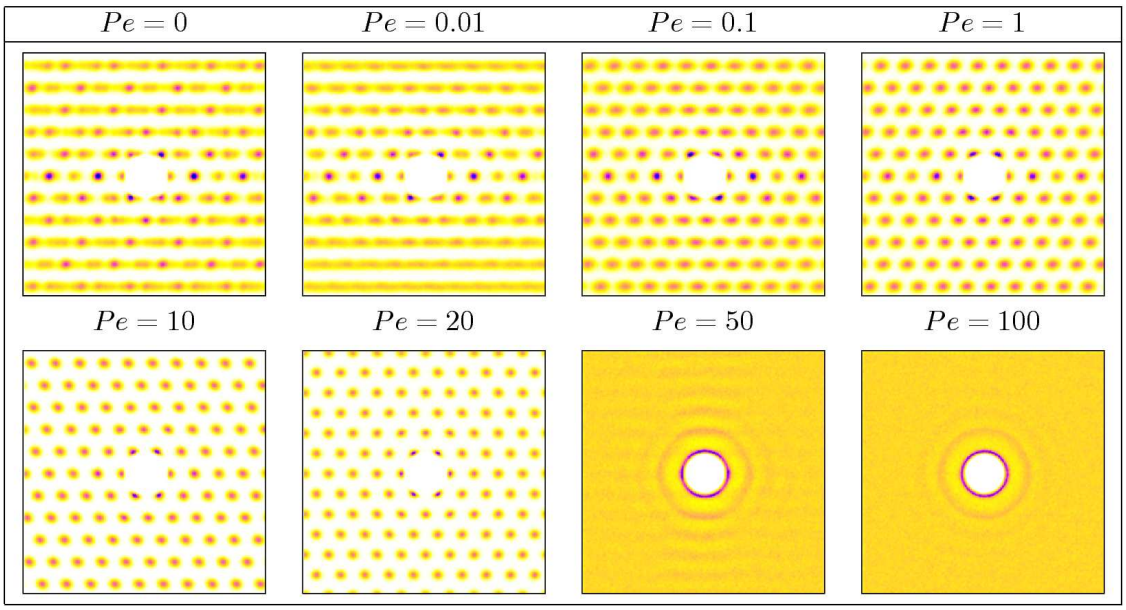

Figure 4.6: End view pair distribution function in a suspension of spherical particles at $\phi = 0.42$ as a function of Pe.

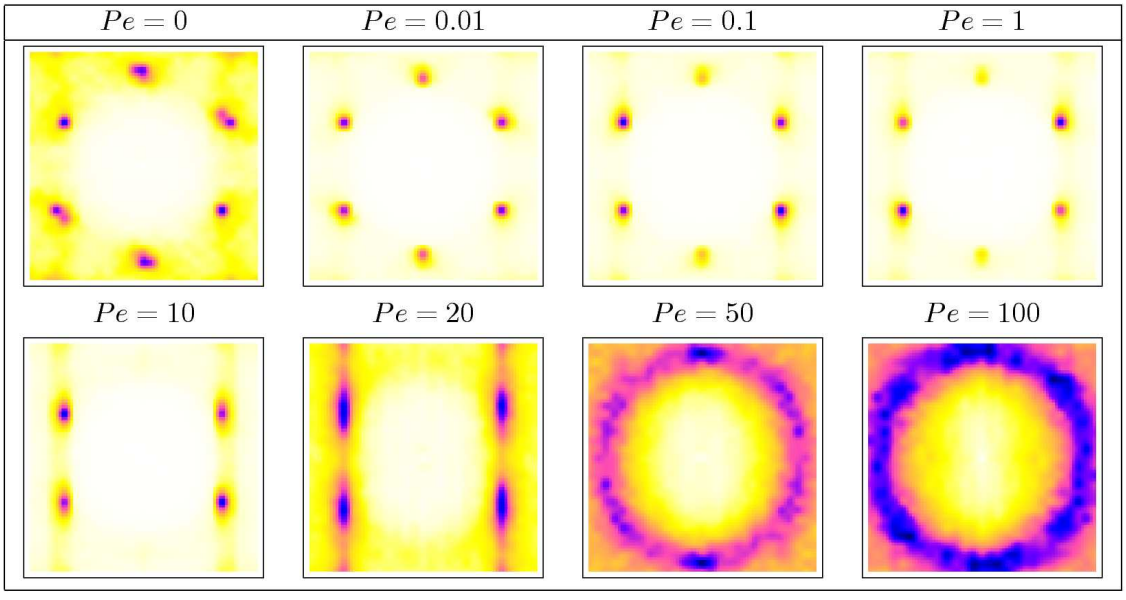

Figure 4.7: Top view structure function in a suspension of spherical particles at $\phi = 0.42$ as a function of Pe.

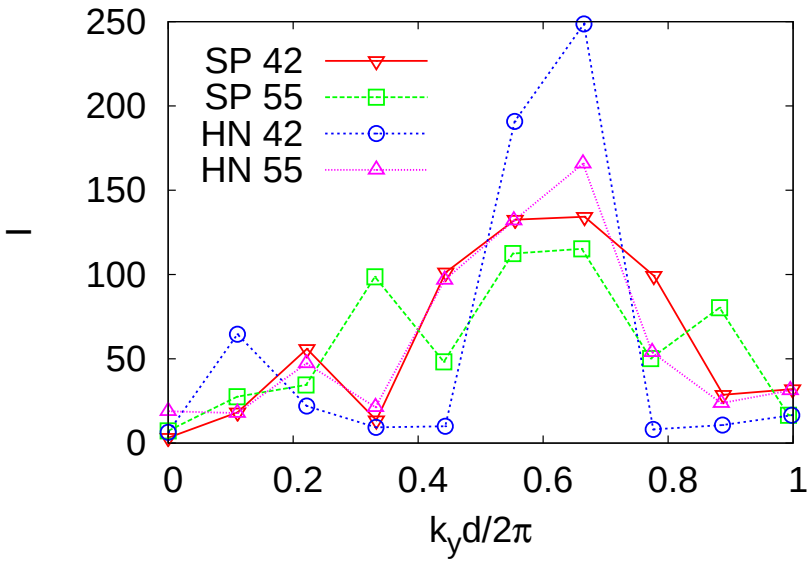

Figure 4.8: Modulation in intensity along k_y with Pe for q_1. In the figure, SP 42 refers to a suspension of spheres at $\phi = 0.42$, SP 55 refers to a suspension of spheres at $\phi = 0.55$, HN 42 refers to a suspension of homonuclear particles at $\phi = 0.42$, and HN 55 refers to a suspension of homonuclear particles at $\phi = 0.55$.

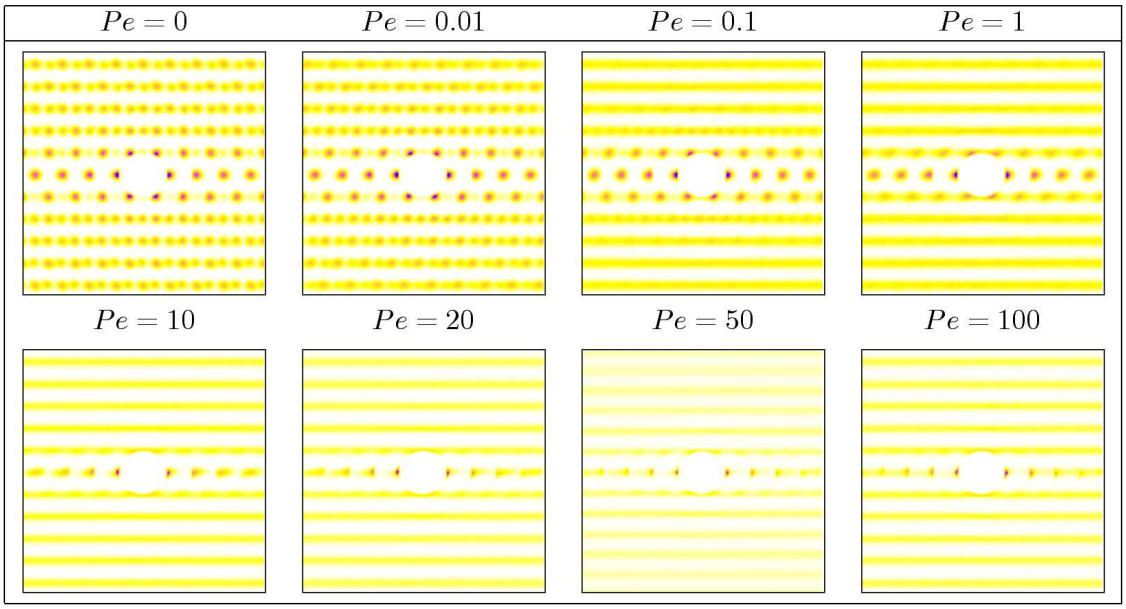

Figure 4.9: Front view pair distribution function in a suspension of spherical particles at $\phi = 0.55$ as a function of Pe.

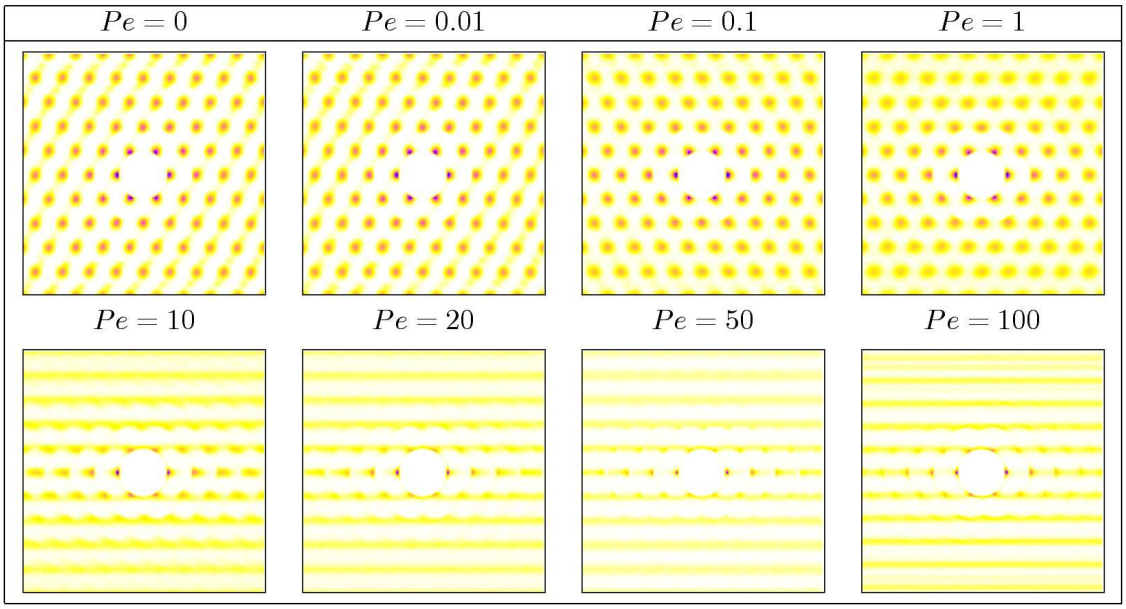

Figure 4.10: Top view pair distribution function in a suspension of spherical particles at $\phi = 0.55$ as a function of Pe.

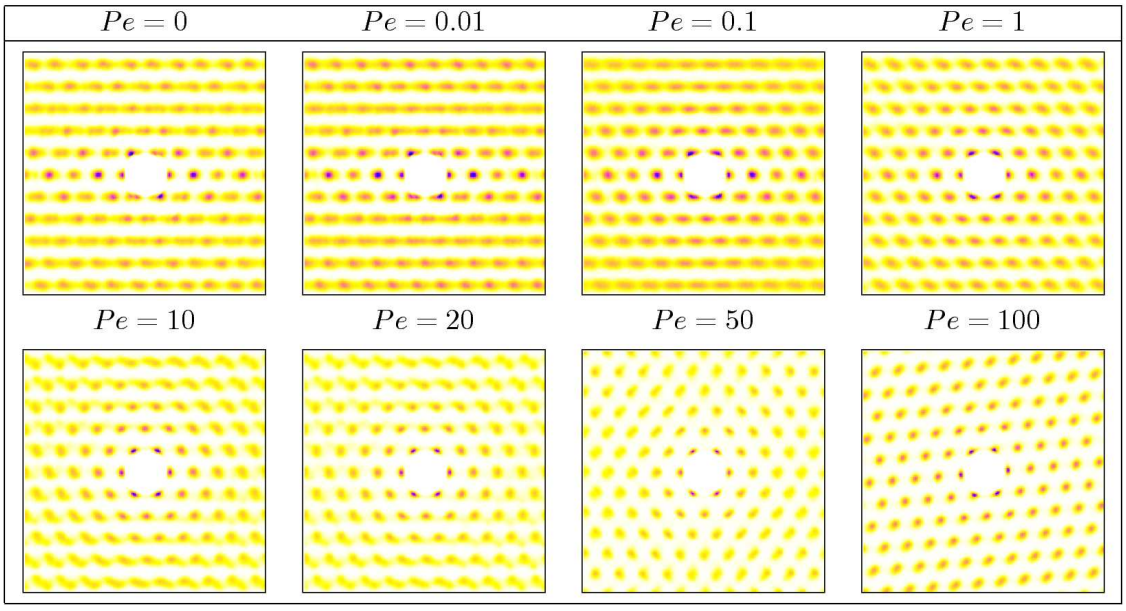

Figure 4.11: End view pair distribution function in a suspension of spherical particles at $\phi = 0.55$ as a function of Pe.

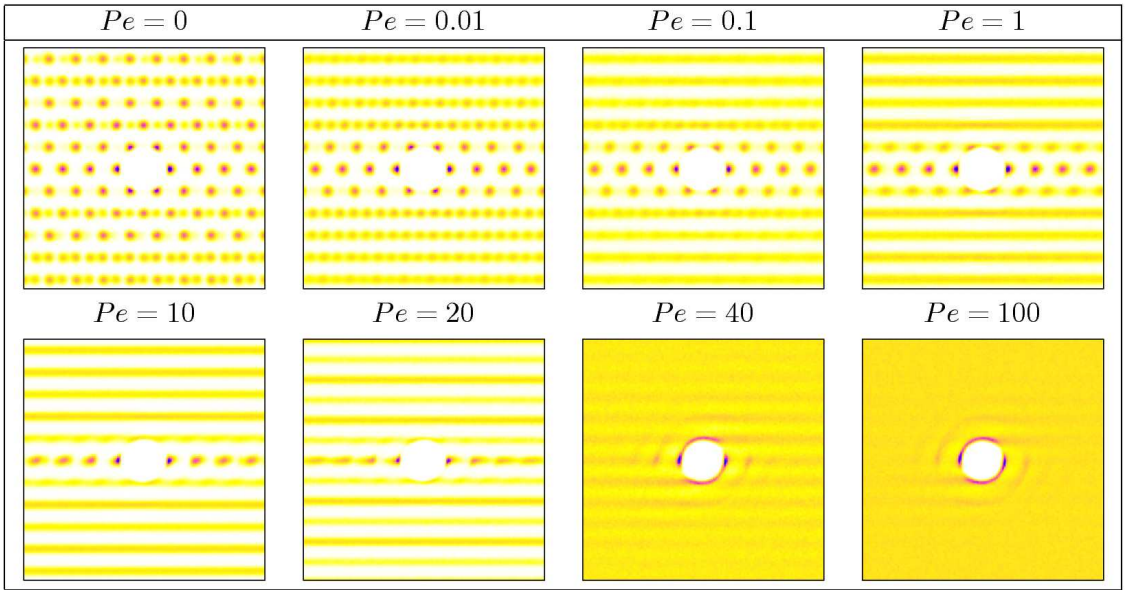

Figure 4.12: Front view pair distribution functions in suspensions of homonuclear particles at $\phi = 0.42$ as a function of Pe.

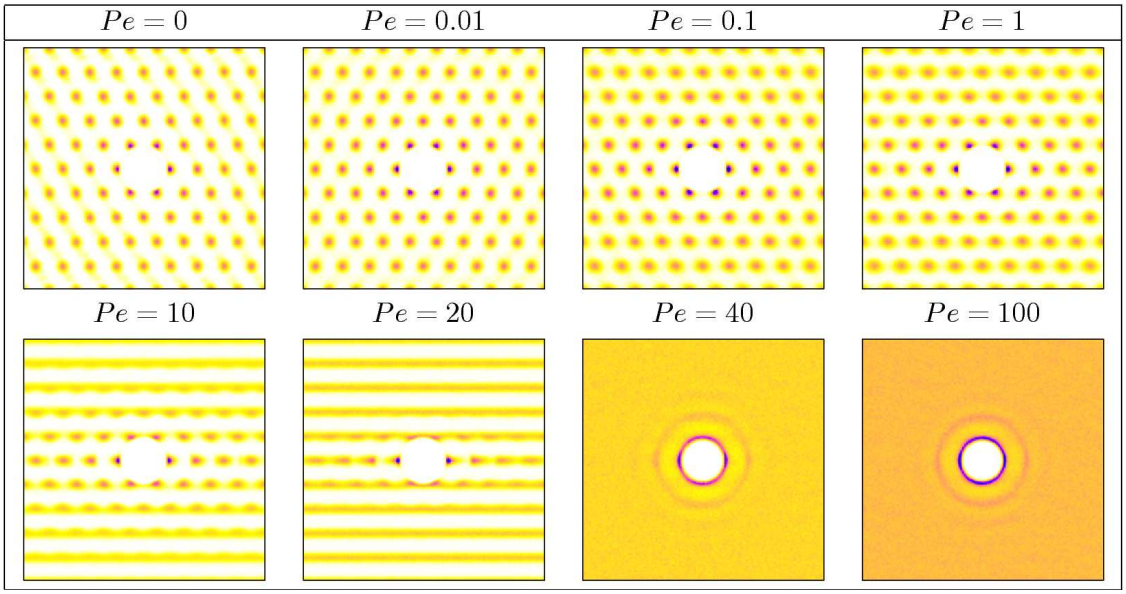

Figure 4.13: Top view pair distribution function in a suspension of homonuclear particles at $\phi = 0.42$ as a function of Pe.

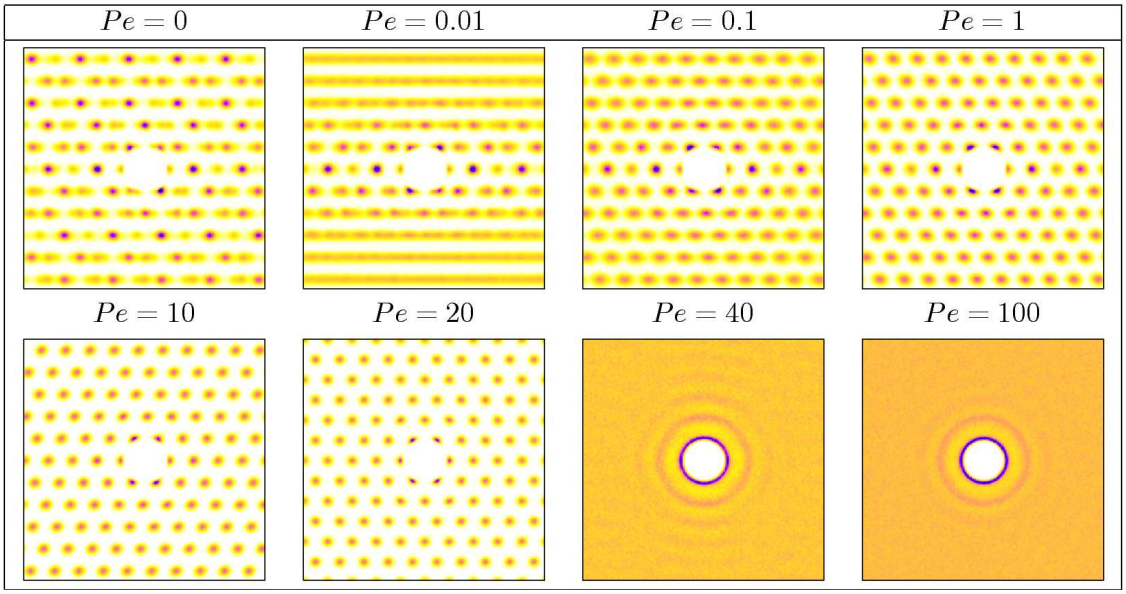

Figure 4.14: End view pair distribution function in a suspension of homonuclear particles at $\phi = 0.42$ as a function of Pe.

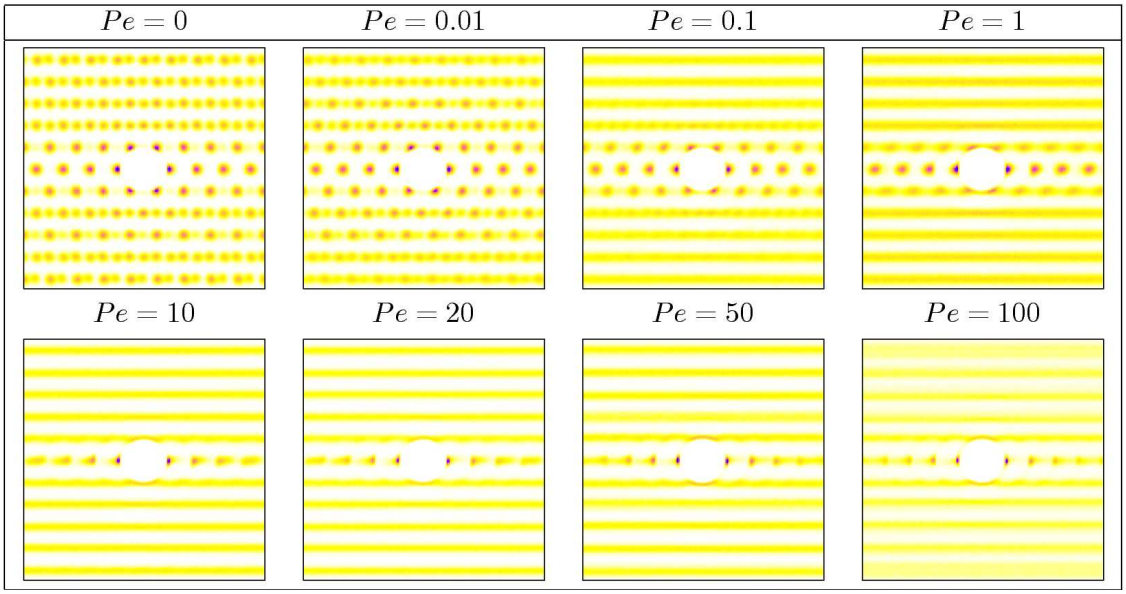

Figure 4.15: Front view pair distribution function in a suspension of homonuclear particles at $\phi = 0.55$ as a function of Pe.

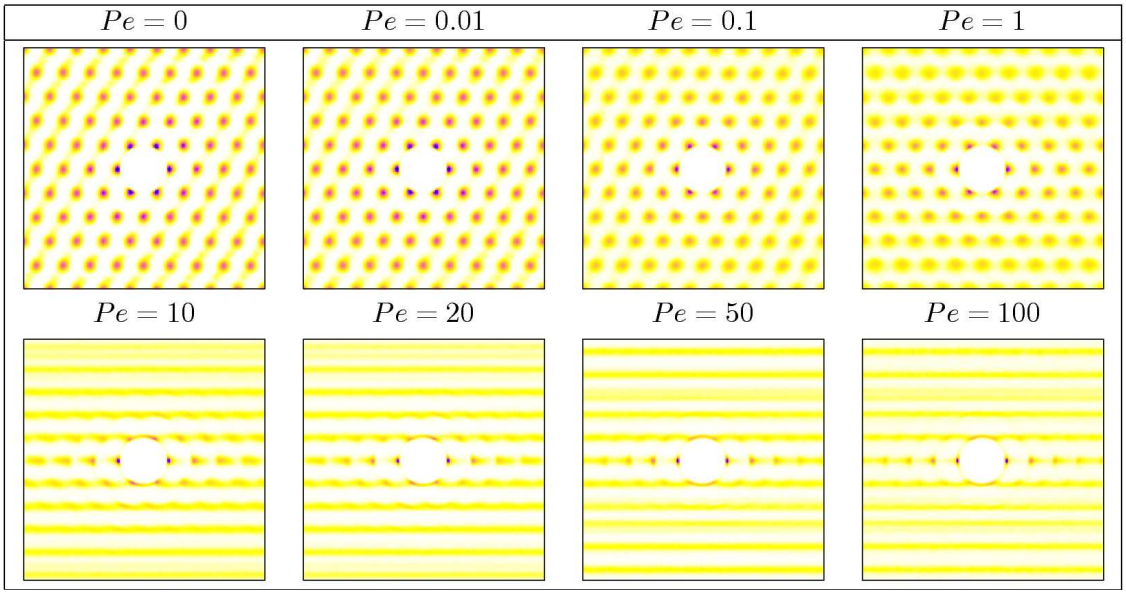

Figure 4.16: Top view pair distribution function in a suspension of homonuclear particles at $\phi = 0.55$ as a function of Pe.

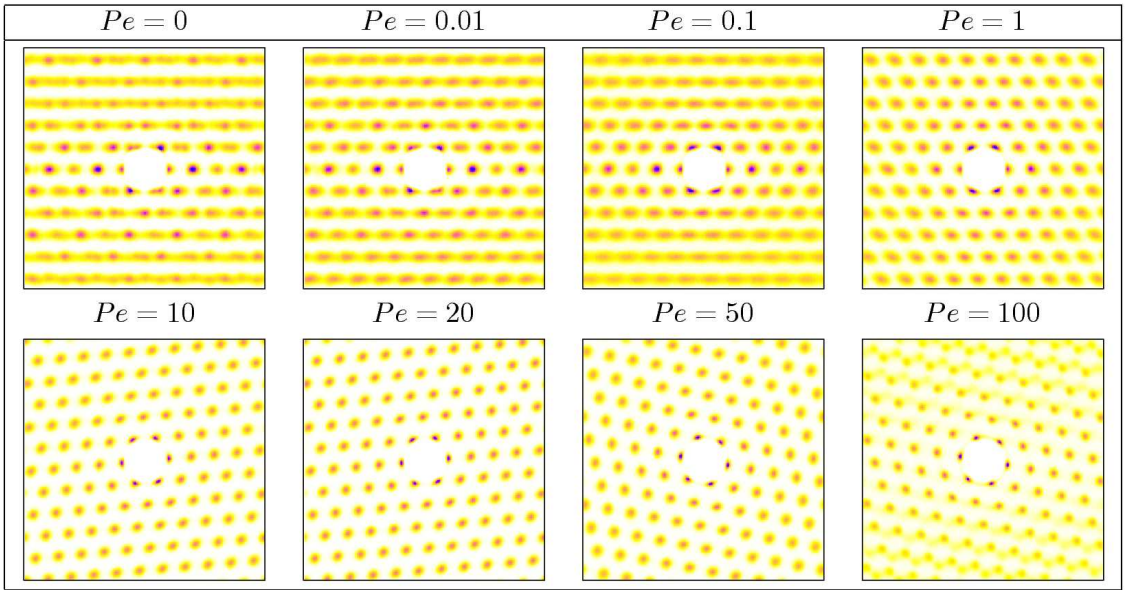

Figure 4.17: End view pair distribution function in a suspension of homonuclear particles at $\phi = 0.55$ as a function of Pe.

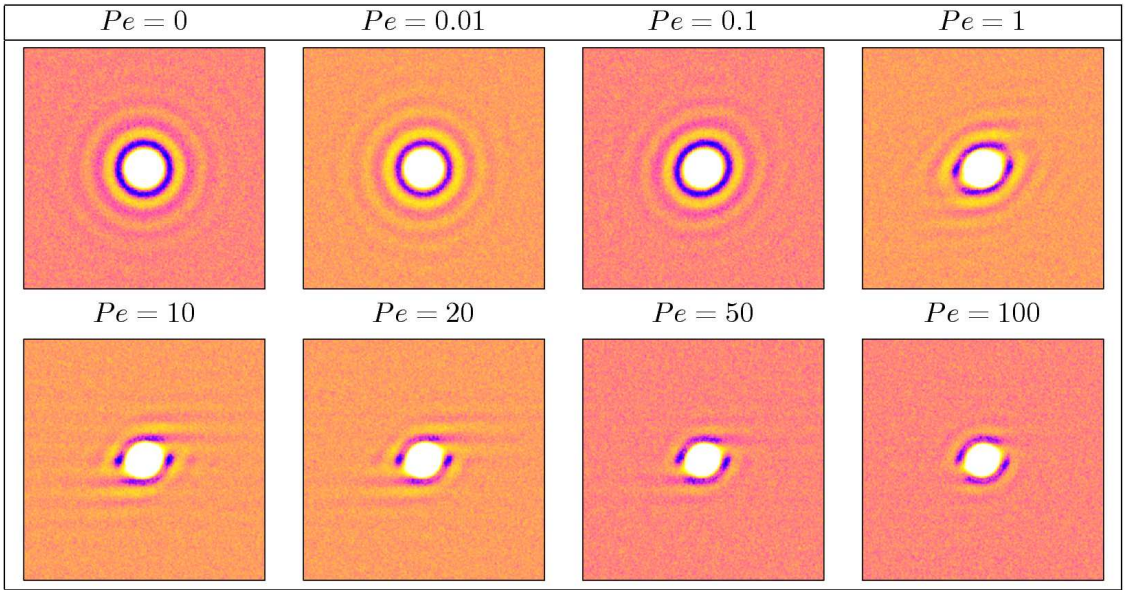

Figure 4.18: Front view pair distribution functions in suspensions of fused-dumbbell particles at $\phi = 0.42$ as a function of Pe.

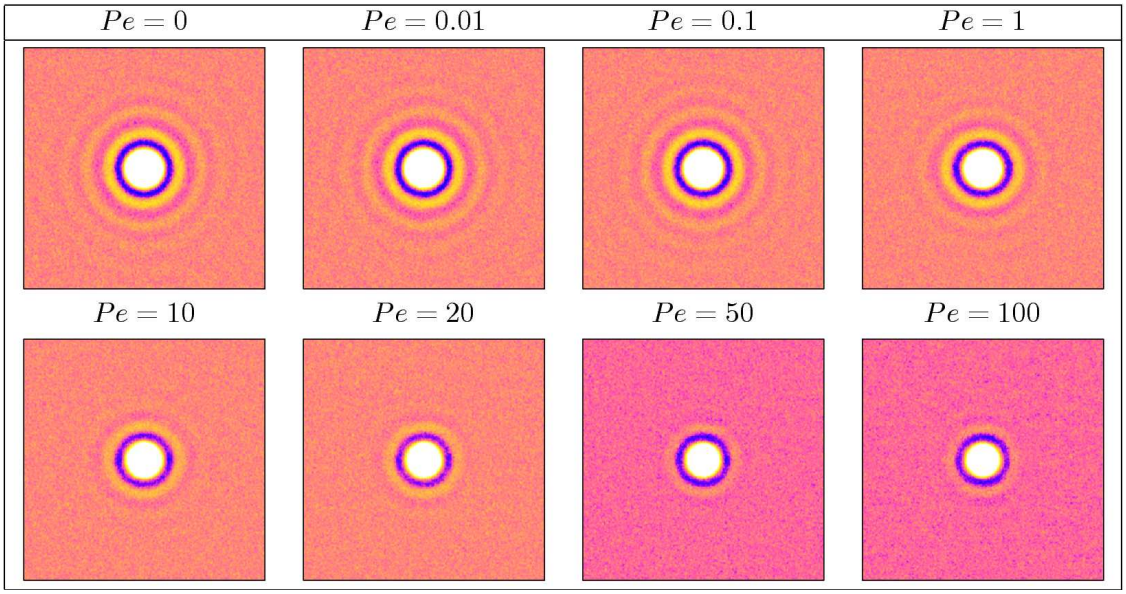

Figure 4.19: Top view pair distribution function in a suspension of fused-dumbbell particles at $\phi = 0.42$ as a function of Pe.

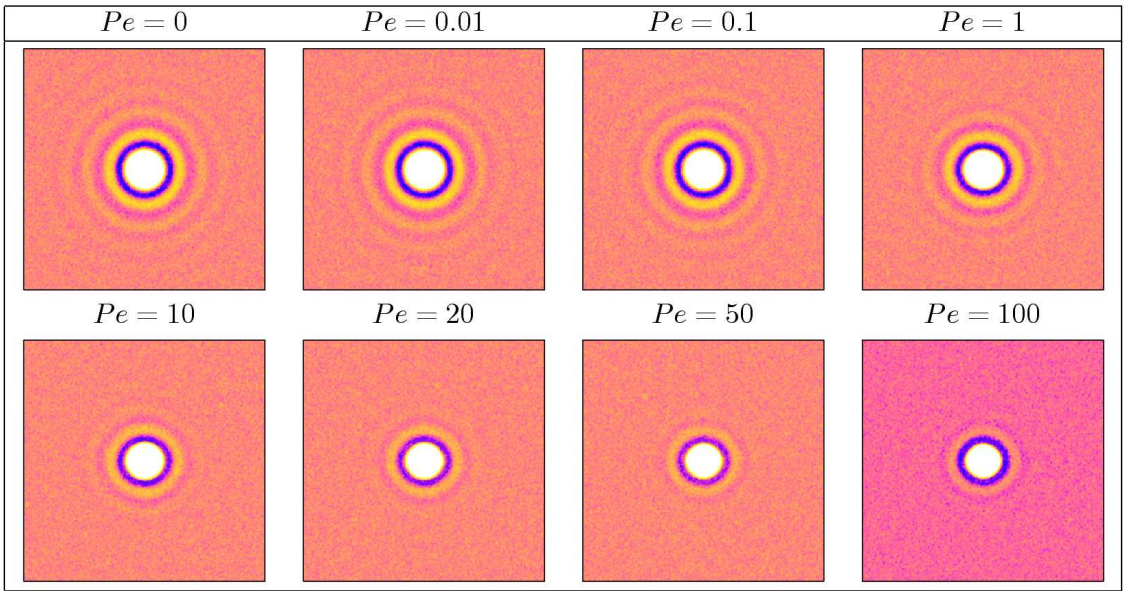

Figure 4.20: End view pair distribution function in a suspension of fused-dumbbell particles at $\phi = 0.42$ as a function of Pe.

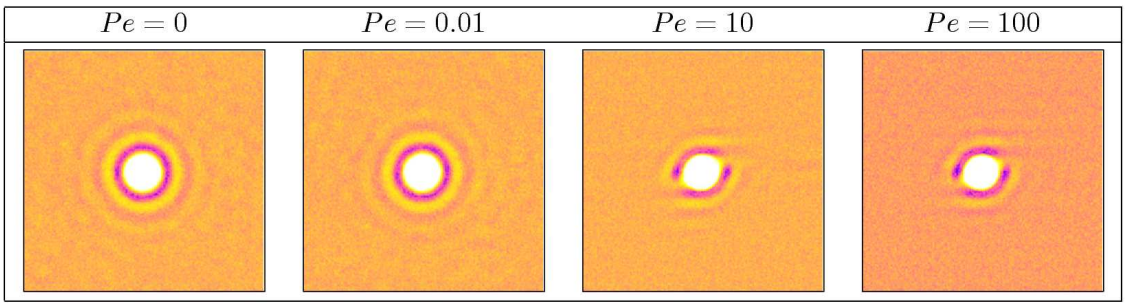

Figure 4.21: Front view pair distribution function in a suspension of fused-dumbbell particles at $\phi = 0.55$ as a function of Pe.

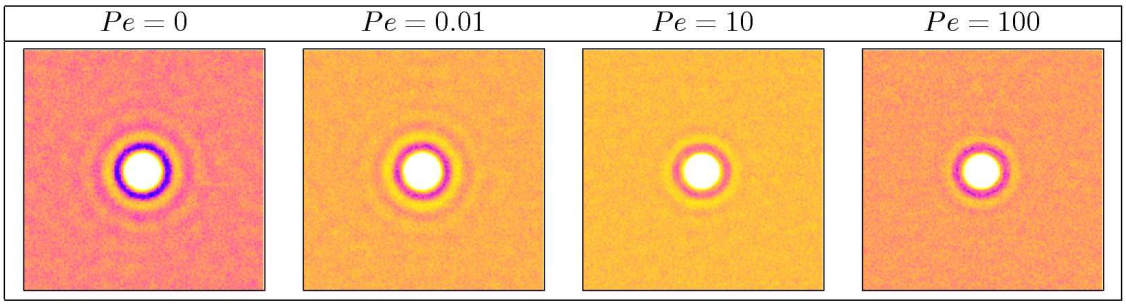

Figure 4.22: Top view pair distribution function in a suspension of fused-dumbbell particles at $\phi = 0.55$ as a function of Pe.

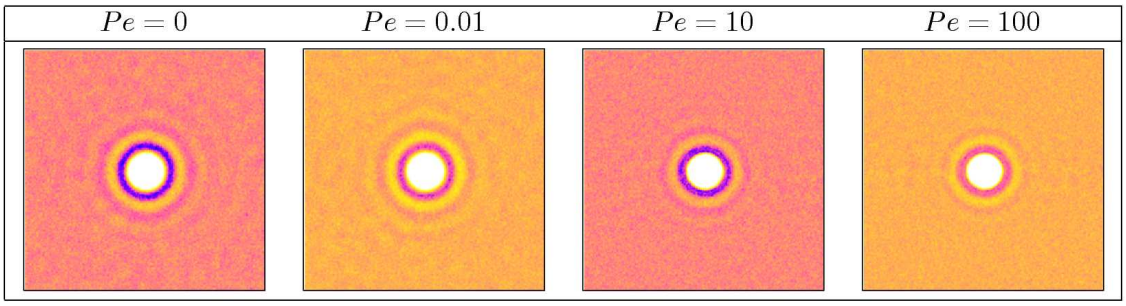

Figure 4.23: End view pair distribution function in a suspension of fused-dumbbell particles at $\phi = 0.55$ as a function of Pe.

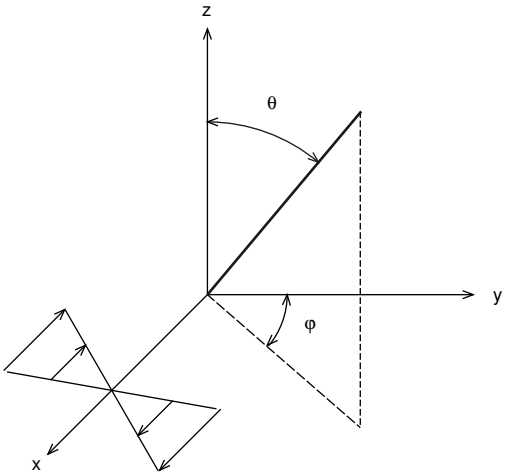

Figure 4.24: Definition used for describing the Jeffery's orbits.

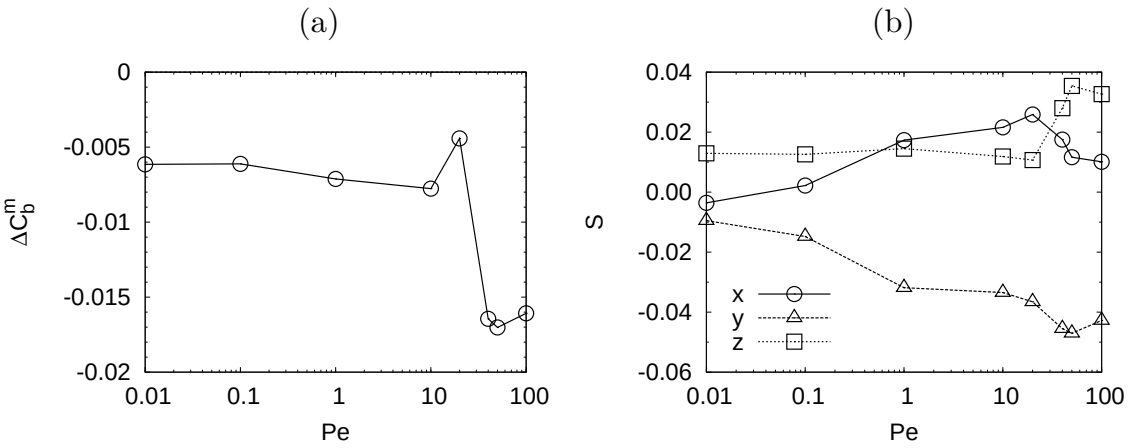

Figure 4.25: Homonuclear particle suspension at $\phi = 0.42$ (a) Change in the mean orbit constant over the infinite dilution value ΔC_b^m as a function of Pe, and (b) Orientational order parameter S along each of the coordinate axes as a function of Pe.

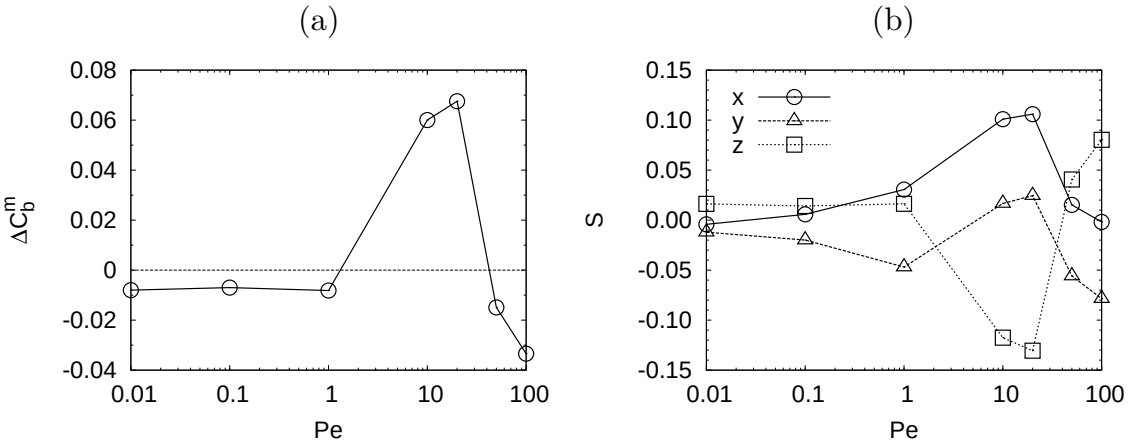

Figure 4.26: Homonuclear particle suspension at $\phi = 0.55$ (a) Change in the mean orbit constant over the infinite dilution value ΔC_b^m as a function of Pe, and (b) Orientational order parameter S along each of the coordinate axes as a function of Pe.

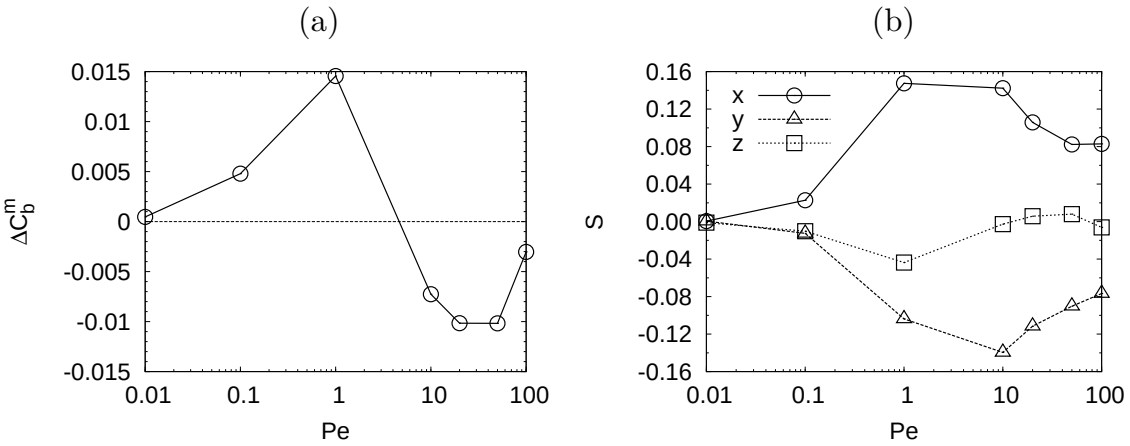

Figure 4.27: Fused-dumbbell particle suspension at $\phi = 0.42$ (a) Change in the mean orbit constant over the infinite dilution value ΔC_b^m as a function of Pe, and (b) Orientational order parameter S along each of the coordinate axes as a function of Pe.

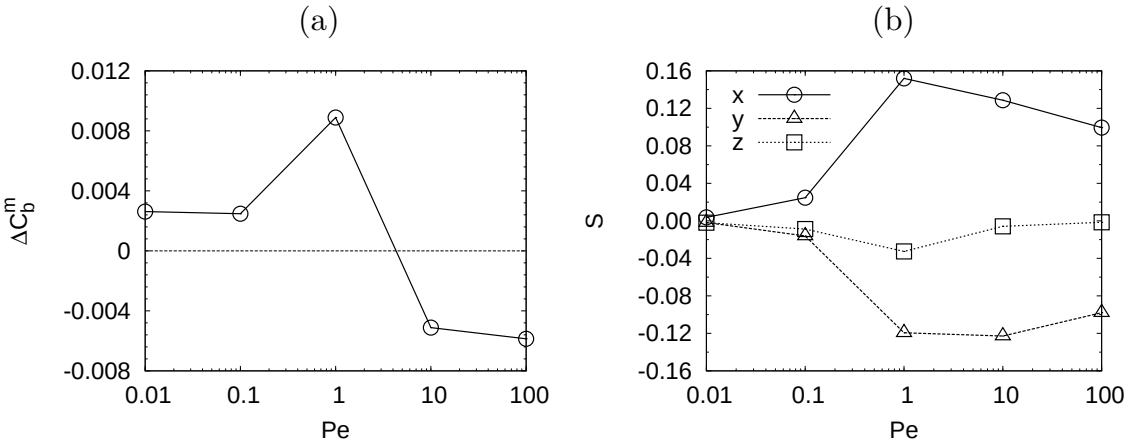

Figure 4.28: Fused-dumbbell particle suspension at $\phi = 0.55$ (a) Change in the mean orbit constant over the infinite dilution value ΔC_b^m as a function of Pe, and (b) Orientational order parameter S along each of the coordinate axes as a function of Pe.

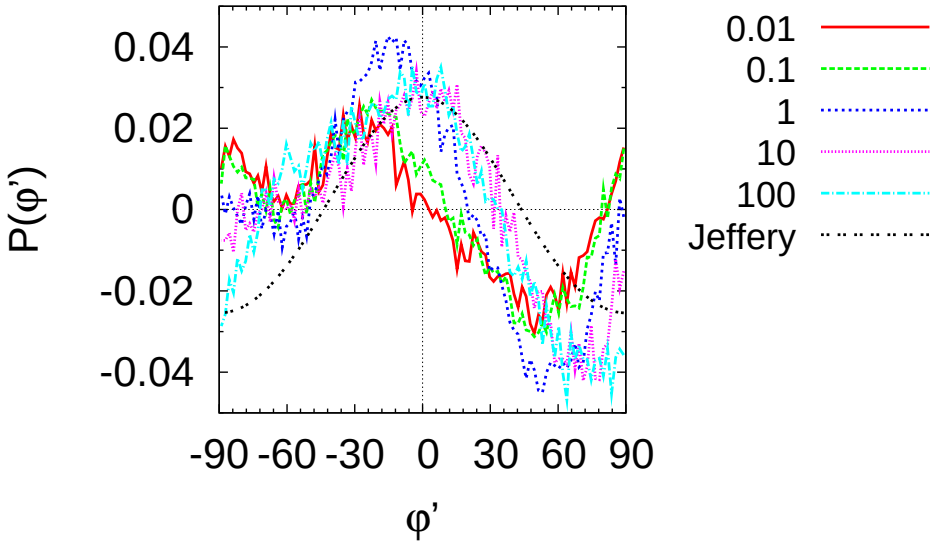

Figure 4.29: Homonuclear particle suspension at $\phi = 0.42$: $P(\varphi')$ where $\varphi' = \varphi - \pi/2$. Angles have been converted to degrees in the figure. Note $\varphi' = 0$ corresponds to the flow direction

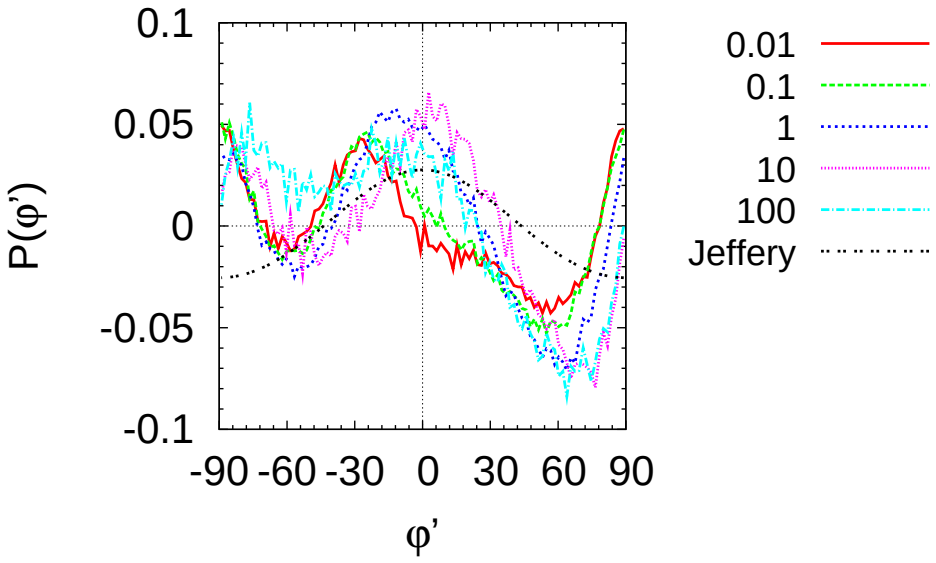

Figure 4.30: Homonuclear particle suspension at $\phi = 0.55$: $P(\varphi')$ where $\varphi' = \varphi - \pi/2$. Angles have been converted to degrees in the figure. Note $\varphi' = 0$ corresponds to the flow direction

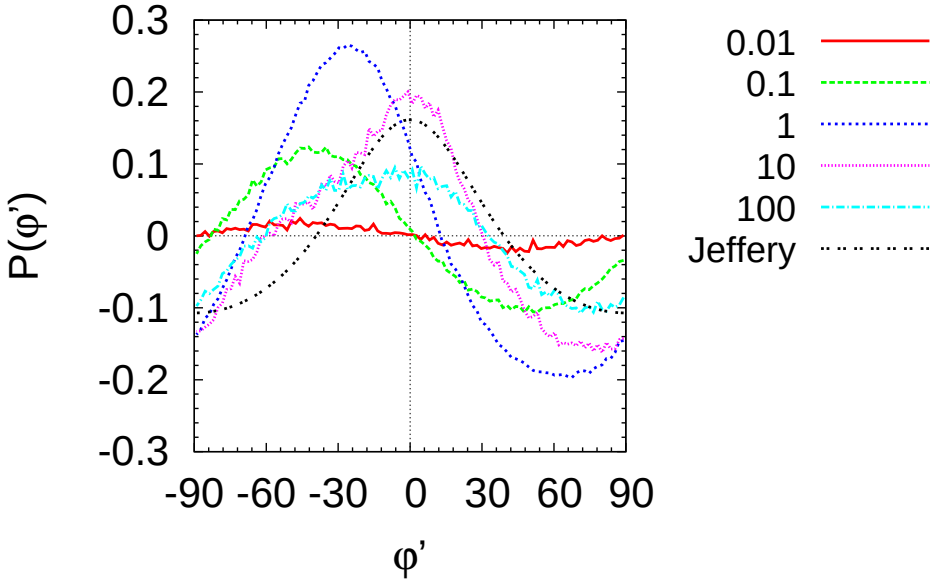

Figure 4.31: Fused-dumbbell particle suspension at $\phi = 0.42$: $P(\varphi')$ where $\varphi' = \varphi - \pi/2$. Angles have been converted to degrees in the figure. Note $\varphi' = 0$ corresponds to the flow direction

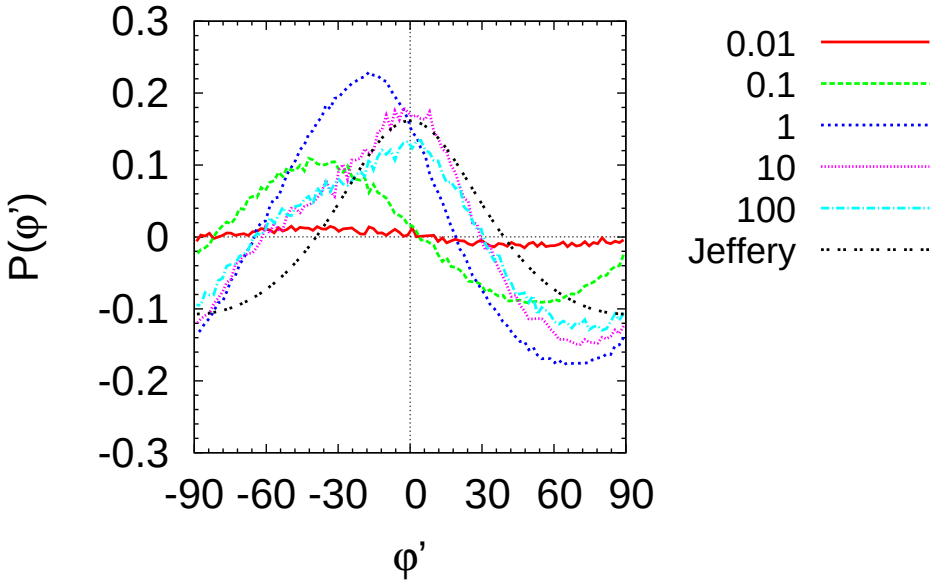

Figure 4.32: Fused-dumbbell particle suspension at $\phi = 0.55$: $P(\varphi')$ where $\varphi' = \varphi - \pi/2$. Angles have been converted to degrees in the figure. Note $\varphi' = 0$ corresponds to the flow direction

References

Ackerson, B.J. 1990. Shear induced order and shear processing of model hard sphere suspensions. *Journal of Rheology*, **34**(4), 553–589.

Ball, R.C., & Melrose, J.R. 1995. Lubrication breakdown in hydrodynamic simulations of concentrated colloids. *Advances in Colloid and Interface Science*, **59**, 19–30.

Ball, R.C., & Melrose, J.R. 1997. A simulation technique for many spheres in quasi-static motion under frame-invariant pair drag and Brownian forces. *Physica A*, **247**, 444–472.

Bell, G.M., Levine, S., & McCartney, L.N. 1970. Approximate Methods of Determining the Double-Layer Free Energy of Interaction between Two Charged Colloidal Spheres. *Journal of Colloid and Interface Science*, **33**(3), 335–359.

Bolhuis, P., & Frenkel, D. 1997. Tracing the phase boundaries of hard spherocylinders. *Journal of Chemical Physics*, **106**(2), 666–687.

Bossis, G., & Brady, J.F. 1984. Dynamic simulation of sheared suspensions. I. General method. *Journal of Chemical Physics*, **80**(10), 5141–5154.

Catherall, A.A., Melrose, J.R., & Ball, R.C. 2000. Shear thickening and orderdisorder effects in concentrated colloids at high shear rates. *Journal of Rheology*, **44**(1), 1–25.

Chen, L.B., Zukoski, C.F., Ackerson, B.J., Hanley, H.J.M, Straty, G.C., Barker, J., & Glinka, C.J. 1992. Structural changes and orientational order in a sheared colloidal suspensions. *Physical Review Letters*, **69**(4), 688–693.

Chen, L.B., Ackerson, B.J., & Zukoski, C.F. 1994a. Rheological and Microstructural transitions in colloidal crystals. *Langmuir*, **10**, 2817–2829.

Chen, L.B., Ackerson, B.J., & Zukoski, C.F. 1994b. Rheological consequences of microstructural transitions in colloidal crystals. *Journal of Rheology*, **38**(2), 193–215.

Chow, M.K., & Zukoski, C.F. 1995. Nonequilibrium behavior of dense suspensions of uniform particles: Volume fraction and size dependence of rheology and microstructure. *Journal of Rheology*, **39**(1), 33–59.

Foss, D.R., & Brady, J.F. 2000. Brownian Dynamics simulation of hard-sphere colloidal dispersions. *Journal of Rheology*, **44**(3), 629–651.

Glotzer, S.C., Solomon, M.J., & Kotov, N.A. 2004. Self-Assembly: From Nanoscale to Microscale Colloids. *AIChE Journal*, **50**(12), 2978–2985.

Gray, J.J., & Bonnecaze, R.T. 1998. Rheology and dynamics of sheared arrays of colloidal particles. *Journal of Rheology*, **42**(5), 1121–1151.

Jogun, S.M., & Zukoski, C.F. 1999. Rheology and microstructure of dense suspensions of plate-shaped colloidal particles. *Journal of Rheology*, **43**(4), 847–871.

Johnson, P.M., van Kats, C.M., & van Blaaderen, A. 2005. Synthesis of Colloidal Silica Dumbbells. *Langmuir*, **21**(24), 11510–11517.

Kern, N., & Frenkel, D. 2003. Fluid-fluid coexistence in colloidal systems with short-ranged strongly directional attraction. *Journal of Chemical Physics*, **118**(21), 9882–9889.

Kim, J.W., Larsen, R.J., & Weitz, D.A. 2006. Synthesis of nonspherical colloidal particles with anisotropic properties. *Journal of American Chemical Society*, **128**(44), 14374–14377.

Loose, W., & Ackerson, B.J. 1994. Model calculations for the analysis of scattering data from layered structures. *Journal of Chemical Physics*, **101**(9), 7211–7220.

Lu, Y., Yin, Y., & Xia, Y. 2001. Three-Dimensional Photonic Crystals with Non-spherical Colloids as Building Blocks. *Advanced Materials*, **13**(6), 415–420.

Mock, E.B., & Zukoski, C.F. 2007. Investigating microstructure of concentrated suspensions of anisotropic particles under shear by small angle neutron scattering. *Journal of Rheology*, **51**(3), 541–559.

Mock, E.B., Bruyn, H. De, Hawkett, B.S., Gilbert, R.G., & Zukoski, C.F. 2006. Synthesis of Anisotropic Nanoparticles by Seeded Emulsion Polymerization. *Langmuir*, **22**(9), 4037–4043.

Pusey, P.N., van Megen, W., Bartlett, P., Ackerson, B.J., Rarity, J.G., & Underwood, S.M. 1989. Structure of Crystals of Hard Colloidal Spheres. *Physical Review Letters*, **63**(25), 2753–2756.

Rastogi, S.R., Wagner, N.J., & Lustigb, S.R. 1996. Rheology, self-diffusion, and microstructure of charged colloids under simple shear by massively parallel nonequilibrium Brownian dynamics. *Journal of Chemical Physics*, **104**(22), 9234–3792.

Russel, W.B., D.A.Saville, & Schowalter, W.R. 1989. *Colloidal Dispersions*. Cambridge University Press.

Saad, Y. 2003. *Iterative Methods for Sparse Linear Systems*. Society for Industrial and Applied Mathematics.

Sierou, A., & Brady, J.F. 2002. Rheology and microstructure in concentrated noncolloidal suspensions. *Journal of Rheology*, **46**(5), 1031–1056.

Sirota, E.B., Ou-Yang, H.D., Sinha, S.K., Chaikin, P.M., Axe, J.D., & Fujii, Y. 1989. Complete phase diagram of a charged colloidal system: A synchrotron X-Ray scattering study. *Physical Review Letters*, **62**(13), 1524–1527.

Stevens, M.J., & Robbins, M.O. 1993. Simulation of shear-induced melting and ordering. *Physical Review E*, **48**(5), 3778–3792.

Stover, C.A., Koch, D.L., & Cohen, C. 1992. Observations of fiber orientation in simple shear flow of semi-dilute suspensions. *J. Fluid Mech.*, **238**, 277–296.

Vega, C., Paras, E.P.A., & Monson, P. A. 1992a. On the stability of the plastic crystal phase of hard dumbbell solids. *Journal of Chemical Physics*, **97**(11), 8543–8548.

Vega, C., Paras, E. P. A., & Monson, P. A. 1992b. Solid-fluid equilibria for hard dumbbells via Monte Carlo simulation. *Journal of Chemical Physics*, **96**(12), 9060–9072.

Versmold, H., , & Dux, Ch. 2000. Scattering experiments on the structure of colloidal dispersions: hexagonal layers or cubic crystals? *Journal of Colloid & Polymer Science*, **278**, 181–185.

Xia, Y., Gates, B., Yin, Y., & Lu, Y. 2000. Monodispersed Colloidal Spheres: Old Materials with New Applications. *Advanced Materials*, **12**(10), 693–713.

Yan, Y.D., & Dhont, J.K.G. 1993. Shear induced structure distortion in nonaqueous dispersions of charged colloidal spheres via light scattering. *Physica A*, **198**(78–107).

Chapter 5

Comparison of Microstructure, Diffusion, and Rheology in Ordered and Disordered Phases of Charged Colloidal Suspensions at Low Shear Rates

Synopsis

Numerical simulations are performed to determine phase behavior and rheology of charged colloidal particle suspensions at a volume fraction of $\phi = 0.33$. It is shown that for a given screening length of the repulsive interaction, there exists a range of surface potential for which both the ordered and disordered metastable states exist. This range is found to have a strong dependence on shear rate having a maximum width around $Pe = 0.5$, where $Pe = \dot{\gamma}a^2/D_0$. The presence of both the ordered and disordered metastable states allow us to characterize both the branches of viscosity as a function of shear rate. In contrast to common wisdom, it's shown that the disordered branch can have a lower viscosity than the ordered branch at low shear rates ($Pe < 0.05$ in this study). This can be attributed to the much smaller effective diffusivity in the ordered state, which leads to a greater distortion of the microstructure and hence stress at the same shear rate. On the other hand, at higher shear rates, ordered states with close packed planes aligned in the flow-vorticity direction are able to minimize the distortive effect of shear, and hence have lower viscosities than the corresponding disordered states. This strange behavior can explain the reduction in stress reported in some experiments on charge stabilized suspensions where a reduction in stress in observed with an order to disorder transition at low shear rates (Chen *et al.*, 1994a; Imhof *et al.*, 1994).

5.1 Introduction

Colloidal suspensions show very interesting phase behavior which depends on a fine balance between Brownian, hydrodynamic, and inter-particle forces. The equilibrium microstructure of charge stabilized suspensions is typically face-centered cubic (FCC) at sufficient strengths of the repulsive interparticle interaction (Sirota *et al.*, 1989; Ackerson, 1990; Chen *et al.*, 1992). Upon shearing, the suspension's microstructure goes through a series of transitions as a function of the shear rate. At low enough shear rates, a 3-dimensional ordering is maintained and suspensions shears via the close packed layers occasionally hopping from one close-packed site to its empty twin in the same plane (Ackerson *et al.*, 1986; Ackerson, 1990; Chen *et al.*, 1992; Mock & Zukoski, 2007). This microstructure is characterized as a strained crystal as particle positions are slightly strained from their equilibrium positions. As the shear rate is further increased, a loss in long range order is observed (Chen *et al.*, 1994a; Versmold *et al.*, 2001; Mock & Zukoski, 2007). Visually, the suspension surface breaks into small crystallites which retain their iridescence, and hence this microstructure is classified as polycrystalline (Chen *et al.*, 1992, 1994b,a). Upon further increase in shear rate, long range order is reestablished in the form of sliding layers (Ackerson, 1990; Chen *et al.*, 1992, 1994a), which is eventually found to disorder at even higher shear rates (Chen *et al.*, 1994b; Chow & Zukoski, 1995).

Microstructural transitions are found to have a profound effect on the rheological properties of particle suspensions. At very low shear rates, viscosity is normally found to decrease with increasing shear rates, which is commonly known as the shear thinning phenomena. This is due to a rapid decrease in Brownian and inter-particle contributions, coupled with a slow increase in the hydrodynamic contribution to viscosity (Bossis & Brady, 1989; Foss & Brady, 2000b). The shear stress of the suspension, though, is normally found to increase with increasing shear rates. Chen *et al.* (1992) first reported an anomalous flow region where the stress is a decreasing function of the shear rate. The point of stress maxima, i.e. the onset of anomalous region, was found to exhibit maximum stored elastic energy as evidenced by the recoverable strain in creep and recovery experiments. Microstructure was found to be polycrystalline before, during, and after the anomalous region. Chen *et al.* (1994a) ob-

served a similar anomalous region, except that the anomalous region coincided with the transition from a strained crystal microstructure to a polycrystalline microstructure, which essentially involves a loss in long range order. In this study too, the stress at the onset of the anomalous region gave a maximum recoverable strain in creep and recovery experiments. Independently, Imhof *et al.* (1994) also reported a similar anomalous flow region in charge stabilized suspensions. In their pressure driven cuvette, they found that there exists a range of shear rates where the crystalline region coexisted with the shear melted region. Beginning from the onset of shear melting and until its completion, the stress was either found to decrease or stay constant, again suggesting that a decrease in viscosity and stress can occur due to disordering.

There are several numerical simulations in the literature that have addressed the low shear rate behavior in colloidal suspensions. Using non-equilibrium molecular dynamics, Stevens *et al.* (1991) developed a phase diagram characterizing suspension microstructure as a function of ionic strength and shear rate. They found that suspension with FCC structure at rest shear melted with increasing shear rates. This was accompanied by a jump in stress. Gray & Bonnecaze (1998) directly tried to address the anomalous stress behavior observed at low shear rates in experiments. In their Stokesian dynamics simulations, they don't observe shear melting and a continuous transition is found from the low shear rate zig-zag motion (strained crystal) to the higher shear rate straight trajectory motion (sliding layer). No anomalous stress behavior was observed when the initial configuration had a FCC lattice with a close packed direction aligned with the flow, which is the configuration normally observed in experiments and simulations. On the other hand, when they started their simulation with a FCC lattice having a close packed direction perpendicular to the flow (FCC2), they were able to observe an anomalous flow region where stress was a decreasing function of shear rate. This anomalous region coincided with a transition from FCC2 lattice to a sliding layer microstructure. This led them to conclude that the anomalous region seen in experiments is associated with the transition of FCC2 lattice in the polycrystals to the sliding layer structure. It must be noted that the mode which would have rotated the FCC2 lattice, so as to align a close packed direction with the flow was disallowed. Indeed, in simulations where such a mode was allowed, FCC2 lattice was found to rotate to the

commonly observed FCC lattice orientation. An interesting set of simulations were recently performed by Butler & Harrowell (2003, 2002). In their non-equilibrium molecular dynamics simulations, they found that, at low shear rates, a simulation started with an ordered state was found to stay ordered and the same was true for simulations started with a disordered state. The stress in the ordered state was found to be higher than in the corresponding disordered state, though this result wasn't discussed any further. They were also able to obtain coexistence between the ordered and the disordered states in the same simulation by employing structured walls, where one wall had particles pinned at perfect (111) FCC layers, while the other wall had particles pinned at an amorphous configuration. The stress in such simulations were found to be in between those of the ordered and the disordered states, and was found to stay constant with increasing shear rate until the completion of shear melting.

There has been a great interest in developing an analytical expression for the low shear rate microstructure and rheology starting from the equilibrium microstructure (Russel, 1976; Batchelor, 1977; Brady, 1993; Brady & Vicic, 1995). The standard approach employed by these authors is to find a solution to the Smoluchowski equation with a perturbation expansion in shear rate. To make the problem tractable, the equations are integrated out over the coordinates of all but two particles, thereby reducing it to a pairwise problem. The first term in the perturbation expansion giving distortion is proportional to Pe, where the shear rate is non-dimensionalized by the infinite dilution diffusivity D_0. In order to improve the agreement of this pair-wise expression for concentrated suspensions, it has been suggested to replace the infinite dilution diffusivity D_0 in Pe by an appropriate effective diffusivity $\bar{D}$ to obtain an effective Peclet number given by $\bar{Pe} = Pe/(\bar{D}/D_0)$. In this respect, several authors have shown that the dominant relaxation process in a concentrated suspension is diffusion from the cage formed by its near neighbors (Segre *et al.*, 1995; Verberg *et al.*, 1997; Banchio *et al.*, 1999). This relaxation process is usually represented by a wave number dependent collective diffusion $D_c(k)$, where k represents the wave number. In particular, collective diffusion computed at the peak of the structure factor k^* is found to be the most relevant measure of structural relaxation as it is found to satisfy the generalized Stokes-Einstein relationship $\mu_r = D_0/D_c^L(k^*)/D_0$ for hard-sphere suspensions, where μ_r is the zero shear viscosity (Segre *et al.*, 1995; Banchio *et al.*, 1999). Apart from $D_c^L(k^*)$, long-time self

diffusivity D_s^L has also been shown to accurately predict the trend in zero shear viscosity in charge stabilized suspensions (lmhof *et al.*, 1994), and collapse the shear rate dependent viscosity at different volume fractions onto a single master curve (Foss & Brady, 2000b,a). All of the above references, therefore, suggest us the use of either $D_c(k^*)$ or D_s^L as a relevant measure of the structural relaxation process in non-dilute suspensions.

The main goal of this work is two fold: first is to show the sensitivity of microstructure on various parameters like shear rate and interparticle interaction strength, and second is to make a direct comparison between various properties of ordered and disordered states including microstructure, rheology and diffusion. One of the important conclusions of this work is that there exists a crossover between the ordered and the disordered phase viscosity, such that the disordered phase has a lower viscosity at low enough shear rate. This result is in direct contrast to the commonly accepted view that the ordered phase is always the lower branch in viscosity.

This paper is organized as follows: In section (5.2), we give a short description of the simulation technique employed in this work. Next, we present the simulation results in section (5.3), which includes a development of a phase diagram, followed by detailed characterization of the microstructure, diffusion and rheology in both the ordered and disordered phases. In section (5.4), we explore in detail the cause behind the crossover phenomena between the ordered and disordered branches of viscosity. We also develop a master curve by collapsing viscosity data for different strengths of interactions. Finally, we give our concluding remarks in section (5.5).

5.2 Formulation

5.2.1 Governing Equation

The motion of colloidal particles is governed by the stochastic Langevin equation

$$m\frac{d\mathbf{U}}{dt} = \mathbf{F}^H + \mathbf{F}^B + \mathbf{F}^P \tag{5.1}$$

In the above equation m is the mass/moment of inertia of the particle, $\mathbf{U}$ is the generalized velocity/angular velocity vector, and $\mathbf{F}^H$, $\mathbf{F}^B$, and $\mathbf{F}^P$ are the generalized force/torque vectors due to the hydrodynamic interaction, thermal fluctuations (Brownian motion), and interparticle interaction respectively. Each of the vectors $\mathbf{U}$, $\mathbf{F}^H$, $\mathbf{F}^B$, and $\mathbf{F}^P$ have $6N_p$ elements, where N_p is the number of particles in the system. On the time scales of interest, inertia of the particles can be neglected to obtain the following form of the governing equation

$$\mathbf{F}^H + \mathbf{F}^B + \mathbf{F}^P = 0 \tag{5.2}$$

The above form was used in this work. In the following sections, we discuss the computation of all the above three types of interactions i.e., $\mathbf{F}^H$, $\mathbf{F}^B$, and $\mathbf{F}^P$.

5.2.2 Hydrodynamic Interaction ($\mathbf{F}^H$)

Colloidal particles are very small, usually having a characteristic length smaller than $10^{-6}m$. Due to its small size, Reynolds number for the fluids motion around the particle is usually negligible, and hence the linear Stokes equation may be used. In Stokes flow, the hydrodynamic force on a particle is a linear function of the fluid velocity, and this linear relationship is usually expressed in the form of a resistance tensor $\mathbf{R}$. In this work, we will restrict ourselves to forces/torques $\mathbf{F}$, and stresslets $\mathbf{S}$ on the particles in a linear ambient flow, which is customarily broken into uniform velocities/angular velocities $\mathbf{U}^\infty$, and a rate of strain tensor $\mathbf{E}^\infty$. Then by definition of the resistance tensor, we have the following relationship between the aforementioned quantities

$$\begin{pmatrix} \mathbf{F} \\ \mathbf{S} \end{pmatrix} = \mathbf{R} \begin{pmatrix} \mathbf{U}^\infty - \mathbf{U} \\ \mathbf{E}^\infty \end{pmatrix} \tag{5.3}$$

where $\mathbf{U}$, refer to the velocities/angular velocities of the particles. In this work, we will use a modified version of the algorithm presented by Ball & Melrose (1997). In our algorithm,

which will be presented in detail in chapter (6), we express the resistance tensor as

$$\mathbf{R} = \mathbf{R}_0 + \mathbf{R}_\delta \tag{5.4}$$

where $\mathbf{R}_0$ is an additional term added to the $\mathbf{R}_\delta$ term in (Ball & Melrose, 1997). $\mathbf{R}_0$ is a diagonal tensor representing an isotropic resistance, which in some ways is a simplification of the many-body hydrodynamic resistance commonly used in Stokesian dynamics method (Bossis & Brady, 1984). In our method, the isotropic resistance depends only on the volume fraction and is obtained by matching the short-time self-diffusivity D_s^s of a hard-sphere suspension with that from Stokesian dynamics technique. These isotropic resistances for various couplings $F-U$, $T-\Omega$, and $S-E$ have been fitted to a second order polynomial in ϕ, and are given by the following equation

$$\begin{aligned} R_0^{FU} &= 1 + 2.725\phi - 6.583\phi^2 \\ R_0^{T\Omega} &= 1 + 0.749\phi - 2.469\phi^2 \\ R_0^{SE} &= 1 + 3.643\phi - 6.951\phi^2 \end{aligned} \tag{5.5}$$

5.2.3 Brownian Interaction ($\mathbf{F}^B$)

Brownian forces and torques can be obtained from fluctuation dissipation theorem and equipartition of energy (Russel *et al.*, 1989), which dictates

$$\begin{aligned} < \mathbf{F}^B > &= 0 \\ < \mathbf{F}^B \mathbf{F}^B > &= 2kT\mathbf{R}_{FU}/\Delta t \end{aligned} \tag{5.6}$$

The above equations can be satisfied using random numbers with special properties. Basically, we write $\mathbf{F}^B$ as

$$\mathbf{F}^B = \sqrt{\frac{2kT}{\Delta t}}\,(\mathbf{A}\boldsymbol{\alpha} + \mathbf{B}\boldsymbol{\beta}) \tag{5.7}$$

where $\boldsymbol{\alpha}$, and $\boldsymbol{\beta}$ are $6N_p$ vectors, whose elements are random numbers, say γ_i, satisfying

the following two properties

$$\begin{aligned} < \gamma_i >= 0 \\ < \gamma_i \gamma_j >= \delta_{ij} \end{aligned} \tag{5.8}$$

With the random numbers satisfying the above properties, we only need to satisfy the following two equations to obtain the agreement of eq (5.7) with eq (5.6)

$$\begin{aligned} \mathbf{A}\mathbf{A}^T &= \mathbf{R}_0^{FU} \\ \mathbf{B}\mathbf{B}^T &= \mathbf{R}_\delta^{FU} \end{aligned} \tag{5.9}$$

5.2.4 Interparticle Interaction ($\mathbf{F}^P$)

The interparticle force considered in this work, is the electrostatic repulsion between charged particles. The presence of the suspending medium complicates the governing equation and no exact solution exists even for a pair of spherical particles (Russel *et al.*, 1989). The approximation used in this work is the linear superposition approximation, which works well in the case of thin double layers, i.e. $\kappa a \gg 1$, where κ^{-1} is the Debye screening length (eq. 5.11), and a is the radius of the particle. Under this approximation, interparticle potential and corresponding repulsive force is given by (Bell *et al.*, 1970)

$$\begin{aligned} U^P &= \epsilon V^2 \left(\frac{a^2}{R}\right) e^{-\kappa(R-2a)} \\ F^P &= \epsilon V^2 (1+\kappa R) \left(\frac{a^2}{R^2}\right) e^{-\kappa(R-2a)} \end{aligned} \tag{5.10}$$

where $\epsilon = \epsilon_0 \epsilon_r$ is the dielectric constant, V is the surface potential of the spherical particle, and R is the separation between the centers. Debye screening length κ^{-1} is given by

$$\kappa^{-1} = \sqrt{\frac{\epsilon k T}{2 N_A e^2 I}} \tag{5.11}$$

where e is the electronic charge, N_A is the Avogadro constant, and I is the ionic strength given by

$$I = \frac{1}{2} \sum_{k=1}^{k=N} c_k z_k^2 \tag{5.12}$$

where c_k and z_k is the concentration and charge number respectively of the ionic species k in the electrolyte.

For simplicity we will write the repulsive force in eq. (5.10) as

$$F^P = F_0(1 + \kappa R)\left(\frac{a^2}{R^2}\right) e^{-\kappa(R-2a)} \tag{5.13}$$

5.2.5 Method of Solution

To solve the governing equation (5.2), we substitute $\mathbf{F}^H$, $\mathbf{F}^B$, $\mathbf{F}^P$ from equations (5.3), (5.7), and (5.13) respectively, to obtain the following system of equations for the unknown velocities of the particles

$$\mathbf{R}_{FU}(\mathbf{U}^\infty - \mathbf{U}) = -\left(\mathbf{R}_{FE}\mathbf{E}^\infty + \mathbf{F}^P + \mathbf{F}^B\right) \tag{5.14}$$

Since the matrix $\mathbf{R}_{FU}$ is symmetric and positive definite, we used the conjugate gradient algorithm (Saad, 2003). Once the velocities are known, the unknown stresslets $\mathbf{S}$ can be computed in a post-processing step as

$$\mathbf{S} = \mathbf{R}_{SU}(\mathbf{U}^\infty - \mathbf{U}) + \mathbf{R}_{SE}\mathbf{E}^\infty \tag{5.15}$$

To evolve the microstructure in time, we used the midpoint method which belongs to the family of second-order explicit Runge-Kutta method (Lambert, 1997). The total shear stress τ in the suspension is found as

$$\tau = \Sigma_{12} = \mu_0\dot{\gamma} + \frac{1}{V}\sum_{i=1}^{N_p} -x_1F_2^P - x_1F_2^B + S_{12} \tag{5.16}$$

where the summation in the above equation is over all the particles in a control volume V, which in this work is taken as the periodic cell. Also note that the total stress tensor $\mathbf{\Sigma}$ is symmetric, as there are no external torques acting on the system and interparticle interactions are central (Batchelor, 1977).

5.3 Results

5.3.1 Phase Diagram

Thermodynamics dictates that the Helmholtz free energy of the system be minimized at constant temperature and volume, where the Helmholtz free energy A is given by

$$A = U - TS \tag{5.17}$$

In the above equation, U is the energy of the system including kinetic and potential, while T and S represent the temperature and entropy of the system respectively. For systems with a repulsive interparticle interaction, the energy of the system U is generally lower in the ordered state. This is easily seen if the ordered state has a close-packed microstructure, as is the case here, resulting in the particles being farthest apart in this configuration. On the other hand, a disordered state usually has a larger entropy due to the availability of a larger number of configurations compared to the ordered state in which particles are restricted to periodic positions. These two contrasting contributions to the free energy implies that one can expect a disorder to order transition with increasing strength of interparticle interaction, as the loss in entropy due to ordering can be made up by the decrease in potential energy. For this reason, this type of disorder to order transition is called energy driven transition, which is in contrast to the entropy driven disorder-order transition in hard-sphere suspensions at high volume fractions (Frenkel, 1999).

The disorder-order transitions are first order transitions and are known to show metastable states, the life-time of which can exceed the observation time. The distinction of these metastable states from equilibrium states is difficult and may require computation of the free energies of the corresponding phases (Binder, 1987). It's not our goal here to compute the free energies, especially because no such comparable description exists for the non-equilibrium system, which is the main focus of this work. Metastable states decay by hetero-phase fluctuations commonly known as the nucleation process in fluid-solid transitions. The dynamics of the nucleation process is controlled by the energy barrier to nucleation and

growth, which can make it extremely slow when the energy barrier exceeds the thermal energy (Binder, 1987). In simulations, the presence of metastable states can also imply coexistence between two phases (Speedy, 1997; Butler & Harrowell, 1995). For example, it is known that hard-sphere fluid is unstable at volume fractions above 0.494, and usually splits into coexisting fluid and solid phases having a volume fraction of 0.494 and 0.545 respectively. In simulations, though, the fluid states are known to exist indefinitely below the melting volume fraction of 0.545 (Woodcock, 1981; Speedy, 1997). Again, no attempt will be made to obtain coexisting disordered and ordered states in the same simulation (see, e.g., (Butler & Harrowell, 2003)).

Our goal so far has been to give some background on disorder-order transitions in charged suspensions, along with some interpretations for the presence of metastable states. We now proceed to present the phase diagram, which details the presence of ordered and disordered states as a function of interaction strength and shear rate. At rest, we find that there exists a range of interaction strength where both the ordered and disordered states were found to be stable (or metastable) in disparate simulations, i.e. simulations started with an ordered state stayed ordered while simulations started with a disordered state stayed disordered. Figure (5.1) shows this region, where the curve F_{max} gives the maximum interaction strength for which the disordered state was found to be stable, while F_{min} gives the minimum interaction strength for which the ordered state was found to be stable. The observation time in all these simulations was 5000 diffusive-time $t_d = a^2/D_0$. Following Stevens & Robbins (1993), we also started simulations with a mixed initial state in which the top half ($y > 0$) of the shear cell had a FCC lattice, while the bottom half ($y < 0$) had an amorphous configuration. Twenty different simulations were performed with the same initial state, but with different random number seeds for the Brownian motion. We found that, depending on the interaction strength, only a certain fraction of the runs completely ordered, while the rest completely disordered. The final state in terms of order/disorder was usually attained within $20t_d$. Using this information, we added $P0$, $P50$ and $P100$ curves in figure (5.1), which respectively refers to the 0%, 50% or 100% of the runs ordering at that particular interaction strength. It is expected that with a preexisting interface, these runs will give a much tighter bound on the stability of the ordered or the disordered phase, as the need for nucleation barrier is

avoided. But, in general, these cannot be expected to give exact information about the true stability of the phases as the shape and size of this interface doesn't mimic the nucleation process, and hence can create a bias of its own which is difficult to quantify. Therefore, $P0$, $P50$ and $P100$ curves should only be considered in a qualitative sense, rather than in a quantitative sense. Same is also true for the F_{max} and F_{min} curves. We have also computed the potential energy of the system in both the ordered and disordered states at various interaction strengths which is tabulated in table (5.1). This proves the argument that the ordered state has a lower potential energy than the disordered state. It should also be noted that the energy differential between the phases increase with increasing interaction strength, which can be considered as a measure of super-cooling. For this reason, the disordered phase quickly transitions to the ordered state at high interaction strengths.

For suspensions under shear, a similar behavior was observed. Namely, simulations started with an ordered state was found to stay ordered, while a simulation started with a disordered state was found to stay disordered for a range of interaction strength as shown in figure (5.1). The width of the region is clearly a strong function of Pe. At low shear rates, the width of the region was initially found to increase with increasing shear rates attaining a maxima around $Pe = 0.5$. Thereafter, the width decreases sharply and almost vanishes by $Pe = 10$. Similar trends are also seen in $P0$ and $P100$ curves, though it is not as sensitive as the runs started with a pure ordered or a pure disordered state. Given such extreme difference in the magnitudes between F_{max} and $P100$ curves, specially for $Pe <= 0.5$, probably implies that the nucleation barrier increases under shear. A similar conclusion was reached in recent Brownian dynamics simulations where an increase in the nucleation barrier was reported with increasing shear rates (Blaak *et al.*, 2004). In those studies, volume fraction was very low and hydrodynamic interactions were neglected. For this reason, perhaps, they see a continuous increase in the nucleation barrier with increasing shear rates. It would be interesting to see if those studies carried out at higher volume fractions with hydrodynamic interactions show a behavior similar to ours, which suggests a reduction in the nucleation barrier at relatively higher shear rates ($Pe > 0.5$).

5.3.2 Microstructure

In this section, we characterize the microstructure in both the ordered and the disordered branches as a function of shear rate. All results will be presented for a representative interaction strength of $F_0 = 35$. To better characterize the microstructure, we will employ various statistical measures including pair distribution functions (PDF) and structure factors. But first we introduce the notation of front, top and end views, which we will refer to often. This is schematically shown in figure (5.2), which shows that the line of sight is perpendicular to the flow-gradient (xy) plane in the front view, to the flow-vorticity (xz) plane in the top view, and to the vorticity-gradient (zy) plane in the end view. PDF and structure factors in the ordered branch with increasing shear rate are shown in figure (5.3). At equilibrium, presheared suspensions show close packed planes stacked in the gradient direction. The top view clearly shows a hexagonal arrangement which is consistent with the arrangement in a close-packed plane. Long range order between different planes is evident by the presence of distinct maxima spots in both the front and the end views. Similarly, the six maxima spots in the structure factor also confirms a close packed microstructure, although the presence of all the six maxima spots imply that there is no definite stacking sequence among the layers. In other words, they imply a registered random stacking or a highly twinned FCC microstructure (Loose & Ackerson, 1994). As the suspension is sheared from rest, a continuous evolution in microstructure is observed. At low shear rates, microstructure retains a three dimensional ordering, but smearing of the peaks relative to the equilibrium microstructure is obvious in the front and end views for $Pe <= 0.01$. This microstructure is normally known as the strained crystal structure as the average position of the particles are slightly strained from their equilibrium positions (Ackerson *et al.*, 1986; Chen *et al.*, 1994b). At intermediate shear rates ($0.1 < Pe < 1.0$), correlation is gradually lost between different layers and a sliding layer microstructure with centering of slipping layers is formed (see figure 5.5). Loss of correlation between different layers is clearly seen in the front view where distinct peaks at equilibrium give way to horizontal bands. In the end view, where each horizontal row corresponds to a layer, a centering of layers is evident as a string of particles in a given layer is located midway between two strings of particles in its two neighboring layers. The loss of

intensity in the top and the bottom peaks in the structure factor is also consistent with this sliding layer microstructure (Ackerson (1990)).

Similarly, we present PDF and structure factors for the disordered branch with increasing shear rate in figure (5.4). An amorphous liquid like structure is obvious in PDF and structure factors at low shear rates, but a distortion of the microstructure becomes evident in the front view at high shear rates, particularly $Pe = 1$. The increased distortion of microstructure of liquid like microstructure with increasing shear is consistent with results from experiments, simulations and theory (Clark & Ackerson, 1980; Brady, 1993; Yan & Dhont, 1993; Brady & Vicic, 1995; Foss & Brady, 2000b).

5.3.3 Diffusion

5.3.3.1 Short-time self-diffusion

Short time self-diffusivity D_s^s gives the instantaneous particle mobility (Foss & Brady, 2000b). Interparticle interactions do not directly effect D_s^s, but only effect it indirectly via the microstructure. In simulations, D_s^s are easily obtained from the following equation

$$D_s^s = \frac{1}{6N_p} < \mathbf{u}^B \cdot \mathbf{u}^B > \Delta t \tag{5.18}$$

where $\mathbf{u}^B$ is a $3N_p$ instantaneous translation velocity vector of the particles due to Brownian interactions $\mathbf{F}^B$. Note that Δt in the above equation should be kept the same as Δt used in computing $\mathbf{F}^B$. Ensemble average in the above equation refers to average over multiple equilibrium configurations obtained from the corresponding $Pe = 0$ runs. The values of D_s^s thus computed for various strengths of interaction in the ordered and the disordered phases are tabulated in tables (5.2) and tables (5.3) respectively. For comparison, we have also tabulated D_s^s for a hard-sphere suspension at $\phi = 0.33$ in table (5.4). There are two clear trends revealed by the data: (i) in a given phase, D_s^s increases with increasing interaction strength, and (ii) for the same interaction strength, D_s^s is larger in the ordered phase than in the disordered phase, both of which are larger than D_s^s in a hard-sphere suspension. These trends can be explained by appealing to differences in the microstructure. In systems with repulsive

interactions, particles are on an average further apart than in a hard-sphere suspension, and hence have higher instantaneous mobility (Horn *et al.*, 2000). Similarly, ordered systems, with a close packed microstructure, have larger average interparticle separation than corresponding disordered systems, and hence have even higher mobility. In a given phase, the effect of increasing interparticle interaction is to further increase the average interparticle separation, and hence results in an increase in particle mobility.

5.3.3.2 Long-time self-diffusion

Long-time self-diffusion D_s^L can be computed from the slope of mean square displacements (MSD) vs. time for $t >> a^2/D_s^s$. In this work, we fitted the following straight line to MSD vs. time curve to obtain D_s^L

$$(\Delta r)^2 = \Delta \mathbf{x} \cdot \Delta \mathbf{x} = 6D_s^L t + b \tag{5.19}$$

i.e. slope of the fit gives $6D_s^L$, while b is simply the intercept of the fit. The MSD in the disordered phase for 3 different interaction strengths are shown in figure (5.6) and corresponding best fits for D_s^L are tabulated in table (5.3). It is clearly seen that increasing interaction strengths result in a decrease in the corresponding D_s^L. This is because for the particles to move long distances, it has to navigate thorough regions of strong repulsive interaction which gets increasingly difficult with increasing strength of repulsion. The same reasoning also explains the much higher D_s^L in a hard-sphere suspension (table 5.4), as the particle motion there isn't inhibited by strong repulsive interactions.

Computing MSD in ordered suspensions turned out to be tricky. We found that MSD in ordered states showed no definite trend with increasing strengths of interparticle interaction as shown in figure (5.7), where the top four curves show the MSD of the particles for four different interaction strengths. On studying the animation of the simulation, we found that the rigid body motion of a periodic cell was contributing significantly to the particles MSD. This rigid body motion can be characterized by the motion of the center of mass of system, which is shown in the bottom four curves in figure (5.7) for the same four interparticle inter-

action. It's obvious that the rigid body motion of the periodic cell makes a very significant contribution to the particles MSD. This is an artifact of the periodic nature of system, which makes such rigid body modes feasible by implicitly requiring the images of the main cell to move along with it. Such modes, for obvious reasons, should not be characterized as diffusion as it will play no role in relaxing any stress/strain in the system. Hence, in this work, D_s^L will be computed from MSD curves in the center of mass frame. These MSD are shown in figure (5.8) and the corresponding D_s^L are tabulated in table (5.2). In contrast to the earlier MSD, the center of mass frame MSD show a clear decreasing trend with increasing strengths of interparticle interaction. It's also interesting to note that D_s^L in the ordered state is almost two orders of magnitudes smaller than the corresponding disordered state D_s^L. This is because in ordered states particles are effectively trapped in periodic positions, and are likely to diffuse freely only at the grain boundaries or by defect diffusion (van Blaaderen *et al.*, 1992; lmhof *et al.*, 1994)). Another possible mechanism to diffuse, not commonly mentioned for equilibrium systems, is the collective motion of a layer so as to change its stacking sequence from one close packed site to its empty twin in the same plane. This is the widely reported flow mechanism at low shear rates (see section 5.3.2), and is certainly possible in equilibrium systems, though the frequency of this transition would definitely be smaller without the assistance of shear.

5.3.3.3 Collective Diffusion

Collective diffusion $D_c(\mathbf{k})$ is another important measure of structural relaxation in suspensions (Segre *et al.*, 1995; Verberg *et al.*, 1997). Physically, $D_c(\mathbf{k})$ represents the relaxation of particle density distributed periodically in space with a wavenumber $\mathbf{k}$, and is normally measured by dynamic light scattering measurements in experiments (Segre *et al.*, 1995). Equivalently, in simulations, we can compute $D_c(\mathbf{k})$ from the decay of the normalized intermediate scattering function $f(\mathbf{k},t)$ defined as $f(\mathbf{k},t) = F(\mathbf{k},t)/F(\mathbf{k},0)$, where $F(\mathbf{k},t)$ is

$$F(\mathbf{k},t) = \frac{1}{N_p}\sum_{i=1}^{N_p}\sum_{j=1}^{N_p}\exp\left(i\mathbf{k}\cdot(\mathbf{x}_i(0)-\mathbf{x}_j(t))\right) \tag{5.20}$$

Note that $F(\mathbf{k}, 0)$ is commonly known as the static structure factor $S(\mathbf{k})$. At large times, $f(\mathbf{k}, t)$ is expected to decay as (Segre *et al.*, 1995)

$$f(\mathbf{k}, t) \propto \exp(-D_c^L(\mathbf{k})k^2 t) \tag{5.21}$$

In this work, we obtained $D_c^L(\mathbf{k})$ by fitting a straight line to $\ln f(\mathbf{k}, t)$ vs. $k^2 t$ curve at long times, where the slope of the fit would gives us $D_c^L(\mathbf{k})$ at the corresponding wave number $\mathbf{k}$. Segre *et al.* (1995) showed that $D_c^L(\mathbf{k})$ computed at the peak of the static structure factor, denoted here by k^*, is the most relevant measure of structural relaxation. Hence, in this work, we will restrict ourselves to computing $D_c^L(k)$ at $k = k^*$. The decay of the intermediate scattering function in the disordered phase is shown in figure (5.9), and the corresponding $D_c^L(k^*)$ are tabulated in table (5.3). $D_c^L(k^*)$ were found to be of the same order as D_s^L, though it was slightly smaller, and, as expected, it showed a decreasing trend with increasing interaction strengths. In contrast to the disordered phase, the ordered phase showed much smaller $D_c^L(\mathbf{k}^*)$ compared to the corresponding D_s^L. Due to this extremely slow decay, we didn't have sufficient data to be able to compute $D_c^L(\mathbf{k}^*)$ in the ordered phase. We do, however, intend to investigate this in future studies.

5.3.4 Rheology

In this section, we present the viscosity and stress results for both the ordered and the disordered phases at a strength of $F_0 = 35$, which is the same strength for which the microstructure was reported in the section (5.3.2). Figure (5.10) shows the corresponding viscosity and stress as a function of Pe. Interestingly, the disordered phase has a lower viscosity at low shear rates ($Pe < 0.05$), while at higher shear rates the ordered phase has a lower viscosity. The total viscosity is customarily broken down into contributions from interparticle, Brownian and hydrodynamic interactions. These contributions are shown in figure (5.11) and tabulated in tables (5.5) and (5.6). Note that the Hydrodynamic contribution is not shown in these figures as it was negligible and showed little variation in this range of Pe, though it must be noted that the hydrodynamic contribution to viscosity was lower in

the ordered state throughout and was found to increase slowly with increasing shear rate. In contrast, both the repulsive and the Brownian interactions make a significant contribution to viscosity at low shear rates, and show a decreasing trend with increasing shear rate. An interesting feature of the interparticle and the Brownian contribution is that both of these show a crossover between the ordered and the disordered branches, albeit at slightly different shear rates. The crossover was at approximately $Pe = 0.05$ for the interparticle contribution, while for the Brownian contribution it was approximately at $Pe = 0.1$. These results suggest that the crossover phenomena between the ordered and disordered branches stems from the interparticle and Brownian contributions to stress. This is consistent with experiments of Chen *et al.* (1992, 1994a), who found that the anomalous flow region, where the stress was a decreasing function of shear rate, was accompanied with a loss in stored elastic energy of the system, which essentially comes from interparticle and Brownian interactions.

The other interesting comparison of the ordered and disordered phase viscosity is the absence/presence of a low shear Newtonian plateau and dynamic yield stress. The viscosity in the disordered phase clearly shows a low shear Newtonian plateau which is consistent with viscosity of disordered suspensions (Foss & Brady, 2000b). Consequently, this also implies the absence of a dynamic yield stress, which isn't surprising at all for disordered suspensions. In the ordered phase, in the regime investigated in this work, no Newtonian plateau was observed as viscosity is found to increase continuously as the shear rate is decreased. The stress plot, though, reveals that the increase in viscosity is not as fast as the decrease in shear rate as $Pe \to 0$, which results in the stress $\to 0$ as $Pe \to 0$. If this trend were to hold at even lower shear rates, which wasn't verified, would indicate an absence of dynamic yield stress in ordered suspensions too. This result need not be surprising as in constant strain rate measurements, the time averaged particle positions tend towards the equilibrium configuration which doesn't contribute to shear stress. There are conflicting reports in the literature on the presence of dynamic yield stress, with some researchers showing its presence (van der Vorst *et al.*, 1997), while some reporting its absence (Barnes & Walters, 1985; Barnes, 1999). The latter references also suggested the presence of a Newtonian plateau in all types of suspensions provided the measurements are made at low enough shear rates. This is clearly the case for disordered suspensions, but our data here

cannot refute or verify this claim for ordered suspensions. We hope to explore this property in detail in future studies with extremely low shear rate simulations for ordered suspensions.

5.4 Discussion

We devote this section to exploring the microstructural origins of the crossover seen in the ordered and disordered phase viscosity and attempt to predict that using equilibrium properties of the suspension, including its microstructure and diffusivity. Based on this predictive model, we also attempt to collapse the shear rate dependent viscosity at different strengths of interparticle interaction on a single master curve and discuss some of its surprising features.

5.4.1 Microstructural distortion

We start here with an analytical expression for the pair distribution function $g(\mathbf{r})$, which at low shear rates can be written as a perturbation expansion in the non-dimensional shear rate $\bar{Pe}$ as

$$g(\mathbf{r}) = g_{eq}(\mathbf{r}) \left(1 + \bar{Pe} f(r) \hat{\mathbf{r}}.\mathbf{E}.\hat{\mathbf{r}} + \mathrm{O}(\bar{Pe}^2)\right) \tag{5.22}$$

where $g_{eq}(\mathbf{r})$ is the microstructure at equilibrium, $f(r)$ gives a measure of the microstructural distortion as a function of the radial separation, while $\hat{\mathbf{r}}.\mathbf{E}.\hat{\mathbf{r}}$ gives the angular dependence of the distortion (Russel, 1976; Batchelor, 1977; Brady & Vicic, 1995). Note that we have used an effective $\bar{Pe} = \dot{\gamma} a^2/\bar{D}$ in the above equation in which the shear rate is non-dimensionalized by an appropriate effective diffusivity $\bar{D}$. A trivial example is a system containing two widely separated particles, in which case the effective diffusivity is simply $\bar{D} = 2D_0$. Many authors have tried, either directly or indirectly, to find an appropriate diffusivity to make equation (5.22) useful for concentrated suspensions (lmhof *et al.*, 1994; Segre *et al.*, 1995; Verberg *et al.*, 1997; Foss & Brady, 2000b,a). Conclusion from these works is that the long time self-diffusion or the collective diffusion computed at the peak of the structure factor is a good measure of the rate of structural relaxation in a suspension. We reported these long-time diffusivity in section (5.3.3), expect for the $D_c^L(\mathbf{k}^*)$ in the ordered phase, which could

not be computed due to the lack of sufficient data. There, it was shown that the D_s^L was almost two orders of magnitude smaller in the ordered phase compared to the disordered phase at the same strength of interaction, while $D_c^L(\mathbf{k}^*)$ was conjectured to be smaller by an even larger magnitude. These results lead us to conclude that the effective $\bar{Pe}$ would be substantially larger in the ordered phase at the same rate of shear, and consequently it should show a much greater distortion of microstructure compared to the disordered phase (cf. equation 5.22). In order to better compare this microstructural distortion in the two phases, we computed two separate radial distribution functions $g(r)$, one in the compressive quadrant and one in the extensional quadrant. These are easily obtained by integrating out the ϕ and θ coordinates in $g(r, \theta, \phi)$ with appropriate limits (see figure 5.12), and are shown in figure (5.13). As expected, no distortion is observed at equilibrium in either of the phases. But, in contrast to the disordered phase, the ordered phase shows a significant distortion even at very low shear rates $10^{-3} \leq Pe \leq 10^{-2}$, which is consistent with our previous claim. At higher shear rates, particularly at $Pe = 1$, the disordered phase begins to show larger distortion of the microstructure. At this Pe, it would not be appropriate to continue using the linear perturbation expansion in equation (5.22). But much qualitative insight can still be gained by investigating the angular dependence of the microstructural distortion. Equation (5.22) tells us that the angular dependence of the distorted microstructure is given by $g_{eq}(r, \theta, \phi)\hat{\mathbf{r}}.\mathbf{E}.\hat{\mathbf{r}}$. If we integrate out the r and θ coordinates, we can obtain the angular dependence of the distortion in the shear plane, which can be shown to be $\propto \sin(2\phi) g_{eq}(\phi)$. Figure (5.14) shows the angular dependence of distorted microstructure in both the ordered and the disordered phases, which clearly shows a greater distortion in the disordered phase. This can be attributed to the fact that in the ordered state most of the nearest neighbors are located in the same plane aligned in the flow-vorticity plane, i.e. $\phi = 0$ (see inset in figure 5.14), and hence don't directly feel the distortive effect of shear ($\sin 2\phi = 0$). In our analysis so far, we haven't investigated the effect of radial separation on microstructural distortion. As per equation (5.22), the radial dependence of the microstructural distortion can be shown to be $\propto g(r)f(r)$, which can be obtained by integrating out all the angular coordinates. We next argue that $g(r)f(r)$ is most likely to be smaller in the ordered state as interparticle separations are larger there on an average, and $f(r)$ is expected to decay with distance

around the first peak as Bossis & Brady (1989) showed for hard-sphere suspensions. So, just like the angular distribution, the radial distribution of the particles can also be expected to cause a relatively smaller distortion in the ordered state in comparison to the disordered state. These arguments show, at least qualitatively, how the ordered states can minimize the distortion of its microstructure as compared to the disordered states. We end with a word of caution that this pair-wise model neglects the many body effects which are obviously important for non-dilute suspensions. The analysis here, therefore, should only be considered in a qualitative sense, though it will be shown later in section (5.4.3) that this model can lead to excellent collapse of the viscosity data from different simulations.

5.4.2 Rheological consequences of microstructural distortion

Next, we discuss the effect of the microstructural distortion on the stress in the suspension. The contribution to stress from the repulsive interaction is given by

$$\tau_R = \frac{1}{V}\sum_{i=1}^{N_p} -x_1 F_2^p - (\mathbf{R}_{SU}\mathbf{R}_{FU}^{-1}\mathbf{F}^p)_{12} \tag{5.23}$$

The second term on the right makes a negligible contribution to the stress as the repulsive interactions from the two compressive quadrants and the repulsive interactions from the two extensional quadrants (see figure 5.12) cancel each other out on an average, and hence lead to negligible velocity and consequently negligible stress. The first term in equation (5.23) can be expressed using pair distribution function as (Verberg *et al.*, 1997; Foss & Brady, 2000a)

$$\tau_R \sim -n^2 \int x_1\, F_2(\mathbf{r})\, g(\mathbf{r})\, d\mathbf{r} \tag{5.24}$$

We note that the equilibrium configuration would not lead to any interparticle shear stress, and any contribution is purely from the distortion in the microstructure due to the presence of shear. A characteristic feature of the distortion under shear is that it leads to accumulation of particles in the compressive quadrant and a depletion in the extensional quadrant at smaller separations as seen in figure (5.13). Since the repulsive force decays exponentially,

one can conclude from equation (5.24) that the positive contribution to stress from the compressive quadrant will dominate the negative contribution to stress in the extensional quadrant, thereby leading to a net positive contribution. From this we can also conclude that larger is the relative distortion between the compressive and the extensional quadrant, more will be the net stress. This explains the crossover seen in the interparticle contribution to stress, as at low shear rates the ordered phase shows a greater relative distortion, while at higher shear rates the disordered phase shows a greater relative distortion between the compressive and extensional quadrants.

The Brownian contribution to stress is more complicated due to the stochastic nature of the Brownian interactions. Bossis & Brady (1989) showed that the Brownian contribution to stress is given by

$$\tau_B = -\frac{kT}{V}\sum_{i=1}^{N_p}[\nabla\cdot(\mathbf{R}_{SU}\mathbf{R}_{FU}^{-1})]_{12} \tag{5.25}$$

It's possible to make progress with this expression by writing it in a form similar to equation (5.24), but that gets too complicated and is unnecessary for qualitative comparisons. Instead, by making a simple argument we show that the Brownian contribution to stress will behave similarly to the interparticle contribution. We begin by revisiting two points already made. First is that the configuration at equilibrium has no Brownian contribution to stress. Second is that relative to the equilibrium configuration, there are more particles at closer separation in the compressive quadrant under shear, and the exact opposite is true for the extensional quadrant. Now, we know that the Brownian motion will tend to homogenize the particle distribution, i.e. it will tend to restore the equilibrium configuration. Therefore, we conclude that Brownian interaction will cause the particles to repel each other at small separations in the compressive quadrant relative to the Brownian interaction at equilibrium. By the same argument, we can conclude that the Brownian interaction will cause the particles to attract each other at small separations in the extensional quadrant relative to the Brownian interaction at equilibrium. Since the Brownian interaction at equilibrium makes no contribution to shear stress, we conclude that the Brownian contribution to shear stress under shear can be understood in terms of a repulsive interaction in the compressive quadrant and an attractive interaction in the extensional quadrant, both of which will give

a positive contribution to stress. This explains the similar trend observed in the Brownian and the interparticle contributions to stress, and consequently the crossover between the ordered and disordered phase viscosity stemming from the Brownian interaction. It is also interesting to note that the ratio of interparticle to Brownian contributions to viscosity, reported in tables (5.5) and (5.6), is almost identical in both the ordered and disordered phase (3.06 vs. 2.84 at Pe=0.001), which further strengthens our above argument that Brownian contribution can be explained by an effective interparticle force.

5.4.3 Master Curve

Here we present viscosity data for various strengths of interparticle interaction and attempt to collapse them on a master curve using the model developed in section (5.4.1). The viscosity data for various strengths of interaction in ordered and disordered phases are shown in figures (5.16) and (5.15) respectively. Now, equations (5.22) and (5.24) suggest a collapse of data when the effective viscosity $\bar{\mu}_r$ is plotted against effective Peclet number $\bar{Pe}$. This plot is shown for the disordered phase in (5.17), where both types of $\bar{D}$ computed in this study, i.e. D_s^L and $D_c(k^*)$, are investigated for its efficacy. From the figure, it can be concluded that $D_c^L(k^*)$ collapses the data better than D_s^L, though the latter is satisfactory too. Also note that the generalized Stokes-Einstein relationship with $D_c^L(k^*)$ is not satisfied for our charge stabilized suspensions ($\bar{\mu}_r \neq 1$), unlike the hard-spheres suspensions which have been reported to satisfy such a relationship (Segre *et al.*, 1995; Banchio *et al.*, 1999). We also note that the effective viscosity is greater than unity ($\bar{\mu}_r > 1$) when using D_s^L as the effective diffusivity, which is consistent with earlier work on charge stabilized suspension (lmhof *et al.*, 1994). Next we present $\bar{\mu}_r$ vs. $\bar{Pe}$ plot for the ordered phase in figure (5.18). Note the figure only includes scaling with D_s^L as $D_c^L(k^*)$ could not be computed. Again, an excellent collapse of data for different strengths of interaction can be seen. Finally, in figure (5.19) we compare the scaled data for both the phases simultaneously, where $\bar{D} = D_s^L$ was used. In the range of shear rates investigated in this study, the ordered phase viscosity branch is mostly below the disordered phase viscosity branch and the crossover between the two branches occurs at $\bar{Pe} \approx 1$ and $\bar{\mu}_r \approx 1$. In figure (5.19) we have also shown a power law fit to the ordered

phase viscosity. The equation of the line is $\bar{\mu}_r = 0.7128\bar{Pe}^{-0.816}$, where the fit was computed only for the shear rate data in the range $\bar{Pe} < 10^3$. For $\bar{Pe} > 10^3$, the viscosity starts to deviate from the above power law fit and eventually plateaus at higher $\bar{Pe}$. At even higher shear rates ($\bar{Pe}$), an order to disorder transition takes place. The deviation from the power law behavior at higher shear rates is most likely due to the microstructural transition from strained crystals to sliding layers. In future studies, we will attempt to collapse both the ordered and disordered branches of viscosity on a single master curve, the success of which will depend on two factors: (i) the existence of a low shear Newtonian plateau in ordered states, and (ii) finding a better measure of structural relaxation in ordered states, perhaps $D_c(k^*)$ will prove to be adequate.

5.5 Conclusion

In conclusion, we numerically investigated the microstructure, diffusion and rheology in charge stabilized suspensions at a volume fraction of $\phi = 0.33$. It was shown that there exists a range of interaction strengths for which both the metastable ordered and disordered phases exists. This range was found to be a strong function of the shear rate. The effect of shear on the microstructure was characterized, and it was shown that the microstructural distortion in the ordered phase is much larger than in the disordered phase at very low rates of shear, while the reverse was found to be true at higher rates of shear. The cause for this behavior was investigated and it was concluded that the slow structural relaxation rate, i.e. diffusivity, in the ordered state was the cause for higher distortion of its microstructure at low shear rates, while at higher shear rates the favorable 3 dimensional distribution of particles led to a lower microstructural distortion in the same. As a direct consequence of this microstructural distortion, it was shown than the disordered phase has a lower viscosity than the ordered phase at low enough shear rates, while at higher shear rates the ordered phase was found to have a lower viscosity. This led to a crossover in the ordered and disordered phase branches of viscosity, which was found to be entirely due to the interparticle and Brownian contributions. We also successfully attempted to collapse the viscosity data at different strengths of interaction with long-time self-diffusivity and found that a crossover

Table 5.1: Energy per particle at equilibrium in the ordered and the disordered state as a function of interparticle strength

$F_0/(4/3kT/a)$	E_o/kT	E_d/kT
25	1.995	2.405
30	2.085	2.611
35	2.230	2.805
40	2.324	2.976
45	2.445	-
100	4.372	-
200	7.561	

Table 5.2: Various short and long-time Diffusivities in the ordered phase

F_0	D_s^s	D_L^s
35	0.7025	0.000626
40	0.7355	0.000545
45	0.7586	0.000408
50	0.7681	0.000265

between the two branches exists in this scaled space too. Surprisingly, this crossover was found to occur at $\bar{Pe} \approx 1$ and $\bar{\mu}_r \approx 1$.

Table 5.3: Various short and long-time Diffusivities in the disordered phase

F_0	D_s^s	D_L^s	$D_c^L(k_m)$
26	0.6116	0.0690	0.0395
35	0.6496	0.0449	0.0241
40	0.6724	0.0345	0.0209

Table 5.4: Short and long-time Diffusivities in a hard-sphere suspension at $\phi = 0.33$

D_s^s	D_L^s
0.3863	0.2155

Table 5.5: Contributions to viscosity for $F_0 = 35$ at different Pe for the ordered phase

Pe	μ_b	μ_h	μ_p
0.001	171.230	2.359	486.401
0.010	28.110	2.363	81.718
0.050	5.700	2.369	17.121
0.100	3.068	2.373	8.748
0.500	-	-	-
1.000	0.508	2.389	1.413

Table 5.6: Contributions to viscosity for $F_0 = 35$ at different Pe for the disordered phase

Pe	μ_b	μ_h	μ_p
0.001	7.060	2.466	21.664
0.010	6.360	2.467	20.363
0.050	3.500	2.471	15.719
0.100	2.920	2.478	12.292
0.500	1.460	2.521	5.809
1.000	0.772	2.559	4.099

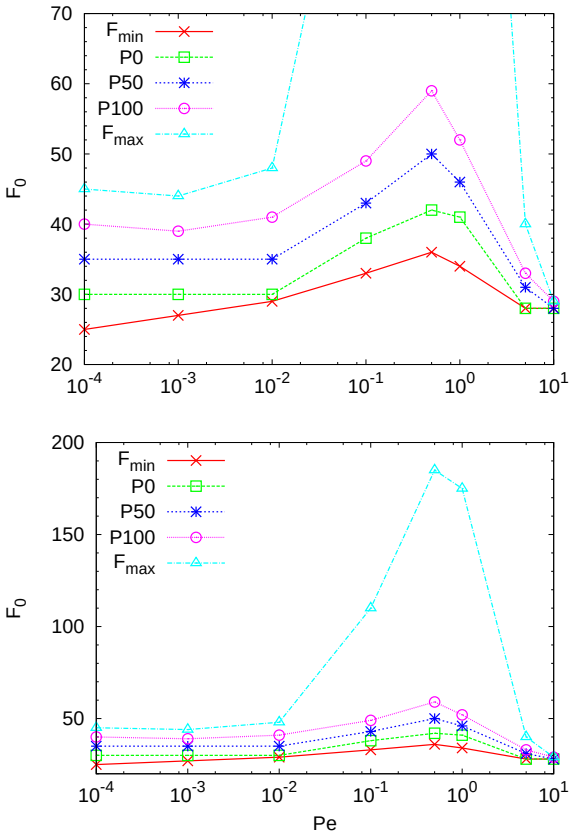

Figure 5.1: Phase diagram showing the existence of both the ordered and disordered states as a function of Pe and F_0. Bottom figure is the full version of the top figure. F_0 is non-dimensionalized by $4kT/3a$.

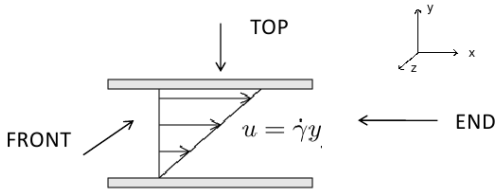

Figure 5.2: Definition of front, top and end views.

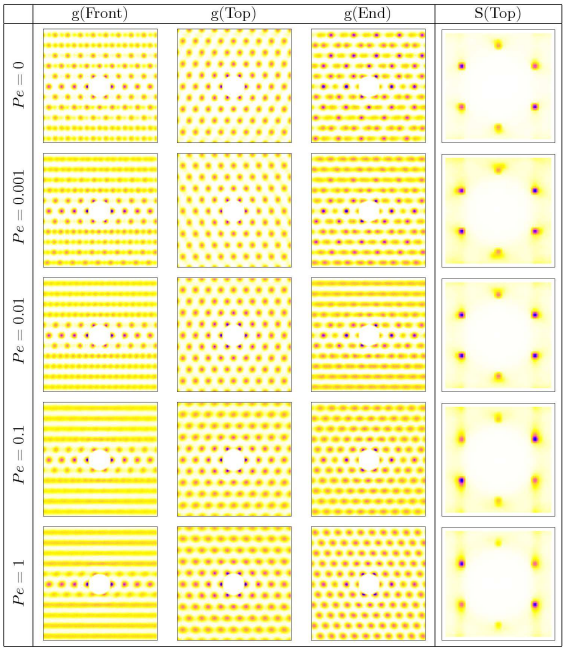

Figure 5.3: Ordered Phase: Pair distribution functions and Structure factors in a Suspension of Spherical Particles at $\phi = 0.33$ and $F_0 = 35$

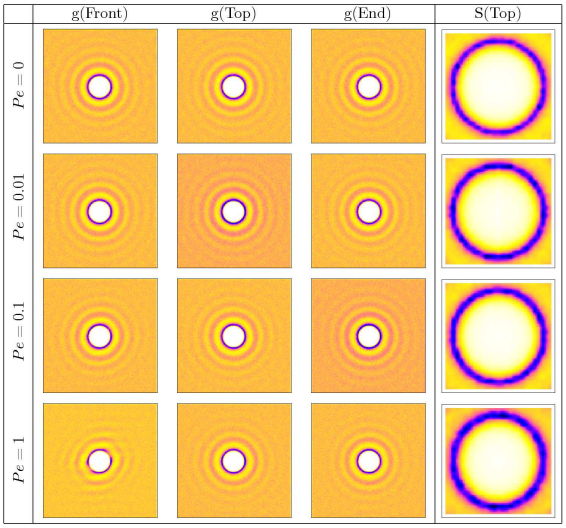

Figure 5.4: Disordered Phase: Pair distribution functions and Structure factors in a Suspension of Spherical Particles at $\phi = 0.33$ and $F_0 = 35$

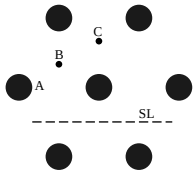

Figure 5.5: FCC close packed sites A, B, and C. Also shown is the sliding layer configuration (SL)

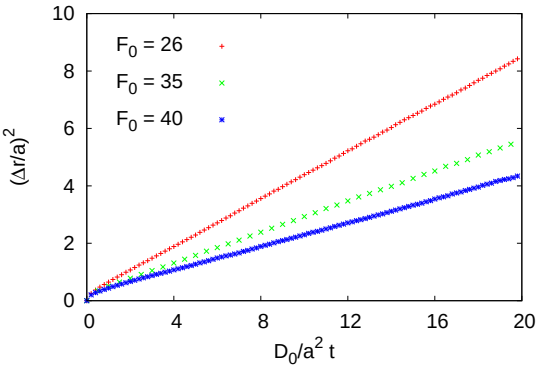

Figure 5.6: Mean square displacement (MSD) in the disordered phase with time for three different interparticle interaction strength

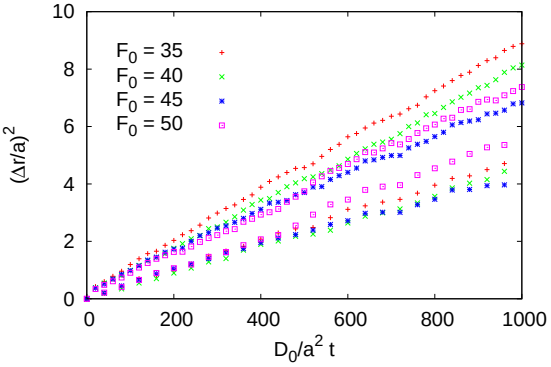

Figure 5.7: Top four curves: mean square displacement (MSD) in the ordered phase with time for four different strengths of the repulsive interaction. Bottom four curves: MSD of the center of mass of a periodic cell with time for the same four strengths of repulsive interaction.

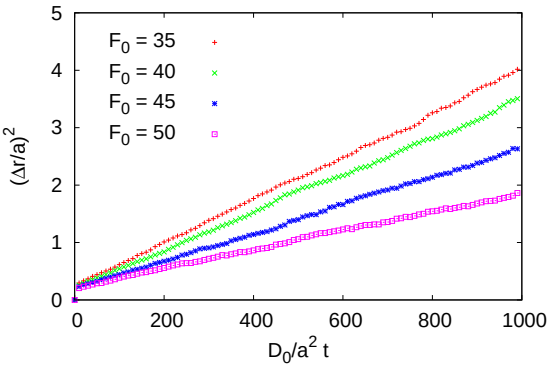

Figure 5.8: Mean square displacements in the ordered phase for four different strengths of the repulsive interaction in the center of mass frame.

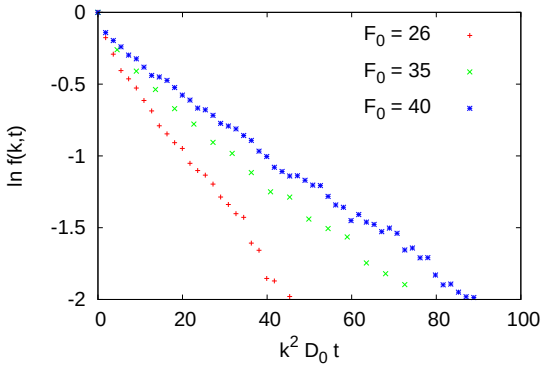

Figure 5.9: Decay of the normalized intermediate scattering functions f(k,t) at the peak of the structure factor for disordered phase at three different interaction strengths.

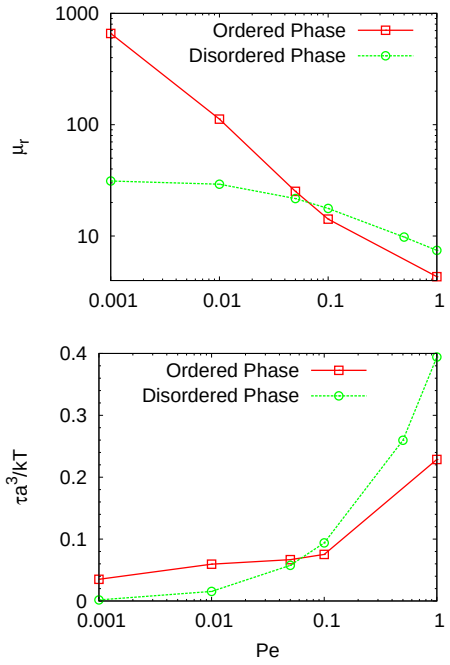

Figure 5.10: Stress and Viscosity at different Pe for $\phi = 0.33$ and $F_0 = 35$.

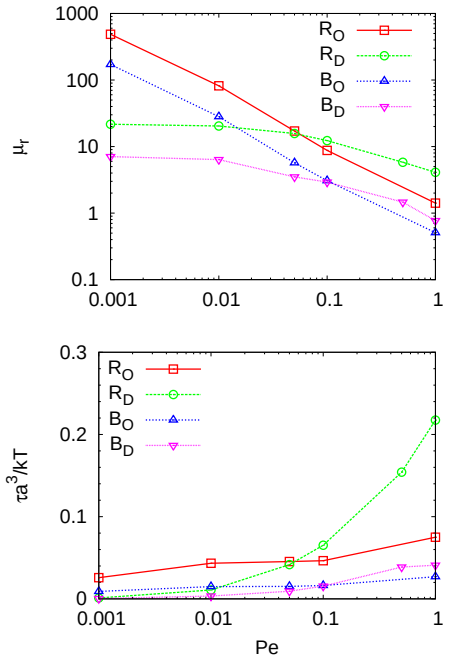

Figure 5.11: Contributions to viscosity at different Pe for $\phi = 0.33$ and $F_0 = 35$ from hydrodynamic (H), Brownian (B) and Repulsive (R) interactions. Subscript 'O' refers to an ordered phase, while subscript 'D' refers to a disordered phase.

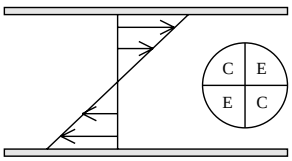

Figure 5.12: Compression and Extension Quadrant in shear flow denoted by C and E respectively.

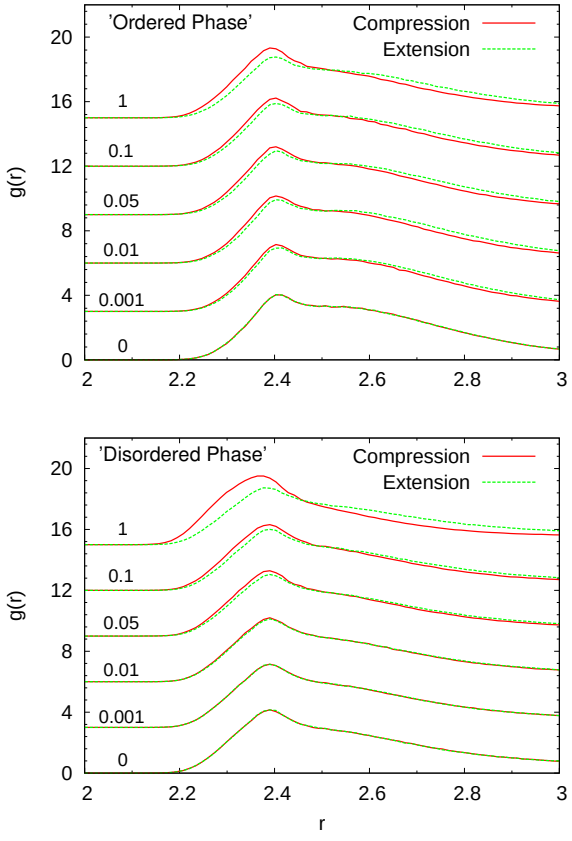

Figure 5.13: g(r) at different Pe for $\phi = 0.33$ and $F_0 = 35$ in the compressional quadrant and extensional quadrant. Curves for different Pe are shifted by 3.0 in the vertical direction.

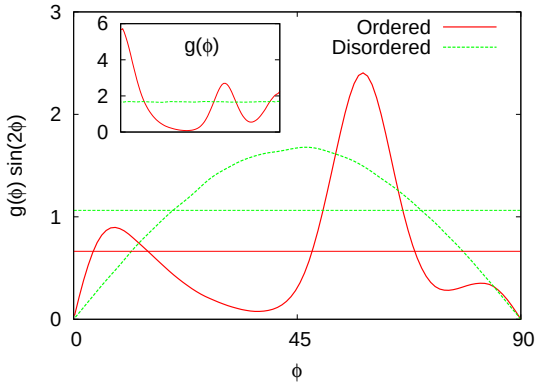

Figure 5.14: g(ϕ) (for $r < 2.5a$ in the compressional quadrant) at rest for $\phi = 0.33$ and $F_0 = 35$. Both the ordered and disordered states are shown.

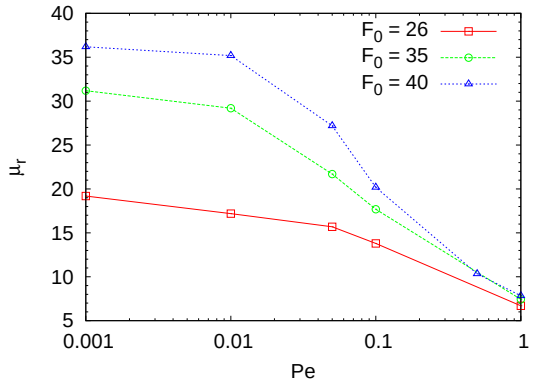

Figure 5.15: Viscosity in the disordered phase for 3 different interaction strengths

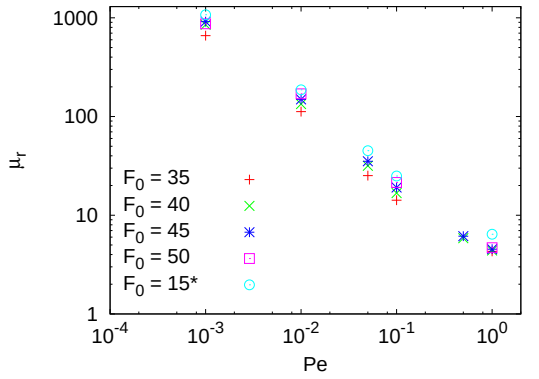

Figure 5.16: Viscosity in the ordered phase for 5 different interaction strengths. All data is for $\phi = 0.33$ except for $F_0 = 15^*$ which is for $\phi = 0.42$ and $\kappa a = 10.9$.

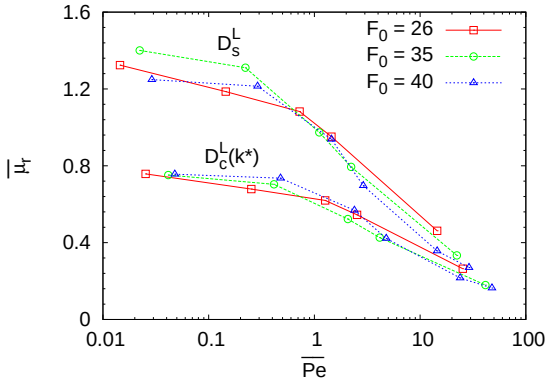

Figure 5.17: Collapse of the viscosity data in the disordered phase with D_s^L and D_c^L. $\bar{\mu}_r = \mu_r * D_{eff}$ and $\bar{Pe} = PeD_0/D_{eff}$, where D_{eff} is either D_s^L and D_c^L.

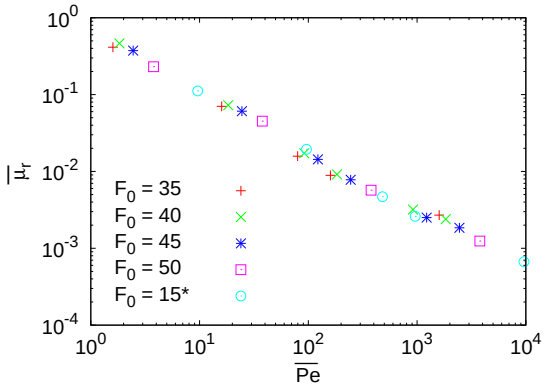

Figure 5.18: Collapse of the viscosity data in the ordered phase with D_s^L. $\bar{\mu}_r = \mu_r D_s^L$ and $\bar{Pe} = PeD_0/D_s^L$. Also see figure (5.16) for notation.

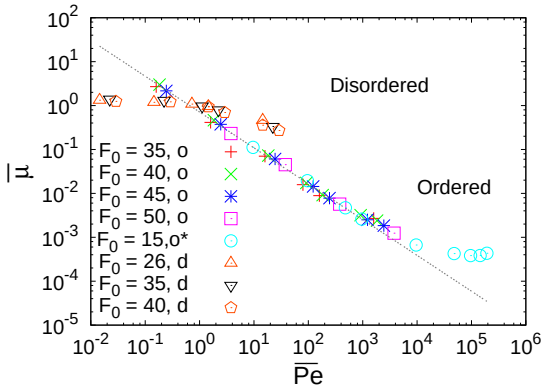

Figure 5.19: Comparing the collapse of the viscosity data with D_s^L in both the ordered and disordered phases from figure (5.17) and figure (5.18). The equation of straight line in the plot is $\bar{\mu} = 0.7128\bar{Pe}^{-0.816}$ which was obtained by fitting a power law to the ordered phase viscosity data for $\bar{Pe} < 10^3$.

References

Ackerson, B.J. 1990. Shear induced order and shear processing of model hard sphere suspensions. *Journal of Rheology*, **34**(4), 553–589.

Ackerson, B.J., Hayter, J.B., Clark, N.A., & Cotter, L. 1986. Neutron scattering from charge stabilized suspensions undergoing shear. *Journal Chemical Physics*, **84**(4), 2344–2349.

Ball, R.C., & Melrose, J.R. 1997. A simulation technique for many spheres in quasi-static motion under frame-invariant pair drag and Brownian forces. *Physica A*, **247**, 444–472.

Banchio, A.J., Nägele, G., & Bergenholtz, J. 1999. Viscoelasticity and generalized StokesEinstein relations of colloidal dispersions. *Journal of Chemical Physics*, **111**(18), 8721–8740.

Barnes, H.A. 1999. The yield stress – a review or '$\pi\alpha\nu\tau\alpha\rho\epsilon\iota$' – everything flows? *Jounral of Non-Newtonian Fluid Mechanics*, **81**, 133–178.

Barnes, H.A., & Walters, K. 1985. The yield stress myth. *Rheologica Acta*, **24**, 323–326.

Batchelor, G.K. 1977. The effect of Brownian motion on the bulk stress in a suspension of spherical particles. *Journal of Fluid Mechanics*, **83**, 97–117.

Bell, G.M., Levine, S., & McCartney, L.N. 1970. Approximate Methods of Determining the Double-Layer Free Energy of Interaction between Two Charged Colloidal Spheres. *Journal of Colloid and Interface Science*, **33**(3), 335–359.

Binder, Kurt. 1987. Theory of first-order phase transitions. *Reports on Progress in Physics*, **50**, 783–859.

Blaak, R., Auer, S., Frenkel, D., & Löwen, H. 2004. Crystal nucleation of colloidal suspensions under shear. *Physical Review Letters*, **93**(6), 068303.

Bossis, G., & Brady, J.F. 1984. Dynamic simulations of sheared suspensions. I. General method. *Journal of Chemical Physics*, **80**(10), 5141–5154.

Bossis, G., & Brady, J.F. 1989. Rheology of Brownian Suspensions. *Journal of Chemical Physics*, **91**(3), 1866–1874.

Brady, J.F. 1993. The rheological behavior of concentrated colloidal dispersions. *Journal of Chemical Physics*, **99**(1), 567–581.

Brady, J.F., & Vicic, M. 1995. Normal Stresses in colloidal dispersions. *Journal of Rheology*, **39**(3), 545–565.

Butler, S., & Harrowell, P. 1995. The shear induced disordering transition in a colloidal crystal: Nonequilibrium Brownian dynamic simulations. *Journal of Chemical Physics*, **103**(11), 4653–4671.

Butler, S., & Harrowell, P. 2002. Factors determining crystal-liquid coexistence under shear. *Nature*, **415**, 1008–1010.

Butler, S., & Harrowell, P. 2003. Simulation of the coexistence of a shearing liquid and a strained crystal. *Journal of Chemical Physics*, **118**(9), 4115–4126.

Chen, L.B., Zukoski, C.F., Ackerson, B.J., Hanley, H.J.M, Straty, G.C., Barker, J., & Glinka, C.J. 1992. Structural changes and orientational order in a sheared colloidal suspensions. *Physical Review Letters*, **69**(4), 688–693.

Chen, L.B., Ackerson, B.J., & Zukoski, C.F. 1994a. Rheological and Microstructural transitions in colloidal crystals. *Langmuir*, **10**, 2817–2829.

Chen, L.B., Ackerson, B.J., & Zukoski, C.F. 1994b. Rheological consequences of microstructural transitions in colloidal crystals. *Journal of Rheology*, **38**(2), 193–215.

Chow, M.K., & Zukoski, C.F. 1995. Nonequilibrium behavior of dense suspensions of uniform particles: Volume fraction and size dependence of rheology and microstructure. *Journal of Rheology*, **39**(1), 33–59.

Clark, N. A., & Ackerson, B.J. 1980. Observation of the coupling of concentration fluctuations to steady-state shear flow. *Physical Review Letters*, **44**(15), 1005–1008.

Foss, D.R., & Brady, J.F. 2000a. Brownian Dynamics simulation of hard-sphere colloidal dispersions. *Journal of Rheology*, **44**(3), 629–651.

Foss, D.R., & Brady, J.F. 2000b. Structure, diffusion and rheology of Brownian suspensions by Stokesian Dynamics simulation. *Journal of Fluid Mechanics*, **407**, 167–200.

Frenkel, Daan. 1999. Entropy-driven phase transitions. *Physica A*, **263**, 26–38.

Gray, J.J., & Bonnecaze, R.T. 1998. Rheology and dynamics of sheared arrays of colloidal particles. *Journal of Rheology*, **42**(5), 1121–1151.

Horn, F.M., Richtering, W., Bergenholtz, J., Willenbacher, N., & Wagner, N. J. 2000. Hydrodynamic and Colloidal Interactions in Concentrated Charge-Stabilized Polymer Dispersions. *Journal of Colloid and Interface Science*, **225**, 166–178.

Imhof, A., van Blaaderen, A., & Dhont, J.K.G. 1994. Shear Melting of Colloidal Crystals of Charged Spheres Studied with Rheology and Polarizing Microscopy. *Langmuir*, **10**, 3477–3484.

Lambert, J.D. 1997. *Numerical methods for ordinary differential systems: The inital value problem*. John Wiley and Sons Ltd.

lmhof, A., van Blaaderen, A., Maret, G., Mellema, J., & Dhont, J.K.G. 1994. Comparison between the long-time self-diffusion and low shear viscosity of concentrated dispersions of charged colloidal silica spheres. *Journal of Chemical Physics*, **100**(3), 2170–2181.

Loose, W., & Ackerson, B.J. 1994. Model calculations for the analysis of scattering data from layered structures. *Journal of Chemical Physics*, **101**(9), 7211–7220.

Mock, E.B., & Zukoski, C.F. 2007. Investigating microstructure of concentrated suspensions of anisotropic particles under shear by small angle neutron scattering. *Journal of Rheology*, **51**(3), 541–559.

Russel, W.B. 1976. Low-Shear Limit of the Secondary Electroviscous Effect. *Journal of Colloid and Interface Science*, **55**(3), 590–604.

Russel, W.B., D.A.Saville, & Schowalter, W.R. 1989. *Colloidal Dispersions*. Cambridge University Press.

Saad, Y. 2003. *Iterative Methods for Sparse Linear Systems*. Society for Industrial and Applied Mathematics.

Segre, P.N., Meeker, S.P., Pusey, P.N., & Poon, W.C.K. 1995. Viscosity and Structural Relaxation in Suspensions of Hard-Sphere Colloids. *Physical Review Letters*, **75**(5), 958–961.

Sirota, E.B., Ou-Yang, H.D., Sinha, S.K., Chaikin, P.M., Axe, J.D., & Fujii, Y. 1989. Complete phase diagram of a charged colloidal system: A synchrotron X-Ray scattering study. *Physical Review Letters*, **62**(13), 1524–1527.

Speedy, R.J. 1997. Pressure of the metastable hard-sphere fluid. *Journal of Physics Condensed Matter*, **9**(41), 8591–8599.

Stevens, M.J., & Robbins, M.O. 1993. Simulation of shear-induced melting and ordering. *Physical Review E*, **48**(5), 3778–3792.

Stevens, M.J., Robbins, M.O., & Belak, J.F. 1991. Shear Melting of Colloids: A Nonequilibrium Phase Diagram. *Physical Review E*, **66**(23), 3004–3007.

van Blaaderen, A., Peetermans, J., Matet, G., & Dhont, J.K.G. 1992. Long-time self-cliff usion of spherical colloidal particles measured with fluorescence recovery after photobleaching. *Journal of Chemical Physics*, **96**(6), 4592–4603.

van der Vorst, B., van den Ende, D., Aelmans, N.J.J., & Mellema, J. 1997. Shear viscosity of an ordering latex suspension. *Physical Review E*, **56**(3), 3119–3126.

Verberg, R., de Schepper, I.M., & Cohen, E.G.D. 1997. Viscosity of colloidal suspensions. *Physical Review E*, **55**(3), 3143–3158.

Versmold, H., Musa, S., & Dux, Ch. 2001. Shear-induced structure in concentrated dispersions: Small angle synchrotron X-ray and neutron scattering. *Langmuir*, **17**, 6812–6815.

Woodcock, L.V. 1981. Glass Transition in the Hard-Sphere Model and Kauzmann's paradox. *Annals of the New York Academy of Sciences*, **371**, 274–298.

Yan, Y.D., & Dhont, J.K.G. 1993. Shear induced structure distortion in nonaqueous dispersions of charged colloidal spheres via light scattering. *Physica A*, **198**, 78–107.

Chapter 6

Fast Lubrication Dynamics Algorithm

6.1 Formulation

6.1.1 Governing Equation

The motion of colloidal particles is governed by the stochastic Langevin equation

$$m\frac{d\mathbf{U}}{dt} = \mathbf{F}^H + \mathbf{F}^B + \mathbf{F}^P \tag{6.1}$$

In the above equation m is the mass/moment of inertia of the particle, $\mathbf{U}$ is the generalized velocity/angular velocity vector, and $\mathbf{F}^H$, $\mathbf{F}^B$, and $\mathbf{F}^P$ are the generalized force/torque vectors due to the hydrodynamic interaction, thermal fluctuations (Brownian motion), and interparticle interaction respectively. Each of the vectors $\mathbf{U}$, $\mathbf{F}^H$, $\mathbf{F}^B$, and $\mathbf{F}^P$ have $6N_p$ elements, where N_p is the number of particles in the system. On the time scales of interest, inertia of the particles can be neglected to obtain the following form of the governing equation

$$\mathbf{F}^H + \mathbf{F}^B + \mathbf{F}^P = 0 \tag{6.2}$$

The above form was used in this work. In the following sections, we discuss the computation of all the above three types of interactions i.e., $\mathbf{F}^H$, $\mathbf{F}^B$, and $\mathbf{F}^P$.

6.1.2 Hydrodynamic Interaction ($\mathbf{F}^H$)

Colloidal particles are very small, usually having a characteristic length smaller than $10^{-6}m$. Due to its small size, Reynolds number for the fluids motion around the particle is usually

negligible, and hence the linear Stokes equation may be used. In Stokes flow, the hydrodynamic force on a particle is a linear function of the fluid velocity, and this linear relationship is usually expressed in the form of a resistance tensor $\mathbf{R}$. In this work, we will restrict ourselves to forces/torques $\mathbf{F}$, and stresslets $\mathbf{S}$ on the particles in a linear ambient flow, which is customarily broken into uniform velocities/angular velocities $\mathbf{U}^\infty$, and a rate of strain tensor $\mathbf{E}^\infty$. Then by definition of the resistance tensor, we have the following relationship between the aforementioned quantities

$$\begin{pmatrix} \mathbf{F} \\ \mathbf{S} \end{pmatrix} = \mathbf{R} \begin{pmatrix} \mathbf{U}^\infty - \mathbf{U} \\ \mathbf{E}^\infty \end{pmatrix} \tag{6.3}$$

6.1.2.1 Stokesian dynamics (SD)

In Stokesian dynamics, the total resistance tensor is expressed as

$$\mathbf{R} = (\mathbf{I} - \boldsymbol{\mathcal{R}})^{-1} \mathbf{R}_{1B} + \mathbf{R}_{lub} \tag{6.4}$$

where $\boldsymbol{\mathcal{R}}$ is the reflection operator based on truncated expansion, while $\mathbf{R}_{lub}$ is the lubrication interaction tensor based on the asymptotic solution of two particles separated by very small gaps.

6.1.2.2 Fast Lubrication Dynamics (FLD)

In this method, we express the overall resistance tensor $\mathbf{R}$ as a sum of a diagonal isotropic resistance tensor $\mathbf{R}_0$ and a pairwise interaction tensor $\mathbf{R}_\delta$ coming from the asymptotic approximation for the lubrication contribution $\mathbf{R}_{lub}$ as

$$\mathbf{R} = \mathbf{R}_0 + \mathbf{R}_\delta \tag{6.5}$$

The $\mathbf{R}_\delta$ interaction is summed pairwise, the computation of which is detailed next. Consider a pair of particles labeled as particle '1' and '2' respectively as shown in figure (6.1). Let the fluid velocity be $\mathbf{v}_1^\infty(\mathbf{x}_1)$ and $\mathbf{v}_2^\infty(\mathbf{x}_2)$ at the center of the respective particles, and let

$\boldsymbol{\Omega}^{\infty}$ be the rotational velocity of the fluid. Also, let $\mathbf{u}_1$,$\mathbf{u}_2$, $\boldsymbol{\omega}_1$, and $\boldsymbol{\omega}_2$ be the translational and rotational velocity of the two particles. Then, based on these, we define the following new quantities: $\mathbf{u}_1^r$,$\mathbf{u}_2^r$, $\boldsymbol{\omega}_1^r$,$\boldsymbol{\omega}_2^r$, $\mathbf{u}_1^c$, and $\mathbf{u}_2^c$

$$\begin{array}{cc} \underline{\text{particle 1}} & \underline{\text{particle 2}} \\ \mathbf{u}_1^r = \mathbf{v}_1^{\infty}(\mathbf{x}_1) - \mathbf{u}_1 & \mathbf{u}_2^r = \mathbf{v}_1^{\infty}(\mathbf{x}_2) - \mathbf{u}_2 \\ \boldsymbol{\omega}_1^r = \boldsymbol{\Omega}^{\infty} - \boldsymbol{\omega}_1 & \boldsymbol{\omega}_2^r = \boldsymbol{\Omega}^{\infty} - \boldsymbol{\omega}_2 \\ \mathbf{u}_1^c = \mathbf{u}_1^r + \boldsymbol{\omega}_1^r \times a\mathbf{d} & \mathbf{u}_2^c = \mathbf{u}_2^r - \boldsymbol{\omega}_2^r \times a\mathbf{d} \end{array} \tag{6.6}$$

where $\mathbf{d}$ is the unit vector along the line joining the centers of two spheres (figure 6.1) while a is the radius of spheres. The forces and torques on the two particles $\mathbf{F}_1$, $\mathbf{F}_2$, $\mathbf{T}_1$, and $\mathbf{T}_2$ are then easily defined in terms of three scalar resistances X^A, Y^A and Y_r^C as follows

$$\begin{aligned} \mathbf{F}_1 &= \left(X^A \mathbf{dd} + Y^A(\boldsymbol{\delta} - \mathbf{dd})\right)(\mathbf{u}_1^c - \mathbf{u}_2^c) \\ \mathbf{F}_2 &= -\mathbf{F}_1 \\ \mathbf{T}_{cm} &= a\mathbf{d} \times \mathbf{F}_1 \\ \mathbf{T}_r &= Y_r^C(\boldsymbol{\delta} - \mathbf{dd})(\boldsymbol{\omega}_1^r - \boldsymbol{\omega}_2^r) \\ \mathbf{T}_1 &= \mathbf{T}_{cm} + \mathbf{T}_r \\ \mathbf{T}_2 &= \mathbf{T}_{cm} - \mathbf{T}_r \end{aligned} \tag{6.7}$$

The three scalar resistance are a function of the interparticle gap δ as are given in the following equation (Kim & Karrila, 1991; Ball & Melrose, 1997)

$$\begin{aligned} X^A &= 6\pi\mu a \left(\frac{a}{4\delta} + \frac{9}{40}\log\frac{a}{\delta}\right) \\ Y^A &= 6\pi\mu a \left(\frac{1}{6}\log\frac{a}{\delta}\right) \\ Y_r^C &= 8\pi\mu a^3 \left(\frac{3}{40}\log\frac{a}{\delta}\right) \end{aligned} \tag{6.8}$$

Note that the term Y_r^C given in Ball & Melrose (1997), denoted by a_{pu}, has an incorrect coefficient (3/160 instead of 3/40 in the expression above). Forces and torques due to the uniform rate of strain tensor $\mathbf{E}^{\infty}$ can similarly be obtained by noting that due to $\mathbf{E}^{\infty}$ we have $\mathbf{u}_1^c - \mathbf{u}_2^c = 2a\mathbf{E}^{\infty}\mathbf{d}$ and $\boldsymbol{\omega}_1^r = \boldsymbol{\omega}_2^r = 0$. Substituting this in equation (6.7), we obtain the following relationship between $\mathbf{F}_1$, $\mathbf{F}_2$, $\mathbf{T}_1$, $\mathbf{T}_2$ and $\mathbf{E}^{\infty}$

$$\begin{aligned} \mathbf{F}_1 &= -\mathbf{F}_2 &&= \left(X^A \mathbf{dd} + Y^A(\boldsymbol{\delta} - \mathbf{dd})\right)(2a\mathbf{E}^\infty \cdot \mathbf{d}) \\ \mathbf{T}_1 &= \mathbf{T}_2 &&= a\mathbf{d} \times \mathbf{F}_1 \end{aligned} \tag{6.9}$$

Next we discuss the isotropic resistance tensor $\mathbf{R}_0$ used in this work. We first note that $\mathbf{R}_0$ consists of three different scalars R^0_{FU}, $R^0_{T\Omega}$, and R^0_{SE}, respectively denoting force-velocity, torque-angular velocity, and stresslet-rate of strain coupling respectively, i.e.

$$\mathbf{R}_0 = \begin{pmatrix} R^0_{FU}\boldsymbol{\delta} & \mathbf{0} & \mathbf{0} \\ \mathbf{0} & R^0_{T\Omega}\boldsymbol{\delta} & \mathbf{0} \\ \mathbf{0} & \mathbf{0} & R^0_{SE}\boldsymbol{\delta} \end{pmatrix} \tag{6.10}$$

In this work, R^0_{FU} and $R^0_{T\Omega}$ were chosen to match the short-time translational and rotational self-diffusivity obtained from SD. The short-time self-diffusivity is related to the mobility of the particle. If $M_{UF} = R^{-1}_{FU}$ is the full $6N \times 6N$ mobility tensor of the N particle system, then the translational and rotational short-time self-diffusivity, denoted here by D_s and D^r_s respectively, are given by

$$D_s = kT\langle (M_{uF})_{ii} \rangle = \frac{kT}{3N}\langle \mathrm{trace}(M_{uF}) \rangle \tag{6.11a}$$

$$D^r_s = kT\langle (M_{\omega T})_{ii} \rangle = \frac{kT}{3N}\langle \mathrm{trace}(M_{\omega T}) \rangle \tag{6.11b}$$

where M_{uF} and $M_{\omega T}$ denote $3N \times 3N$ block sub-matrices of M_{UF} representing the (velocity, force) and (angular velocity, torque) coupling respectively and $\langle \cdot \rangle$ represents an ensemble average. To compute these quantities exactly for a given configuration using SD is computationally intensive, as it requires $O(N)$ distinct simulations with the $O(N \ln N)$ algorithm. Sierou & Brady (2001) gave an efficient algorithm to compute the short-time translational and rotational diffusivity using a sampling technique with uncorrelated random numbers. We follow their approach here. In short, an external generalized force/torque vector $\mathbf{F}^e$ of length $6N_p$ is applied on the system of particles, with $\mathbf{F}^e$ satisfying: $\langle \mathbf{F}^e \rangle = 0$ and $\langle F^e_i F^e_j \rangle = \delta_{ij}$.

The resulting velocity/angular velocity $\mathbf{U}^e$ of the force-free particles satisfies

$$U_i^e = (M_{UF})_{ij} F_j^e \tag{6.12}$$

The ensemble average of the dot product $\langle \mathbf{U}^e \cdot \mathbf{F}^e \rangle$ therefore satisfies

$$\langle U_i^e F_i^e \rangle = \langle (M_{UF})_{ii} \rangle \tag{6.13}$$

To extract the translational and rotational diffusivity, the dot product in the above equation is restricted to the components representing (velocity, force) and (angular velocity, torque) respectively. The convergence of diffusivity in this random sampling process depends upon both the number of random force/torque vectors employed per Monte Carlo configuration, and the number of Monte Carlo configurations employed. The convergence behavior for both sampling parameters is illustrated in Figure (6.2) for a volume fraction of $\phi = 0.5$ and two different system sizes with $N = 64$ and $N = 1000$ particles. The thin lines in the figure show the convergence in the translational diffusivity with the number of random force/torque vectors employed per configuration, while the thick line shows the same quantity averaged over all the individual configurations in the figure. From the theory of the variance in the mean of random uncorrelated numbers, the difference between the true mean and the computed mean (standard deviation) is expected to decay as $N_R^{-1/2}$, where N_R is the number of realizations and applies both to the number of random force/torque vectors employed per configuration and the number of Monte Carlo configurations employed for computing the mean. To better quantify the convergence behavior, we computed the coefficient of the $N_R^{-1/2}$ decay term. These coefficients, non-dimensionalized by the corresponding converged diffusivity, are $(.112, .032)$ and $(.031, .004)$ for the 64 and 1000 particle system respectively, where the first number in parenthesis corresponds to the convergence with number of force/torque vectors employed, while the second number in the parenthesis corresponds to the convergence with the number of Monte Carlo configurations. The numbers in the parenthesis are essentially the standard deviation of the corresponding set of numbers whose mean is being computed. The above numbers reveal that the convergence

with the number of random force/torque vectors is almost an order of magnitude slower than the convergence with the number of Monte Carlo configurations. In addition, as expected, the convergence is faster for larger system size. For lower volume fractions, the convergence was found to be faster than the $\phi = 0.5$ case discussed here. In this work, we obtained the diffusivity by averaging over one hundred independent configurations, with ten random force/torque vectors $\mathbf{F}^e$ employed per configuration. Diffusivity from FLD simulations can be similarly computed. As noted earlier, the values of R^0_{FU} and $R^0_{T\Omega}$ were chosen so that D_s and D^r_s matched the corresponding values from SD. We employed a system size of $N = 1000$ particles for this matching procedure. This procedure essentially matches the average of the eigenvalues of the mobility matrices obtained from the two algorithms. This should be obvious from equation (6.11). It would also be interesting to compare the agreement in the eigenvalue spectrum of the two mobility matrices. These comparisons are shown in Figures (6.3) and (6.4) for the translational and rotational mobility matrix respectively. For each of these plots, we have used two different flavors of FLD denoted as δ FLD and $\delta - \log\delta$ FLD. In the δ FLD version all the $\log\delta$ level terms are omitted and only $1/\delta$ terms are retained; in the $\delta - \log\delta$ version all the terms up to the $\log\delta$ level are retained. As could be seen in these plots, a considerably better agreement in the eigenvalue spectrum is obtained with the $\delta - \log\delta$ FLD version than with the δ FLD . We now report the best fit values of R^0_{FU}, $R^0_{T\Omega}$, and R^0_{SE} resistance as detailed above. These are shown in figures (6.5) and (6.6) for the $\delta - \log\delta$ FLD version and δ FLD version respectively. A lubrication cutoff of $2.5a$ was used in FLD for this calculation. We also briefly note that the R^0_{SE} is obtained by matching the viscosity obtained in FLD simulations with that obtained from SD simulations. Again, Montecarlo configurations were employed for this matching procedure.

6.1.3 Brownian Interaction ($\mathbf{F}^B$)

Brownian forces and torques can be obtained from fluctuation dissipation theorem and equipartition of energy (Russel *et al.*, 1989), which dictates

$$\begin{aligned} < \mathbf{F}^B > &= 0 \\ < \mathbf{F}^B \mathbf{F}^B > &= 2kT\mathbf{R}_{FU}/\Delta t \end{aligned} \tag{6.14}$$

Brownian forces and torques due to the isotropic resistance is easily obtained as

$$\mathbf{F} = \sqrt{\mathbf{R}_0^{FU}}\,\boldsymbol{\beta} \tag{6.15}$$

where $\boldsymbol{\beta}$ is a vector of uncorrelated random numbers of length $6N$ whose individual components satisfy

$$\langle \beta_i \rangle = 0 \tag{6.16a}$$

$$\langle \beta_i \beta_j \rangle = \delta_{ij} \tag{6.16b}$$

The Brownian forces and torques stemming from the $\mathbf{R}_\delta$ interaction can be computed pairwise. This is similar to the technique of Ball & Melrose (1997), which is reproduced here for completeness. In this method, we first define three mutually orthogonal vectors $\mathbf{p}$, $\mathbf{q}$, and $\mathbf{d}$. For each pair, we also define 5 random numbers α_1–α_5 satisfying

$$\langle \alpha_i \rangle = 0 \tag{6.17a}$$

$$\langle \alpha_i \alpha_j \rangle = \delta_{ij} \tag{6.17b}$$

Based on these quantities, the Brownian forces and torques satisfying equation (6.14) are easily obtained as follows

$$
\begin{aligned}
\mathbf{F}_1 &= \sqrt{X^A}\,\mathbf{d}\,\alpha_1 \;+\; \sqrt{Y^A}\,(\mathbf{p}\,\alpha_2 + \mathbf{q}\,\alpha_3) \\
\mathbf{F}_2 &= -\mathbf{F}_1 \\
\mathbf{T}_{cm} &= a\mathbf{d} \times \mathbf{F}_1 \\
\mathbf{T}_r &= \sqrt{Y_r^C}\,(\mathbf{p}\,\alpha_4 + \mathbf{q}\,\alpha_5) \\
\mathbf{T}_1 &= \mathbf{T}_{cm} + \mathbf{T}_r \\
\mathbf{T}_2 &= \mathbf{T}_{cm} - \mathbf{T}_r
\end{aligned}
\tag{6.18}
$$

6.1.4 Method of Solution

To solve the governing equation (6.2), we substitute $\mathbf{F}^H$, $\mathbf{F}^B$, $\mathbf{F}^P$ to obtain the following system of equations for the unknown velocities of the particles

$$
\mathbf{R}_{FU}(\mathbf{U}^\infty - \mathbf{U}) = -\left(\mathbf{R}_{FE}\mathbf{E}^\infty + \mathbf{F}^P + \mathbf{F}^B\right) \tag{6.19}
$$

Since the matrix $\mathbf{R}_{FU}$ is symmetric and positive definite, we used the conjugate gradient algorithm (Saad, 2003). Once the velocities are known, the unknown stresslets $\mathbf{S}$ can be computed in a post-processing step as

$$
\mathbf{S} = \mathbf{R}_{SU}(\mathbf{U}^\infty - \mathbf{U}) + \mathbf{R}_{SE}\mathbf{E}^\infty \tag{6.20}
$$

To evolve the microstructure in time, we used the midpoint method which belongs to the family of second-order explicit Runge-Kutta method (Lambert, 1997). The total shear stress τ in the suspension is found as

$$
\Sigma = 2\mu_0\mathbf{E}^\infty + \frac{1}{V}\sum_{i=1}^{N_p} -\mathbf{x}\mathbf{F}^P - \mathbf{x}\mathbf{F}^B + \mathbf{S} \tag{6.21}
$$

where the summation in the above equation is over all the particles in a control volume V, which in this work is taken as the periodic cell. Also note that the total stress tensor $\mathbf{\Sigma}$ is symmetric, as there are no external torques acting on the system and interparticle interactions are central (Batchelor, 1977).

6.2 Preconditioner

Here we discuss some preconditioning strategies to speed-up the convergence of conjugate gradient algorithm. As a reminder, we solve the following system of equations in FLD to obtain the unknown velocities/angular velocities $\mathbf{U}$ of the particles

$$\mathbf{R}_{FU}\mathbf{U} = -(\mathbf{F}^p + \mathbf{F}^B + \mathbf{R}_{FE}\mathbf{E}^\infty) \tag{6.22}$$

The rate of convergence of the iterative technique depends on the condition number of the matrix $\mathbf{R}_{FU}$, with the condition number defined as the ratio of maximum to minimum eigenvalue $\lambda_{max}/\lambda_{min}$ of the matrix. In order to speed-up the rate of convergence, a preconditioner $\mathbf{P}$ can be employed as follows

$$\mathbf{P}^{-1}\mathbf{R}_{FU}\mathbf{U} = -\mathbf{P}^{-1}(\mathbf{F}^p + \mathbf{F}^B + \mathbf{R}_{FE}\mathbf{E}^\infty) \tag{6.23}$$

If the matrix $\mathbf{P}$ approximates the original matrix $\mathbf{R}_{FU}$ well, then the condition number of the matrix $\mathbf{P}^{-1}\mathbf{R}_{FU}$ is likely to be closer to unity than the original matrix $\mathbf{R}_{FU}$. At the same time, $\mathbf{P}^{-1}$ should be relatively inexpensive to compute, so that a reduction in overall computational time can be achieved. This is a special challenge in FLD, as the matrix-vector product $\mathbf{R}_{FU}\mathbf{U}$, which is the basic step involved at each of the iteration, is itself very inexpensive. This essentially dictates that the inverse of the preconditioner matrix $\mathbf{P}$ should be known analytically in advance, so that no additional time is spend computing it at each iteration. In this spirit, we developed the following two preconditioning strategies: first is simply a diagonal matrix, while the other is a block-diagonal matrix. These are discussed next.

6.2.1 Diagonal preconditioner

The diagonal preconditioner requires 6 diagonal elements for each particle, which can be thought of as the effective resistance to the velocities/angular velocities along each of the three coordinate axis, which in turn leads to forces/torques along those directions respectively. The first three diagonal elements, which gives the resistance to translational velocities

are obtained as

$$\mathbf{P}_i^{FU} = \left(R_0^{FU} + \sum_j (X^A - Y^A)\mathbf{dd} \right) \boldsymbol{\delta} \tag{6.24}$$

where the sum is over all the neighbors (j) within the lubrication cutoff of the reference particle (i), while $\boldsymbol{\delta}$ is the Kronecker delta function. The next three diagonal elements representing resistance to angular velocities are taken as

$$\mathbf{P}_i^{T\Omega} = R_0^{T\Omega} \boldsymbol{\delta} \tag{6.25}$$

which essentially implies an isotropic resistance. Finally, we note that the R_0^{FU} in this preconditioner was taken to be the same as R_0^{FU} of FLD, while $R_0^{T\Omega}$ was usually different. For example, $R_0^{T\Omega}/(8\pi\mu a^3) = 2$ was found to work well for a variety of problems.

6.2.2 Block-diagonal preconditioner

The next preconditioner is a block diagonal preconditioner, which is recommended over the diagonal preconditioner due to its superior convergence property. The overall form of the block-diagonal preconditioner can be expressed as

$$\mathbf{P} = \begin{pmatrix} \mathbf{P}_1 & 0 & 0 & 0 & 0 \\ 0 & \mathbf{P}_2 & 0 & 0 & 0 \\ 0 & 0 & . & 0 & 0 \\ 0 & 0 & 0 & . & 0 \\ 0 & 0 & 0 & 0 & \mathbf{P}_{N_p} \end{pmatrix} \tag{6.26}$$

where $\mathbf{P}_i$'s are 6×6 blocks for each particle i. Each of the $\mathbf{P}_i$'s are further broken down into 3×3 block-diagonal form as shown in the following equation

$$\mathbf{P}_i = \begin{pmatrix} \mathbf{R}_i^{FU} & 0 \\ 0 & \mathbf{R}_i^{T\Omega} \end{pmatrix} \tag{6.27}$$

in which the $\mathbf{R}_i^{FU}$ block is obtained as

$$\mathbf{R}_i^{FU} = R_0^{FU}\boldsymbol{\delta} + \sum_j X^A \mathbf{dd} + Y^A(\boldsymbol{\delta} - \mathbf{dd}) \tag{6.28}$$

while the $\mathbf{R}_i^{T\Omega}$ block is again kept as a diagonal matrix

$$\mathbf{R}_i^{T\Omega} = R_0^{T\Omega}\boldsymbol{\delta} \tag{6.29}$$

In this preconditioner, it proved useful to use different values of the isotropic resistances R_0^{FU} and $R_0^{T\Omega}$ than those in FLD. Typical values for these isotropic resistances are $R_0^{FU}/(6\pi\mu a) = 3.5$ and $R_0^{T\Omega}/(8\pi\mu a^3) = 5$. Having defined the preconditioner matrix $\mathbf{P}$, we note that its inverse can be obtained as

$$\mathbf{P}^{-1} = \begin{pmatrix} \mathbf{P}_1^{-1} & 0 & 0 & 0 & 0 \\ 0 & \mathbf{P}_2^{-1} & 0 & 0 & 0 \\ 0 & 0 & . & 0 & 0 \\ 0 & 0 & 0 & . & 0 \\ 0 & 0 & 0 & 0 & \mathbf{P}_{N_p}^{-1} \end{pmatrix} \tag{6.30}$$

Each of the 6×6 inverse of blocks $\mathbf{P}_i$ can in turn be obtained as

$$\mathbf{P}_i^{-1} = \begin{pmatrix} (\mathbf{R}_i^{FU})^{-1} & 0 \\ 0 & (\mathbf{R}_i^{T\Omega})^{-1} \end{pmatrix} \tag{6.31}$$

Each of the sub-blocks in the above equation are easily inverted analytically. Once the inverse of the preconditioner $\mathbf{P}^{-1}$ is found, it seamlessly integrates with the preconditioned conjugate gradient technique (Shewchuk, 1994; Saad, 2003). For this reason, it was important to keep the preconditioner matrix symmetric.

6.3 Results

We now compare the results of dynamic simulations obtained from FLD and SD. First, we consider a non-Brownian suspension at a volume fraction of $\phi = 0.55$. The pair distribution function in the end view, i.e. in the vorticity-gradient plane are shown in figures (6.8) and figures (6.9) for simulations with δ FLD and $\delta - \log \delta$ FLD respectively.

The distribution of small-gaps, which plays a critical role in determining the rheological properties of the suspension, are shown in figures (6.10) and (6.11) with δ FLD and $\delta - \log \delta$ FLD respectively. Again, considerably better agreement with SD result is obtained in simulations performed with log level terms ($\delta - \log \delta$ FLD).

Next, we present results for a Brownian suspension at a volume fraction of $\phi = 0.45$. The pair distribution function in the front view, i.e. the flow-gradient plane, is shown in figure (6.12), the viscosity is shown in figure (6.13), the first normal stress difference is shown in figure (6.14), and the second normal stress difference is shown in figure (6.15). Again, like the gap distribution function, much better agreement with SD results is obtained when log level terms are included ($\delta - \log \delta$ FLD). Good agreement with SD result is also seen in the normal stress differences.

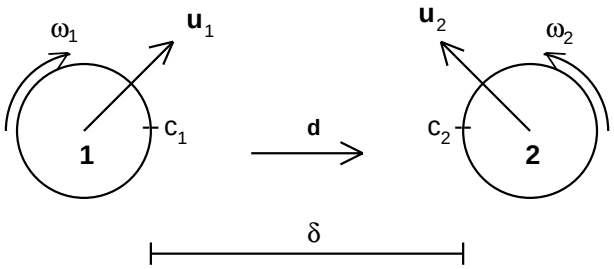

Figure 6.1: Definition of terms used in the description of lubrication interactions.

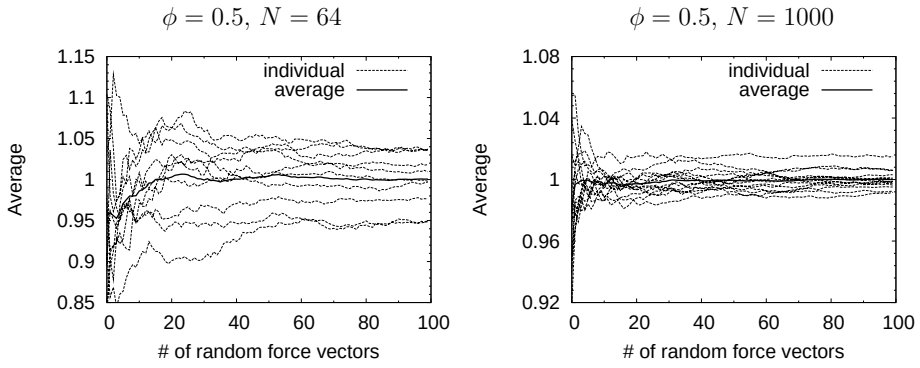

Figure 6.2: Thin lines: Convergence of diffusivity with the number of random force/torque vectors employed for a single Monte Carlo configuration. Thick line: Corresponding average over all the Monte Carlo configurations in the figure. All values have been non-dimensionalized by the final converged average shown by the thick line in corresponding plots.

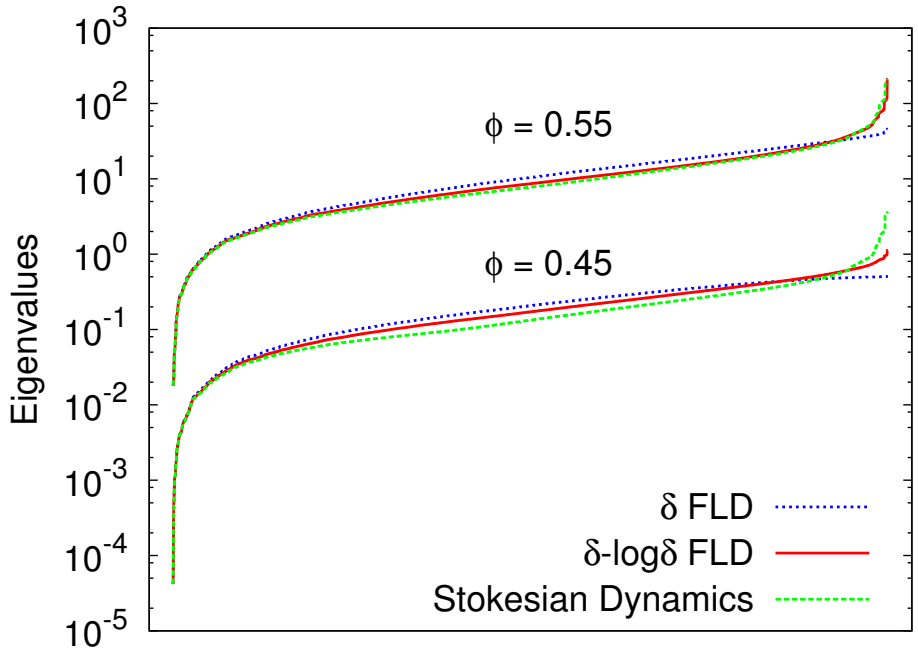

Figure 6.3: Eigenvalues of M_{UF} for two different volume fractions. Eigenvalues for $\phi = 0.55$ system are multiplied by 100 for clarity

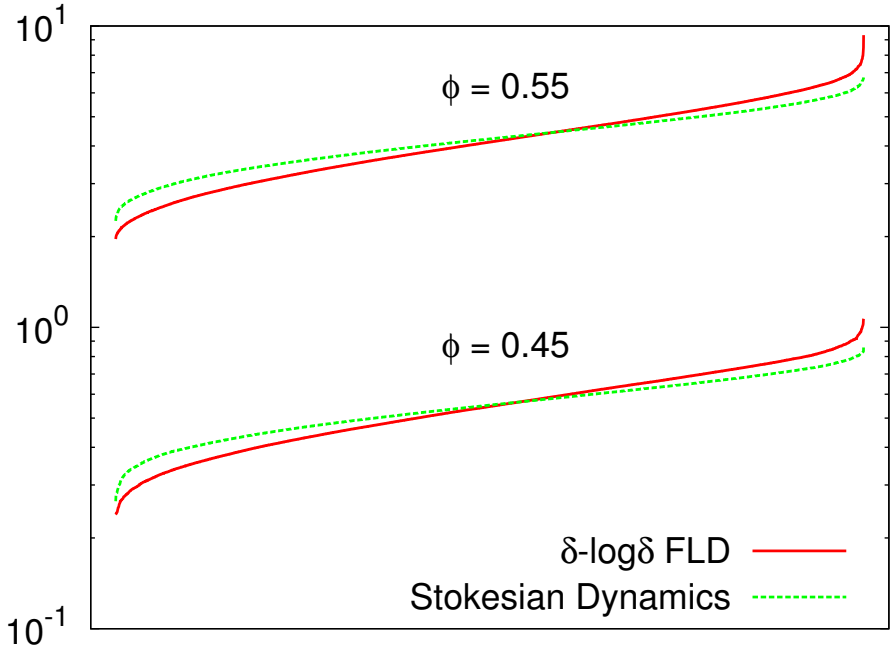

Figure 6.4: Eigenvalues of $M_{T\Omega}$ for two different volume fractions. Eigenvalues for $\phi = 0.55$ system are multiplied by 10 for clarity

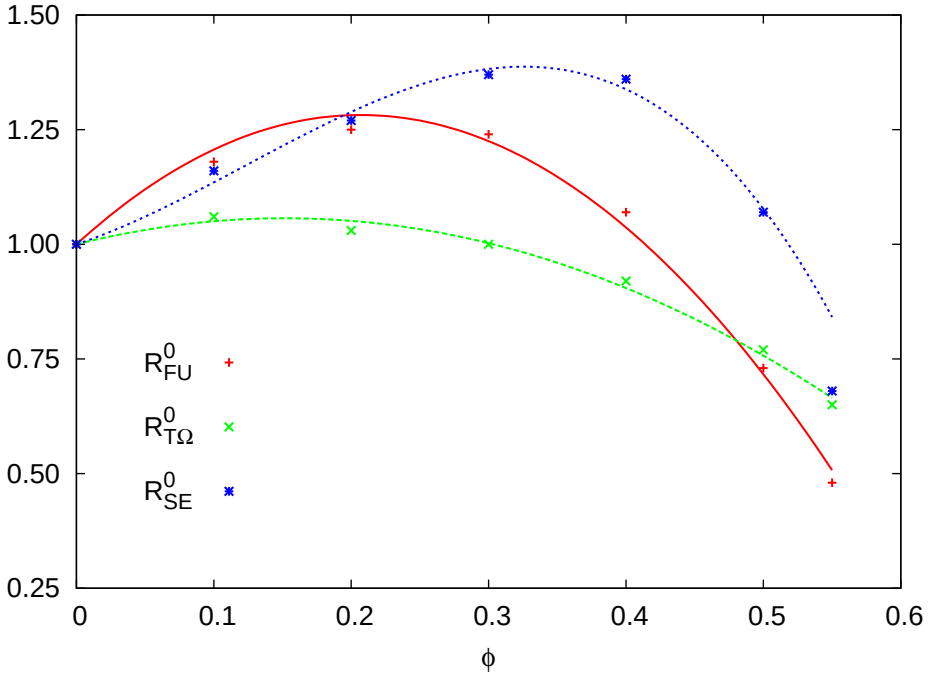

Figure 6.5: Optimal isotropic constants. Best fits in the plots are given by $R^0_{FU} = 1 + 2.725\phi - 6.583\phi^2$, $R^0_{T\Omega} = 1 + 0.749\phi - 2.469\phi^2$, $R^0_{SE} = 1 + 0.9972\phi + 4.8409\phi^2 - 13.0510\phi^3$. Lubrication cutoff of $2.5a$ was used in this calculation.

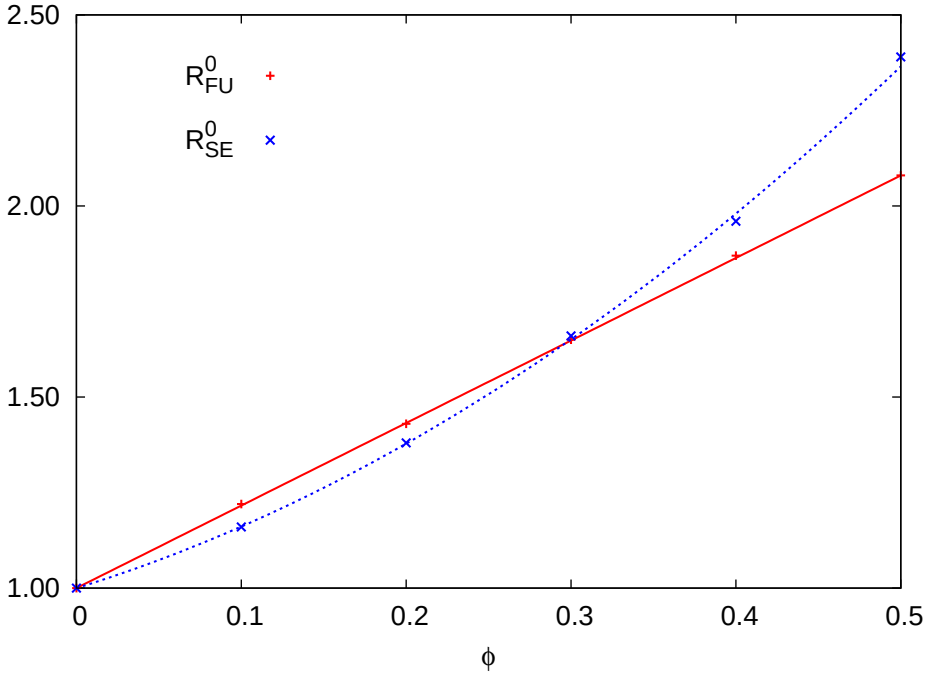

Figure 6.6: Optimal isotropic constants. Best fits in the plots are given by $R^0_{FU} = 1 + 2.16\phi$, and $R^0_{SE} = 1 + 1.33\phi + 2.80\phi^2$.Lubrication cutoff of $2.5a$ was used in this calculation.

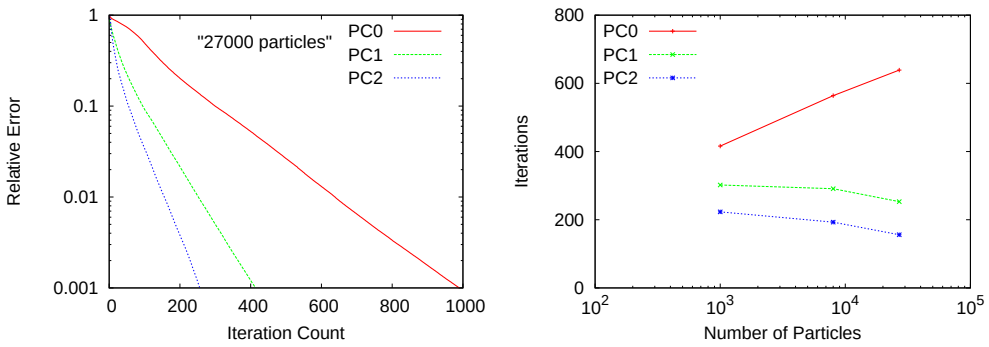

Figure 6.7: Convergence of the conjugate gradient algorithm with a dynamic configuration at $\phi = 0.55$. PC0 implies no preconditioner, PC1 implies a diagonal preconditioner, and PC2 implies a block tridiagonal preconditioner (see text)

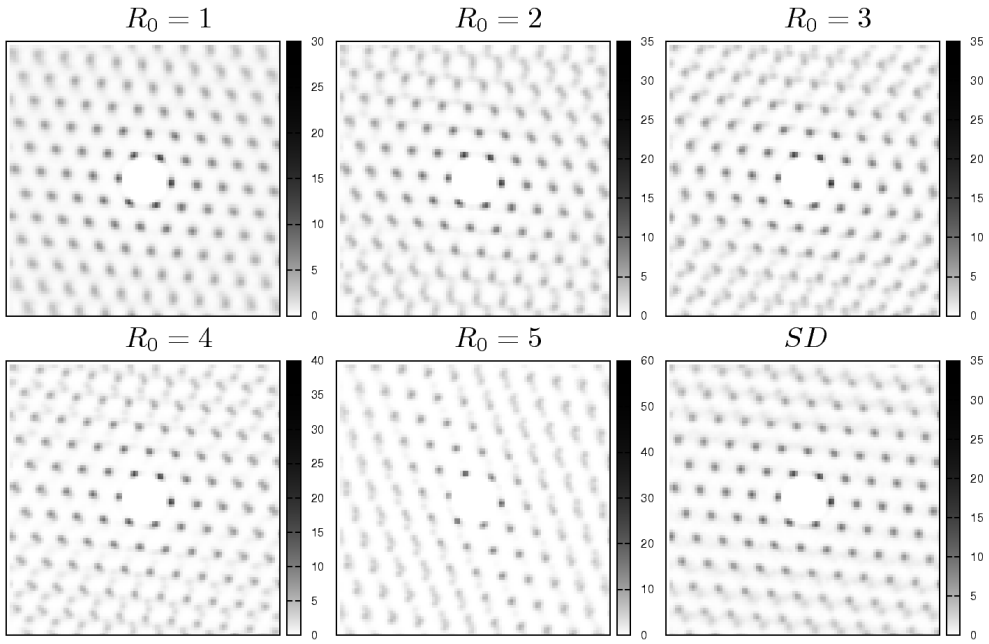

Figure 6.8: End view pair distribution function in simulations performed with δ FLD algorithm as a function of R_0 at $\phi = 0.55$

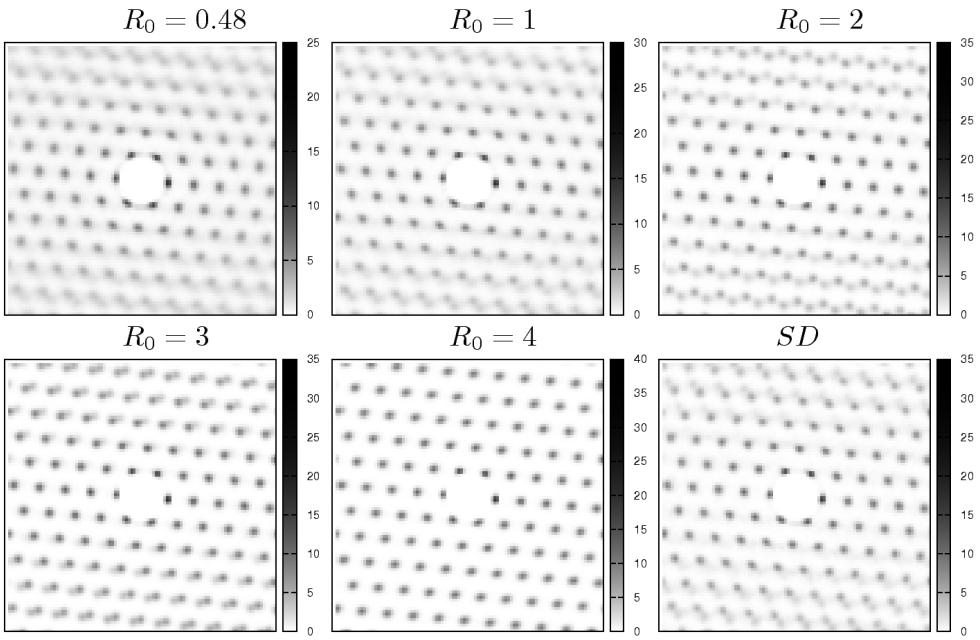

Figure 6.9: End view pair distribution function in simulations performed with $\delta - \log \delta$ FLD algorithm as a function of R_0 at $\phi = 0.55$. $R_0^T = 1$ was kept fixed

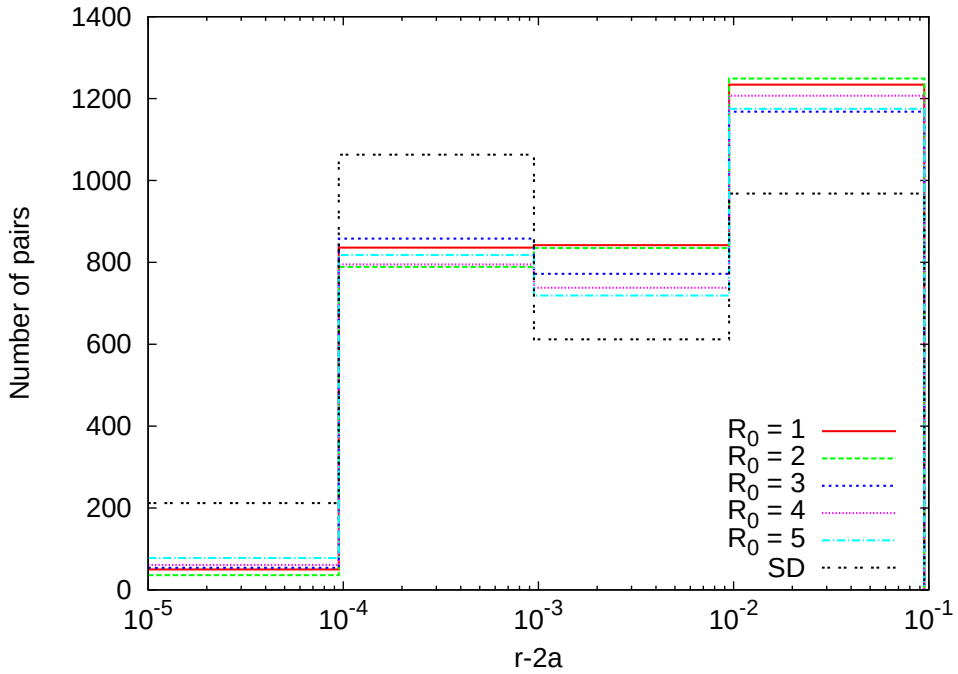

Figure 6.10: Gap distribution function in simulations performed with δ FLD algorithm as a function of R_0 at $\phi = 0.55$

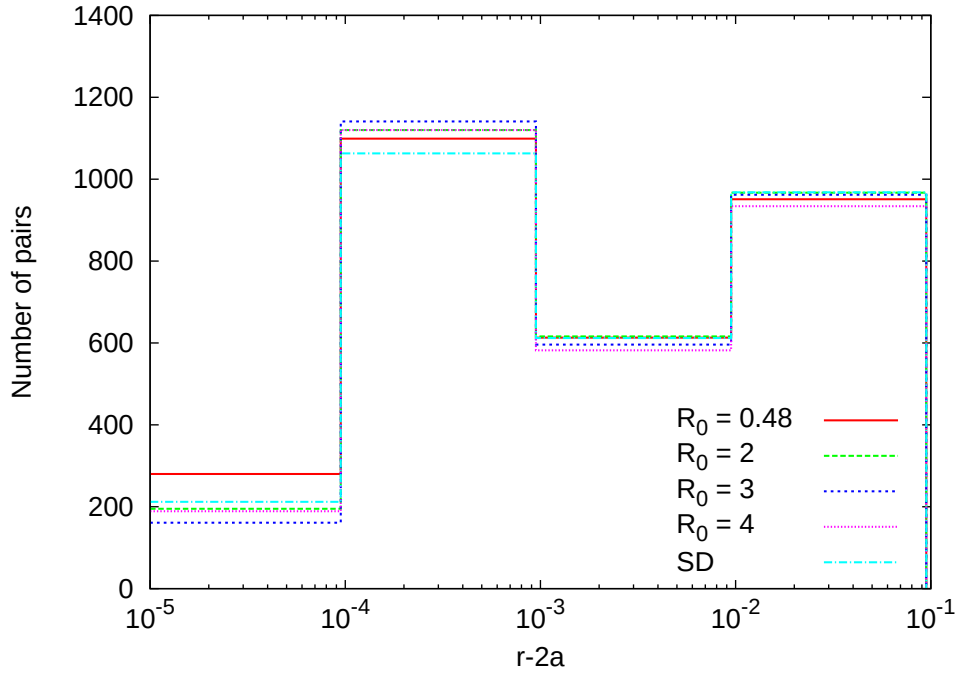

Figure 6.11: Gap distribution function in simulations performed with $\delta - \log \delta$ as a function of R_0 at $\phi = 0.55$. $R_0^T = 1$ was kept fixed

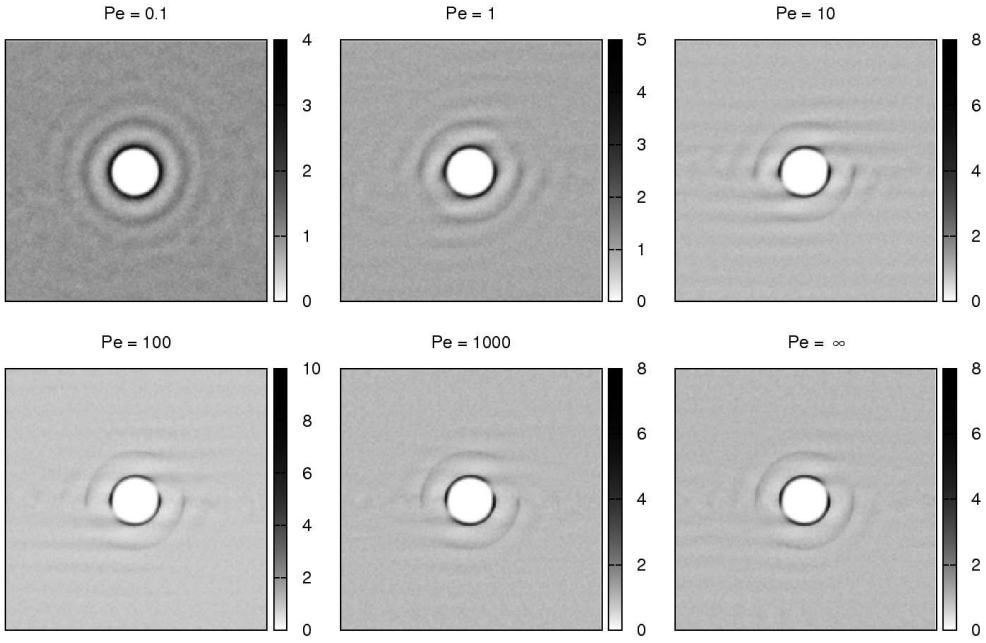

Figure 6.12: Front view pair distribution function for $\phi = 0.45$ with Pe

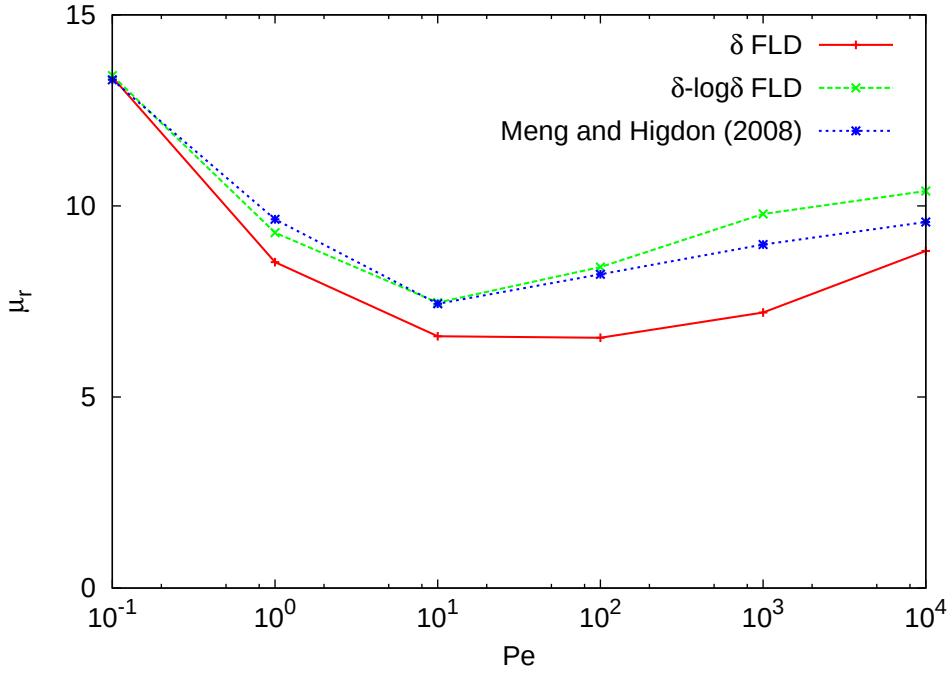

Figure 6.13: Viscosity for a $\phi = 0.45$ Brownian suspension with Pe

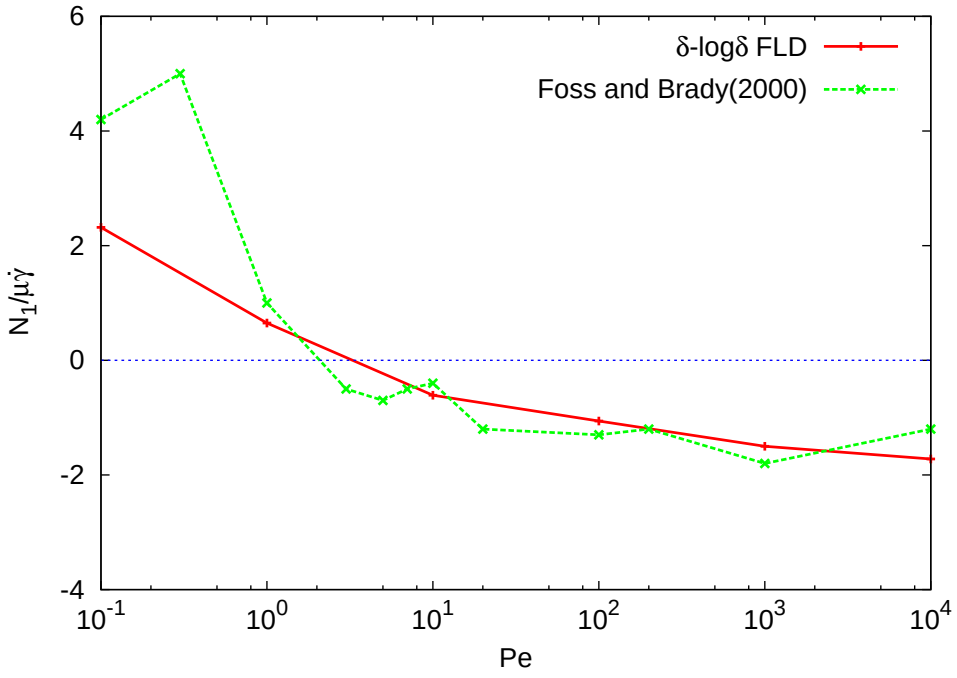

Figure 6.14: First normal stress difference for a $\phi = 0.45$ Brownian suspension with Pe

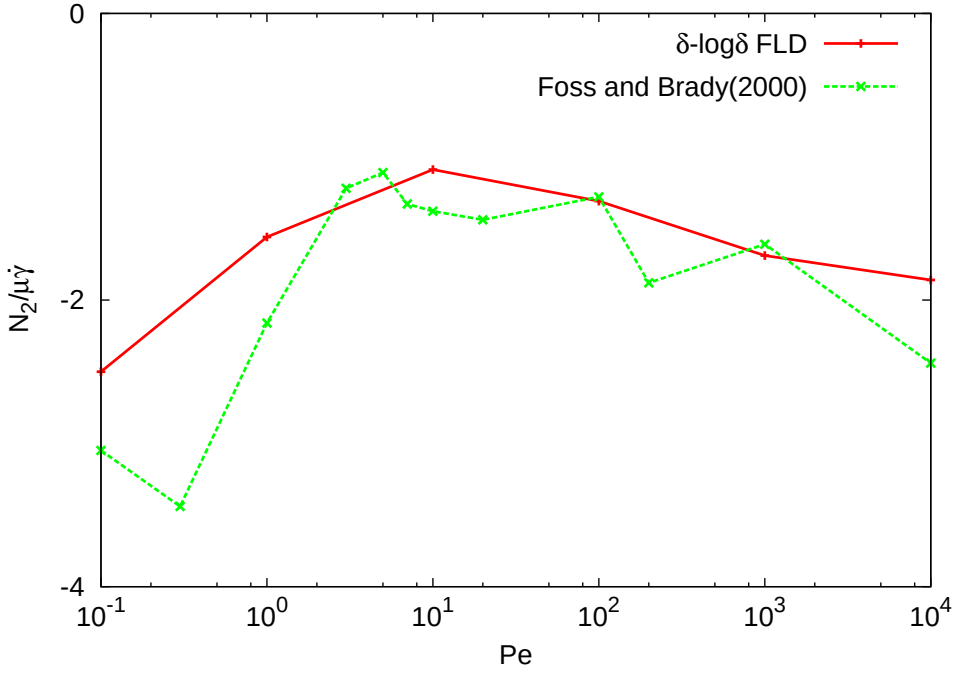

Figure 6.15: Second normal stress difference for a $\phi = 0.45$ Brownian suspension with Pe

References

Ball, R.C., & Melrose, J.R. 1997. A simulation technique for many spheres in quasi-static motion under frame-invariant pair drag and Brownian forces. *Physica A*, **247**, 444–472.

Batchelor, G.K. 1977. The effect of Brownian motion on the bulk stress in a suspension of spherical particles. *Journal of Fluid Mechanics*, **83**, 97–117.

Kim, Sangtae, & Karrila, Seppo J. 1991. *Microhydrodynamics: Principles and Selected Applications*. Butterworth-Heinemann.

Lambert, J.D. 1997. *Numerical methods for ordinary differential systems: The inital value problem*. John Wiley and Sons Ltd.

Russel, W.B., D.A.Saville, & Schowalter, W.R. 1989. *Colloidal Dispersions*. Cambridge University Press.

Saad, Y. 2003. *Iterative Methods for Sparse Linear Systems*. Society for Industrial and Applied Mathematics.

Shewchuk, J. R. 1994. *An Introduction to the Conjugate Gradient Method Without the Agonizing Pain*. Technical Report CMU-CS-TR-94-125. Carnegie Mellon University. See also http://www.cs.cmu.edu/~quake-papers/painless-conjugate-gradient.ps.

Sierou, A., & Brady, J.F. 2001. Accelerated Stokesian Dynamics simulations. *Journal of Fluid Mechanics*, **448**, 115–146.

Chapter 7

Shear Thickening in Suspensions of Spherical and Non-spherical Particles

7.1 Introduction

Shear thickening is the property in which suspensions show an increasing viscosity with an increasing rate of shear. In general, shear thickening is disadvantageous as it can damage processing equipments, yet there are several applications which make use of this property constructively. An example is the use of shear thickened suspensions in body armor (Decker *et al.*, 2007). Over the years, shear thickening has been the focus of many research efforts. Early on, an order to disorder transition with an increasing rate of shear was thought to be the primary cause of the shear thickening phenomena. First conclusive evidence for this was provided by Hoffman (1972), who found that the thickening was accompanied by a microstructural transition in which two dimensional hexagonal packing of spheres broke up into less ordered arrays of spheres. In his review of the shear thickening phenomena, Barnes (1989), too, concluded that shear thickening was caused by an order-disorder transition. Further proof was provided by Chow & Zukoski (1995b) who found that, for charge stabilized suspensions, thickening was observed when the hexagonal order was degraded. They also noticed that there was a critical volume fraction for thickening, as they didn't see such a behavior for $\phi < 0.4$. Later, Chow & Zukoski (1995a) did an interesting set of experiments in which they varied the tool gap of the rheometer to characterize its effect on rheology. They found that shear rate marking the onset of shear thickening decreased with decreasing gap for gaps smaller than 76 particle-diameters. Based on this and previous observations, they put forth a scaling argument for the onset of shear thickening and its volume fraction dependence. They argued that, during shear melting, if density fluctuations are unable to relax by diffusion on a time scale shorter than $\dot{\gamma}^{-1}$, large clusters will form that will

ultimately percolate across the rheometer tool gap, thereby causing shear thickening. Since particle diffusivity decreases with increasing volume fractions, therefore, above a critical volume fraction, the density fluctuations would no longer relax faster than $\dot{\gamma}^{-1}$, hence causing shear thickening.

Order-disorder transition was widely accepted as the root cause of shear thickening, yet there was mounting evidence against the necessity or the sufficiency of it. In their experiments, Laun *et al.* (1992) found that one of the samples showed no signs of ordering at any shear rate (consequently no order to disorder transition), yet it showed a shear thickening behavior. In order to make it consistent with the order-disorder transition mechanism, they attributed this to the polydispersity of the sample which would smear the scattering peaks, even if order was present in the system. A few years later, Bender & Wagner (1996) also found no signs for an order-disorder transition in near hard-sphere suspensions that otherwise showed a shear thickening behavior. Using turbidity and flow-small angle neutron scattering experiments they concluded that particles cluster reversibly in shear thickened state, which was proposed to be the cause for the shear thickened state. They found similar behavior in their later experiments (Maranzano & Wagner, 2001), which led them to conclude that order-disorder transition is not necessary for shear thickening and that it was caused due to the formation of hydroclusters.

Simulations have played a pivotal role in advancing our understanding of suspension properties. In fact, the strongest evidence for the formation of clusters at high shear rates was first reported in Stokesian dynamics simulations (Bossis & Brady, 1984; Brady & Bossis, 1985). In their 2-D simulations at infinite Peclet number, they showed the formation of elongated particle clusters along the compression axis which resulted in an enhanced dissipation rate and hence enhanced viscosity. Later Stokesian dynamics studies on non-Brownian charge stabilized monolayer suspensions at varying rates of shear (Boersma *et al.*, 1995; Dratler *et al.*, 1997), however, showed an order-order disorder transition at the onset of shear thickening. Melrose *et al.* (1996), using a pairwise lubrication based model, showed that the viscosity increases logarithmically with shear rate in the thickening regime. They also mentioned (without proof) that viscosity increases logarithmically with the inverse of the smallest gaps. Moreover, they noted that an enhanced lubrication model over that for normal hard-spheres

is needed to explain the high viscosities observed in experimental suspensions. For example, they showed that by using the squeeze lubrication model for a polymer brush coated particle (Potanin & Russel, 1995, 1996), substantially stronger thickening could be obtained. In their work, Phung *et al.* (1996) presented a scaling argument for the rate of viscosity increase in particle suspensions. They contend that shear thickening results from the formation of non-compact clusters (e.g. chain like clusters), with the viscosity contribution from a cluster scaling as $N^{3\alpha}$ when the largest length scale of the cluster scales as N^{α} (N being the number of particles in the cluster). So, if $\alpha > 1/3$ (i.e. a non-compact cluster), then uncontrolled shear thickening can be obtained as N becomes arbitrarily large. Farr *et al.* (1998) presented a theory for discontinuous shear thickening which is commonly observed in experiments at high volume fractions, typically $\phi > 0.5$, where the shear rate essentially stays constant despite increasing the applied stress by orders of magnitude (Hoffman, 1972; Laun *et al.*, 1992; Frith *et al.*, 1996; Maranzano & Wagner, 2001). Their model is essentially a kinetic theory for the aggregation of clusters aligned along the compression axis to form even larger clusters. As per this model, the main criterion for discontinuous shear thickening is that the cluster's length should become arbitrarily large before it tumbles to the extensional quadrant, where it doesn't experience the compressional force any more and hence the clusters cannot grow further. With this theory, they predicted a minimum volume fraction of $\phi = 0.515$ for spherical particle suspensions to show a discontinuous shear thickening. Catherall *et al.* (2000) and Melrose & Ball (2004) showed that thickening can occur with or without an order-disorder transition and that different rates of thickening can be obtained by using different models for lubrication or interparticle forces. Krishnamurthy *et al.* (2005) derived a micromechanical model for the onset of shear thickening in polymer stabilized dispersions. Their model further develops the argument already presented, namely the life-time of clusters–defined as the ratio of the squeeze lubrication hydrodynamic resistance to the effective spring constant of the interparticle force–should be much larger than the convective time scale. Moreover, the above ratio should be computed at a gap which is obtained by balancing the hydrodynamic squeeze lubrication force and the interparticle force.

Several research efforts have characterized the shear thickening phenomena in anisotropic particle suspensions. In his review, Barnes (1989) mentions that the anisotropic particles

tend to produce shear thickening more readily and do so at a lower volume fraction. In particular, a rod shaped particle suspension shows a stronger shear thickening behavior than a disk shaped particle suspension. In his rheological measurements on aqueous cylindrical particle suspensions ($L/D \sim 10$), Bergstrom (1996) found a shear thickening behavior at a volume fraction as low as $\phi = 0.1$, which became discontinuous at $\phi = 0.172$. He attributed this shear thickening behavior to the misalignment of the particles at high rates of shear, though no evidence was provided. Egres & Wagner (2005) did a comprehensive microstructural, orientational, and rheological analysis of acicular particles of varying particle aspect ratios ($L/D \sim 2, 4$ & 7). They found that these anisotropic particle suspensions demonstrated both continuous and discontinuous reversible shear thickening, with the critical volume fraction for the onset of discontinuous shear thickening decreasing with the increasing particle aspect ratio, though the critical stress for shear thickening was found to be nearly independent of particle anisotropy and volume fraction. They also showed that the slight variation in critical stress could be attributed to the slight variation in the minor axis diameter of the particles, as that is the relevant dimension to consider for flow aligned particles. Using small angle scattering experiments, they showed that long-axis particle alignment with the flow direction was maintained throughout the range of shear stresses investigated, including the shear thickening regimes for both continuously and discontinuously shear thickening suspensions. Based on scattering and transient rheological experiments, they concluded that the cause for reversible shear thickening in acicular particles is similar to that in spherical particle suspensions, namely the formation of flow aligned hydroclusters. Recently, Meng & Higdon (2008a,b) performed Stokesian dynamics simulations on plate-like particle ($L/D \in [3, 5, 7]$) suspensions of low to moderate volume fractions ($\phi \leq 0.3$). They found that the particles showed a high degree of alignment with the flow at high rates of shear, and that the thickening occurs due to the increase in number of particle pairs separated by small gaps. Though the particles were found to be aligned with the flow on an average, with the microstructure corresponding to that of sliding layers, yet there were two significant departures from that mechanism which contributed to the thickening behavior. First mechanism corresponded to the particles occasionally tumbling out of layers, and the second mechanism was the formation of transient particle stacks. They concluded that the interaction of the tumbling

particles and the particle stacks with the sliding layers contribute significantly to the thickening behavior due to the formation of small gaps in such processes. They also mentioned that their simulations showed a weaker thickening in suspensions of plate-like particles than in suspensions of spherical particles.

7.2 Preliminary Results

To unequivocally address the rate of increase in viscosity as function of the characteristic gap present in the system, we performed controlled minimum gap simulations. The gaps can be controlled by the use of a short range repulsive force, which in this work had the following form:

$$\frac{\mathbf{F}^P}{8\pi\mu a^2\dot{\gamma}} = \begin{cases} C^P\left(\frac{\delta_{min}}{\delta}\right)\left(\eta - \frac{1}{2}\eta^2\right)^3\mathbf{d} & \text{if} \quad \delta < \delta_{min} \\ \mathbf{0} & \text{if} \quad \delta \geq \delta_{min} \end{cases} \tag{7.1}$$

where C typically had a value of $C = 10$. The repulsive force, as given by the above equation, is zero when the gap between the particles is greater than δ_{min}, but rises sharply (though continuously) for gaps smaller than it. We also use a numerical cutoff δ_{num} to cap off any gaps smaller than it to avoid large forces. Typically, we have used $\delta_{num} = 10^{-2}\delta_{min}$ in this work. We note that for the above form of the repulsive force one can take δ_{min} as the characteristic minimum gap present in the system. We now present results for the viscosity as function of δ_{min} for two highly concentrated suspensions ($\phi = 0.60$ and $\phi = 0.62$). Figure (7.1) shows the viscosity as a function of inverse δ_{min} at a volume fraction of $\phi = 0.60$. Simulations at this volume fraction were performed both with and without the *log* level terms in the lubrication interaction. Surprisingly, the viscosity was found to increase only logarithmically with gap when the *log* level terms were included in the lubrication interaction. In simulations where *log* level terms were absent, the viscosity was essentially found to plateau as δ_{min} was reduced. This result also shows the importance of retaining the *log* level terms in the lubrication approximation for accurate rheology. At a volume fraction of $\phi = 0.62$, the viscosity was again found to increase logarithmically with δ_{min} as shown in figure (7.2). Note that this volume fraction is very close to the random close packing volume fraction $\phi_{rcp} = 0.64$ in

suspensions of spheres.

7.3 Conclusions

Based on the results presented above, we conclude that the viscosity increases only logarithmically as a function of the characteristic minimum gap present in the system. The study also shows the importance of using *log* level terms in the lubrication interactions to predict the rheology accurately. The logarithmic increase in viscosity as a function of minimum gap present in the system also has implications on our understanding of the discontinuous shear thickening phenomena. If this rate of increase in viscosity with the characteristic gap were to hold, it would be difficult to obtain a sudden discontinuous rise in viscosity with increasing shear rates in systems explored here; though, a bifurcation type of behavior at smaller gaps cannot yet be ruled out.

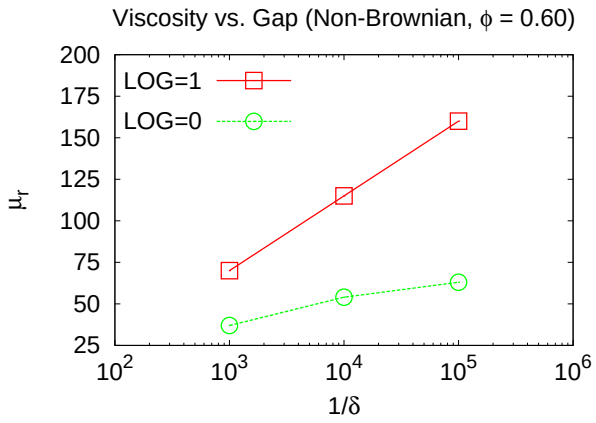

Figure 7.1: Viscosity vs. inverse gap $(1/\delta)$ at $\phi = 0.60$. LOG=1 data were obtained from simulations in which the *log* level terms were present, while LOG=0 data were obtained from simulations in which *log* level terms were absent.

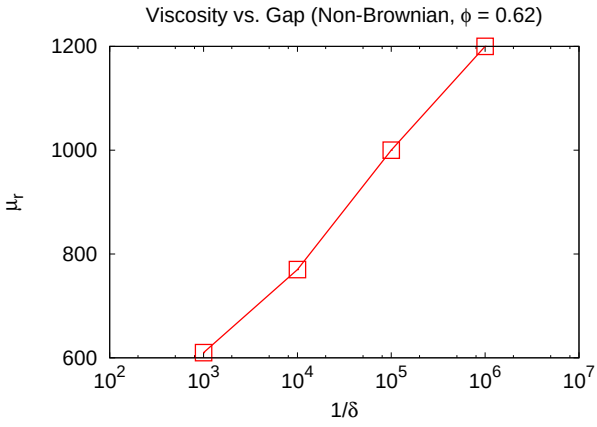

Figure 7.2: Viscosity vs. inverse gap $(1/\delta)$ at $\phi = 0.62$. Simulations were done with *log* level terms present.

References

Barnes, H.A. 1989. Shear-thickening (dilatancy) in suspensions of nonaggregating solid particles dispersed in newtonian liquids. *Journal of Rheology*, **33**(2), 329–366.

Bender, J., & Wagner, N.J. 1996. Reversible shear thickening in monodisperse and bidisperse colloidal dispersions. *Journal of Rheology*, **40**(5), 899–916.

Bergstrom, L. 1996. Rheological properties of Al_2O_3-SiC whisker composite suspensions. *Journal of Material Science*, **31**, 5257–5270.

Boersma, W.H., Laven, J., & Stein, H.N. 1995. Computer simulations of shear thickening of concentrated dispersions. *Journal of Rheology*, **39**(5), 841–860.

Bossis, G., & Brady, J.F. 1984. Dynamic simulation of sheared suspensions. I. General method. *Journal of Chemical Physics*, **80**(10), 5141–5154.

Brady, J.F., & Bossis, G. 1985. The rheology of concentrated suspensions of spheres in simple shear flow by numerical simulation. *Journal of Fluid Mechanics*, **155**, 105–129.

Catherall, A.A., Melrose, J.R., & Ball, R.C. 2000. Shear thickening and orderdisorder effects in concentrated colloids at high shear rates. *Journal of Rheology*, **44**(1), 1–25.

Chow, M.K., & Zukoski, C.F. 1995a. Gap size and shear history dependencies in shear thickening of a suspension ordered at rest. *Journal of Rheology*, **39**(1), 15–32.

Chow, M.K., & Zukoski, C.F. 1995b. Nonequilibrium behavior of dense suspensions of uniform particles: Volume fraction and size dependence of rheology and microstructure. *Journal of Rheology*, **39**(1), 33–59.

Decker, M.J., Halbach, C.J., Nam, C.H., Wagner, N.J., & Wetzel, E.D. 2007. Stab resistance of shear thickening fluid (STF)-treated fabrics. *Composites Science and Technology*, **67**, 565–567.

Dratler, D.I., Schowalter, W.R., & Hoffman, R.L. 1997. Dynamic simulation of shear thickening in concentrated colloidal suspensions. *Journal of Fluid Mechanics*, **353**, 1–30.

Egres, R.G., & Wagner, N.J. 2005. The rheology and microstructure of acicular precipitated calcium carbonate colloidal suspensions through the shear thickening transition. *Journal of Rheology*, **49**(3), 719–746.

Farr, R.S., Melrose, J.R., & Ball, R.C. 1998. Kinetic theory of jamming in hard-sphere startup flows. *Physical Review E*, **55**(6), 7203–7211.

Frith, W.J., d'Haene, P., Buscall, R., & Mewis, J. 1996. Shear thickening in model suspensions of sterically stabilized particles. *Journal of Rheology*, **40**(4), 531–548.

Hoffman, R.L. 1972. Discontinuous and Dilatant Viscosity Behavior in Concentrated Suspensions. I. Observation of a Flow Instability. *Transactions of The Society of Rheology*, **16**(1), 155–173.

Krishnamurthy, L., Wagner, N.J., & Mewin, J. 2005. Shear thickening in polymer stabilized colloidal dispersions. *Journal of Rheology*, **49**(6), 1347–1360.

Laun, H.M., Bung, R., Hess, S., Loose, W., Hess, O., Hahn, K., Hadicke, E., Hingmann, R., Schmidt, F., & Lindner, P. 1992. Rheological and small angle neutron scattering investigation of shear-induced particle structures of concentrated polymer dispersions submitted to plane Poiseuille and Couette flow. *Journal of Rheology*, **36**(4), 743–787.

Maranzano, B.J., & Wagner, N.J. 2001. The effects of particle size on reversible shear thickening of concentrated colloidal dispersions. *Journal of Chemical Physics*, **114**(23), 10514–10527.

Melrose, J.R., & Ball, R.C. 2004. Continuous shear thickening transitions in model concentrated colloidsThe role of interparticle forces. *Journal of Rheology*, **48**(5), 937–960.

Melrose, J.R., van Vliet, J.H., & Ball, R.C. 1996. Continuous Shear Thickening and Colloid Surfaces. *Physical Review Letters*, **77**(22), 4660–4663.

Meng, Q., & Higdon, J.J.L. 2008a. Large scale dynamic simulation of plate-like particle suspensions. Part I: Non-Brownian simulation. *Journal of Rheology*, **52**(1), 1–36.

Meng, Q., & Higdon, J.J.L. 2008b. Large scale dynamic simulation of plate-like particle suspensions. Part II: Brownian simulation. *Journal of Rheology*, **52**(1), 37–65.

Phung, T., Brady, J.F., & Bossis, G. 1996. Stokesian Dynamics simulation of Brownian suspensions. *Journal of Fluid Mechanics*, **313**, 181–207.

Potanin, A.A., & Russel, W.B. 1995. Hydrodynamic interaction of particles with grafted polymer brushes and applications to rheology of colloidal dispersions. *Physical Review E*, **52**(1), 730–737.

Potanin, A.A., & Russel, W.B. 1996. Erratum: Hydrodynamic interaction of particles with grafted polymer brushes and applications to rheology of colloidal dispersions. *Physical Review E*, **54**(6), 6973.

Chapter 8

Conclusions

We conclude here by summarizing some of the key aspects of this work. We break this summary into two parts: in the first part we summarize the computational algorithms developed in this work, while in the second part we summarize the key results from the physical studies we performed. These are presented next.

(I) Computational Algorithms

(a) *Stokesian Dynamics (chapter 2)*: In this research, the traditional Particle-Mesh-Ewald (PME) Stokesian Dynamics technique was extended to model hydrodynamic interactions in suspensions of non-spherical dicolloidal particles. A dicolloidal particle was modeled as two fused spheres of varying radii and center-to-center separations. We showed that the boundary condition for a single dicolloidal particle in flows of up to linear order was well satisfied by a distribution of low order Stokes singularities along the axis of symmetry of the particle. These singularities include Stokeslet, Stokes-doublet, Potential dipole, and Potential quadrupole. The locations and strengths of these singularities were found by minimizing the norm of the error in no-slip boundary condition. The knowledge of the one-body singularity solutions, which need to be computed only once per particle shape, completely defines the far-field many-body term in Stokesian Dynamics. For the near field lubrication interactions, asymptotic solutions for a pair of spherical particles were used with corrections for the truncated spherical geometry inherent in the dicolloidal particles. The far-field interactions together with the near-field interactions complete the Stokesian Dynamics approximation to the hydrodynamic resistance tensor. The approach outlined here is a general approach and can be easily adapted to other particle shapes like spheroids, discs, cylindrical fibers and various compound shapes.

(b) *Fast Lubrication Dynamics (chapter 6)*: This algorithm (FLD) is a reduced computational expense version of the Stokesian Dynamics technique which retains most of its desirable features. In this algorithm, we replace the far-field many-body interactions by properly calibrated isotropic resistances. The near field lubrication interactions are computed as usual with modifications to ensure a smooth transition at the lubrication cutoff distance. The isotropic resistances are tuned to match the average translational and rotational mobilities obtained from the full Stokesian Dynamics technique, which also gives a good match in the full eigenvalue spectrum. Microstructure and rheology obtained from FLD simulations are in excellent agreement with those from Stokesian Dynamics simulations over a wide range of volume fractions spanning from dilute to highly concentrated systems. A critical feature of the method is the use of an efficient physics based preconditioner. This preconditioner ensures an O(N) operation count independent of the system parameters in contrast to previous lubrication approaches with higher operation count scaling. FLD typically runs 100× faster than Stokesian Dynamics technique, which makes a variety of interesting problems accessible to numerical investigations.

(II) Physical Studies

(a) *Hydrodynamic transport properties in equilibrium suspensions of dicolloids (chapter 2)*: In a first series of studies using the Stokesian Dynamics technique, we computed the viscosity and self-diffusion in suspensions of dicolloids in equilibrium configurations over a wide range of volume fractions ($0 \leq \phi \leq 0.5$). Surprisingly, in the non-dilute regime, the viscosity at any given volume fraction was found to be a non-monotonic function of the aspect ratio, with the minima occurring for a particle with an aspect ratio of approximately 1.5. This property correlates well with the maxima in close-packing or even the random close-packing at an aspect ratio of approximately 1.5. A similar trend was observed in translational self-diffusion, but not in rotational self-diffusion which was found to decrease monotonically with aspect ratio.

(b) *Microstructure, orientation, and rheology in non-Brownian suspensions of dicolloids (chapter 3)*: In a second series of studies using the Stokesian Dynamics technique,

we performed dynamic simulations on sheared dicolloidal particle suspensions. A disordered microstructure was obtained for all particle shapes, except for suspensions of spherical and dicolloidal particles with small degree of anisotropy at a volume fraction of $\phi = 0.55$. Again, for disordered suspensions, a non-monotonic variation in viscosity with aspect ratio was observed. In disordered suspensions, both the first and the second normal stress differences were negative. Orientation behavior of the dicolloids showed a very interesting variation with volume fraction. At low volume fractions, particles with fore-aft symmetry showed a shift to higher Jeffery's orbit constant, i.e. a shift towards an alignment in the flow-gradient plane. On the other hand, particles without fore-aft symmetry showed very little change in orientational order at low volume fractions in comparison to the corresponding infinite dilution values. At higher volume fractions, relative to the dilute results, all particle shapes showed a shift towards lower orbit constants, i.e. towards an alignment with the vorticity direction. This orientational behavior was explained using a novel micromechanical model based on the coupling of a particle's angular velocity and the hydrodynamic stresslet through the mobility tensor.

(c) *Microstructure, orientation and rheology in sheared Brownian suspensions of dicolloids (chapter 4)*: We used Fast Lubrication Dynamics to study charged Brownian suspensions of dicolloidal and spherical particles at volume fractions $\phi = 0.42$ and $\phi = 0.55$ over a wide range of Pećlet numbers: $0 \leq Pe \leq 100$. All the microstructural transitions observed in experiments were captured. These include crystalline, strained crystalline, polycrystalline, sliding layers, strings, and amorphous states. Orientation behavior of the dicolloidal particles again showed interesting transitions with Pećlet number. At rest, the suspension was found to be orientationally disordered, but around $Pe = 10$ an increased flow-gradient alignment was observed in homonuclear particle suspensions at $\phi = 0.55$, while an increased flow alignment was observed in suspensions of fused-dumbbells at both the volume fractions. At higher shear rates ($Pe > 50$), consistent with the study on non-Brownian suspensions, a gradual shift towards vorticity alignment with increasing Pećlet number was observed .

(d) *Order disorder effects in charged colloidal suspensions and its rheological consequences*

(chapter 5): In this study, we performed simulations to determine the phase behavior and rheology in charged spherical particle suspensions using the Fast Lubrication Dynamics technique. It was found that, for a given screening length of the repulsive interaction, there existed a range of surface potentials for which both the ordered and disordered states were metastable. A phase diagram was constructed in shear rate vs. interaction strength which gave the region where both the ordered and disordered states were metastable. This region was found to have a strong dependence on the shear rate and showed a maximum width around $Pe = 0.5$. The presence of both the ordered and disordered states allowed us to characterize both the branches of viscosity as a function of shear rate. In contrast to the common view, it was found that the disordered branch can have a lower viscosity than the ordered branch at low enough shear rates ($Pe < 0.05$ in this study). This was attributed to the much smaller diffusivity in the ordered state, which leads to a greater distortion of the microstructure and hence stress at the same shear rate. On the other hand, at higher shear rates, ordered states with close packed planes aligned in the flow-vorticity direction were able to minimize the distortive effects of shear, and consequently have lower viscosities than the corresponding disordered states. This study can answer the unexplained stress reduction due to an order to disorder transition in some experimental studies on charge stabilized suspensions at low shear rates.

(e) *Discontinuous shear thickening transition (chapter 7)*: The goal of this study, which is still in progress, is to investigate the discontinuous shear thickening transition in colloidal suspensions. This kind of behavior is commonly reported in experimental studies at high volume fractions, but has yet to be observed in numerical studies on colloidal suspensions. In preliminary work, using Fast Lubrication Dynamics, we have found that the viscosity increases only as the $\log \delta$, where δ is the characteristic gap in the system. This behavior persists at gaps as low as $10^{-6}\times$radius and for volume fractions as high as $\phi = 0.62$. This logarithmic increase in viscosity possibly rules out pure hydrodynamics as a sole mechanism for a sudden discontinuous rise in viscosity with small increases in the shear rate. More studies are underway to clarify the dynamics in this near jamming region.

Appendix A

One Body Coefficients

In this appendix, we give additional detail on the calculation of the coefficients for the singularities that describes the one body solution in any arbitrary linear flow field (similar to equation 2.9). To begin, we may without loss of generality choose a frame with the z axis aligned along the axis of the dicolloid particle (Figure 2.8). Any combination of uniform and linear flows can be written as a linear combination of 11 independent flows . In the frame aligned with the particle, a set of 11 independent flow fields may be chosen as follows: three uniform velocities

$$\boldsymbol{u}_1 = (1,0,0) \qquad \boldsymbol{u}_2 = (0,1,0) \qquad \boldsymbol{u}_3 = (0,0,1) \tag{A.1}$$

three rotational velocities

$$\boldsymbol{\omega}_1 = (1,0,0) \qquad \boldsymbol{\omega}_2 = (0,1,0) \qquad \boldsymbol{\omega}_3 = (0,0,1) \tag{A.2}$$

and five rate of strain tensors: e_1 to e_5

$$\begin{gathered}
\boldsymbol{e}_1 = \begin{pmatrix} -1 & 0 & 0 \\ 0 & -1 & 0 \\ 0 & 0 & 2 \end{pmatrix} \quad \boldsymbol{e}_2 = \begin{pmatrix} 1 & 0 & 0 \\ 0 & -1 & 0 \\ 0 & 0 & 0 \end{pmatrix} \quad \boldsymbol{e}_3 = \begin{pmatrix} 0 & 1 & 0 \\ 1 & 0 & 0 \\ 0 & 0 & 0 \end{pmatrix} \\
\boldsymbol{e}_4 = \begin{pmatrix} 0 & 0 & 1 \\ 0 & 0 & 0 \\ 1 & 0 & 0 \end{pmatrix} \quad \boldsymbol{e}_5 = \begin{pmatrix} 0 & 0 & 0 \\ 0 & 0 & 1 \\ 0 & 1 & 0 \end{pmatrix} \quad \boldsymbol{e}_6 = \begin{pmatrix} 1 & 0 & 0 \\ 0 & 0 & 0 \\ 0 & 0 & -1 \end{pmatrix}
\end{gathered} \tag{A.3}$$

Here e_6 is defined for convenience as a linear combination $e6 = (e_2 - e_1)/2$.

Now, let $\boldsymbol{p}^{\Theta l}$ represent the solution for the coefficient of the Stokeslet at location 'l' in a flow Θ, where Θ could be one of the following: $\boldsymbol{u}_1$, $\boldsymbol{u}_2$, $\boldsymbol{u}_3$, $\boldsymbol{\omega}_1$, $\boldsymbol{\omega}_2$, $\boldsymbol{\omega}_3$, $\boldsymbol{e}_1$, $\boldsymbol{e}_2$, $\boldsymbol{e}_3$, $\boldsymbol{e}_4$, $\boldsymbol{e}_5$. In a similar fashion, let $\boldsymbol{q}^{\Theta l}$ be the coefficient of Stokes doublet at location l in a flow Θ, $\boldsymbol{s}^{\Theta l}$ be the coefficient of Potential dipole at location l in a flow Θ, and $\boldsymbol{t}^{\Theta l}$ be the coefficient of Potential quadrupole at location l in a flow Θ. For a given particle shape, these coefficients need be computed just once for the 11 independent flows above. In fact, for axisymmetric particles, a number of these flows are equivalent by symmetry, and the set reduces to 7 independent flows consisting of $\boldsymbol{u}_1, \boldsymbol{u}_3, \boldsymbol{\omega}_1$, $\boldsymbol{\omega}_3$, e_3, e_4, e_6.

To transform from a global lab frame to the local particle frame, a simple orthogonal transformation is required defined by a 3×3 matrix $\boldsymbol{C}$ whose columns are the components of the base vectors for the particle frame referred to the lab frame. By standard tensor algebra, vectors $\boldsymbol{v}^g$ in the global frame are translated to vectors $\boldsymbol{v}^p$ in the particle frame via

$$\boldsymbol{v}^p = \boldsymbol{C}^T \boldsymbol{v}^g \tag{A.4}$$

and similarly, tensors $\boldsymbol{T}$ are transformed according to

$$\boldsymbol{T}^p = \boldsymbol{C}^T \boldsymbol{T}^g \boldsymbol{C} \tag{A.5}$$

For a particle imposed in a general flow field, the solution procedure is as follows. Compute the coefficients for the 7 independent local flow fields and store the results. This is an initialization procedure. For given global field quantities $(\boldsymbol{U}, \boldsymbol{\Omega}, \boldsymbol{E})$ transform to the local frame and assemble the solution $\boldsymbol{p}, \boldsymbol{q}, \boldsymbol{s}, \boldsymbol{t}$ from linear superposition of the 7 reference solutions. Transform the coefficients back to the global frame using the inverse transform matrix $\boldsymbol{C}^{-1}$. Of course, since $\boldsymbol{C}$ is an orthogonal transform, $\boldsymbol{C}^{-1} = \boldsymbol{C}^T$. This completes the computation of the coefficients of the singularity solution for particles at arbitrary orientations immersed in an arbitrary linear flow field.

Solutions for the coefficients of the one body singularity solutions for the 7 independent reference flows for all particle shapes considered in this work may be obtained from the

authors on request.

Appendix B

Statistical Measures of the Microstructure

In this chapter, we give a brief overview of some of the important microstructures observed in spherical suspensions at rest, and under shear. We also discuss two of the important statistical measures of the microstructure, pair distribution function and structure factor.

B.1 Some Standard Microstructures

Suspensions at rest, which forms an ordered state, usually have a close packed structure. For presheared suspensions, the close packed planes are oriented in the flow-vorticity plane as shown in Fig (B.1). These close packed planes are stacked on top of each other in the gradient direction. This introduces the concept of registration, and stacking sequence. In order to better understand these, we define the concept of close packed sites A,B, and C. Consider a reference layer, and assume the locations occupied by the particles are called the 'A' sites (Fig B.1a). In a close packed structure, the particles in the neighboring layers then sits in the hollows formed by the particles in the reference layer. Note that there are two such possible locations, named 'B', and 'C' in Fig (B.1a), which are also referred as close packed twin sites. We call a system registered, if all the particles occupy close packed sites, i.e. A, B, or C. Stacking sequence, as the name implies, is the sequence which gives the locations occupied by a sequence of layers in terms of A, B, and C. Now, there are two important types of stacking sequences, which leads to the definition of the face-centered cubic (FCC) and hexagonally close packed (HCP) crystals. A FCC crystal has the stacking sequence given by ABCABC... (or its twin ACBACB...), and HCP has a stacking sequence given by ABABAB... (or its twin ACACAC...). A system can also show a random sequence, which is called registered random stacking (RRS).

Suspension at low rates of shear, maintains a close packed structure, and shears by hopping from one close packed site to its twin, e.g. from B to C (Fig B.1b). This is normally referred to as the strained crystalline microstructure (Chen *et al.*, 1994), as particles are strained to the elastic limit before they jump from one close packed site to it's twin.

At high rates of shear, a sliding layer microstructure is observed. The microstructure is shown in Fig (B.1c). In this case, the particles move in a straight trajectory. Also, a row of particles centers itself between two rows of particles in the neighboring layers. This is shown by the dashed lines in Fig (B.1c).

B.2 Pair Distribution Functions

Pair distribution function gives the probability of finding a second particle at a given location $(\mathbf{x}, \mathbf{y}, \mathbf{z})$, given a (reference) particle is at the origin. So, the number of particles in a bin of volume $d\mathbf{x}d\mathbf{y}d\mathbf{z}$ located at $\mathbf{x}, \mathbf{y}, \mathbf{z}$, could be given by

$$dP_2(\mathbf{x}, \mathbf{y}, \mathbf{z}) = \rho g(\mathbf{x}, \mathbf{y}, \mathbf{z}) d\mathbf{x}d\mathbf{y}d\mathbf{z} \tag{B.1}$$

which assumes that a reference particle is at the origin. In the above equation, $P_2(\mathbf{x}, \mathbf{y}, \mathbf{z})$ refers to the number of particle pairs at a relative separation of $(\mathbf{x}, \mathbf{y}, \mathbf{z})$, and ρ is the number density of particle pairs in the system given by

$$\rho = \frac{N_p(N_p - 1)}{V} \tag{B.2}$$

where N_p is the number of particles in the system, and V is the volume of the system. Equation (B.1) can be used to calculate the pair distribution function $g(\mathbf{x}, \mathbf{y}, \mathbf{z})$, from the known particle positions.

In our results, we would normally report the pair distribution functions in the front, top, and end views. To understand this nomenclature, consider a plane couette flow as shown in Fig (B.2). Then, as shown in the previous figure, the front view denotes the view of the velocity-gradient plane (**x**-**y**), top view denotes the view of the velocity-vorticity plane (**x**-**z**),

and end view denotes the view of the vorticity-gradient plane (**z**-**y**). Mathematically, pair distribution function in the front view refers to $g(\mathbf{x}, \mathbf{y}, 0)$, in the top view refers to $g(\mathbf{x}, 0, \mathbf{z})$, and in the end view refers to $g(0, \mathbf{y}, \mathbf{z})$.

Pair distribution functions can also be used to investigate the correlations between particles located in different layers. We call this as the inter-layer pair distribution functions. This can be particularly helpful in finding the stacking sequence. Also note that the particles located in different layers are in relative motion. So, these inter-layer pair distribution functions can also be used to infer the style of particle motion, and the trajectory followed. In this work, we will restrict our attention to inter-layer pair distribution functions for adjacent layers and for layers separated by a single layer. Mathematically, these can be expressed as $g(\mathbf{x}, l_y, \mathbf{z})$, and $g(\mathbf{x}, 2l_y, \mathbf{z})$, where l_y is the inter layer separation. We now outline the procedure for inferring the stacking sequence from the inter-layer pair distribution function. For a perfect FCC crystal, $g(\mathbf{x}, l_y, \mathbf{z})$ will show peaks at one of the close packed twin sites, e.g. at B sites. Then $g(\mathbf{x}, 2l_y, \mathbf{z})$ will show peaks at C sites. For a HCP crystal, $g(\mathbf{x}, l_y, \mathbf{z})$ would show an equal probability at B, and C sites, while $g(\mathbf{x}, 2l_y, \mathbf{z})$ will show peaks at A sites. A registered random stacking would show equal probability at both B, and C sites in $g(\mathbf{x}, l_y, \mathbf{z})$. $g(\mathbf{x}, 2l_y, \mathbf{z})$ would show equal probability at B, and C sites, both of which would be half of the probability at the A sites. These probabilities for site occupancy, stems from the fact that FCC lattice can be generated by displacing a layer by a vector $\mathbf{a_1}$ from the previous, while HCP lattice can be generated by alternating between $\mathbf{a_1}$, and $\mathbf{a_2}$ (Loose & Ackerson, 1994). $\mathbf{a_1}$ can be a vector pointing from a 'A' site to a 'B' site, in which case $\mathbf{a_2}$ is the vector pointing from a 'A' site to a 'C' site.

B.3 Structure Factor

Microstructure in colloidal suspensions are mostly investigated by diffraction (scattering) experiments. The diffraction intensity, which is the observed quantity, is related to the structure factor, which as the name implies is related to the microstructure. In the following section, we give the relationship between diffraction intensity, structure factor, and the actual particle positions.

B.3.1 Relationship of Diffraction Intensity and Structure Factor with Microstructure

The treatment in this section follows that in the book by Guinier (Guinier, 1963). Lets consider a system of N particles with locations $\mathbf{x_1}$, $\mathbf{x_2}$, ..., $\mathbf{x_n}$. Let f_1, f_2, ..., f_n be the scattering factors (form factors) for the N particles. It is assumed that the object is small enough that absorption can be neglected. Let $\mathbf{S_0}$, and $\mathbf{S}$ be the unit vectors directed respectively along the incident beam, and in the direction of observation. The resultant amplitude, due to the interference of waves originating from each of the particles, is given by (note the phase for all the waves is with respect to an imaginary wave originating from the origin)

$$A = \sum_{n=1}^{n=N} f_n \; exp\; (-2\pi i \frac{\mathbf{S} - \mathbf{S_0}}{\lambda} . \mathbf{x_n}) \tag{B.3}$$

Let us define $\mathbf{s} = \frac{\mathbf{S}-\mathbf{S_0}}{\lambda}$ as a point in the reciprocal space and in this space the diffracted amplitude is given by

$$A(\mathbf{s}) = \sum_{n=1}^{n=N} f_n \; exp\; (-2\pi i \mathbf{s}.\mathbf{x_n}) \tag{B.4}$$

The scattered intensity due to N particles, $I_N(\mathbf{s})$, is therefore

$$I_N(\mathbf{s}) = A(\mathbf{s}) A^*(\mathbf{s}) \tag{B.5}$$

Using the value of $A(\mathbf{s})$, we obtain

$$I_N(\mathbf{s}) = \sum_{n=1}^{n=N} f_n \; exp\; (-2\pi i \mathbf{s}.\mathbf{x_n}) \sum_{m=1}^{m=N} f_m \; exp\; (2\pi i \mathbf{s}.\mathbf{x_m}) \tag{B.6}$$

which simplifies to

$$I_N(\mathbf{s}) = \sum_{n=1}^{n=N} \sum_{m=1}^{m=N} f_n f_m \exp\; (-2\pi i \mathbf{s}.(\mathbf{x_n} - \mathbf{x_m})) \tag{B.7}$$

which can be written as (assuming $f_i = F \; \forall \; i$)

$$I_N(\mathbf{s}) = NF^2 + F^2 \sum_{(n,m),n\neq m} 2\cos(2\pi \mathbf{s}.\mathbf{x}_{nm}) \tag{B.8}$$

where $\mathbf{x}_{nm} = \mathbf{x}_n - \mathbf{x}_m$, and each pair is considered just once. We then define the interference function as follows

$$\mathcal{I}(\mathbf{s}) = \frac{I_N(\mathbf{s})}{NF^2} \tag{B.9}$$

So, the interference function can be written as

$$\mathcal{I}(\mathbf{s}) = 1 + \frac{1}{N} \sum_{(n,m),n\neq m} 2\cos(2\pi \mathbf{s}.\mathbf{x}_{nm}) \tag{B.10}$$

Note that in all our results the interference function will be reported as the structure factor. So, the structure factor is directly related to the real Fourier transform of the pair distribution function. Hence, structure factor is also known as pair correlations in the reciprocal space.

B.3.2 Interpreting the Structure Factor

For a registered hexagonally close packed layers system, structure factor shows six fold maxima in the k_x-k_z plane as shown in Fig (B.3), though for a perfect FCC system peaks in the inner ring would be suppressed (Loose & Ackerson, 1994). To obtain the stacking sequence, the modulation in intensity along k_y is investigated for a fixed k_x, and k_z corresponding to the location of one of the peaks. In our results, we will report the modulation in intensity along the maxima denoted by q_1 in the Fig (B.3), for which $k_x = \frac{2\pi}{d}$, and $k_z = \frac{2\pi}{\sqrt{3}d}$, where d is the crystal lattice parameter $2a(\frac{\phi_{max}}{\phi})^{\frac{1}{3}}$. For a perfect FCC crystal, $q_1(k_y)$ would show delta-function maxima at $\frac{k_y d}{2\pi} \in [0.41, 0.81]$, while for a perfect HCP crystal, it would show delta-function maxima at $\frac{k_y d}{2\pi} \in [0, 0.61]$. For registered random stacking, a broad maxima would be observed around $\frac{k_y d}{2\pi} = 0.61$. Exact curve for the modulation in intensity along $q_1(\frac{k_y d}{2\pi})$ has been worked out for an arbitrary stacking sequence (Loose & Ackerson, 1994),

and is given by the following equation

$$q_1(k_y) = |F(q_1)|^2 \frac{3\alpha(1-\alpha)}{4(1-2\alpha)(1-\cos^2(\sqrt{2/3}k_y d) + 5\alpha^2 + 4\alpha^2\cos(\sqrt{2/3}k_y d)} \tag{B.11}$$

In the above equation α gives the stacking sequence. For a FCC crystal, $\alpha = 1$, while for a HCP crystal, $\alpha = 0.0$. A random stacking sequence leads to $\alpha = 0.5$. Curve fitting can be used to obtain the value of α from a known $q_1(k_y)$ (Versmold *et al.*, 2000).

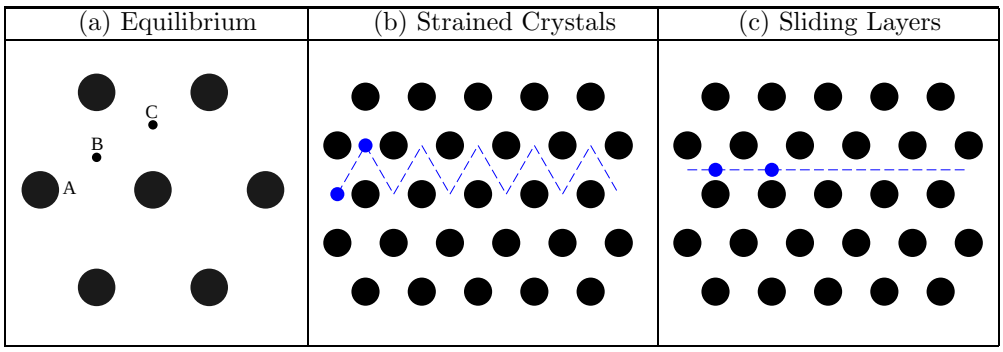

Figure B.1: Layered microstructure in suspensions: (a) Stacking of hexagonal layers at equilibrium. Sites occupied by particles in the base layer is denoted by A (large spheres), while those of the adjacent layers (small spheres) are denoted by B and C. Only one of the B or C sites can be occupied at a time, (b) Strained crystal microstructure, and (c) Sliding layer microstructure.

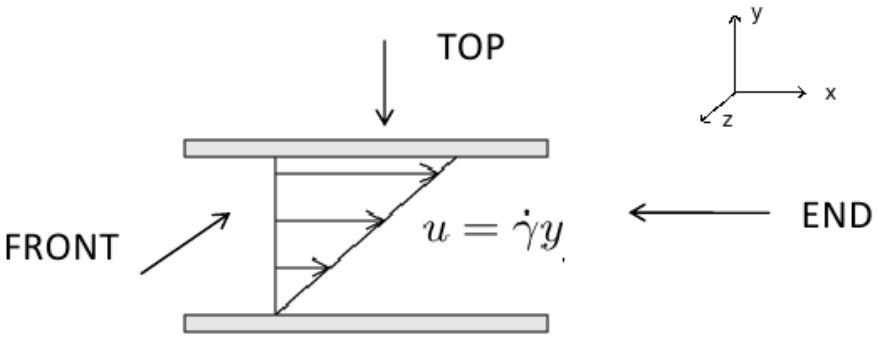

Figure B.2: Definition of Views

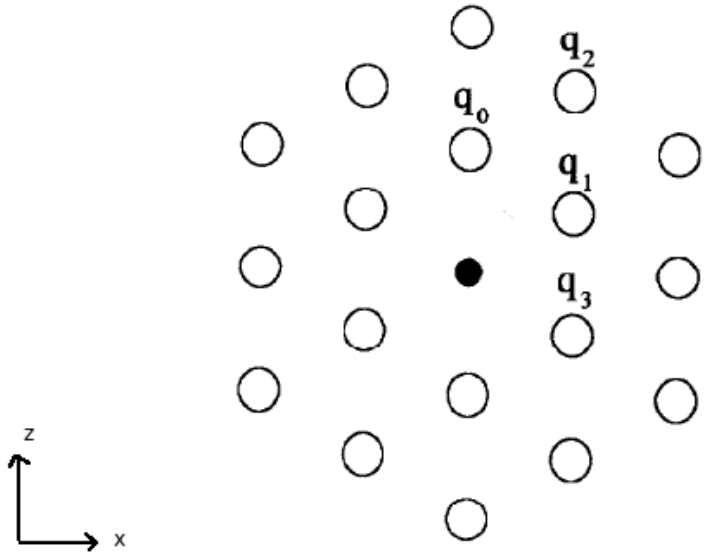

Figure B.3: Location of the peaks in the structure factor for hexagonally packed layers stacked in the gradient direction (taken from Chen *et al.* (1994)).

References

Chen, L.B., Ackerson, B.J., & Zukoski, C.F. 1994. Rheological consequences of microstructural transitions in colloidal crystals. *Journal of Rheology*, **38**(2), 193–215.

Guinier, A. 1963. *X-Ray Diffraction In Crystals, Imperfect Cystals, and Amorphous Bodies*. W. H. Freeman and Company.

Loose, W., & Ackerson, B.J. 1994. Model calculations for the analysis of scattering data from layered structures. *Journal of Chemical Physics*, **101**(9), 7211–7220.

Versmold, H., , & Dux, Ch. 2000. Scattering experiments on the structure of colloidal dispersions: hexagonal layers or cubic crystals? *Journal of Colloid & Polymer Science*, **278**, 181–185.

Appendix C

Rheology in Charged Brownian Suspensions of Spheres and Dicolloids

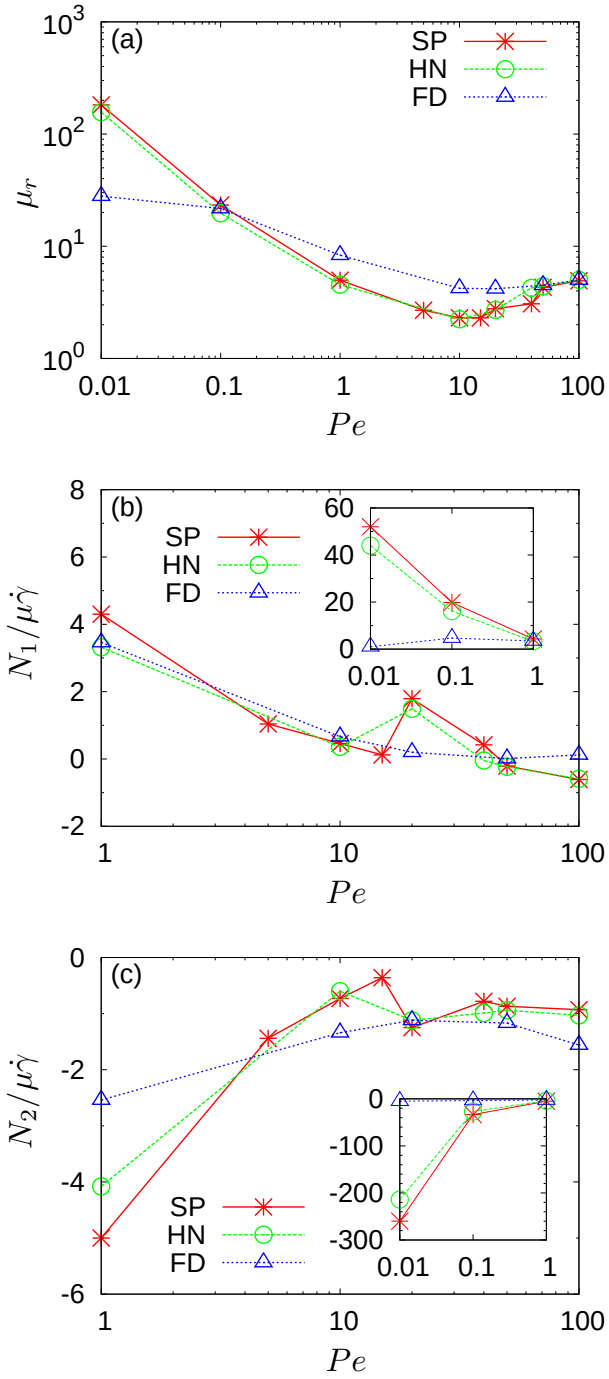

Figure C.1: (a) Viscosity (μ_r), (b) first normal stress difference (N_1), and (c) second normal stress difference (N_2) at a volume fraction of $\phi = 0.42$. These results correspond to the Brownian suspensions presented in chapter (4). Inset in (b) and (c) have the same axes as the main figure. In the figures, sphere is denoted by SP, homonuclear by HN, and fused-dumbbell by FD.

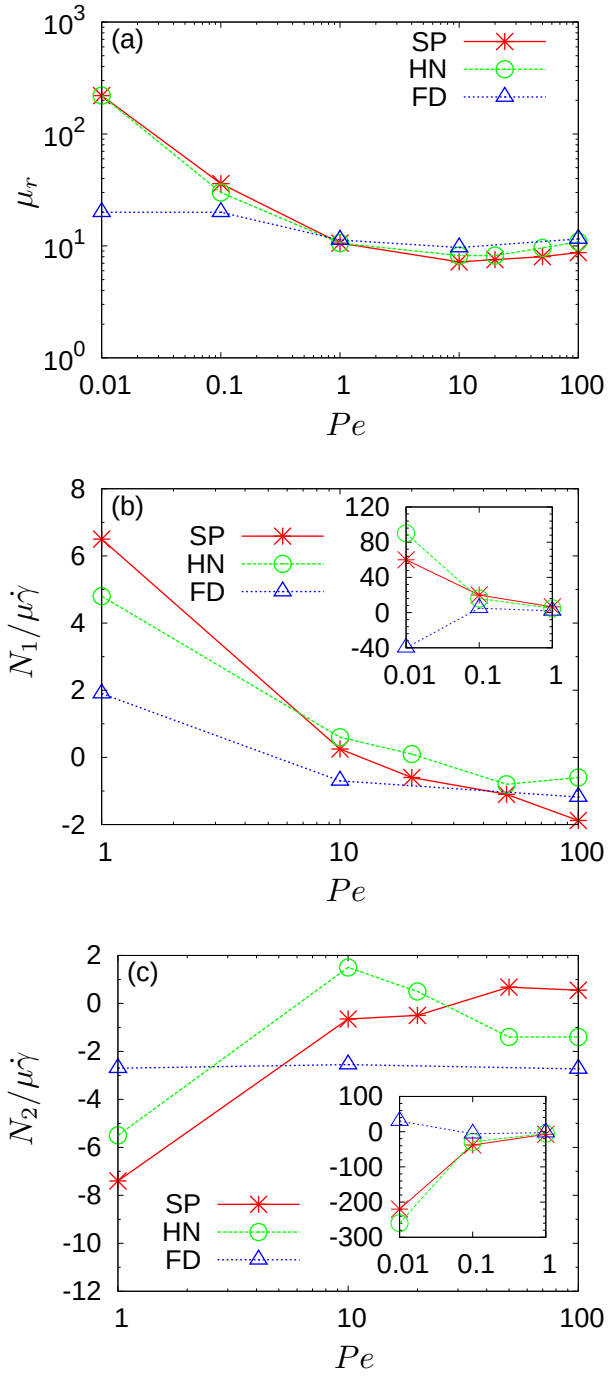

Figure C.2: (a) Viscosity (μ_r), (b) first normal stress difference (N_1), and (c) second normal stress difference (N_2) at a volume fraction of $\phi = 0.55$. These results correspond to the Brownian suspensions presented in chapter (4). Inset in (b) and (c) have the same axes as the main figure. In the figures, sphere is denoted by SP, homonuclear by HN, and fused-dumbbell by FD.